JOHANNES GUTENBERG-UNIVERSITÄT MAINZ

Synthesis of Carbohydrate Antigens against Serotype 3 *Streptococcus pneumoniae* and Supramolecular Hydrogels Crosslinked via Cucurbit[8]uril Host-Guest Complexation

Dissertation

zur Erlangung des Grades

„Doktorin der Naturwissenschaften“

im Promotionsfach Chemie

am Fachbereich Chemie, Pharmazie, Geographie und Geowissenschaften

der Johannes Gutenberg-Universität Mainz

vorgelegt von

Yuqing Wang

geboren in Beijing, China

Mainz, 2024

Datum der Abgabe: 24. September 2024

Datum der mündlichen Prüfung: 28. November 2024

Every action you take is a vote for the type of person you wish to become.

No single instance will transform your beliefs,

but as the votes build up, so does the evidence of your new identity.

– James Clear

To my family

who showed me unconditional love

and taught me the value of hard work and consistency.

Preamble

This thesis was started in April 2021 and completed in September 2024 at the Department of Chemistry of Johannes Gutenberg University Mainz. Partial sections of the thesis have been published in international scientific journals or are in preparation for submission.

D77 – Dissertation Johannes Gutenberg University Mainz

Acknowledgements

Collaborations and Contributions

Kurzzusammenfassung

Aufgrund des Potentials zum Aufbau von komplexen und dynamischen Strukturen haben supramolekulare Materialien zunehmend Aufmerksamkeit in der biomedizinischen Forschung bekommen. Durch die Anwendung von synthetischen Ansätzen werden Bausteine für die Entwicklung von supramolekularen multivalenten Glycokonjugat-Impfstoffen und Biotinten im Rahmen dieser Arbeit hergestellt.

Die Arbeit beginnt mit einem Einleitungskapitel 1, um eine Übersicht über den aktuellen Stand der Forschung im Hinblick auf die Entwicklung von Kohlenhydrat-Impfstoffen, Technologien sowie Materialien für Bioprinting und die Untersuchungsmethoden von Hydrogeldynamik darzustellen. Unter jedem Thema werden verschiedene Konzepte zu Materialdesign und Synthesemethoden anhand von Beispielen aus der aktuellen Forschung erläutert. Kapitel 3 setzt den Fokus auf die Synthese von Kohlenhydrat-basierte Epitope für den Einsatz in supramolekularen Glycokonjugat-Vakzinen gegen den Serotyp 3 des Bakteriums *Streptococcus pneumoniae*. Da Cellobiuronsäure als die kleinste Antigeneinheit bewiesen ist, werden verschiedene Vorstufen und Derivate davon aus Cellobiose synthetisiert. Für Synthese von Oligomeren der Cellobiuronsäure, ähnlich wie die Polysaccharide aus der Bakterienkapsel, werden Methoden für die regioselektive Schützung der Position O-3' entwickelt. Somit kann anschließend die Herstellung des Monomers und die Verknüpfung von 1,3'-β glykosidischen Bindungen zum Aufbau längerer Saccharid-Strukturen ermöglicht werden. Im Kapitel 4 werden supramolekulare Hydrogele aus interpenetrierende Netzwerken (IPN) vorgestellt, deren Vernetzung durch Cucurbit[8]uril (CB[8])-basierte Wirt-Gast-Komplexierung sowie Photochemie eingeleitet ist. Diese Hydrogele sollen als Biotinten für Bioprinting eingesetzt werden. Durch Nutzung von funktionalisierten sternförmigen Polyethylenglykol-Makromeren und CB[8] werden Hydrogel-netzwerke erhalten, die schnelle Stressrelaxation, scherverdünnende und selbstheilende Eigenschaften sowie Formstabilität nach dem abgeschlossenen Druckvorgang aufweisen. Um die Anwendungs-möglichkeiten der CB[8]-vernetzte Hydrogelnetzwerke zu erweitern wird die Diffusion von gelösten Substanzen über *fluorescence recovery after photobleaching* (FRAP) untersucht. Durch Zugabe von Kleinmolekül-Farbstoffen und Farbstoffproteinen, die entweder als frei-diffundierende Spezies fungieren, oder mit einem CB[8] Erkennungsmotif versehen sind, wird der Einfluss von Größe des Moleküls und der Bindungskinetik auf das Diffusionsverhalten analysiert.

Abstract

Supramolecular functional materials have become increasingly popular within biomedical research due to its potential of building up complex and dynamic structures. Using synthetic bottom-up approaches, building blocks for the creation of supramolecular multivalent glycoconjugate vaccines and biomaterial inks for 3D-bioprinting are synthesized in the present work.

The thesis starts with introductory chapter 1 to give an overview of the current state of research regarding the development of carbohydrate vaccines, technologies and materials for bioprinting applications as well as investigation of dynamics within hydrogel networks. Within each subchapter, different concepts of material design and synthetic methods are elucidated based on present examples from the research. Chapter 3 focuses on the synthesis of carbohydrate epitopes for the usage in supramolecular glycoconjugate vaccines against serotype 3 *Streptococcus pneumoniae*. Since cellobiuronic acid has been proven to be the smallest antigen unit, different precursors and derivatives are synthesized from cellobiose. For the synthesis of cellobiuronic acid oligomers that are similar to the capsular polysaccharides, methods for site-selective O-3' functionalization are developed to prepare the monomer unit, which can be further assembled into longer structures through 1,3'-β glycosylations. In chapter 4, supramolecular interpenetrating network (IPN) hydrogels crosslinked through cucurbit[8]uril (CB[8]) mediated host-guest complexation and photochemistry are introduced as biomaterial inks. Using functionalized star-shaped poly(ethylene glycol) (PEG) macromers, hydrogel networks exhibiting fast stress relaxation, shear-thinning and self-healing properties as well as post-printing form stability are formed and studied under cell culture and bioprinting conditions. To expand the application of the CB[8] crosslinked hydrogel platforms, the solute diffusion is investigated in chapter 5 via fluorescence recovery after photobleaching (FRAP) experiments. By incorporating small molecule dyes and fluorescent proteins either as free diffusing species or with decoration of CB[8] binding motifs, the impact of molecule size and binding kinetics on the diffusion process are assessed.

Table of Contents

1 Introduction

1.1 Antibacterial Carbohydrate Vaccines

1.1.1 Vaccine Immunology

In human health care worldwide, fighting against pathogens such as bacteria, viruses and parasites has always been one of the greatest tasks. To cure infectious diseases, patients are treated using antibiotic, antiviral and antiparasitic medications. Owing to the issues with antibiotic resistance and evolution of multi-drug resistant bacteria strains, the need of developing preventative strategies through vaccination to protect human from infections has become increasingly urgent in current research.[1]

In the first vaccines developed in history, attenuated or killed organism were used, which showed long-lasting immunity against the corresponding pathogens. Using this approach, the British surgeon Edward Jenner was able to protect children from smallpox in 1796 by injecting cowpox, which was obtained through draining purulence from cow blisters.[1] Following this discovery, similar techniques have been applied over decades. Though whole cell vaccines are highly effective, the cultivation of high quantities of pathogen was difficult and attenuated microorganisms were able to cause unexpected infections in individuals.[2] Therefore, subunit vaccines containing microbial components like secreted toxins, virus-like particles or cell-surface glycans were often considered as the safer option.[3] Besides the safety issue, subunit vaccine approach can be produced with better batch-to-batch consistency, induce targeted immune responses towards specific pathogenic determinants and may enable development of vaccines for cases where the traditional whole cell approach has failed, for example against human immunodeficiency viruses (HIV).[4] Despite multiple advantages, subunit vaccines usually lack pathogen-associated molecular patterns (PAMPs) that are necessary for the recognition by innate immune cells through stimulation of pattern-recognition receptors (PRRs), and thus require additional immunostimulatory compounds (adjuvants) for higher vaccine efficacy. In addition, vaccination has to take place several times (boosters) to ensure sufficient long-term immunity.

In general, the induction of long-term protective immune responses (by contact with the pathogen or through vaccination) involves different compartments across the body, each with its own cell composition and function (Figure 1.1). Tissues directly exposed to the outer environment, such as skin, lungs and mucosal sites, are the first locations to detect extraneous organisms or compounds through immune cells.[5] Vaccines are typically administered intramuscularly, subcutaneously or intradermally, leading to a local innate immune cell infiltration, activation and antigen uptake.[6,7] Components of the vaccine are endocytosed, fragmented by antigen-presenting cells (APC) and presented on major histocompatibility complex (MHC) molecules on the surface of the APCs. When the vaccine contains adjuvants, innate immune cells (e.g. dendritic cells and macrophages) can immediately respond by

cytokine production that attract immune cells to the injection site. The activation of dendritic cells and their signaling to T helper cells (Th cells) are critical for the outcome of the immune response.[8,9]

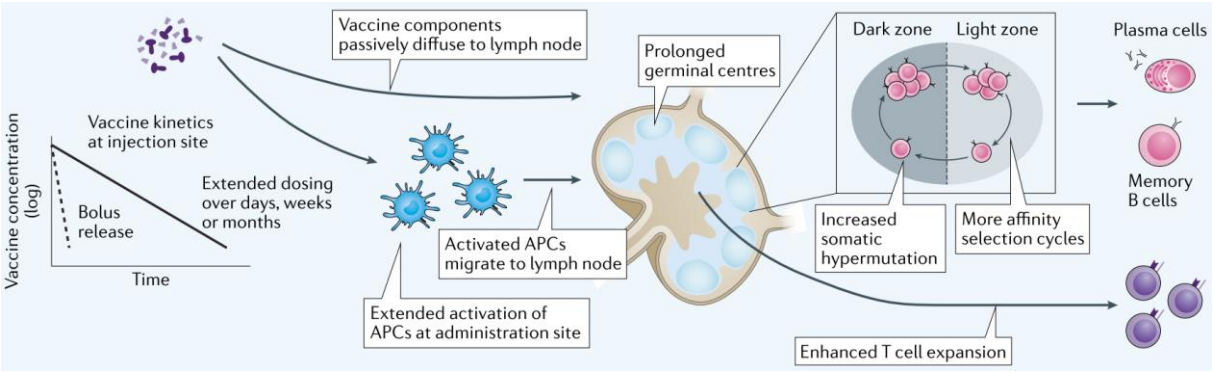

Figure 1.1: Immunological responses after the administration of a vaccine. Reprinted with permission from ref[5]. Copyright © 2021, Springer Nature Limited.

After the initial vaccine response at the administration site, activated cells and vaccines components enter the lymphatics and travel to the draining lymph nodes, where maturation of B and T cells as well as the development of an adaptive immune response take place.[10,11] In the T cell zone, migratory dendritic cells can either present antigens directly to T cells or transfer antigens to lymph node-resident dendritic cells[12,13], which can activate $CD8^+$ T cells. Their interaction with major histocompatibility complex (MHC) class I molecules accompanied by co-stimulatory and cytokine signals leads subsequently to maturation and expansion of antigen-specific cytotoxic T cells.[14,15] Furthermore, $CD4^+$ T helper cells are activated by APCs to promote humoral immunity. In the B cell follicles, antigen-specific B cells are activated due to antigen presentation (through APCs or passive diffusion[16]) and stimulation by $CD4^+$ T cells.[17] In activated B cells, antibodies (immunoglobulins, Ig) of different isotypes are produced by class switch recombination. Initially, naive mature B cells secrete immunoglobulin M (IgM), which can provide a fast but limited protection against pathogens attributed to its low antigen affinity. By activation of various receptors on B-cells, such as B-cell receptor (BCR), CD40 and toll-like receptors (TLR)[18], class switch recombination can be induced to express antibodies with higher affinity, including IgG and IgA.[5] Antigen-activated B cells can form transient germinal centers that is divided into the dark zone and the light zone. B cells cycle through both compartments and undergo proliferation as well as somatic hypermutation in the dark zone followed by affinity based selection in the light zone.[19] This process promotes antibody affinity maturation of B cells, which leave the germinal center as plasma cells, long-lived plasma cells or memory B cells.[20]

A successful vaccine is characterized by a long-term protection through neutralizing antibody production and cell-mediated immunity. Upon pathogen exposure, antibodies can recognize and bind to the antigens on the surface of the pathogen, in order to prevent infection of the host cells. Concurrently, T cells can be directly activated to kill infected cells to eliminate the pathogen.[5]

1.1.2 Carbohydrate Conjugate Vaccines

Upon exposure to a pathogen (bacteria, viruses, fungi, and parasites), an immune response is caused by recognition of the exogenous proteins, lipids, and carbohydrates. Though proteins are highly efficient in generating long-term immunity, they are not always directly presented on the surface of the pathogen to be detected from the immune system. Therefore, the densely distributed, unique glycan structures on the pathogen's surface have become alternative targets to induce specific immunity.[21]

In 1923, the first connection between the pneumococcal bacteria and their capsular polysaccharide (CPS) was introduced by Heidelberger and Avery.[22] The CPS of *Streptococcus pneumoniae* (*S. pneumoniae*) was later on found to be able to induce specific antibody production and protection against the bacteria, forming the foundation of carbohydrate vaccines.[23]

One of the multiple challenges in developing carbohydrate-based vaccines is related to their T-cell independent immune response. Proteins typically can be processed and presented on MHC II molecules to activate $CD4^+$ T cells, which can further generate high affinity antibodies and long-term immune responses. In contrast, binding of pure carbohydrate antigens to B-cell receptors (in case of polysaccharide vaccines) can only activate antigen-specific B cells without involving $CD4^+$ helper T cells, that generates immunoglobulin M (IgM) antibodies, leading to a weaker, short-lived immunity. In order to address $CD4^+$ helper T cells, exogeneous T-cell epitopes must be included, for example in form of a carrier protein.[21] To this end, various approaches for conjugating carbohydrates to proteins have been developed. Using tetanus toxoid (TT), diphtheria toxoid (DT) or a detoxified variant of DT (CRM197)[24] as protein carriers, glycan-specific antibodies and immunological memory can be successfully induced across different age groups.[25,26]

In a typical approach of antibacterial glycoconjugate vaccine production, glycans are isolated from cultured bacteria that are killed before by heat. After isolation through precipitation and purification via gel permeation chromatography, ultracentrifugation or enzymatic treatment, the CPS are depolymerized to obtain shorter fragments of glycans.[1] The conjugation to carrier proteins is achieved using chemical activation methods.[27] The anomeric carbon on the reducing end is usually used to attach the carbohydrate to a lysine side chain of the protein through reductive amination.[28] As an alternative, the saccharide can be oxidized using periodate to generate other aldehyde groups that can subsequently undergo reductive amination.[29] Adjuvants such as aluminum phosphate or aluminum hydroxide are often added to improve the immunogenicity of the carbohydrate antigens. Formulated vaccines can be obtained as a lyophilized powder containing glycoconjugates adsorbed to aluminum salts or suspension, which also facilitates the storage of the vaccines.[30]

Despite the enormous success of various marketed glycoconjugate vaccines against *Haemophilus influenzae* type b (Hib) and *S. pneumoniae*, the production approach using CPS from cultured bacteria is not applicable for all bacterial strains. Some polysaccharides are too labile to be isolated, others might

be too stabile to be depolymerized.[31,32] Due to the biotechnological production of antigens, it is impossible to precisely and reproducibly control the chain length of the polysaccharide, epitope number and distribution, leading to large variation of the immune response. Moreover, isolated CPS mostly contain protein or nucleotide contaminations. To obtain more structurally defined carbohydrate antigens, different methods providing access to semi-synthetic glycoconjugate vaccines have been established.[33–35] In those cases, the carbohydrate epitopes are synthesized through chemical modifications of glycan building blocks and conjugated to isolated protein carriers. Synthesized glycan structures can be readily produced with an activated spacer, through which the conjugation chemistry can be realized easily.[36] Until today, only one semi-synthetic glycoconjugate vaccine has been marketed and administrated against Hib in South America.[37]

Besides the approaches of replacing isolated CPS by synthetic glycans, several research groups focus on developing synthetic vaccine carriers such as glycolipids, peptides or polymeric materials that are self-stimulating, so that the vaccines would no longer necessitate the addition of adjuvants. When developing a vaccine, it is desirable to generate a system that can help to achieve a multivalent immune response. The use of a supramolecular vaccine platform enables to easily combine antigens with other immunostimulatory components. The individual components can be produced with defined structures and stored separately for prolonged periods. Upon mixing, they can self-assemble into larger architectures carrying different components. One of such systems has been reported by Besenius et al. based on C_3-symmetric peptide amphiphiles as monomers, which can self-organize driven by the formation of β-sheet structures. The resulting one-dimensional fibers can be observed through transmission electron microscopy (TEM). When the monomers are decorated with different immunoactive substances, it is easy to achieve formulation of a multivalent vaccine, which has been studied for antitumor vaccines.[38] Through additional presentation of mannose as water-soluble units, the pathogen-like particles can be specifically taken up by macrophages from the host immune system.[39]

1.1.3 Vaccination against Streptococcus Pneumoniae

The bacteria known as *Streptococcus pneumoniae* (*S. pneumoniae*) are potentially deadly pathogens, whereas children and the elderly are particularly affected by infections. Based on the surrounding polysaccharide capsule, the bacteria can be classified into more than 100 serotypes.[40] As the capsular polysaccharides (CPS) are responsible for the pathogenicity of the bacteria and are accessible to the immune system, the fragments of the CPS can be used as antigens for immunization.

The first pneumococcal vaccines were licensed in the 1970s containing CPS of 14 and 23 different serotypes (Pneomovx23, Merck).[41,42] Since the immune response to a polysaccharide vaccine occurs purely via B cells without the participation of T cells, the vaccine has failed to effectively induce protection against the pathogen in infants. Therefore, the polysaccharide vaccine is only recommended for children over the age of 2 years.[43] To stimulate T-cell dependent immune response, the polysaccharides were attached to carrier proteins, forming glycoconjugate vaccines. Owing to the development of pneumococcal glycoconjugate vaccines with a 10-valent (Synflorix, GSK) or 13-valent (Prevnar13, Pfizer) formulation, the incidence of disease has significantly decreased. Administration with pneumococcal glycoconjugate vaccines has also been included in the general immunization program worldwide.[44]

Although the isolation of polysaccharides from bacteria is conceptually simple, it is complex to carry out. Commercial conjugate vaccines also show that some antigens undergo undesirable reactions during manufacturing[34,45], with antigens to some serotypes lacking sufficient immunological potency[46], and antigen loading is often inconsistent[3]. Therefore, development of semi-synthetic and fully synthetic vaccines has gained increasing attention. For the immunization against serotype 3 *S. pneumoniae*, a semisynthetic vaccine approach has been reported (Figure 1.2).[47] The smallest antigenic unit cellobiuronic acid is synthesized from monosaccharide building blocks and the disaccharide antigen is attached to the carrier CRM197 (a non-toxic mutant of diphtheria toxoid).

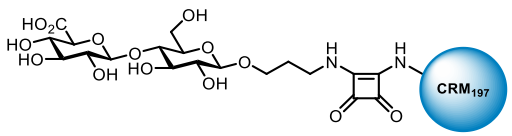

Figure 1.2: Glycoconjugate vaccine against serotype 3 *S. pneumoniae*.[48]

Besides the purity, the structure of the carbohydrate antigen (length, terminal unit and glycan modification) has a significant effect on the outcoming immune response.[49] Studies on structure-activity relationships for semisynthetic glycoconjugates with regard to antigen length and terminal unit have been carried out for serotype 3 *S. pneumoniae*, showing that conjugates with longer carbohydrate units can induce a stronger immune response.[50]

1.2 Strategies for Carbohydrate Synthesis

Carbohydrates are important substances that participate in various biochemical processes in organisms, especially in metabolism, cellular communication and recognition.[51] In contrast to other gene-coded biopolymers such as proteins and nucleic acid polymers, carbohydrates exit in huge diversity and complexity.[52] In contrast to oligosaccharides from natural sources, synthetic oligosaccharides are structurally precisely defined and their production under laboratory conditions can be clearly traced. It is therefore of great interest to produce oligosaccharides using chemical methods and thus replace the inhomogeneous oligosaccharides from biotechnological production processes.[53]

Despite advances in carbohydrate synthesis, chemical production of complex oligosaccharides remains a difficult and time-consuming process with challenges in terms of the stereo- and regioselective outcome. Some key factors here are the reactivity of the glycosyl donor and promotors as well as steric influences and participation of protecting groups[54,55], that will be further discussed in this section.

1.2.1 The Anomeric Effect

The anomeric effect describes a frequently observed phenomenon in carbohydrate chemistry, which is the preferred axial (α) configuration of the heteroatom substituent X on the anomeric center in pyranoses (Figure 1.3).[56]

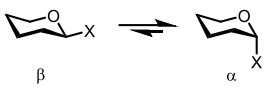

Figure 1.3: Equilibrium between both anomeric configurations.

The first explanation was proposed by Edward in 1955 based on the dipole-dipole interaction between the C5-O bond in the ring and the bond from the C1 atom to the electronegative substituent X.[57] The orientations of the C-O and C-X bond dipole moments for both anomers are shown in Figure 1.4. While both dipole moments in the β-anomer have similar orientation, they are almost antiparallel to each other in the α-anomer. The axial arrangement of substituent X therefore leads to a compensation of the two dipole moments, resulting in higher stability of the α-anomer.

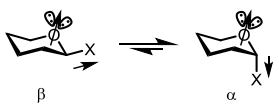

Figure 1.4: Representation of the dipole orientations in the α- and β-anomer.

However, the electrostatic model does not provide a prediction of bond angles or bond lengths at the anomeric center. Based on orbital interactions, a second model was then presented.[58] As shown in

Figure 1.5, the non-bonding n orbital of the ring oxygen and the anti-bonding σ* orbital of the C-X bond are aligned to each other in the α-anomer, so that the electrons from the non-bonding orbital can be donated into the σ* orbital and thus lower the energy. In contrast, both orbitals in the equatorial position of substituent X do not interact with each other. This leads to a higher stability of the α-anomer and at the same time explains the longer C-X bond in the α-anomer compared to the β-anomer based on the occupation of the antibonding σ* orbital.

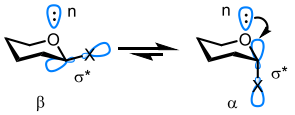

Figure 1.5: Representation of the interactions between the non-binding n orbital and anti-bonding σ* orbital.

1.2.2 Site-selective Functionalization with Orthogonal Protecting Groups

The concept of an orthogonal system was first introduced by Baranay and Merrifield regarding the installation of different protecting groups in peptide synthesis, whereas each of them can be cleaved selectively without affecting the others.[59] This was later adopted in other areas of organic chemistry.[60] In the context of carbohydrate synthesis, orthogonality can be defined in two ways. First, the activation conditions in an orthogonal glycosylation between two fully protected building saccharide blocks determines which component is the glycosyl donor and which is the glycosyl acceptor. In this way, self-condensation can be prevented. Second, orthogonal also means a combination of protecting groups of different reactivity on a saccharide building block, in which a hydroxyl group can be selectively deprotected to create a reactive site.[61]

Oligosaccharides can be synthesized through a divergent or a convergent strategy. In a divergent synthesis, the target glycan structure is built up starting from the reducing end and the following saccharide building blocks are introduced as glycosyl donors (electrophiles) to the glycosyl acceptor (nucleophiles). In case of the convergent method, different building blocks can be assembled regardless of their order in the desired compound. However, the convergent method has only been made possible by the numerous developments of protecting groups at the anomeric center, which can be selectively activated.[61] For example, a bromoglycoside and a thioglycoside can each be selectively activated in the presence of the other, so that the protecting group at the anomeric center is converted into a leaving group.[62,63]

To be able to construct oligosaccharides with glycosidic linkages on the correct position, synthetic methods for selective functionalization of hydroxyl (OH) groups on a carbohydrate building block are explored. The hydroxyl group at the anomeric center is naturally the most reactive site in the molecule due to the hemiacetal function. In a monosaccharide, from which the anomeric center is blocked by a

protecting group, a significantly higher reactivity of the primary hydroxyl group compared to the secondary hydroxyl groups can be observed due to steric demand[64], so that the primary OH groups can be selectively functionalized with bulky groups, such as silyl ethers[65,66], triphenylmethyl esters[67], trimethylacetyl(pivaloyl)esters[68] and arenesulfonates. In individual cases, selective glycosylations of primary OH groups have also been achieved.[69,70] The reactivity of secondary OH groups in pyranoses and furanoses can be distinguished when introducing bulky protecting groups. In pyranoses, equatorial OH groups are generally favored over axial OH groups (Figure 1.6A).[71] Equatorial positions adjacent to other equatorial substituents are less accessible, leading to higher relative reactivity of the position that is flanked by at least one axial substituent (Figure 1.6B and C).[72] Owing to this reason, the configuration of the anomeric center is also critical for the selective functionalization. In case of furanose derivatives, the secondary OH group on position C5 of a hexofuranoside exhibits higher reactivity than the OH groups from the 5-membered ring. Between position C2 and C3, the reactivity can differ due to steric effects caused by *cis*-substituents. In an α-ribofuranoside, position C3 is more favored compared to C2 (Figure 1.6D), while there is no selectivity within the β-derivative (Figure 1.6E).[73] In addition, sterically demanding protecting groups can also leads to shielding of free hydroxyl groups. For example, an attack on the hydroxyl group at position C4 is prevented by the *tert*-butyldimethylsilyl protecting group (TBDMS) on position C6, so that functionalization can take place selectively at position C3 (Figure 1.6F).[74]

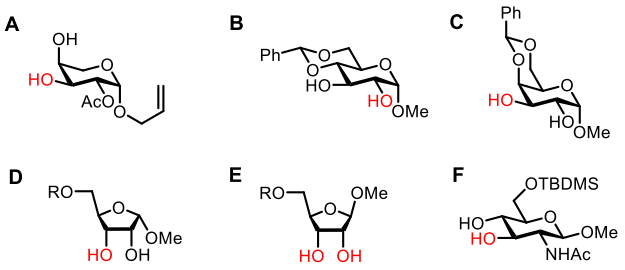

Figure 1.6: Structure of carbohydrate building blocks exhibiting different regioselectivities driven by steric effects. Preferred positions for functionalization are marked in red.

Differences in relative acidities of the hydroxyl groups can also be exploited for site-selective functionalization. Saccharides with protected anomeric center usually show selective reaction of the OH group on position C2 in the presence of a strong base.[75–77] This is caused by the inductive electron-withdrawing effect of the anomeric center, which can enhance the acidity of the OH group on position C2. The presence of a strong base can also lead to migration of various types of protecting groups within a 1,2- or 1,3-diol or through an intermolecular reaction, leading to undesired transformation of the selectively protected products.[78–81]

Besides the intrinsic reactivity pattern, formation of cyclic products involving diol groups in carbohydrates has been one of the most effective methods to distinguish OH group reactivity, which includes formation of acetals[82,83], ketals[84], boronic esters and silylenes. By formation of a 5- or 6-

membered ring, the functionalization is controlled by thermodynamic factors such as steric, torsional, and angle strain. Depending on the protecting group reagent, additional kinetic factors in terms of ring size and accessibility of OH groups are also involved. The cyclic products can also serve as a precursor to monofunctionalized building blocks through selective ring-opening reactions.[85–87]

Furthermore, multiple classes of reagents and catalyst have been developed for site-selective acylation of OH groups. For example, the choice of the leaving group can affect regioselective outcome of benzoylation. While the usage of benzoyl chloride as acylation reagent shows less preference between equatorial C2 and C3 OH groups, a selective 2-*O*-acylation can be achieved utilizing benzoylimidazole[88], benzoyl cyanide[89], benzoic anhydride, 1-(benzoyloxy)benzotriazole[90] and benzoyloxime reagent[91]. The OH groups can also be activated towards complexation with organotin[92,93] and organoboron catalysts[94,95] as well as transition metal based promotors[96–98], in order to perform selective functionalizations.

1.2.3 Chemical Glycosylation

In 1893, Emil Fischer made a groundbreaking discovery about the activation of the glucose hemiacetal, laying the foundation for carbohydrate chemistry. In an acid-promoted glycosylation, the hydroxyl group of the hemiacetal was substituted with methanol (Figure 1.7) and thus produced the first synthetic glycoside.[99] Along with the development of various glycosylation methods, including Koenigs-Knorr reaction using glycosyl halides[100] and Schmidt glycosylation using glycosyl imidates[101,102] as donors as well as different variations[103,104], larger glycan structures are now accessible through stereoselective synthesis.

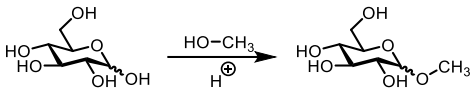

Figure 1.7: Fischer glycosylation of glucose with methanol.

Using the acid-catalyzed method, a product mixture of stereoisomers differing in the anomeric configuration is obtained. whereas the α-configuration is preferred due to the anomeric effect. The stereoselectivity with regard to the formation of the α- or β-anomer usually depends directly on the mechanism of glycosylation and the neighboring group participation of the substituent at position 2.[105] When a glycosyl donor is activated by a promotor, different intermediates can be formed before the nucleophilic attack of the glycosyl acceptor. In case of a Schmidt glycosylation using trifluoromethanesulfonic acid as promotor (Figure 1.8), the activated glycosyl donor can exist as oxocarbenium ion, solvent adduct or triflate adduct. The ratio between individual species is strongly dependent on the electronic structure of the donor molecule and the reaction conditions.[106,107] The

nucleophilic attack by the acceptor species can occur following a S_N1 or S_N2 type reaction, leading to different stereoselective outcomes.

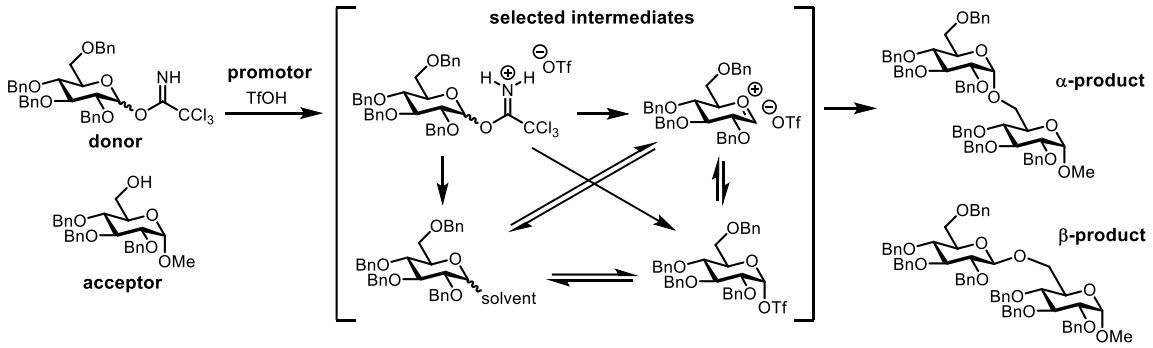

Figure 1.8: Starting materials, selected intermediates, and products of a Schmidt glycosylation.

The stereoselectivity is often controlled by the usage of participating groups, usually via protecting groups on the C2 position. As shown in Figure 1.9, an acetoxonium ion can be formed from an oxocarbenium ion in the presence of an acyl protecting group on position C2, so that one side of the anomeric center is blocked. Therefore, the attack by the acceptor can only take place from the other side of the anomeric center, leading to the formation of the 1,2-*trans* product. The stereoselectivity is higher for acyl protecting groups that are sterically more demanding.[108] Besides acyl protecting groups, other groups such as cyanomethyl ether[109], cyanobenzyl ether[110] can also be used for neighboring group participation. Furthermore, methods for stereoselective control over more distant protecting groups (remote group participation) within the same saccharide building block, for example with picoloyl and picolinyl groups[111], or even across a glycosidic bond have also been studied and reported.[112–114]

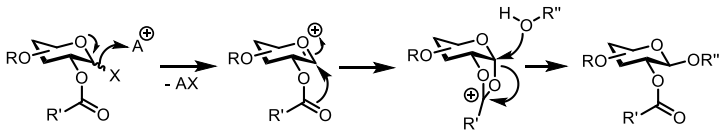

Figure 1.9: Glycosylation with neighboring group participation from position C2.

When investigating stereoselectivity, Garegg et al. observed a solvent effect in Koenigs-Knorr glycosylation performed with a glucose-based donor. While the use of a polar solvent (acetonitrile) led in part to the undesired α-product despite the presence of a benzoyl group at position 2, usage of an apolar solvent (dichloromethane) gave only the β-product regardless of the acceptor reactivity.[115] The same observation was subsequently confirmed by other scientists.[34,116] In later reports from the same group, the effect was explained according to an ion-pair mechanism.[117] By utilizing a polar solvent, the S_N1 mechanism is favored, so that an anomeric mixture of the desired glycoside is obtained. The weaker the nucleophilicity of the glycosyl acceptor, the stronger is the effect. When an apolar solvent is used, the oxocarbenium ion is less stabilized, so that the reaction proceeds preferentially according to the S_N2 mechanism.

An often overlooked factor influencing stereoselectivity is the shape of the acceptor and donor molecules and how well they fit together. In general, neighboring group effects are dominant in the stereochemical control of glycosylation. In 1991, Spijker et al. showed unexpected results in glycosylation reactions using a fucosyl donor in the D and L configuration. While 1,2-*trans* selectivity was achieved with the L-configurated donor, an anomeric mixture was obtained using the D-configuration donor. This observation subsequently led to the introduction of the concept of double stereodifferentiation[118], which states that both the participating neighboring group and the absolute stereoconfiguration of the reactants play a significant role in the stereochemical control at the anomeric center. Similar effects on stereoselectivity were also investigated for various ring-inverted conformers of glycosyl acceptors. By changing the flexibility of the ring conformation, the yield and stereoselectivity could be influenced.[119,120] The results also indicate that the steric conformation is responsible for the reactivity, which is often referred to as a steric "match" or "mismatch".[121,122]

1.2.4 Automated Glycan Assembly

To accelerate the chemical production of glycans, strategies using automated platforms have been developed over the past decades, including electrochemical assembly[123], fluorous-assisted solution-phase[124] and HPLC-assisted synthesis[125]. In analogy to solid-phase peptide and nucleotide synthesis, automate glycan assembly (AGA) has been developed as a solid-phase supported method for glycan synthesis, beginning with a modified peptide synthesizer in 2001 until the first commercial Glyconeer 2.1 Synthesizer has been introduced in 2017.[126]

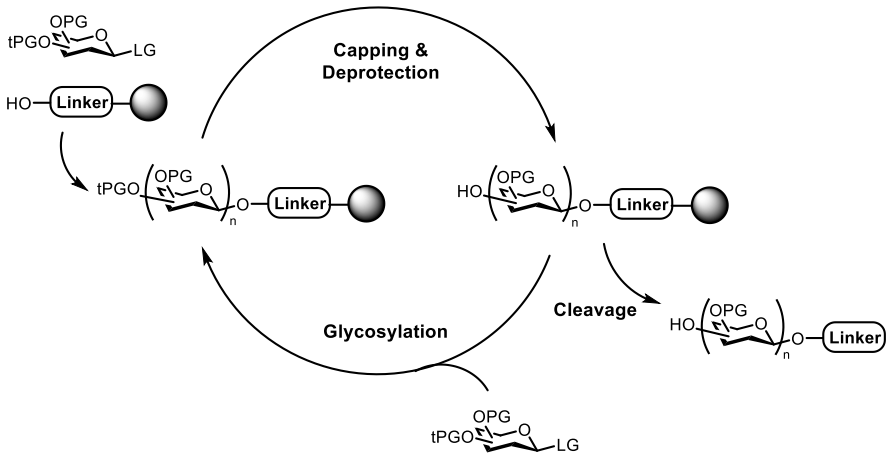

Figure 1.10: Schematic representation of oligosaccharide synthesis through automated glycan assembly.

In solid-phase synthesis, a solid-phase resin equipped with a linker is used to couple different protected saccharide building blocks, so that the effort in terms of purification is minimized. Typically, the saccharide building blocks are designed and synthesized with a temporary protecting group (tPG) including fluorenylmethyloxycarbonyl (Fmoc), levulinoyl (Lev), 2-naphthylmethyl (Nap) and *p*-

methoxybenzyl (PMB) group that can be selectively cleaved off without affecting the other permanent protecting groups (PG). For the glycosylation, a reagent combination of *N*-iodosuccinimide (NIS) and trifluoromethanesulfonic acid (HOTf) is usually used to activate thioglycoside donors, while trimethylsilyl trifluoromethanesulfonate (TMSOTf) is used as promotor in the case of phosphate and imidate donors. As depicted in Figure 1.10, the cleavage of tPG results in a free hydroxyl group that functions as an acceptor for subsequent chain growth through chemical glycosylation with further glycan building blocks. By repetitive cycles consisting of glycosylation, capping and deprotection steps, the glycan chains can be extended into desired oligo- or polysaccharide structures.[127] To date, different types of linkers have been explored for the usage in AGA (Figure 1.11). Besides metathesis labile[128,129] and base labile linkers[130,131], photolabile linkers have become popular due to the orthogonal cleavage conditions to the protecting groups installed on the saccharide building blocks and the cleavage of the photosensitive group releases the product into the solution without additional reagents.[132,133] Depending on the linker design, the glycans can be obtained pre-conjugated to a linker or as hemiacetals, which can be modified into glycosyl halides, phosphates or trichloroacetimidates.[134]

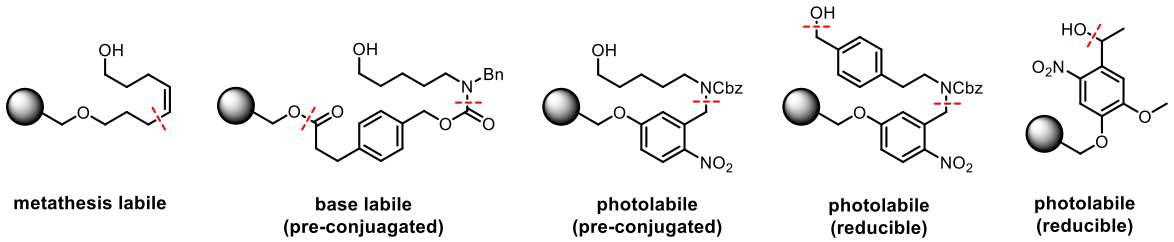

Figure 1.11: Solid-phase resins equipped with different linkers.

1.3 Cucurbituril Host-Guest Chemistry

The acidic condensation of formaldehyde and glycoluril was first reported by Behrend et al. in 1905, which yielded an insoluble polymeric substance with high stability in the presence of aggressive reagents.[135] The structure of the condensation product was encoded almost 80 years later using modern characterization tools including nuclear magnetic resonance (NMR) spectroscopy and X-ray crystallography, showing that the insoluble compounds are macrocycles comprising of six glycouril units. Based on its structural similarity to pumpkins, the compound was named cucurbituril, which was referred later as cucurbit[6]uril or CB[6].[136] With control over the reaction temperature, other members of the cucurbituril family cucurbit[*n*]uril (CB[*n*] with n = 5, 7, 8, 10, 13, 14 and 15) were synthesized and isolated (Figure 1.12).[137–139]

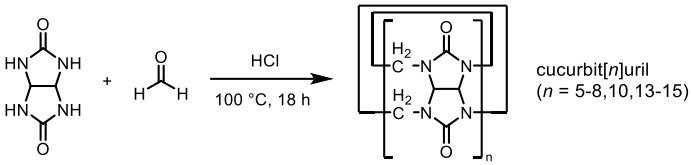

Figure 1.12: Condensation reaction of glycoluril and formaldehyde formation cucurbit[*n*]uril.

One of the key events leading to increasing popularity of cucurbiturils is related to their ability of noncovalent binding. Depending on the size of the cavity, binary and ternary host-guest inclusion and exclusion complexes can be formed (Figure 1.13A).[140] While CB[6] and CB[7] are able to form 1:1 complexes, CB[8] with its larger cavity can include two guests to form either a 1:2 homodimer or 1:1:1 heteroternary complex with high affinities (K_{eq} up to 10^{14} M^{-2}).[140–143] As shown in Figure 1.13B, cucurbiturils possess a hydrophobic cavity surrounded by two hydrophilic rims of carbonyl groups. The complexation with guest molecules is therefore driven by the release of high-energy water from the hydrophobic cavity. According to the observations in NMR experiments, guest molecules carrying apolar and cationic units are preferred for the encapsulation by CB[*n*] due to the hydrophobic effect and the ion-dipole interactions, whereas hydrogen bonding can also contribute to stabilization of the complexes.[144]

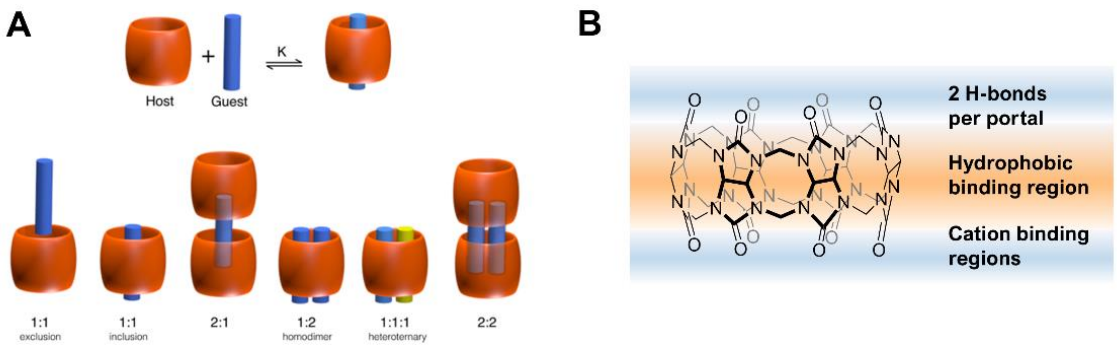

Figure 1.13: A) CB[*n*] inclusion and exclusion complexes. Reprinted with permission from ref.[140]. Copyright © 2015, American Chemical Society. B) Molecular structure of CB[6] and representation of different binding regions.

Owing to the ability of forming reversible host-guest complexes, cucurbiturils have become attractive for various research areas, especially for the design of supramolecular polymeric materials.[145–148] Along with the development of functionalization methods of the water-soluble CB[7][143], the host-guest complexation is further used for bioorthogonal conjugation, which has also been termed as non-covalent click chemistry.[149] Besides high affinity binding events, cucurbiturils have been widely exploited as molecular containers for catalyzed and templated chemical reactions.[150] Various examples have been reported for oxidation[151], hydrolysis[152], photodimerization[153,154], 1,3-dipolar cycloadditions[155], and photofragmentation[156]. In the context of CB[8], the formation of the ternary complex can promote the reaction between two components by specific spatial arrangement within the CB[8] cavity, leading to efficient and selective reaction outcomes.[157]

1.4 Bioprinting

The ability to fabricate biologically functional constructs is crucial for creating biological tissue.[158] However, the development of a bioink, a printable, cell-loaded biomaterial, remains a major challenge due to diverse requirements. While printability is highly dependent on the physical properties of the material, the formation of functional tissues requires interactions between the cells and the extracellular matrix to direct cell behavior. In the past decades, numerous advancements have been achieved in both improving the printing technology and formulating biomaterial inks that are suitable for the chosen technique[159,160], especially formation of dynamic hydrogel networks, which will be elucidated in this section.

1.4.1 Bioprinting Technologies

Three-dimensional bioprinting requires techniques to form constructs through layer-wise or volumetric programmed nozzle-based and light-based methods. To successfully print a biologically active construct, both printing resolution and speed are important parameters. Overall, bioprinting technologies can be classified into four categories: extrusion, inkjet printing, light-induced forward transfer (LIFT) and vat-polymerization (Figure 1.14).[161]

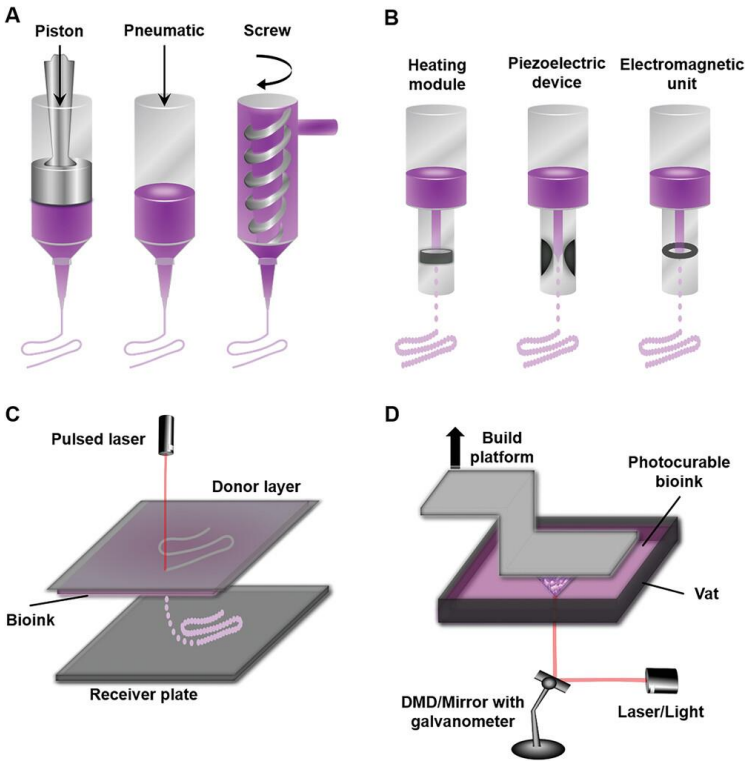

Figure 1.14: Schematic showing the different bioprinting modalities. A) Extrusion. B) Inkjet. C) LIFT. D) Vat-photopolymerization. Reprinted with permission from ref.[159]. Copyright © 2021 Wiley-VCH GmbH.

In extrusion-based bioprinting (Figure 1.14A), the biomaterial ink is extruded through a nozzle to form filaments that are overlapped in a layer-by-layer manner to fabricate 3D constructs. The bioink can be extruded through pressure-controlled pneumatic actuation or flow rate-controlled mechanical impulses.[162] After the extrusion, the 3D constructs can be used as delivered or further modified via physical, chemical and or photochemical crosslinking, leading to solidification of the material.[163] Due to high level of shear stress during nozzle extrusion, shear-thinning materials are required as bioink for this technique to maintain the cell viability.[164,165] Though an extrusion-based method is simple to perform, printing with high resolution is challenging[166], since it can only be achieved using nozzles of smaller diameters, which imposes limits towards printing speed and the resulting feature size.

In case of inkjet bioprinting (Figure 1.14B), a liquid, low viscosity bioink is used[167], from which small droplets are produced and deposited under thermal, piezoelectric or electromagnetic actuation to create high-resolution constructs.[168] In general, the inkjet printing is faster than extrusion, while the droplet size depends on the nozzle diameter. Owing to the usage of a low viscosity bioink, printing with high cell viability can be achieved. However, a post-printing modification, usually through photochemical crosslinking has to be carried out to assure print fidelity.[169]

The LIFT bioprinting (Figure 1.14C) is achieved through laser-induced transfer of the biomaterial ink from a donor layer onto the receiver plate.[170] The donor slide is comprised of transparent material coated with an optically absorbing layer of gold, whereas the bioink is coated onto the metal surface. Upon irradiation with a pulsed laser, the bioink from the donor layer evaporates and forms droplets that are transferred to the receiver plate, leading to fast and accurate formation of 3D constructs. However, the method is not suitable for high throughput fabrication so far.[171]

In vat-polymerization bioprinting (Figure 1.14D), light is used to cure a liquid, photosensitive resin, which contains photoinitiator as well as reactive monomers and macromers. The light source used can be ultraviolet (UV), visible or near-infrared (NIR) light.[172–175] A 3D construct is created through layer-wise irradiation by the laser beam and resin solidification though photochemical crosslinking of the precursors. To ensure cell viability, the processing temperature, toxicity of precursors and UV exposure have to be controlled.[159]

Using conventional bioprinters, constructs comprised of a single type of bioink can be fabricated. Depending on the application, 3D constructs containing different cell types with a spatial arrangement are desired. Therefore, multi-material bioprinters have been developed to enable incorporation of graded composition and properties[176–178], so that improvements in multi-functional systems[179], vascularized structures[180,181] as well as customizable tissues and organs[182,183] have been achieved.

1.4.2 Bioinks Requirements

It is remarkably challenging to develop a biomaterial ink that fulfills the requirements in terms of its physical, chemical and biochemical properties, so that they are printable and can concurrently maintain cell viability as well as induce desired cellular response.[184] While the printability is mainly governed by the physical properties, including viscosity, stiffness, nonlinear viscoelasticity, surface tension and density, the matrix stiffness and stress relaxation can further affect cellular behavior.[185–188] The choice of polymeric material, the concentration, pH value, degree of chemical modification and type of crosslinking mechanism can further affect the materials properties.

For extrusion based bioprinting, hydrogels are often used as bioinks, as they structurally resemble the native extracellular matrix (ECM). The main requirements in terms of material properties include shear-thinning behavior, rapid gelation or self-healing as well as suitable surface tension and viscosity that allow the formation of filaments.[161] According to the classical "top-down" approach, non-covalently cross-linked, natural polysaccharides (hyaluronic acid[189], chitosan[190], alginates[191]) and proteins (gelatin[192], collagen[193]) are often used as scaffold materials. However, this class of materials has limitations in the application with living cells due to thermally induced gel formation, shrinkage-related shape changes and lack of tunability.[194] Therefore, the interests have been shifted towards synthetic alternatives including pluronics[195], poly(ethylene glycol)[196], poly(*N*-isopropylacrylamide)[197,198] and poly(2-oxazoline-*co*-2-oxazine)[199,200], which are structurally more defined and the material properties can be easily adjusted through crosslinking density or incorporation of dynamic crosslinks. However, such platforms alone typically exhibit low cytocompatibility[201], so that adhesive tripeptide arginine-glycine-aspartic acid (RGD)[202] or matrix metallopeptidase (MMP) cleavable sites[203,204] are added to create a biologically active environment for cell culture application (Figure 1.15).

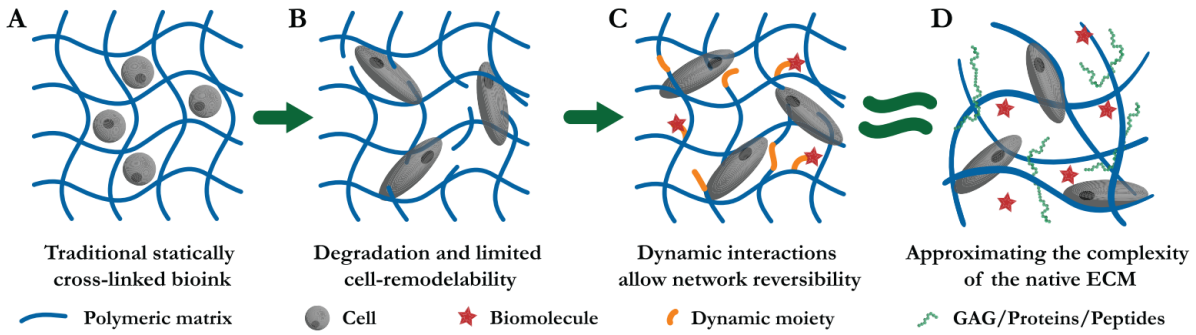

Figure 1.15: Evolution of bioinks toward mimicking the biological extracellular matrix (ECM). Reprinted with permission from ref.[160] Copyright © 2020 The Authors. Published by WILEY-VCH Verlag GmbH&Co. KGaA, Weinheim.

1.4.3 Dynamic Hydrogel Networks

Compared to a hydrogel based on a single synthetic polymer, the native extracellular matrix (ECM) is much more complex and dynamic. To better emulate the native ECM microenvironment, multiple approaches for responsive hydrogel networks using dynamic interactions have been developed, which can be categorized into multimaterial bioinks, interpenetrating network (IPN) bioinks, nanocomposite bioinks, supramolecular bioinks and bioinks based on dynamic covalent chemistry (DCvC) (the first four categories are schematically shown in Figure 1.16).[158]

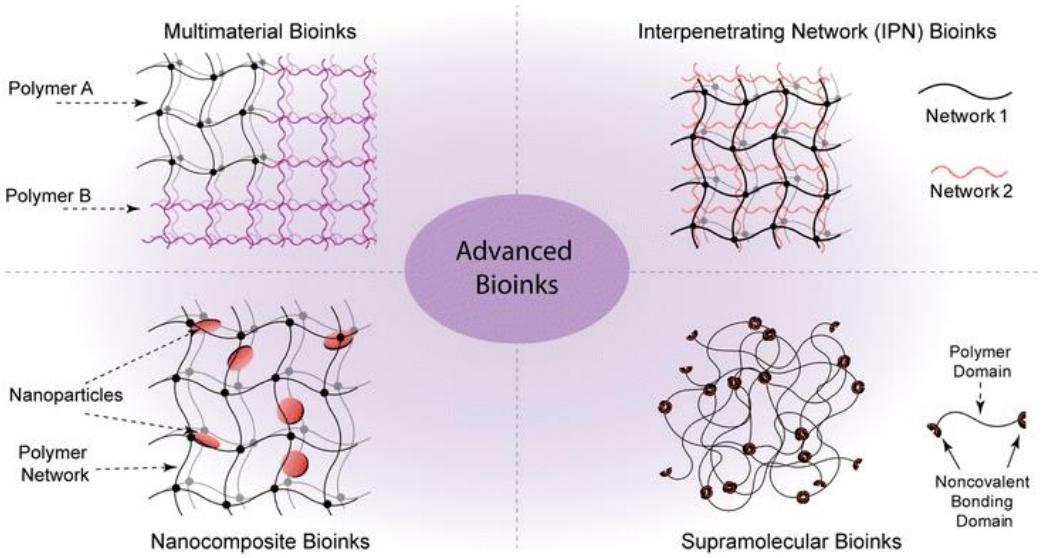

Figure 1.16: Advanced bioinks classified into four categories. Reprinted with permission from ref.[158] Copyright © 2016, Biomedical Engineering Society.

Multimaterial bioinks are formed using two networks that are covalently crosslinked with each other. With this approach, different (bio-)mechanical properties can be combined, so that mechanically robust, cytocompatible biomaterial inks can be obtained. For example, an ionically crosslinked alginate network itself does not interact with cells, which can be overcome by incorporating a second gelatin network that contains cell adhesive RGD domains, giving a multimaterial bioink with improved viscosity and cytocompatibility.[205]

In contrast to multimaterial bioinks, IPN bioinks are composed of two separate networks that only have limited interactions with each other.[206–209] In a typical approach, a flexible primary network and a stiff secondary network are formed through different crosslinking methods. As a result, IPN hydrogels often exhibit a linear combination of the mechanical properties that are characteristic for the single networks. As a subset of IPN hydrogels, double network (DN) hydrogels are synthesized through formation of the primary hydrogel with randomly distributed secondary network monomers, that are crosslinked in the following step, leading to hydrogel networks with extraordinary stiffness and toughness.[207,210]

The addition of small amounts of nanoparticles into polymeric gels can result in significant changes in the mechanical properties and behavior under physiological conditions.[211,212] The bioactive potential was studied for example by combining a poly(ethylene glycol) dimethacrylate (PEGDMA) gel with hydroxyapatite nanoparticles for bone tissue engineering, resulting in high viability of human mesenchymal stem cells (hMSCs) and upregulated bone-related gene expression compared to the pure PEGDMA scaffold.[213] The hydrogels can be further designed by incorporating additional properties such as controlled drug release, electrical conductivity, photo-responsiveness and magnetism, depending of the type of nanoparticles.

In the past years, dynamic covalent chemistry (DCvC) has been frequently applied within the field of biomaterial engineering. Examples for DCvC hydrogels are networks using boronate and Schiff base crosslinks. Due to the reversibility of those covalent bonds, DCvC networks are inherently shear-thinning, self-healing and also recyclable. Since the dynamics of DCvC hydrogels are reflected by the equilibrium constant K_{eq} of the dynamic covalent bond formation, the mechanical properties of the networks can be tuned by varying the crosslinking chemistry. Based on this, hydrogels composed of oxidized alginate using a combination of hydrazone and oxime crosslinks have been reported, demonstrating the dependence of mechanical properties on the crosslinking chemistry, whereas higher equilibrium constants result in stiffer hydrogels (Figure 1.17).[214]

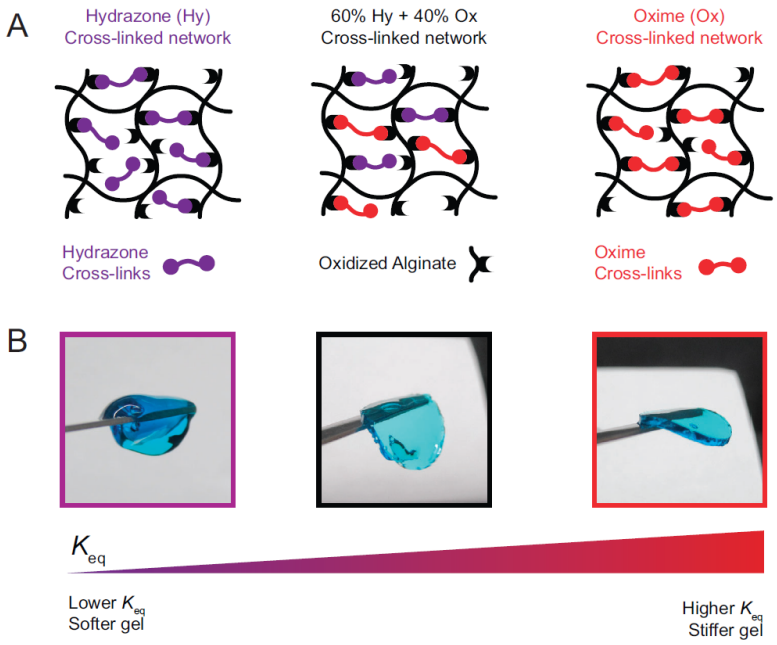

Figure 1.17: Dynamic covalent hydrogels based on hydrazone and oxime crosslinked hydrogel networks and the dependence of hydrogel stiffness on the equilibrium constant K_{eq}. A) Schematic hydrogel networks. B) Photos of the hydrogels displaying differences in stiffness. Reprinted with permission from ref.[214] Copyright © 2021 The Authors. Advanced Healthcare Materials published by Wiley-VCH GmbH.

A major challenge for printing cell-loaded scaffolds is to develop materials that can withstand repeated mechanical stress. Inspired by nature, supramolecular hydrogels consisting of materials crosslinked by

reversible, non-covalent interactions have received increasing attention.[194,215,216] Besides shear-thinning and self-healing properties[160], supramolecular hydrogels can adapt to growing cells and they can be formed using complex, multicomponent systems similar to native ECM. Though numerous advancements were made in the development of supramolecular bioinks based on polypeptide hydrogels[217,218], polypeptide-DNA complexes[219], hydrogels with DNA crosslinks[220] and hydrogels crosslinked by host-guest-complexation[165,206], there are challenges in terms of overcoming low viscosity and the lack of print fidelity. Therefore, supramolecular bioinks usually require post-printing modifications to stabilize the 3D structures and prevent the dissolution of the gel under wet conditions as in most biomedical applications. One example has been reported by Burdick et al. using hyaluronic acid modified with methacrylates as well as β-cyclodextrin (CD) or adamantane (Ad) units (Figure 1.18).[165] The polymers can form a physically crosslinked hydrogel through supramolecular host-guest complexation in the first step. Upon irradiation with UV light, the methacrylate moieties are polymerized to form additional chemical crosslinks, giving stiffer hydrogels that remain dynamic.

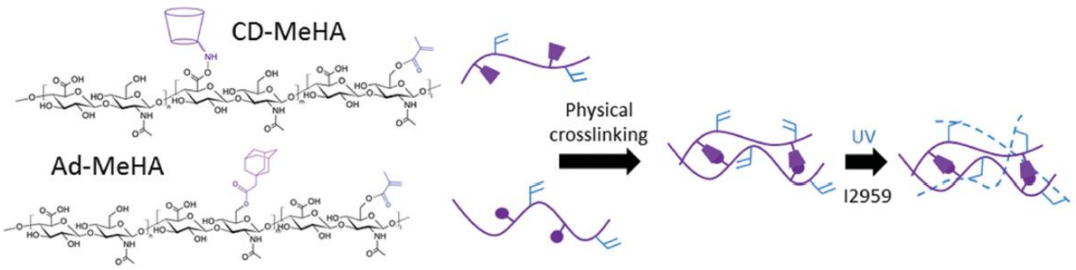

Figure 1.18: Hyaluronic acid modified with methacrylates (blue) as well as guest and host molecules (purple). The macromers are crosslinked through physical host-guest complexes and a secondary crosslinking of methacrylates with UV light exposure. Reprinted with permission from ref.[165] Copyright © 2015 WILEY-VCH Verlag GmbH & Co. KGaA, Weinheim.

1.5 Dynamics of Hydrogel Networks

Owing to the ability to mimic cellular environment, hydrogels have become promising candidates for numerous biomedical applications. Since the structural dynamics of hydrogels can largely affect their physical, chemical and biochemical properties, it is important to understand the underlying mechanisms and interactions within the hydrogel networks to be able to design the hydrogels accordingly.[221] In this section, approaches to investigate dynamic features of associative networks and diffusion behavior through different experimental methods will be illustrated.

1.5.1 Rheological Properties of Associative Networks

In terms of investigating a hydrogel material, rheology is a powerful tool to determine mechanical properties including structure viscosity, frequency-dependent viscoelasticity and time-dependent flow

behavior (rheopexy or thixotropy).[222] Due to dynamic interactions within the associative networks, hydrogels usually show non-linear responses to the applied condition during a rheological experiment. In case of structure viscosity, the viscosity of the sample can deviate from an ideal Newtonian fluid when increasing the shear rate in a rotation experiment, leading to observation of shear-thinning or shear-thickening behavior. The time-dependent change of flow behavior can be ascribed to structural rearrangement (reversible or irreversible) as a response to repeated mechanical stress.

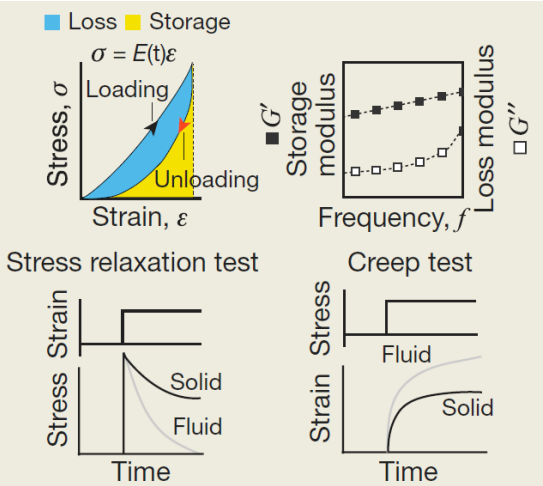

Figure 1.19: Stress-strain curves and frequency-dependent viscoelasticity of viscoelastic materials. Adapted and reprinted with permission from ref.[223] Copyright © 2020, Springer Nature Limited.

Unlike solid or liquid material that exhibit pure elastic or viscous properties, hydrogels generally display both elastic and viscous attributes at the same time.[223] Depending on the type of dynamic interactions, the material properties can be dominated by either the elastic or viscous contribution (Figure 1.19). This can be studied using oscillatory shear rheology, which is performed under an oscillating movement of the measuring geometry. The moving profile is defined by the angular frequency ω and the shear strain γ, whereas values of the storage modulus G' and the loss modulus G'' can be obtained from the complex shear modulus G^*. While the storage modulus G' shows the solid contribution of a material and the storage of deformation energy according to the Hooke's law, the properties of an ideal Newtonian fluid and the energy dissipation after material deformation are represented by the loss modulus G''. By applying a varying angular frequency, the viscoelasticity of the hydrogel material can be evaluated. Since the angular frequency is a reciprocal measure of time, mechanical properties of the same material on different time scales can be analyzed. If G' is larger than G'', the solid contribution dominates the mechanical properties and vice versa. As shown in Figure 1.20, a covalent network can be seen as a pure elastic solid with certain flexibility depending on the degree of connectivity. When the covalent network is physically entangled with polymers or a weak network, relaxation can occur through rearrangements of the flexible polymers or the secondary network and thus release from the physical entanglements, resulting in properties of viscoelastic materials. A higher viscous contribution is given by substitution of the covalent network with weakly crosslinked networks such as networks with supramolecular

crosslinks and physically entangled polymers. Depending on the ratio of elastic and viscous contributions, the materials can be classified as viscoelastic or viscoplastic.

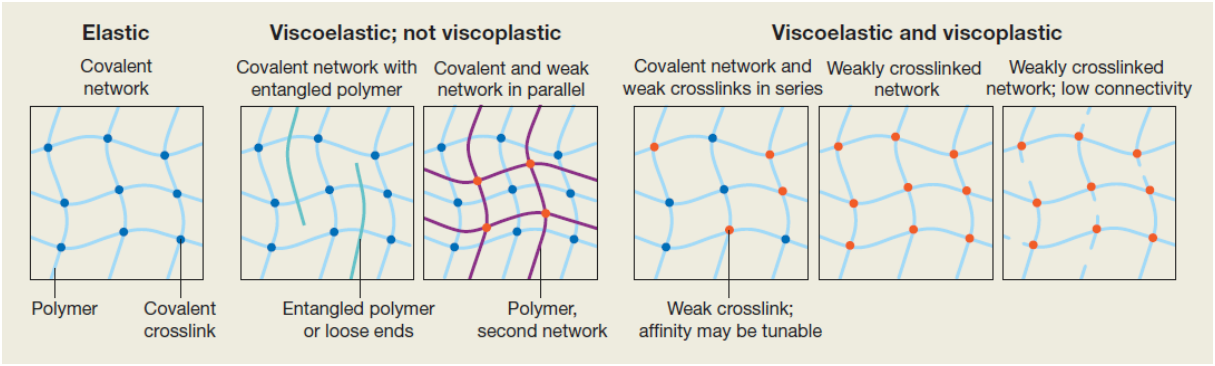

Figure 1.20: Material Properties depending on the type of crosslinking mechanism and the degree of connectivity. Reprinted with permission from ref.[223] Copyright © 2020, Springer Nature Limited.

Within an associative network, the rheological data can directly reflect the crosslinking mechanisms and dissociation kinetics of associative groups. Using a transient network crosslinked by metal-ligand coordination, it has been demonstrated by Yount et al. that the time scale, at which a transition from an elastic solid to a viscous liquid takes place (characterized by the crossover frequency ω_0) is governed by the small molecule dynamics.[224] The dynamic, viscoelastic properties of the associative networks are scaled through the dissociation rate of the crosslinks independent of their association. This finding has provided simple scaling relationships of the material relaxation and the exchange kinetics. By performing rheology experiments and computer simulations using hyaluronic acid modified with CB[7] or guest molecules, Cai et al. have further developed a model to predict frequency-dependent mechanical properties from the binding and polymer parameters (Figure 1.21A)[225], showing that the mechanical response within the terminal, low frequency regime is dominated by the binding event, while the high frequency regime is dependent on the polymer relaxation itself (e.g. sticky Rouse or sticky reptation model). The intermediate regime is influenced by both contributions from the binding and the polymers that include ligand exchange and physical entanglements between polymer chains. Using polymers decorated with guest molecules that exhibit different binding affinities to cucurbit[7]uril (CB[7]) (adamantane (Ada) > xylylenediamine (Xyl) > phenylalanine (Phe)), the theory of Yount et al. has been verified. While hydrogels with high affinity guest molecules show a transition from liquid to solid behavior (lower crossover frequency for the case with highest binding affinity), the hydrogel with Phe as guest molecule remains a liquid over the entire test window, since the dissociation rate is much higher.

Using the existing relationships between structure and properties, material with complex dynamic properties can be created for the desired application. The mechanical properties of the same material type can be further tuned by adjusting the polymer size and concentration, degree of functionalization as well as degree of connectivity.

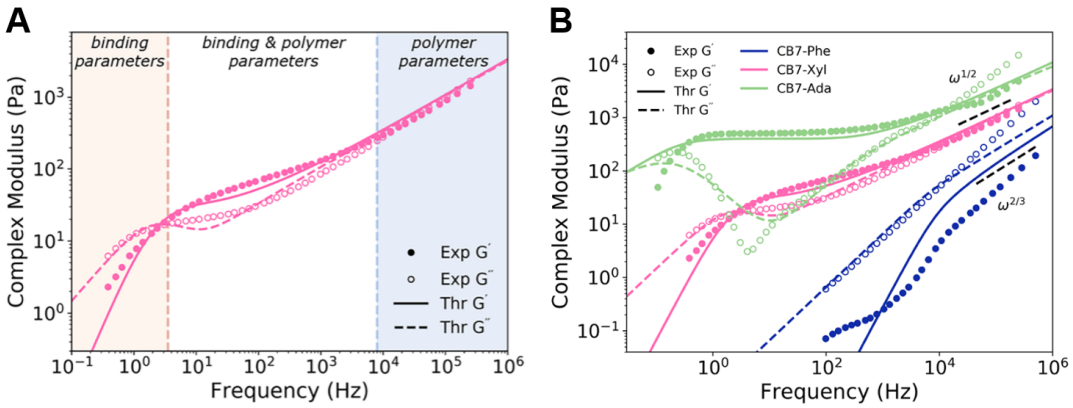

Figure 1.21: A) Comparison between experimental data and model prediction. B) Rheological measurements and model prodictions of different hyaluronic acid host-guest polymers. Adapted and reprinted with permission from ref.[225] Copyright © 2022 The Authors. Published by American Chemical Society.

1.5.2 Diffusion within Hydrogel Networks

Besides the mechanical properties, network dynamics can largely affect the diffusion behavior of solute molecules due to size dependency or participation in binding events.[226,227] Better understanding of the diffusion behavior of both solute molecules and the network components is therefore relevant for network design towards intended application, such as drug delivery, infiltration of physiological entities and viability of encapsulated cells. To date, diffusion within hydrogels has been widely studied using mathematical models based on parameters including mesh size, crosslink density, crosslink dynamics and solute hydrodynamic radius.[228–230]

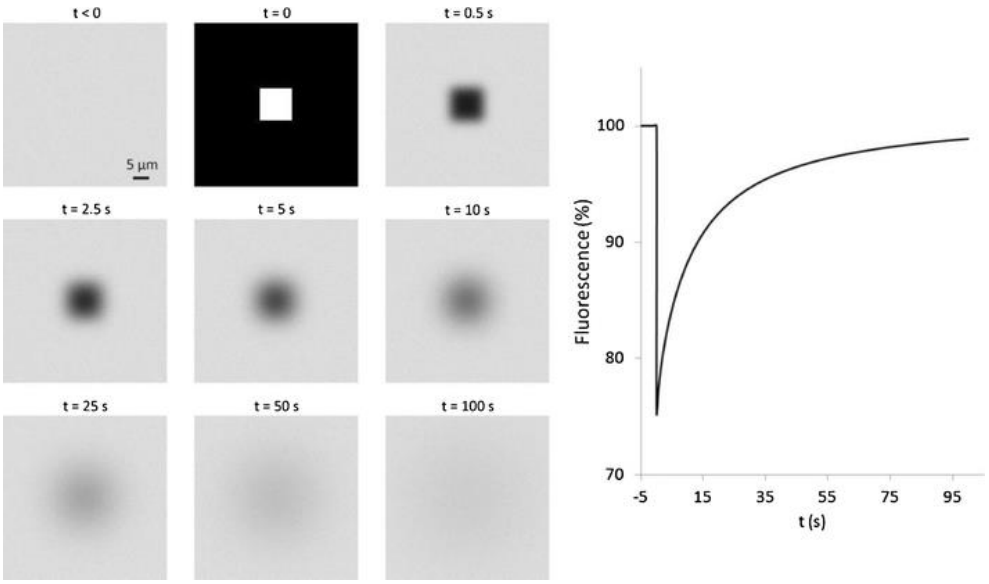

Figure 1.22: Illustration of a FRAP experiment, showing fluorescence microscopy images at different time points *t* on the left and the fluorescence recovery curve on the right. Reprinted with permission from ref.[231] Copyright © 2013, Springer Science Business Media New York.

To study molecular dynamics, fluorescence recovery after photobleaching (FRAP) has been one of the most popular methods due to its applicability within living cells.[231] In a typical procedure, the sample is bleached using a high intensity laser, resulting in a local decrease of the fluorescence intensity within the so-called region of interest (ROI). Due to diffusion of active dyes into the ROI, recovery of the fluorescence intensity can be observed, which reflects diffusion and binding dynamics (Figure 1.22).[232]

The impact of crosslink dynamics on the solute diffusion within polymer networks has been studied by Braegelman et al. through FRAP experiments using star-shaped poly(ethylene glycol) which is end-functionalized with adamantane (Ada) and xylylenediamine (Xyl) that exhibit different binding affinities to cucurbit[7]uril (CB[7]).[226] First, fluorescent FITC-dextran particles of different sizes were added into PBS buffer or hydrogel with Xyl guest molecules for the comparison of free diffusing and encapsulated fluorescent particles. As shown in Figure 1.23A, the samples with free diffusing particles (in PBS) of different sizes display fast fluorescent recovery after the bleaching process, while the diffusion of the fluorescent particles is significantly decelerated within the hydrogels with increasing particle size. A direct comparison is demonstrated by the fluorescent images of the hydrogel samples containing 70k and 250k particles (Figure 1.23B), indicating that the diffusion is strongly dependent on the particle size (or hydrodynamic radius). When comparing the diffusion within a quasi-static (with high affinity guest molecule Ada) and a dynamic hydrogel (with low affinity guest molecule Xyl) with identical topology, surprising results were obtained, indicating a faster diffusion of the fluorescent particles in the static hydrogel. After the initial results, the samples were further analyzed using confocal microscopy, leading to the observation of heterogeneous fluorescent fields within the Ada sample. This phenomenon was more profound in case of samples with larger particles, which was explained by limited diffusion and distribution of fluorescence particles and their aggregate formation over time within the static hydrogel.

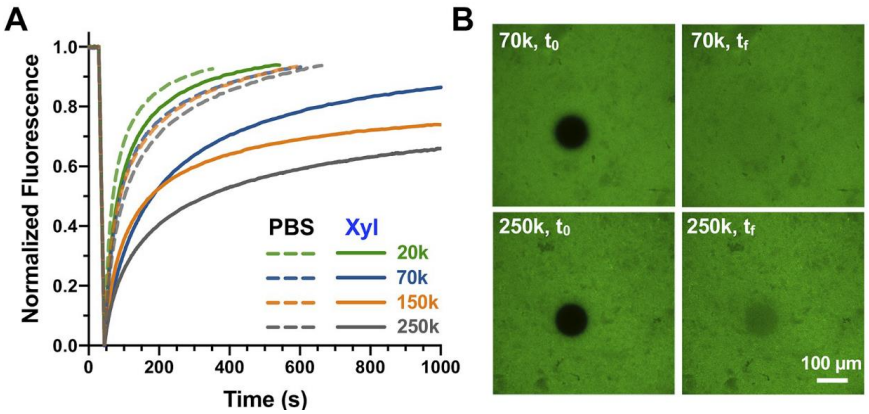

Figure 1.23: A) Fluorescence recovery after photobleaching (FRAP) data for free (PBS) and hydrogel encapsulated (Xyl) FITC-dextran probes. B) Images of the hydrogel immediately after the photobleaching (t_0) and the end of measurement (t_f). Adapted and reprinted with permission from ref.[226] Copyright © 2022, American Chemical Society.

The quantitative determination of diffusion constants is usually based on simplified mathematical models, so that the values obtained are not always comparable. As a complementary method, forced

Rayleigh scattering (FRC) has been used to characterize self- and tracer-diffusion within associative networks.[227] This method works according to a similar principle as FRAP by generating a concentration grating of dye-labeled polymers. Through diffusion of the polymers, an exponential decay of the grating and thus intensity of diffracted light can be observed. Depending on the time scale of the molecular diffusion, other methods including fluorescence correlation spectroscopy (FCS), single particle tracking (STP) and nuclear magnetic resonance diffusometry (NMRd) can be applied to gain more insight into the molecular dynamics.

2 Objectives

Over the past decades, numerous advancements have been achieved in developing synthetic materials for biomedical applications. Following the inspiration from nature, supramolecular chemistry has received significant interests due to its ability of building up complex and dynamic biomimetic systems. Due to reversible, non-covalent interactions, self-assembling structures can respond to their external stimuli, making them attractive for the design of innovative and functional biomaterials.

To explore the potential of supramolecular chemistry, the present work focuses on the development of synthetic building blocks to create biomaterials that are aimed to be applied as multivalent antibacterial vaccines carrying carbohydrate epitopes and dynamic biomaterial inks for 3D bioprinting.

In the first part of the thesis, carbohydrate epitopes are to be synthesized for supramolecular glycoconjugate vaccines against serotype 3 *Streptococcus pneumoniae*. Using the disaccharide cellobiose as a starting material, cellobiuronic acid derivatives conjugated to an amine-carrying linker are to be obtained through orthogonal protection of the saccharide building block, linker conjugation via chemical glycosylation and regioselective oxidation (chapter 3). In order to resemble the structure of capsular polysaccharides (CPS) of the pathogen, methods for regioselective protection of the position O-3’ are to be developed that allow subsequent formation of 1,3’-β glycosidic linkages between the saccharide building blocks to synthesize cellobiuronic acid oligomers.

In the second part of the thesis, supramolecular hydrogels consisting of single or interpenetrating networks crosslinked through cucurbit[8]uril (CB[8]) mediated host-guest complexation and photochemistry are formed using end-functionalized star-shaped poly(ethylene glycol) (PEG) macromers. Based on this hydrogel design, biomaterial inks for extrusion bioprinting are to be created and studied in terms of their mechanical properties, cytocompatibility and applicability within the bioprinting setup (chapter 4). To gain more insight into the dynamic features of the hydrogel networks crosslinked by CB[8] host-guest complexation, the impact of networks dynamics on solute diffusion was further investigated. Through fluorescence recovery after photobleaching (FRAP) studies, the influence of size and binding kinetics on the solute diffusion are assessed (chapter 5), which can provide key information for design of biomaterials intended for applications including biochemical recognition and drug delivery platforms.

3 Synthesis of Carbohydrate Epitopes for Supramolecular Antibacterial Vaccines

3.1 Motivation and Concept

The bacteria known as *Streptococcus pneumoniae* (*S. pneumoniae*) are potentially deadly pathogens. Children and the elderly are particularly affected by infections. Depending on the structure of the polysaccharide on the bacterium capsule, *S. pneumoniae* has been classified into more than 100 serotypes.[233] Due to the development of antibiotic-resistant *S. pneumoniae* strains, alternative treatment methods are being sought, and increasing research focus has been placed on early immunization strategies with efficient vaccines.[234]

Despite its inclusion into the 13-valent pneumococcal conjugate vaccine, *S. pneumoniae* serotype 3 remains a significant cause for epidemiology worldwide.[235] Since the carbohydrate epitopes are usually isolated from cultured bacteria and undesired side reactions can take place during its conjugation to protein carriers, the production of commercial glycoconjugate vaccines often suffer from poor batch-to-batch reproducibility.[1] In order to create vaccines with discrete chemical structures and controllable immunization efficiency, this work focuses on a bottom-up strategy for the formulation of a supramolecular, fully synthetic vaccine against *S. pneumoniae* serotype 3 using the approach previously developed by Straßburger et al.[38,236]

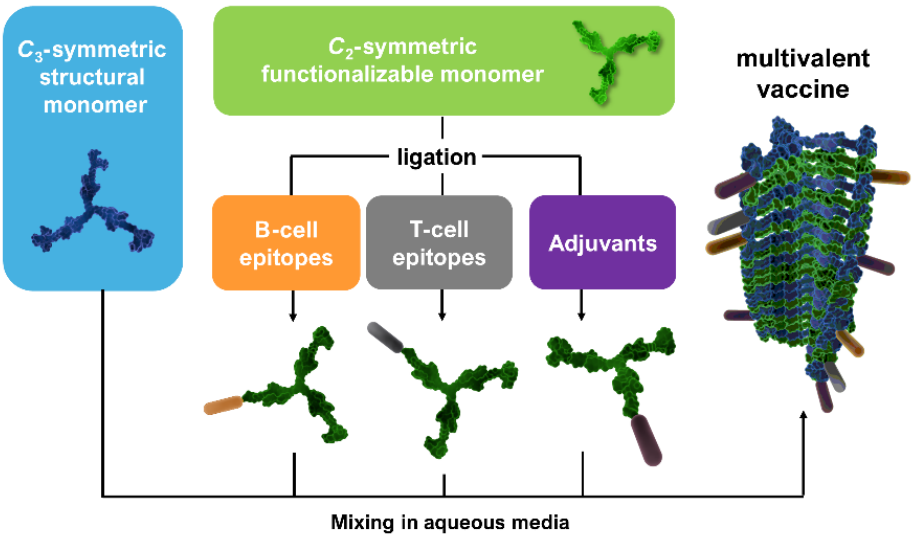

Figure 3.1: Concept of multivalent supramolecular vaccine formation using C_3-symmetric structural monomer and C_2-symmetric monomer functionalized with immune active components.

According to this approach, a modular vaccine toolbox consisting of self-assembling C_3-symmetric structural monomer and C_2-symmetric monomer functionalized with immune active components is required (Figure 3.1). For an effective immune response, the toolbox includes monomers decorated with

B-cell epitopes (bacterial antigens), T-cell epitopes as well as adjuvants. By mixing those monomers in aqueous media, they are able to undergo copolymerization and form nanorods that present various immune active moieties on the surface. The optimal immunization efficacy of the multivalent vaccine can be achieved by adjusting the ratio between the individual components.

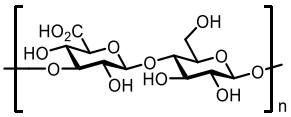

Figure 3.2: Chemical structure of *S. pneumoniae* serotype 3 capsular polysaccharide.

The capsular polysaccharide (CPS) of serotype 3 (ST3) consists of cellobiuronic acid units connected through 1,3'-β-glycosidic linkages (Figure 3.2). The disaccharide cellobiuronic acid has already been proven as the smallest antigenic unit (B-cell epitope) that can be used for immunization. However, the investigation of immunization efficacy using oligomeric analogs of cellobiuronic acid can be interesting. Therefore, glycotopes of different lengths and terminal units need to be synthesized in this work (Figure 3.3). In contrast to the conventional approach for the synthesis of oligosaccharides which uses monosaccharide building blocks, the disaccharide cellobiose (monomeric unit of cellulose) is chosen here as the starting material. This approach avoids additional synthesis steps for the formation of the β-1,4-glycosidic bonds between glucose and glucuronic acid building blocks and is more time and cost efficient. By introducing orthogonal protecting groups, it is possible to performe regioselective deprotection, glycosylation or further modifications, such as oxidation of position O-6 or O-6' in the present case to obtain glycotopes with alternating glucose and glucuronic acid units.

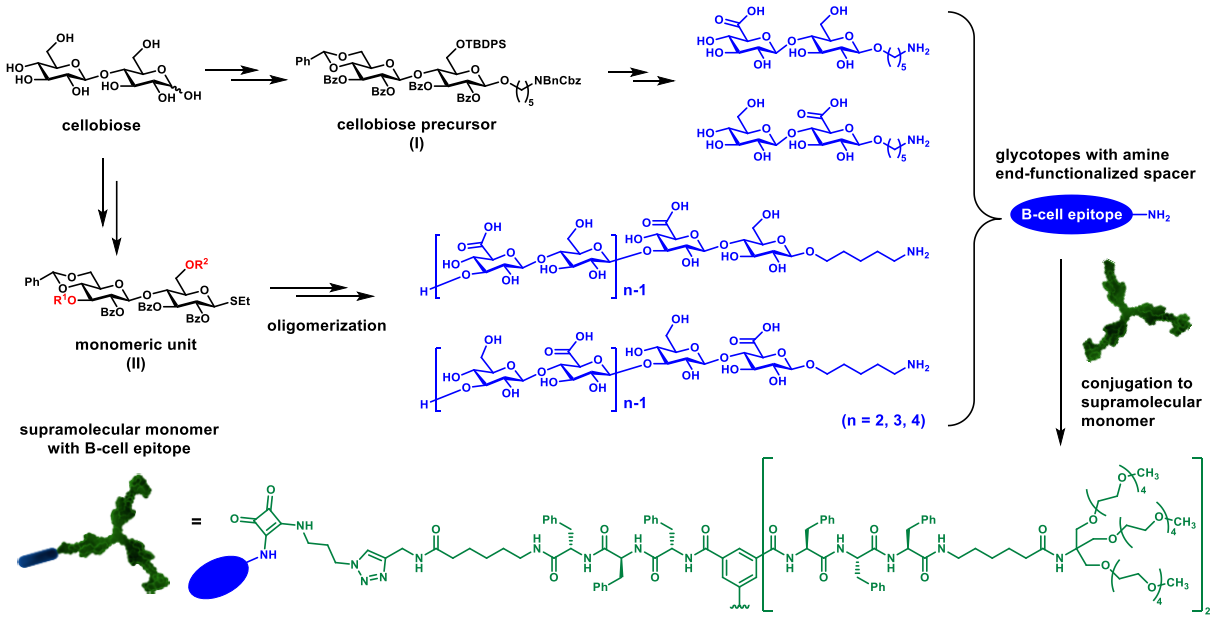

Figure 3.3: Reaction paths for the synthesis of B-cell epitopes from cellobiose with different lengths and terminal units as *S. pneumoniae* ST3 antigens and the conjugation to functionalizable supramolecular monomer.

In the first part of the project, a cellobiose precursor (**I**) with orthogonal protecting groups on positions O-6 and O-6' is designed and synthesized. Through regioselective deprotections and modifications, disaccharide antigens with glucuronic acid or glucose as terminal unit can be obtained. The second part of the projects focuses on the regioselective installation of protecting group R^1 to position O-3' in the presence of a sterically demanded protecting group R^2 on position O-6. To obtain glycotopes with longer sequences, the fully protected cellobiose donor (**II**) can be oligomerized through reactions in solution or automated glycan assembly (AGA) or flow chemistry. Finally, the glycotopes can be conjugated to the C_2-symmetric monomer through the amine function of the spacer, forming a functionalized monomer that can be used for the formulation of multivalent vaccines.

3.2 Results and Discussion

According to the concept, *S. pneumoniae* ST3 antigens with different length and terminal units need to be synthesized. The antigens should be pre-conjugated to an amine carrying spacer that provide the possibility for further conjugation reactions to monomers or proteins that function as vaccine carriers. This subchapter starts with the preparation of the spacer and cellobiosyl donors with orthogonal protecting groups on the positions O-6 and O-6'. Subsequently, the glycosylation, regioselective deprotection and oxidation with disaccharide antigens as products will be elucidated. Finally, the regioselective protection of position O-3' will be discussed that offers the opportunity for the synthesis of cellobiuronic acid oligomers.

3.2.1 Spacer Synthesis

The amine carrying spacer was synthesized following the procedure by Noti et al.[237] As shown in Figure 3.4, the synthesis starts with the protection of the amine function of 5-amino-1-pentanol with a benzyoxycarbonyl (Cbz) protecting group. The reaction was conducted using benzyl chloroformate (CbzCl) as a reagent, tetrahydrofuran (THF) as solvent and $NaHCO_3$ as a scavenger for the HCl formed in the reaction. The product **I-1** was obtained with a yield of 95% and was subjected to a reaction with trityl chloride in pyridine at 80 °C. After purification via flash chromatography, the trityl protected spacer **I-2** was obtained with a yield of 26%. In the next step, the benzyl group was introduced using sodium hydride (NaH) in form of an oil suspension for the deprotonation of the carbamate and benzyl bromide (BnBr) for the alkylation. The crude product **I-3** was directly converted utilizing *p*-toluenesulfonic acid monohydrate ($TsOH \cdot H_2O$) in a solvent mixture of dichloromethane (DCM) and methanol (MeOH). In this step, the trityl group was cleaved off, giving the desired spacer **I-4** with free hydroxyl group with a yield of 44% after 2 steps.

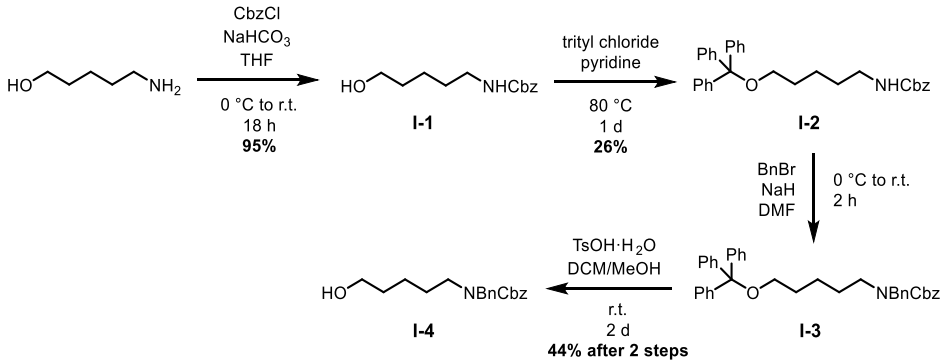

Figure 3.4: Reaction scheme for the synthesis of *N*-(benzyl)benzyloxycarbonyl-5-aminopentan-1-ol (**I-4**) starting from 5-amino-1-pentanol.

3.2.2 Synthesis of Orthogonally Protected Thioglycosides as Glycosyl Donors

Compared to glycosyl halides (e.g. Koenigs-Knorr glycosylation) or trichloroacetimidates (Schmidt glycosylation), thioglycosides exhibit higher long-term stability and are less affected by various reaction conditions in terms of introduction of protecting groups, which makes them attractive for the design of glycosyl donors. Furthermore, the donor activation takes place at room temperature, so that they are applicable for solid-phase synthesis.

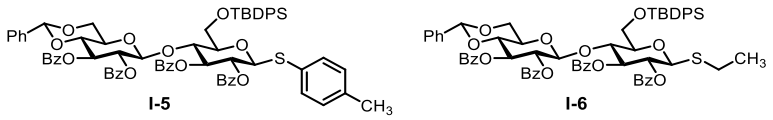

Figure 3.5: Structures of desired thioglycoside donors.

In this work, the thioglycosides **I-5** and **I-6** shown in Figure 3.5 are anticipated as glycosyl donor for the glycosylation of the spacer. Both have the same protecting group pattern except the thiol used on the reducing end. Tolyl thioglycosides are slightly more stable, but at the same time less easy to activate than ethyl thioglycosides. The glycosylation conditions and outcomes will be further studied in the next section. While position O-6 is protected by *tert*-butyldiphenylsilyl group (TBDPS, cleavable by fluoride), positions O-4'/O-6' are protected using the benzylidene acetal group (cleavable under acidic conditions), so that a selective deprotection and oxidation of one of the primary alcohols can be performed. To the remaining OH-groups, benzoyl groups (Bz, cleavable under alkaline conditions) are installed. The choice of ester group is important for the stereoselectivity of the glycosylation, since the ester group on position O-2 participate in the glycosylation reaction. The general mechanism of a glycosylation is usually described as substitution reactions (shown in Figure 3.6).[238]

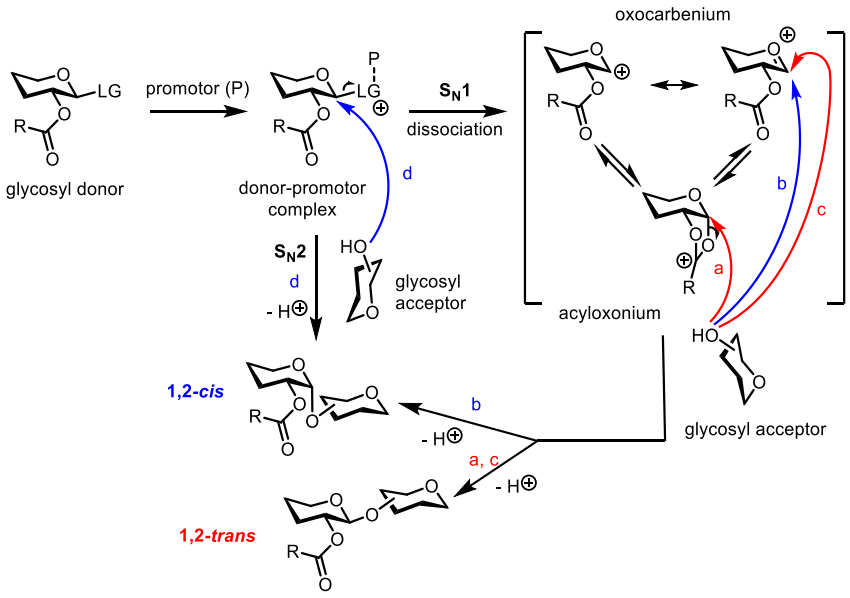

Figure 3.6: General mechanisms of a chemical glycosylation reaction.[238]

The glycosylation takes place when the anomeric center is activated by the promoter. If the reaction proceeds following a S_N1-type mechanism without the participation of a neighboring group at position O-2, no stereoselective product formation will occur (b, c). The outcome will be an α/β-mixture of products. However, preferential formation of the α-product is expected due to the anomeric effect (b). In the presence of a participating group at position O-2, one side of the anomeric center is blocked by the formation of the so-called acyloxonium cation (a). The nucleophilic attack by the glycosyl acceptor can only happen from the other side, so that the 1,2-*trans* product is formed.[239] Except ester functions, other O-2 substituents can also lead to the formation of the 1,2-*trans* glycoside. These include, for example, cyanomethyl ether, cyanobenzyl ether, picolonyl and picolinyl groups.[109,240–242] If the mechanism corresponds to an S_N2-type reaction, the anomeric center is attacked from the back side of the leaving group (d). This leads to an inversion of the stereochemical configuration and stereoselective formation of the 1,2-*cis* product. In general, the reaction type depends on the leaving group ability and the nucleophilicity of the glycosyl acceptor. [45] The more nucleophilic the acceptor and the worse the leaving group, the higher is the tendency for a reaction according to the S_N2-type mechanism.[243]

Based on previous knowledges[244], the direct synthesis of a tolyl thioglycoside from cellobiose is not efficient due to long reaction time and low yield. An alternative route through a bromoglycoside intermediate **I-7** is suggested and shown in Figure 3.7.

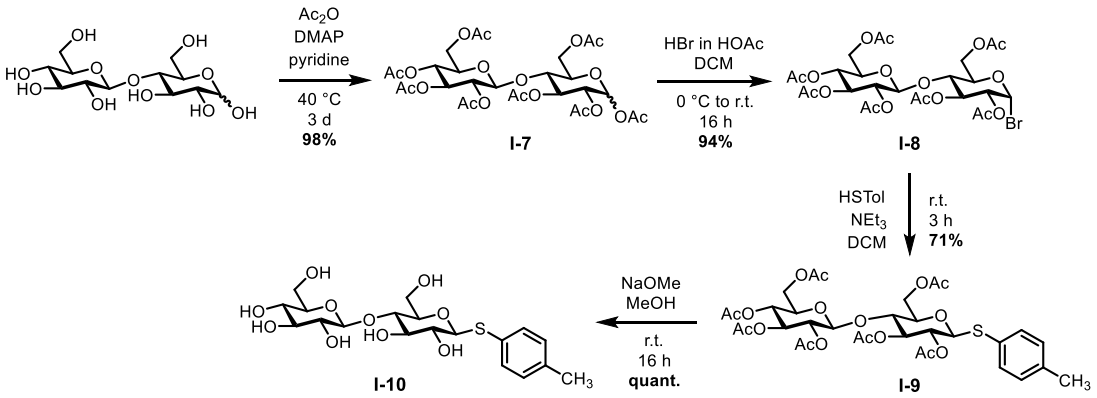

Figure 3.7: Synthesis of Tolyl thioglycoside **I-10** from cellobiose.

In the first step, peracetylation of cellobiose using acetic anhydride (Ac_2O), 4-diaminopyridine (DMAP) as a catalyst and pyridine as a solvent was carried out according to the procedure reported by Veleti et al.[245] The product **I-7** was obtained with an excellent yield of 98% and subjected to a reaction in DCM with 33% solution of hydrobromic acid in acetic acid proposed by Polt et al.[246], giving the thermodynamically favored α-bromoglycoside **I-8** with 94% yield.

The stereochemistry on the anomeric centers in carbohydrates can be determined via nuclear magnetic resonance spectroscopy (NMR). In a proton NMR spectrum, the stereochemical information is revealed by the chemical shift of the anomeric proton signal as well as the ^3J-coupling between the protons on

positions C-1 and C-2. For example, in the bromoglycoside **I-8**, an α-configuration can be found on position C-1 and position C-1' is β-configurated (Figure 3.8). In case of the α-configuration, the C-H bond is parallel to the C-O bond from position C-5 (in red), so that a shift of the electron density can occur from the σ_{CH} into the σ^*_{CO} orbital. In contrast, the C-H and C-O bond are showing in different directions in the β-configuration. As a result, the local electron density around the anomeric proton is lower for the α configurated saccharide, leading to higher chemical shift for the signal.

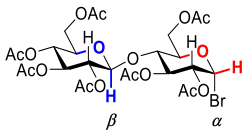

Figure 3.8: Structure of the α-bromoglycoside **I-8**.

In Figure 3.9, the proton NMR spectrum of the α-bromoglycoside **I-8** is shown. The proton signal with a chemical shift of 6.52 ppm can be attributed to the proton on the α-configurated C-1, whereas the doublet at 4.54 ppm corresponds to the β-configurated position C-1'.

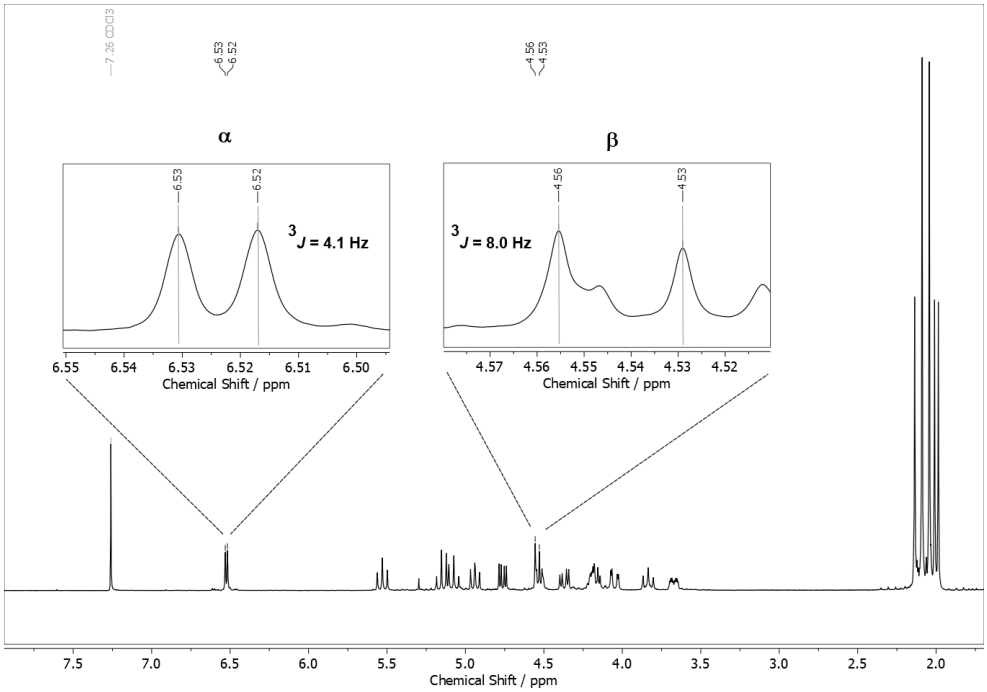

Figure 3.9: ^{1}H-NMR spectrum of α-bromoglycoside **I-8**.

The difference in the ^3J-coupling can be explained using the dihedral torsion angle ϕ between C-H bonds on positions 1 and 2. As shown in Figure 3.10, the torsion angle is 60° for the α-configuration in the Newman projection and 180° in case of a β-glycoside. The antiperiplanar position of the C-H bonds favors the orbital interaction and leads to a stronger coupling. The correlation between the vicinal coupling constant and the torsion angle is also known as Karplus equation.[247]

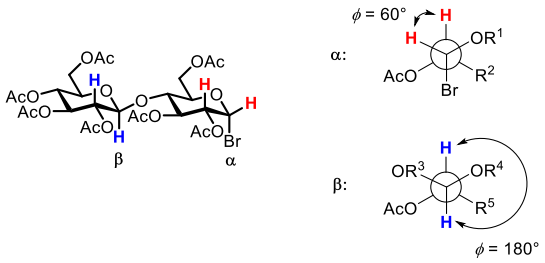

Figure 3.10: Schematic representation of the anomeric centers from the α-cellobiosyl bromide **I-8** in Newmann projections.

The bromoglycoside **I-8** was subsequently converted into the tolyl thioglycoside using *p*-thiocresol as a reagent, triethylamine as a base and DCM as a solvent following the procedure by Tsvetkov et al. The thioglycoside **I-9** was successfully obtained with a yield of 71%. It should be mentioned that this method is only suitable for aromatic thiols (pK_a ≈ 5–7) and not for less acidic aliphatic thiols (pK_a ≈ 10–11).[248] This reaction presumably takes place via both S_N1 and S_N2 mechanism. In the case of S_N1 reaction, the cleavage of the leaving group bromide occurs spontaneously under the formation of oxocarbenium ion. Due to the participation of the neighboring acetyl group, the lower side of position C-1 is blocked, so that the nucleophilic attack can only follow from the upper side. When the reaction follows the S_N2 mechanism, the nucleophilic attack by the thiolate occurs from the back side of the leaving group. Both mechanisms lead to the formation of a β-thioglycoside.

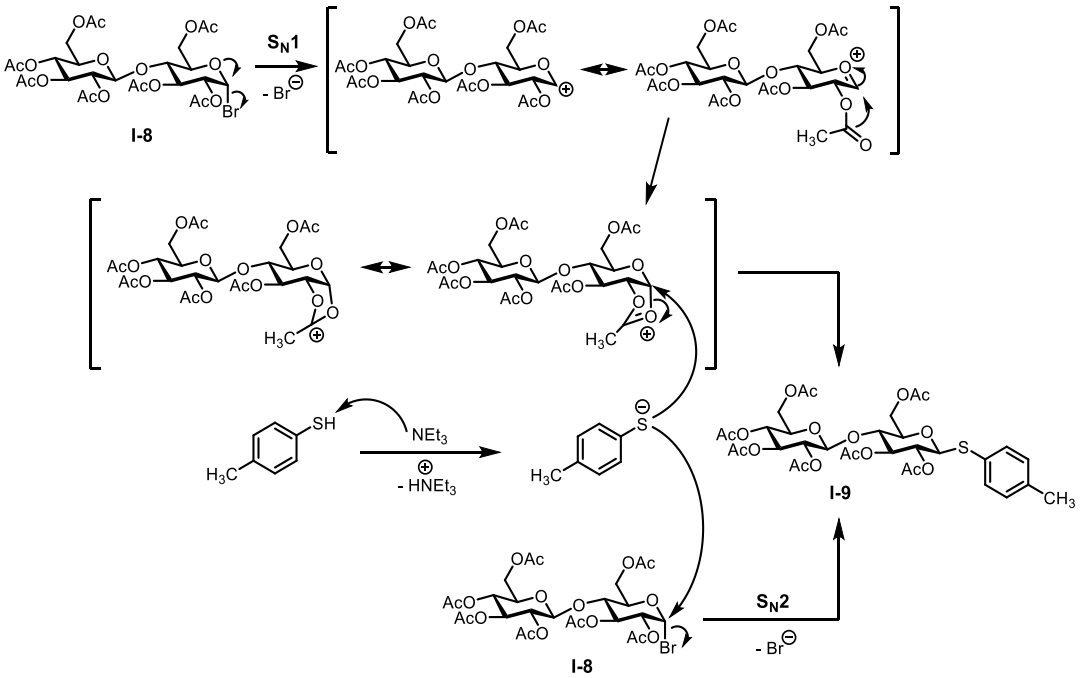

Figure 3.11: Mechanisms for the tolyl thioglycoside formation.

Under Zemplén conditions[249], the acetyl groups were cleaved off in a transesterification. The deprotected thioglycoside **I-10** was obtained with quantitative yield. The catalytic cycle of the transesterification under Zemplén conditions is shown in Figure 3.12.[250,251] First, a H-bond complex is

formed from methanol and methanolate, which performs a nucleophilic attack to the positively polarized carbonyl carbon of the acetyl protecting group. This produces a tetrahedral intermediate from which an alcohol, which in this case is a saccharide, is cleaved off to form the acetic acid methyl ester. The catalyst is regenerated after the protonation of the saccharide.

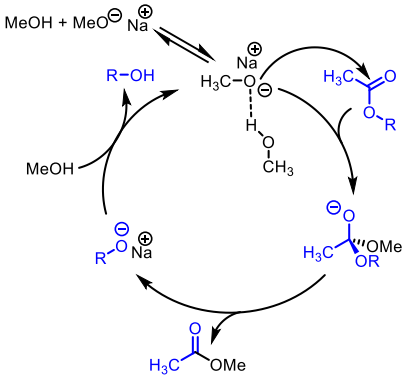

Figure 3.12: Mechanism of acetyl protecting group cleavage under Zemplén conditions proposed by Ren et al.[252]

According to the procedures developed previously[244], the protection of O-4' and O-6' was carried out with an optimized method inspired by the work from Bols et al.[253] The reaction was conducted using benzylidene dimethyl acetal (BDMA) as a reagent, *p*-toluenesulfonic acid monohydrate ($TsOH \cdot H_2O$) for the acidic condition and dimethylformamide (DMF) as a solvent. By heating up to 60 °C and reducing the pressure to 200 mbar, the methanol formed during the reaction was removed to shift the equilibrium to the side of the products. The benzylidene protected cellobioside **I-11** was obtained with a yield of 31%.

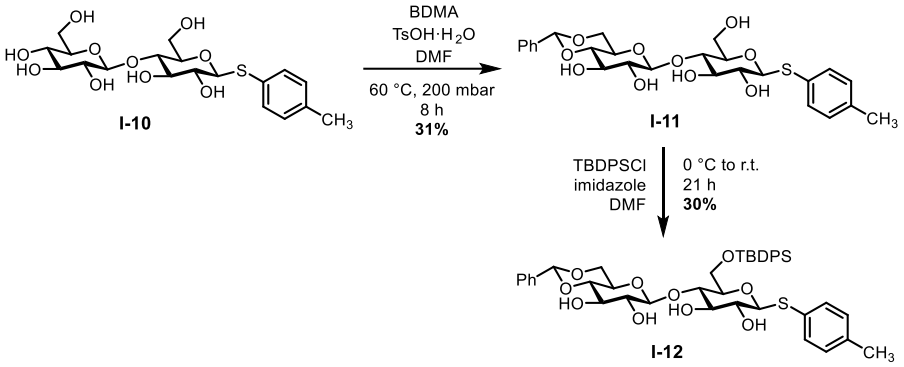

Figure 3.13: Reactions for the protection at O-4' and O-6' of tolyl thioglycoside **I-10** with benzylidene dimethyl acetal (BDMA) and the protection of O-6 using TBDPSCl to obtain the partially protected thioglycoside **I-12**.

The mechanism of the benzylidene acetal formation under acidic conditions is illustrated in Figure 3.14. Through protonation of the benzylidene dimethyl acetal and release of one equivalent methanol, the hemiacetal of benzaldehyde is formed and attacked by the nucleophilic hydroxyl group on the position C-6, giving the mixed acetal **I-10a** by releasing one equivalent of proton. By further protonation of the mixed acetal, another hemiacetal is formed under generation of one equivalent of methanol. The

hemiacetal is attacked by the hydroxyl group on position C-4' to form the benzylidene protected cellobioside **I-11**.

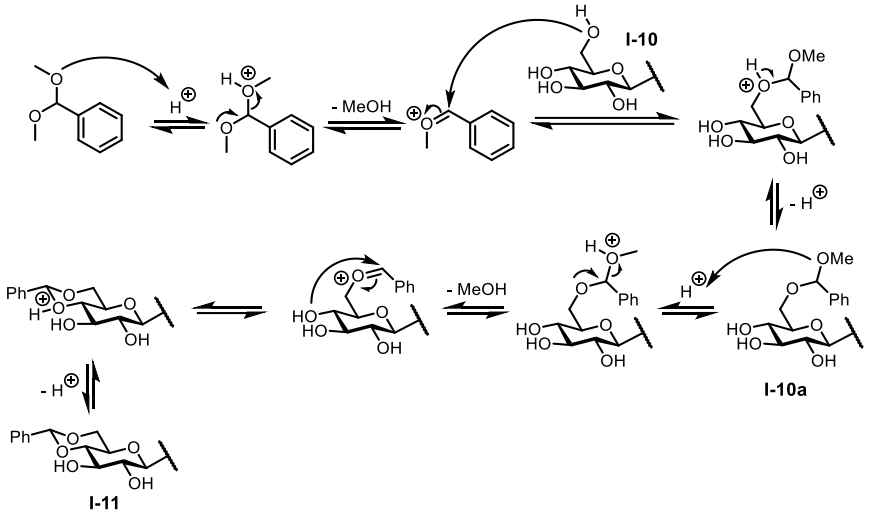

Figure 3.14: Mechanism for the benzylidene acetal formation on positions O-4' and O-6' using BDMA under acidic conditions.

To make sure that the acetal group was introduced to the right positions, heteronuclear multiple bond correlation (HMBC) spectrum was measured and analyzed. This method detects the correlation between a proton and a heteronuclear (in this case a carbon) over more than one bond distance. The spectrum in Figure 3.15 shows correlation of the acetal proton at 5.68 ppm to carbons C-4' at 80.5 ppm and C-6' at 69.2 ppm, the carbonyl carbon at 102.7 ppm also shows correlation to the proton H-6'b at 4.01 ppm, leading to the conclusion that the benzylidene group is attached to the positions O-4' and O-6'.

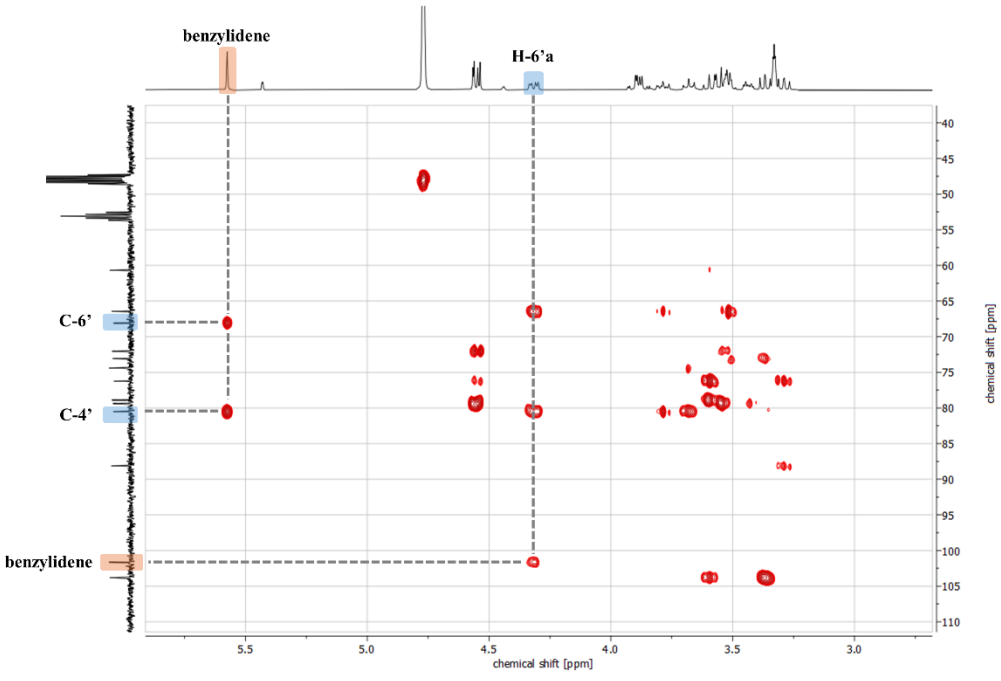

Figure 3.15: Fragment of HMBC spectrum of benzylidene-protected cellobioside **I-11**.

The introduction of TBDPS group was performed under the conditions published by Hanessian et al. using *tert*-butyldiphenylsilyl chloride (TBDPSCl) and imidazole in DMF.[65] The desired product **I-12** was obtained with a yield of 30% after purification via flash chromatography. The mechanistic pathway is shown in Figure 3.16.[254] First, the silyl chloride is activated by imidazole, forming the imidazolium salt, which is attacked by the nucleophilic hydroxyl group of the primary alcohol, while releasing the imidazole. The silyl ether is formed after the deprotonation.

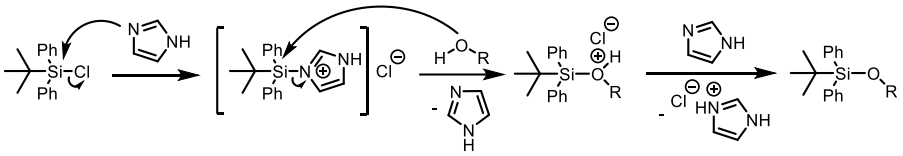

Figure 3.16: Mechanism for the formation of silyl ether using TBDPSCl and imidazole.

It is noticeable, that the total yield after 2 steps is only around 30%. Since the back reaction during the benzylidene protection is suppressed by the reduction of pressure, multiple products were formed during the reaction, especially the ones with protection of the position O-6 that has comparable reactivity to O-6' (see structures **I-11a** and **I-11b** in Figure 3.17), leading to drastic loss of the starting material and poor reproducibility of the outcoming yield of the desired product.

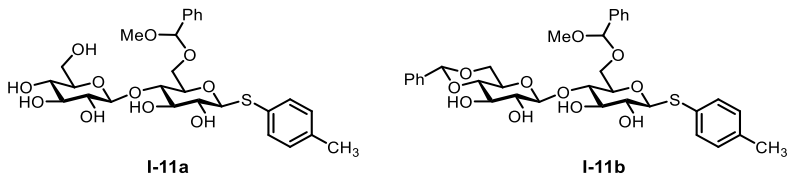

Figure 3.17: Side products formed during introduction of benzylidene protecting group.

Therefore, alternative reaction conditions are required, where the acetal formation is performed under dynamic equilibrium, so that the thermodynamically favored 4',6'-protected cellobioside **I-11** can be formed in larger amount. The first approach (upper reaction in Figure 3.18) was to change the toluenesulfonic acid to trifluoromethanesulfonic acid (HOTf), since it can be used in organic solvent and has a much lower pK_a value around -15. The reaction was able to be carried out at ambient temperatures, whereas the acid was added dropwise at 0 °C to avoid side reactions such as activation of the anomeric center. A large portion of the starting material was converted already after 2 to 5 hours, but the ratio of the products formed was adjusted towards increased fraction of the 4',6'-protected cellobiose with time. After a total reaction time of 3 days, the desired product was isolated with a yield of 35%. Even though the yield is only slightly increased compared to the previous method, but the reproducibility is improved.

Inspired by the work of Mukherjee et al. using $Mg(OTf)_2$ as catalyst for 4,6-protection with benzylidene acetal[255], the analogous reaction on cellobiose for 4',6'-protection was tested (second reaction in Figure

3.18). Since $Mg(OTf)_2$ is derived from HOTf, it is considered as a Lewis superacid with high acidity of the cation.[256] Due to its high solubility in organic solvents and long-term stability, $Mg(OTf)_2$ has been widely used in water-free organic catalysis.[257–259] In case of acetal formation, $Mg(OTf)_2$ is expected to higher the carbonyl reactivity of the aldehyde or ketone. Unfortunately, the usage of this catalyst (10 mol%) led to no conversion of the educt after days when monitored via thin-layer chromatography (TLC), which could be explained by interactions between $Mg(OTf)_2$ and the solvent DMF which is also a carbonyl compound. In the original reaction[255], the acetal formation is performed in acetonitrile, which however cannot solubilize the starting material **I-10**.

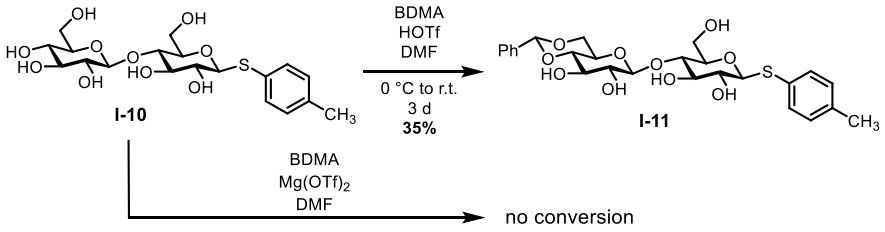

Figure 3.18: Alternative approaches for the formation of 4',6'-protected cellobioside **I-11**.

Surprisingly, it was found that the combination of the Brønsted acid HOTf with the Lewis acid $Mg(OTf)_2$ can efficiently promote the formation of the acetal (Figure 3.19). Using this method, the desired product **I-11** was obtained with a yield of 70%.

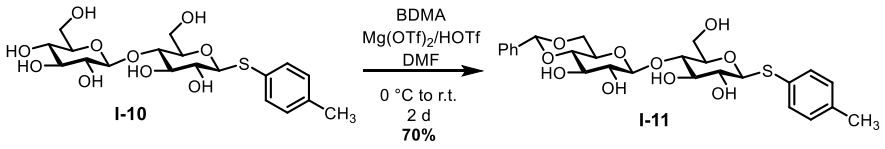

Figure 3.19: 4',6'-protection with benzylidene group using a combination of acidic catalysts $Mg(OTf)_2$ and HOTf.

Noticeably, the 4',6'-protected cellobioside **I-11** has polar and apolar sides in the molecule, leading to poor solubility in most solvents and thus challenging isolation of the pure product. To simplify the purification process, the introduction of the benzylidene group and the TBDPS group were performed in a one-pot reaction (Figure 3.20), which enabled 37% of the desired product **I-12** to be obtained.

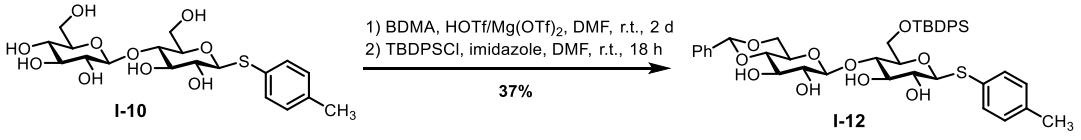

Figure 3.20: One-pot reaction for the protection at O-4' and O-6' of tolyl thioglycoside **I-10** with benzylidene acetal and position O-6 with silyl group.

In the last step of the donor synthesis, the remaining free hydroxyl groups should be protected, so that they are not able to function as glycosyl acceptors in a glycosylation reaction. As mentioned above, the usage of participating protecting group is important for the stereoselective outcome of the glycosylation.

Particularly in this case, a β-glycoside is desired, since all the anomeric centers of the *S. pneumoniae* ST3 antigen are β-configurated. Referring to the glycosylation mechanism with neighboring group participation, the benzoyl group directs the formation of 1,2-*trans* glycoside, which is the desired β-glycoside for cellobiose. When comparing the benzoyl protecting group with the acetyl group, differences can be found in the donor reactivity, stereoselectivity in the glycosylation and the protecting group stability. It has been demonstrated that a glycosyl donor with an O-2 benzoyl group exhibits higher donor reactivity than the acetyl protected analog, but with less stereoselectivity[108], which is less intuitive, since the benzoyl group is expected to provide more steric hindrance than the acetyl group. The acetyl group, nevertheless, can be transferred to a free hydroxyl group of the glycosyl acceptor during a Lewis acid promoted glycosylation, which is an undesirable side reaction that has been observed in various glycosylation reactions.[260–262]

Based on the protocol by Lefeber et al.[263], the conversion of the OH-groups into benzoyl esters was carried out in DCM using benzoyl chloride (BzCl) as reagent, pyridine as the base and DMAP as a catalyst (Figure 3.21). In the first experiment, 10 equivalents (eq.) of BzCl were added (2.5 eq. per OH-group). After 18 hours, the reaction was quenched, and the main product was isolated by flash chromatography with a yield of 45%.

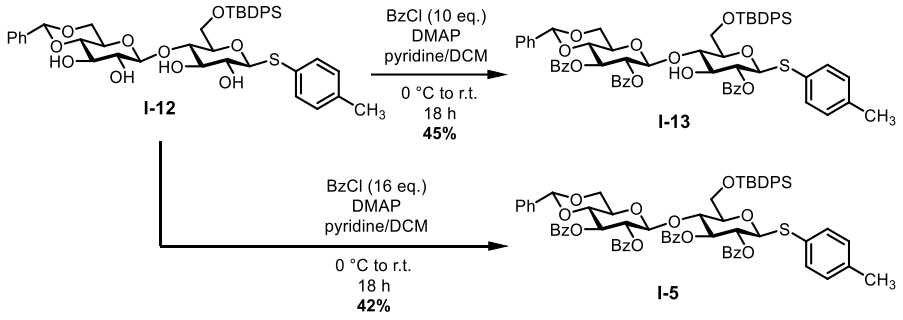

Figure 3.21: Benzoylation of the remaining free OH-groups of tolyl thioglycoside.

The structure of the product was unraveled through a combination of different NMR measurements, showing unexpectedly a cellobiose with only 3 instead of 4 benzoyl groups. A general hint for successful acylation of the hydroxyl group from the saccharide is the shift of ring proton signals to a higher chemical shift. In the ^{13}C-NMR spectrum, only 3 ester groups were detected that correlate to protons H-2, H-2' and H-3' in the HMBC spectrum (shown in Figure 3.22). This implies that, despite the excess of benzoyl chloride added to the reaction mixture, the position O-3 remained unprotected (**I-13** in Figure 3.21). This regioselectivity can be explained by the steric hindrance caused by the bulky TBDPS group, which may prevent the ester formation on position O-3.

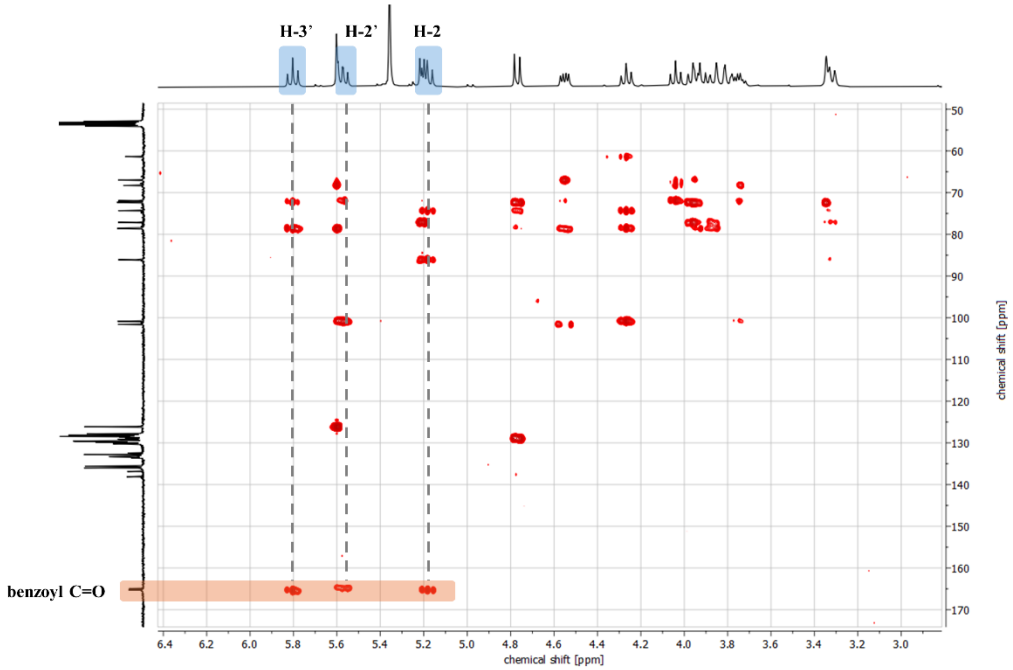

Figure 3.22: Fragment of HMBC spectrum of the cellobioside **I-13** showing correlation of the benzoyl carbonyl groups to protons H-2, H-2' and H-3'.

It is likely that traces of the fully protected saccharide were formed, so the reaction was repeated using 16 equivalents of BzCl (4 eq. per OH-group). After the same amount of reaction time, the desired product **I-5** was able to be isolated with 42% yield, which is also confirmed by the NMR measurements (the HMBC spectrum is shown in Figure 3.23). Conceivably, higher amount of the reagent and extended reaction time would possibly further optimize the outcome of the reaction.

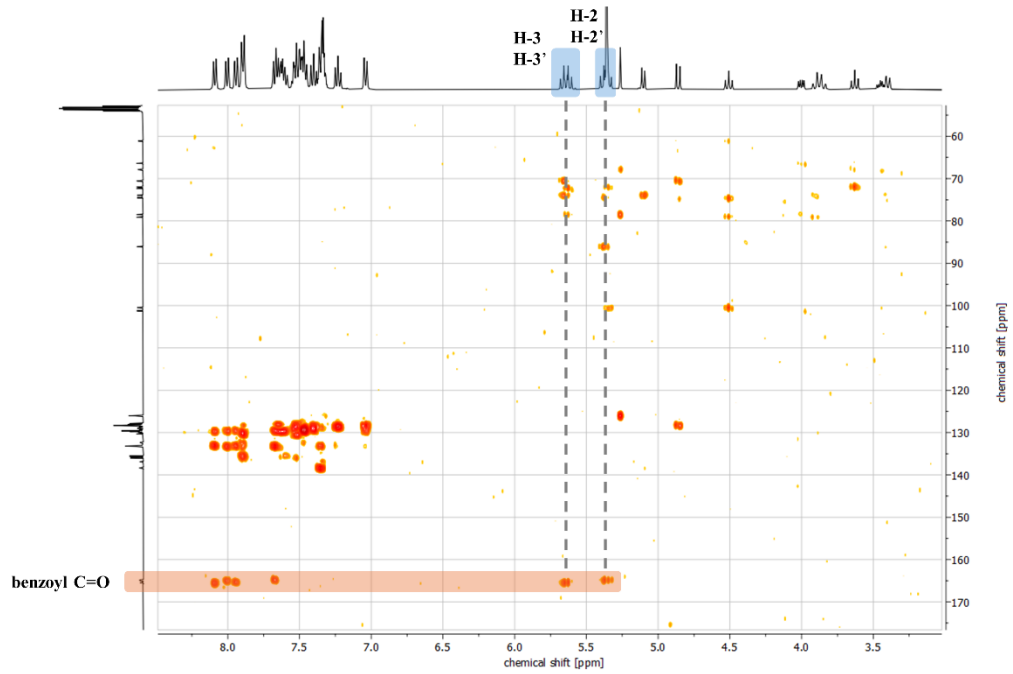

Figure 3.23: HMBC spectrum of the cellobioside **I-5** showing correlation of the benzoyl carbonyl groups to protons H-2, H-3, H-2' and H-3'.

For the synthesis of the ethyl thioglycoside, a similar reaction pathway was designed (Figure 3.24) starting with the peracetylation of cellobiose and the conversion to thioglycoside. In contrast to the tolyl thioglycoside, the glycosylation of peracetylated cellobiose with ethanethiol as glycosyl acceptor was successfully performed in a one-step synthesis following the procedure reported by Tomoo et al.[264] In this reaction, boron trifluoride etherate ($BF_3{\cdot}OEt_2$) was used as a Lewis acid promotor, giving the desired thioglycoside donor **I-14** with a yield of 92%.

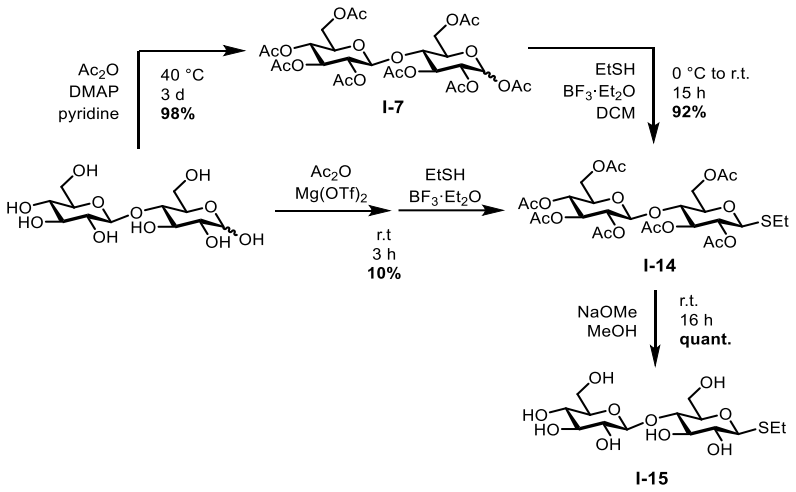

Figure 3.24: Reaction pathways for the synthesis of ethyl thioglycoside **I-15**.

An alternative method was provided by the protocol developed from Mukherjee et al.[255] In a one-pot reaction, cellobiose was peracetylated using acetic anhydride under catalysis with $Mg(OTf)_2$, and further converted into the ethyl thioglycoside under similar conditions as the first method, but within much shorter reaction time. Though the usage of $Mg(OTf)_2$ should stimulate both reaction steps, only 10% of the product was obtained.

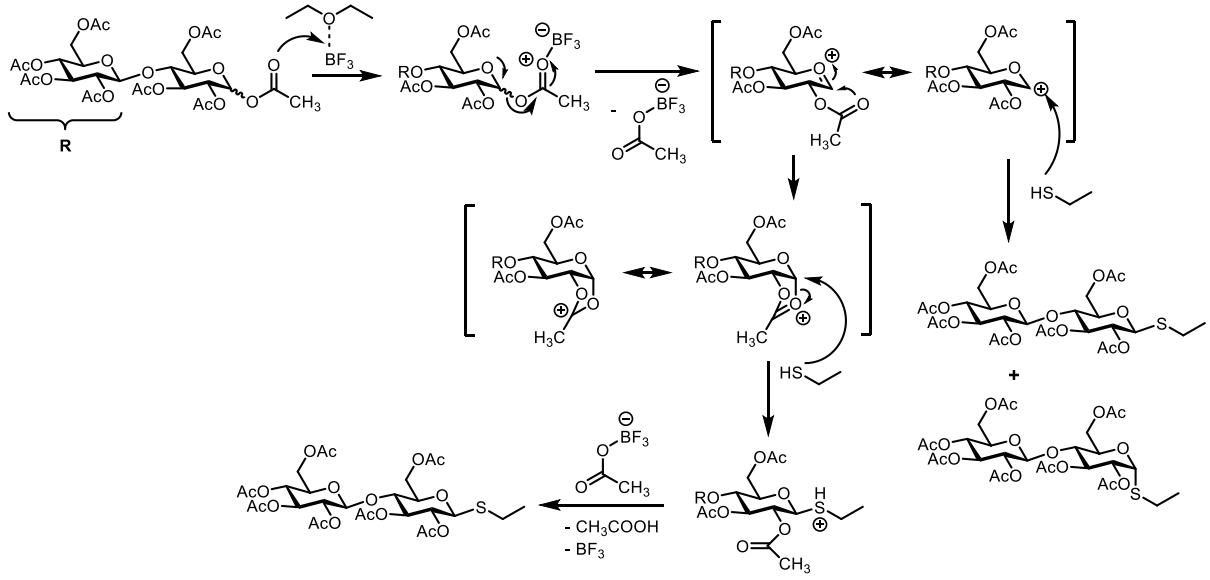

Figure 3.25: Mechanisms of boron trifluoride etherate mediated ethyl thioglycoside formation with neighboring group participation.

The mechanism for the thioglycosylation is shown in Figure 3.25. The acetyl group on the anomeric center is activated by the Lewis acid boron trifluoride etherate, leading to the release of one equivalent acetic acid under formation of the oxocarbenium species. When the acetyl group on position C-2 participates in the reaction, the formation of orthoester blocks the lower side of the activated anomeric center, so that ethanethiol can only attack from the upper side, giving the β-thioglycoside. Concurrently, ethanethiol can also attack the carbenium ion from both sides, resulting in formation of both α- and β-thioglycoside. The total anomeric ratio of α:β = 1:40 was determined in the proton NMR spectrum. Subsequently, the acetyl groups were cleaved off under Zemplén conditions[249], and the product **I-15** was obtained in quantitative yield.

Following the same procedures for the tolyl thioglycoside, the positions O-4' and O-6' were protected using BDMA and the combination of HOTf and $Mg(OTf)_2$ as acid catalysts. The benzylidene protected thioglycoside **I-16** was successfully obtained with a yield of 88%. It has to be mentioned that the ethyl thioglycoside **I-15** is more sensitive to acidic conditions than tolyl thioglycoside **I-10**, and can be activated partially by HOTf. Nevertheless, the yield is higher than the previous case with the tolyl thioglycoside, because the starting material and side products are more polar, so that the isolation of **I-16** required less effort. The product was further subjected to a reaction with TBDPSCl and imidazole in DMF to protect the OH-group on position C-6. The protection was much more efficient than with the tolyl thioglycoside, since the ethyl group on the anomeric center performed less steric hindrance. Therefore, it was able to isolate the product **I-17** with a yield of 89%. In the final step, the remaining hydroxyl groups were protected using BzCl and DMAP in a solvent mixture consisting of pyridine and DCM to synthesize the glycosyl donor **I-6**. The much higher yield of 91% compared to 45% for the tolyl thioglycoside can also be explained by less steric crowding when the tolyl group is substituted by the ethyl group.

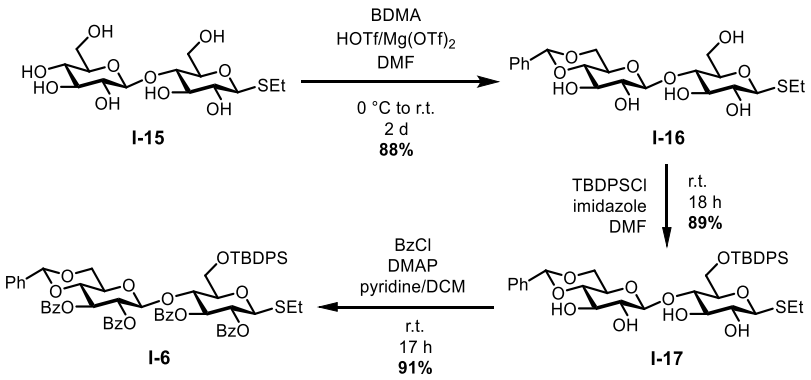

Figure 3.26: Introduction of orthogonal protecting groups to obtain the glycosyl donor **I-6**.

3.2.3 Glycosylation of Spacer with Thioglycosides

To be able to present the B-cell epitopes on the surface of the supramolecular vaccine, the antigens have to be conjugated to a spacer component. Therefore, a protected amino alcohol **I-4** was synthesized that can be used as glycosyl acceptor in an *O*-glycosylation. Since the outcome of a chemical glycosylation often depend on various parameters, especially relative reactivities of donor and acceptor as well as donor activation conditions, the glycosylation will be studied using two different thioglycoside donors (**I-5** and **I-6**) with either the combination of *N*-iodosuccinimide (NIS) and silver triflate (AgOTf) as promotor or under milder conditions using an in situ synthesized dimethyl(methylthio)sulfonium triflate (DMTST) (Figure 3.27).

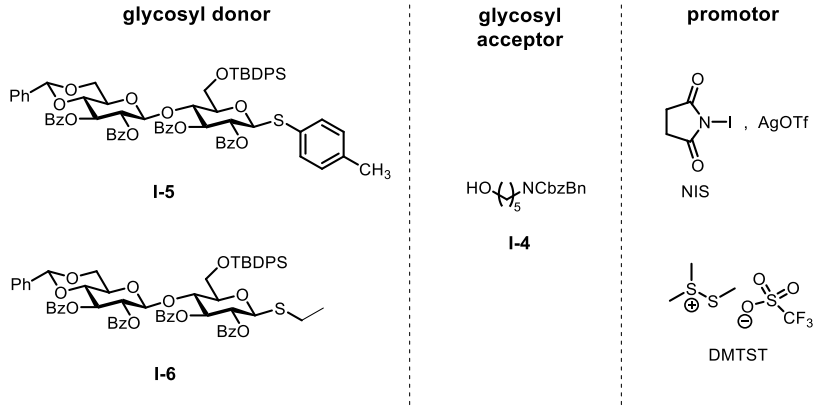

Figure 3.27: Protected cellobioside donors, acceptor and promoters for the glycosylation reaction.

The glycosylation using tolyl thioglycoside **I-5** as glycosyl donor and NIS/AgOTf as promotor was performed following the protocol by Konradsson et al.[265] Glycosyl donor and acceptor were used in a 1:1.1 ratio with 1.3 eq. of each promotor component in DCM in the presence of 4 Å molecular sieves (MS).

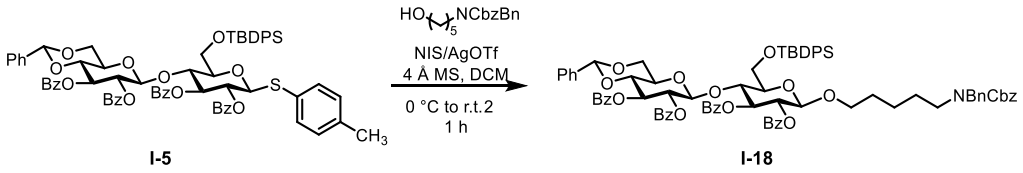

Figure 3.28: Glycosylation of spacer **I-4** with tolyl thioglycoside **I-5** using NIS/AgOTf as promotor.

The glycosylation mechanism using tolyl thioglycoside **I-5** as glycosyl donor and reagent combination AgOTf/NIS proposed in literature[108,266] is shown in Figure 3.29. The reaction of NIS with the Lewis acid AgOTf first leads to the formation of iodonium with triflate as counter ion. The binding of iodonium by the sulfur atom of the thioglycoside leads to activation of the anomeric center under formation of the oxocarbenium ion, iodine and tolyl disulfide. Due to the electrophile nature of oxocarbenium ion (especially when an electron withdrawing benzylidene group is present), it is likely that a covalent bond is formed between the anomeric center and the triflate counter ion, giving the thermodynamically

favored α-triflate. In this case, the glycosyl acceptor can only attack the anomeric center from the back side of the triflate, leading to the stereoselective formation of the β-*O*-glycoside. If the anomeric center is not blocked by the triflate, the β-selectivity is achieved due to participation of the benzoyl group installed on position C-2.

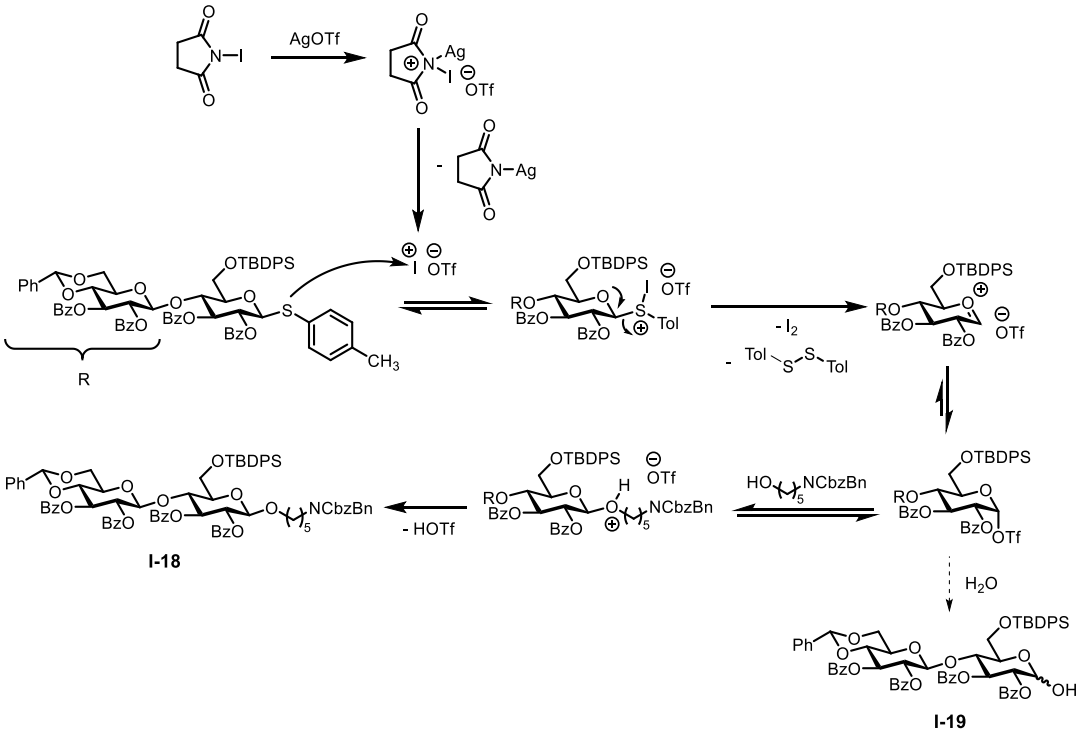

Figure 3.29: Mechanism for the glycosylation using thioglycoside as glycosyl donor and AgOTf/NIS as promotor.

After 21 hours of reaction time, the glycosylation was quenched using triethylamine. By subjecting the crude product to flash chromatography, the desired product was only obtained with a yield around 10% but with further impurities. Since the proton NMR spectrum didn't show clear infromation for the molecular structures, a measurement was conducted on an electrospray ionization mass spectrometry (ESI-MS) to assess the molecular weight of the isolated compounds. The mass spectrum (Figure 3.30) demonstrates that the desired glycosylation product **I-18** is formed (*m/z* = 1415.5280 for $[M+Na]^+$), while hydrolyzed glycosyl donor **I-19** was formed as a anomeric mixture at the same time (m/z = 1107.3566 for $[M+Na]^+$). It was also noticed that large amounts of benzaldehyde were formed during the reaction, implicating cleavage of the benzylidene group from positions O-4' and O-6', which is possible due to the generation of HOTf during the glycosylation. The reaction can be therefore optimized by addition of a weak base.

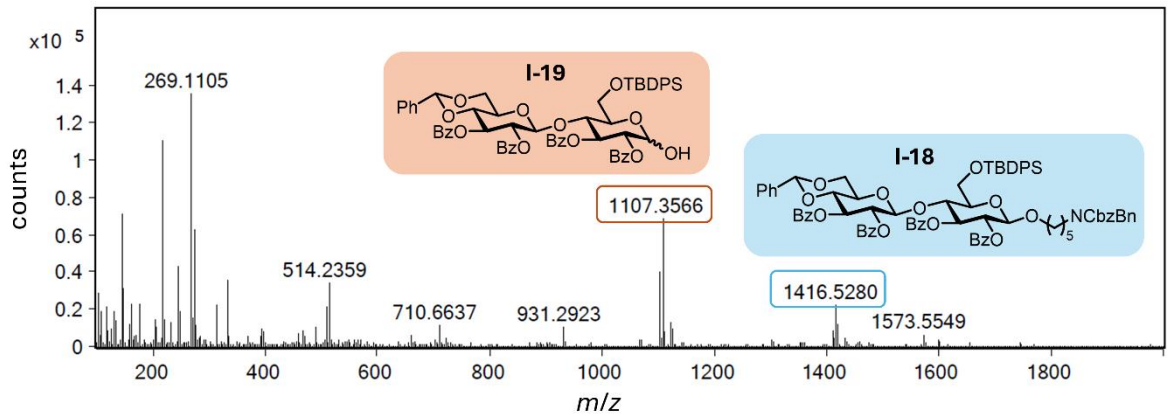

Figure 3.30: ESI-MS spectrum of fractions isolated from the AgOTf/NIS-promoted glycosylation of tolyl thioglycoside **I-5** and spacer **I-4**.

In order to avoid cleavage of protecting groups, the glycosylation with the same donor-acceptor combination was conducted following the procedure reported by Takai et al. using mild DMTST as promotor, which is synthesized from methyl disulfide and methyl triflate (MeOTf).[267] Unfortunately, no donor activation was observed even hours after addition of the promotor, implicating low donor reactivity towards activation using DMTST.

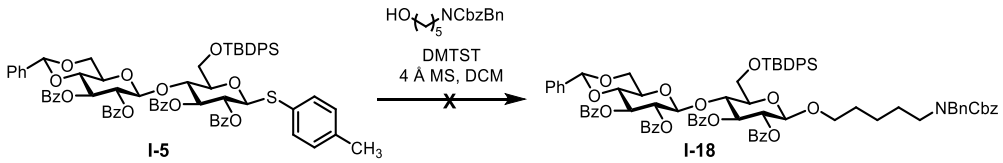

Figure 3.31: Glycosylation of spacer **I-4** with tolyl thioglycoside **I-5** using DMTST as promotor.

According to the mechanism of DMTST promoted glycosylation[267,268] (Figure 3.32), the activation of the anomeric center involves a methylsulfenylation of the sulfur atom on the reducing end. It is known that donor reactivity can be lower when a bulky TBDPS group is present on position O-6.[269] In combination with a benzoyl group on O-2 and a tolyl group linked to the sulfur atom, the steric crowding effect might be too strong, so that the anomeric center is not any more accessible for the promotor. Furthermore, disaccharide donors with β-configurated interglycosidic linkage and O-4'/6' benzylidene protection are generally considered less reactive.[270] Once the sulfur atom is methylsulfenylated, the oxocarbenium ion can be formed under release of the disulfide. Similar to iodonium promoted glycosylation described above, the α-triflate represents the active donor species, which can subsequently undergo the same β-glycosylation reaction.

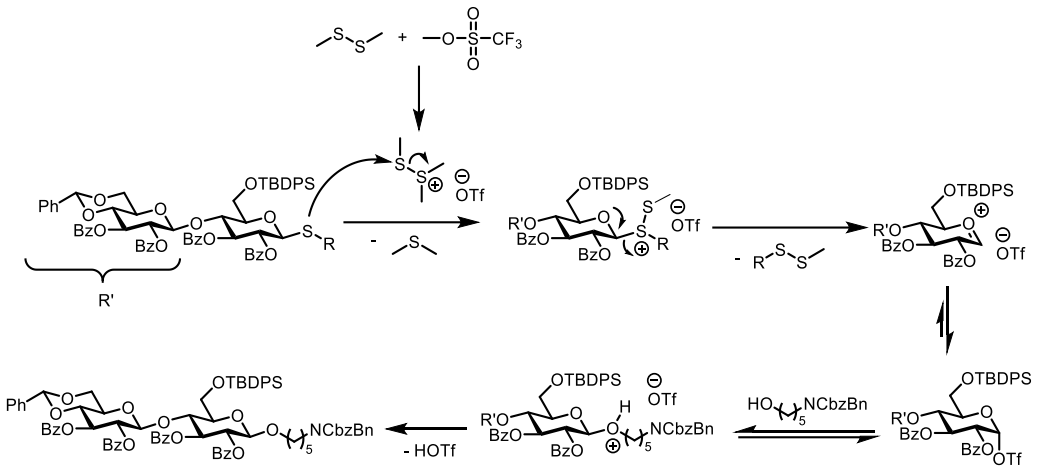

Figure 3.32: Mechanism for the glycosylation using thioglycoside as glycosyl donor and DMTST as promotor.

When changing to less sterically hindered ethyl thioglycoside **I-6** (Figure 3.33), conversion of the donor was already observed 30 minutes after addition of the promotor. In the first experiment, 3.0 eq. DMTST was synthesized by mixing methyl disulfide and methyl triflate in a 1:1 ratio and added to the donor-acceptor mixture that was dried over freshly activated 4 Å molecular sieves. The reaction was monitored via TLC and quenched after completion of donor conversion (21 hours after promotor addition). The desired β-glycosylation product was obtained with 13% yield after purification via flash chromatography (entry 1, Table 3.1). The loss of starting material is mainly caused by two side reactions: cleavage of the benzylidene group and formation of α-glycosylation product.

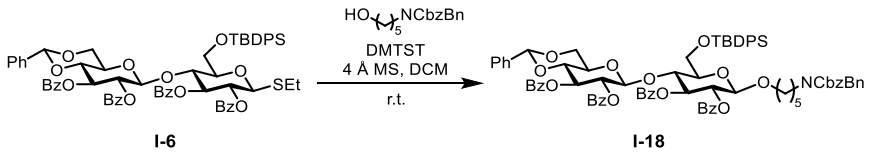

Figure 3.33: Glycosylation of spacer **I-4** with ethyl thioglycoside **I-6** using DMTST as promotor.

Even though the donor-promotor system is designed for selective β-glycosylation, it is challenging to predict the stereoselective outcome of a glycosylation reaction due to occurrence of various mechanisms and interconversion between different intermediates. Since the formation of intermediate α-triflate is crucial for the β-selectivity, the amount of methyl triflate was increased to 6.0 eq. with respect to the glycosyl donor. With similar reaction time (entry 2 in Table 3.1), the product was obtained with an enhanced yield of 40% instead of 13%, proving that higher amount of methyl triflates supports the formation of activated glycosyl donor and leads to higher conversion of the donor into desired glycosylation product. The glycosylation was accompanied by the cleavage of benzylidene group, leading to deprotection of donor and the glycosylation product. The products formed was able to function as glycosyl acceptors and undergo further undesired glycosylation reactions. The comparison of the glycosylation outcomes after different reaction times (entry 2 and 3 in Table 3.1) demonstrates an increase of the yield with reaction time, referring to a higher reaction rate of the glycosylation than

benzylidene cleavage. However, when the donor conversion is completed, the reaction will only exceed with the cleavage of benzylidene group, leading to loss of the product. It is though difficult to forecast the perfect reaction time when the conversion is completed, while the least of benzylidene groups is cleaved off.

It is reported that the application of a preactivation strategy by activation of the glycosyl donor prior to the addition of the acceptor afford unique stereoselectivity regardless its electronic nature.[105,108,271–273] Therefore, the preactivation method was exploited for the current glycosylation reaction. Surprisingly, the reaction was completed already after 2.5 h and the desired product was obtained with a yield of 52%. Due to full conversion of donor into either glycosyl triflate or participation of the O-2 benzoyl group, the S_N2-like displacement by the glycosyl acceptor takes place with high reaction rates and excellent β-selectivity. The fast conversion is also beneficial in terms of avoiding undesired side reactions related to the cleavage of benzylidene groups.

Table 3.1: Reaction conditions for the glycosylation of spacer **I-4** with orthogonally protected ethyl thioglycoside **I-6** using DMTST as promotor and yield.

entry	Pre-activation of donor	Methyl disulfide	MeOTf	Reaction time	Yield
1	No	3.0 eq.	3.0 eq.	19 h	13%
2	No	3.0 eq.	6.0 eq.	20 h	40%
3	No	3.0 eq.	6.0 eq.	5 h	33%
4	Yes	3.0 eq.	6.0 eq.	2.5 h	52%

3.2.4 Synthesis of Cellobiuronic Acid Antigens by Regioselective Modifications

The glycosylation product **I-18** was used for further modifications to obtain B-cell epitopes against serotype 3 *S. pneumoniae*. Since the protecting groups installed on position O-6 and O-6' are orthogonal, one of the groups can be selectively cleaved off, so that a subsequent oxidation of the primary alcohol into the corresponding carboxylic acid can take place. Using this strategy, two B-cell epitopes carrying either a glucose (Glc) or glucuronic acid (GlcA) at the non-reducing terminus and a 5-aminopentyl spacer at the reducing end can be synthesized.

For the synthesis of antigen GlcA-β-(1→4)-Glc, the modification was performed following the protocol by Xiong et al.[274] In the first step, the benzylidene group was cleaved off under acidic conditions using a 10% aqueous solution of trifluoroacetic acid (TFA) and DCM as solvent (Figure 3.34). The 4',6'-diol **I-20** was obtained after purification via flash chromatography with a yield of 85%.

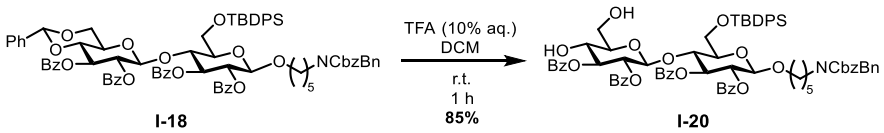

Figure 3.34: Cleavage of benzylidene protecting group from **I-20** under acidic conditions.

The complete cleavage of benzylidene group was confirmed by the disappearance of the singlet proton signal at 5.25 ppm in the ^{1}H-NMR spectrum (Figure 3.35).

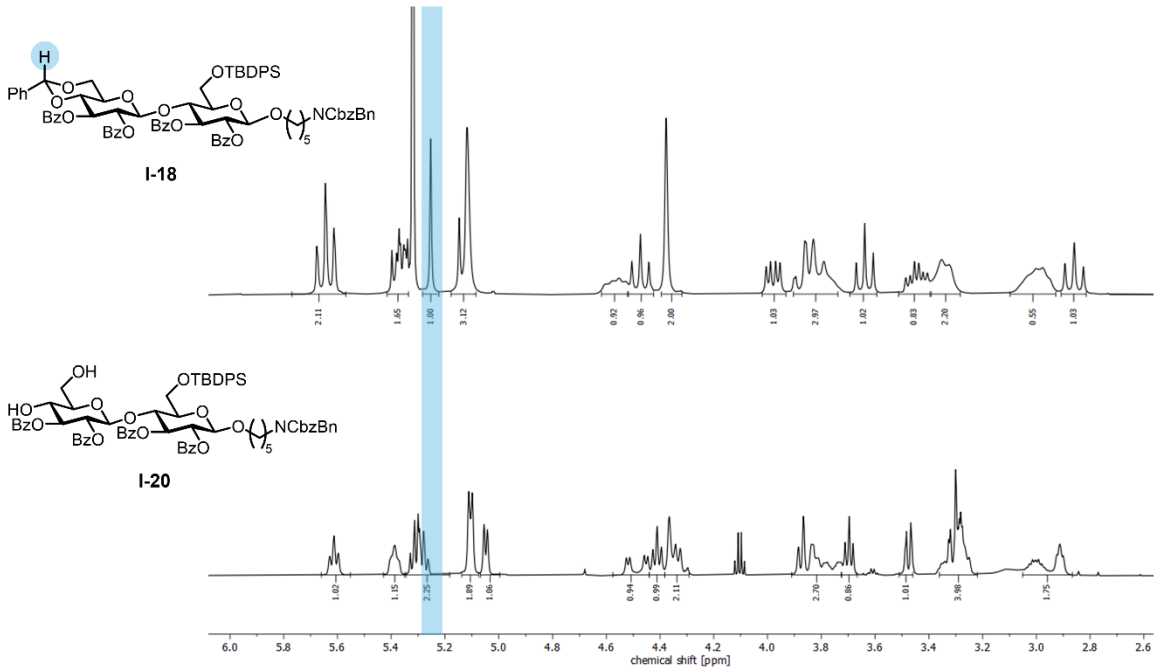

Figure 3.35: Fragments from ^{1}H-NMR spectra of cellobioside **I-18** and **I-20**.

In the next step, a regioselective oxidation of **I-20** into the corresponding carboxylic acid was carried out followed by methylation of carboxylic acid (Figure 3.36). The oxidation of the hydroxyl group on position O-6' was performed with 2,2,6,6-tetramethyl-1-piperidinyloxy (TEMPO) as an oxidative catalyst and (diacetoxyiodo)benzene (BAIB) as co-oxidant with high regioselectivity.

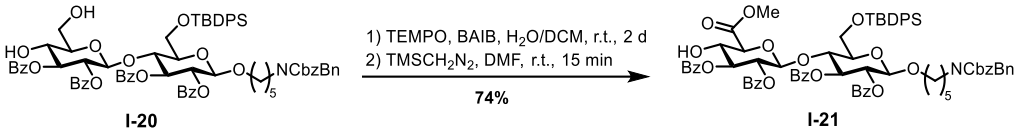

Figure 3.36: Regioselective oxidation of O-6' position of diol **I-20** and subsequent methylation of the carboxylic acid.

It is reported that the addition of BAIB allows the oxidation to be performed under mild conditions by minimizing the amount of TEMPO.[275] The mechanism for TEMPO mediated oxidation of the primary alcohol with BAIB as co-oxidant is shown in Figure 3.37.[276] The reaction starts with the disproportionation of the TEMPO radical into an oxoammonium ion and hydroxylamine under acid catalysis. The oxoammonium is the active oxidizing agent which converts a saccharide with a primary hydroxyl group into the corresponding carboxylic acid. The oxidizing agent itself is reduced to the hydroxylamine, which is oxidized by the co-oxidant BAIB to regenerate the TEMPO radical. This results in the release of iodobenzene and acetic acid that can catalyze the initial dismutation of the TEMPO radical, thereby completing the reaction cycle.

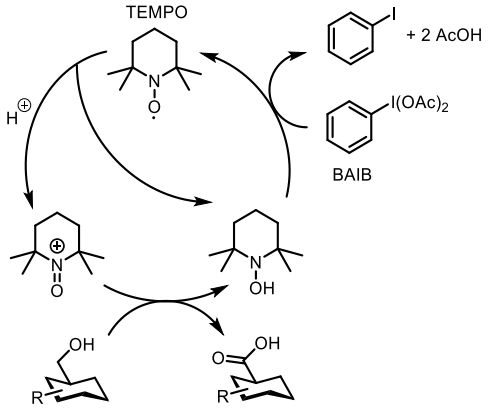

Figure 3.37: Mechanism for TEMPO mediated oxidation of primary hydroxyl group with BAIB as a co-oxidant.

To simplify the purification process, methylation of the carboxylic acid was performed with a 1 M solution of trimethylsilyldiazomethane ($TMSCH_2N_2$) in hexane according to the procedure reported by Susanto et al.[277] Compared to diazomethane, TMS-diazomethane is less toxic and explosive, so that it can be prepared with a larger scale and stored over months without degradation.[278] The mechanism (Figure 3.38) involves a proton abstraction by TMS diazomethane from the carboxylic acid and subsequent nucleophilic attack by the carboxylate under release of nitrogen. The reaction can be conducted at ambient temperatures with high efficiency (reaction completed within minutes). During

aqueous work-up of the reaction mixture, trimethylsilylmethyl ester hydrolyzes into the corresponding methyl ester and trimethylsilanol. The methyl ester **I-21** was isolated with a yield of 74% over 2 steps.

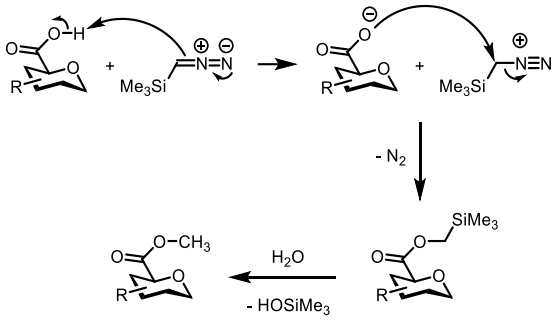

Figure 3.38: Mechanism for methylation of carboxylic acid using TMS-diazomethane.

The successful oxidation of position C-6' and methylation was proven via a combination of heteronuclear single quantum coherence (HSQC) and HMBC experiments. The HSQC technique shows correlation of protons and carbon atoms over ^{1}J coupling and provides insight into direct attachment of protons to the carbons including the information about numbers of protons attached to the carbon. In the HSQC spectrum (Figure 3.39), only one remaining primary carbon from the saccharide can be found at 61.1 ppm, which is assignable to position C-6 due to the correlation to protons H-6a and H-6b. A further look into the HMBC spectrum reveals that the carbonyl carbon atom from the methyl ester at 168.3 ppm correlates to the methyl group and the proton H-4' (^{3}J coupling), indicating that position C-6' is oxidized to carboxylic acid which is protected by a methyl group.

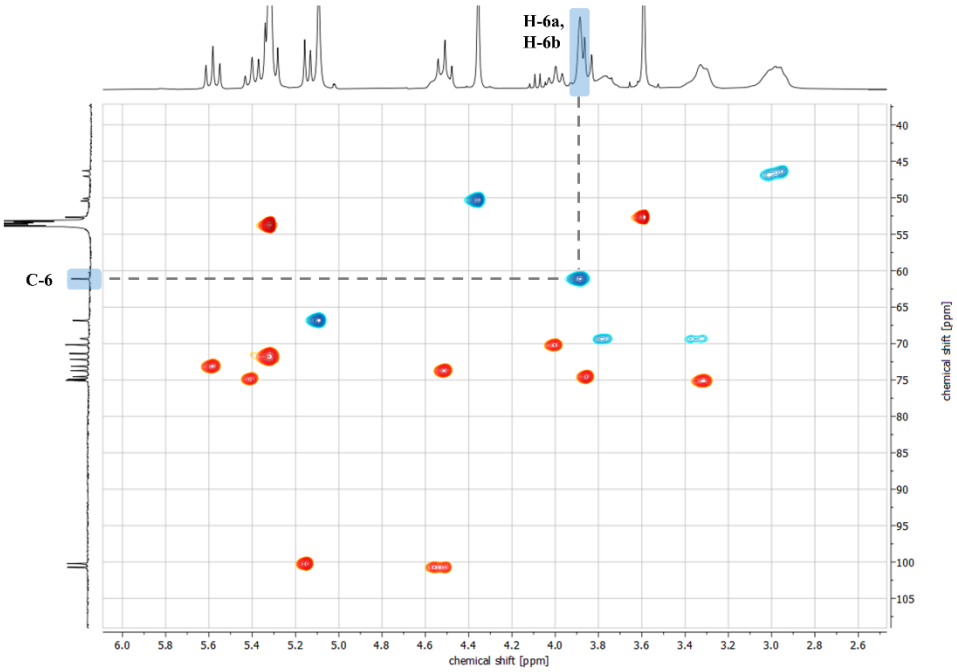

Figure 3.39: Fragment from HSQC spectrum of oxidized cellobioside **I-21**.

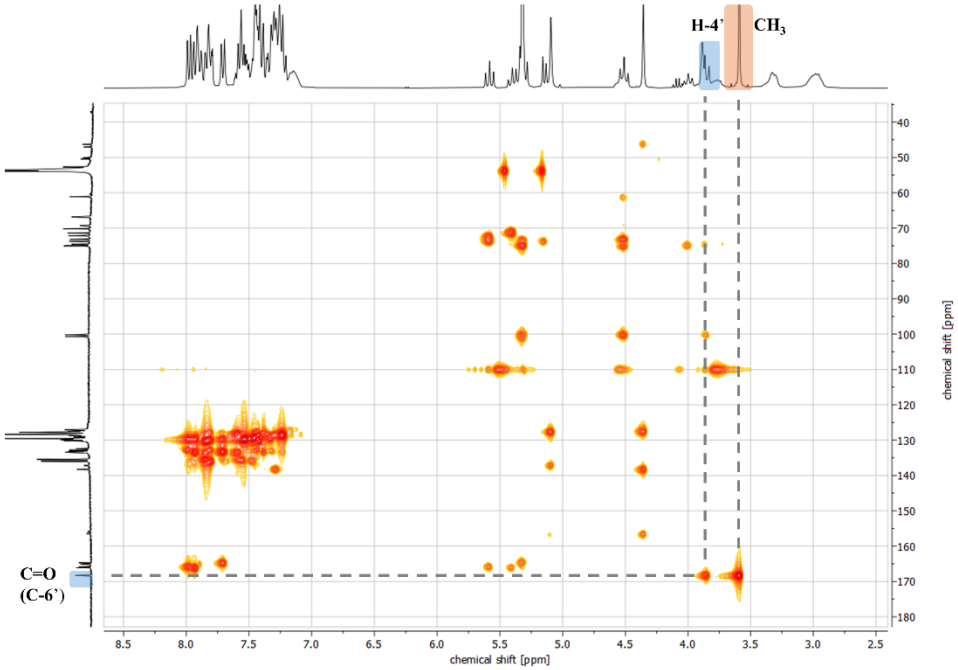

Figure 3.40: Fragment from HMBC spectrum of oxidized cellobioside **I-21**.

The global deprotection of **I-21** was conducted in 3 synthetic steps starting with the cleavage of the TBDPS group using fluoride including reagents. Therefore, two fluoride sources were exploited: tetrabutylammonium fluoride (TBAF) and hydrogen fluoride-pyridine (HF·pyridine) complex (Figure 3.41).

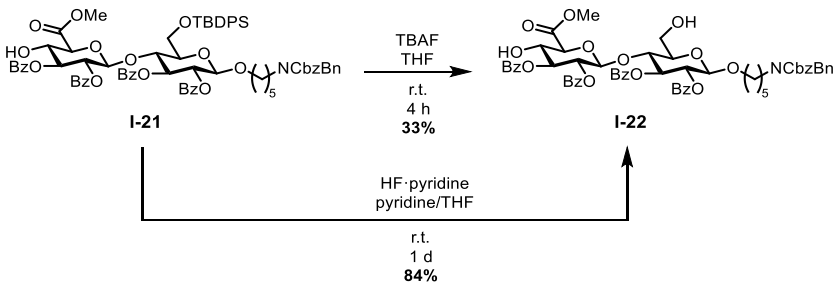

Figure 3.41: Reaction conditions for the cleavage of TBDPS protecting group.

In the first method, the cleavage of TBDPS group was conducted using 1.5 eq. of a 1 M TBAF solution in THF following the procedure by Liu et al.[279] Under those conditions, the conversion of the starting material was completed in several hours. Due to formation of various side products, the desired product **I-22** was only obtained with a yield of 33% after purification via flash chromatography. There are two possible reasons for side reactions. One is presumably the remaining water in the TBAF solution that is highly nucleophilic in the presence of fluoride ions [280,281], which leads to alkaline hydrolysis of the methyl and benzoyl esters. The second reason is based on the explanation that fluoride in THF is a strong base that can affect base labile groups.[282] When performing the silyl removal with HF-pyridine complex

according to Zhang et al.[283], the cleavage was much slower than the first method, but no significant formation of side products was observed. The desired product **I-22** was isolated with a yield of 84%.

The cleavage of silyl group in presence of fluoride is claimed to be driven by the formation of a strong Si-F bond.[284] As shown in Figure 3.42, fluoride induced desilylation undergoes an analogous mechanism as a S_N2 reaction.[285] It starts with the nucleophilic attack by fluoride, forming the pentavalent siliconate intermediate, from which the alkoxide is eliminated, subsequently. Through final aqueous work-up, the alkoxide is protonated to give the free alcohol and the fluorosilane is hydrolyzed into silanol.

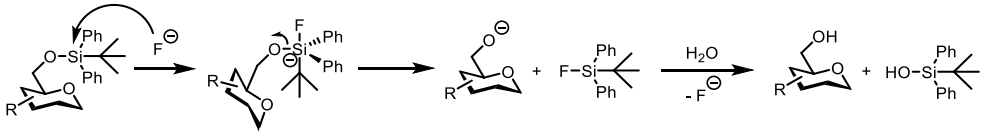

Figure 3.42: Mechanism for TBDPS cleavage using a fluoride source.

The cleavage of benzoyl and methyl groups was performed under alkaline hydrolysis with a 1 M aqueous lithium hydroxide (LiOH) solution. Deprotected cellobiuronic acid **I-23** was directly subjected to hydrogenolytic cleavage of the remaining Cbz and benzyl groups on the spacer amine function under hydrogen atmosphere with 10% Pd/C catalyst.

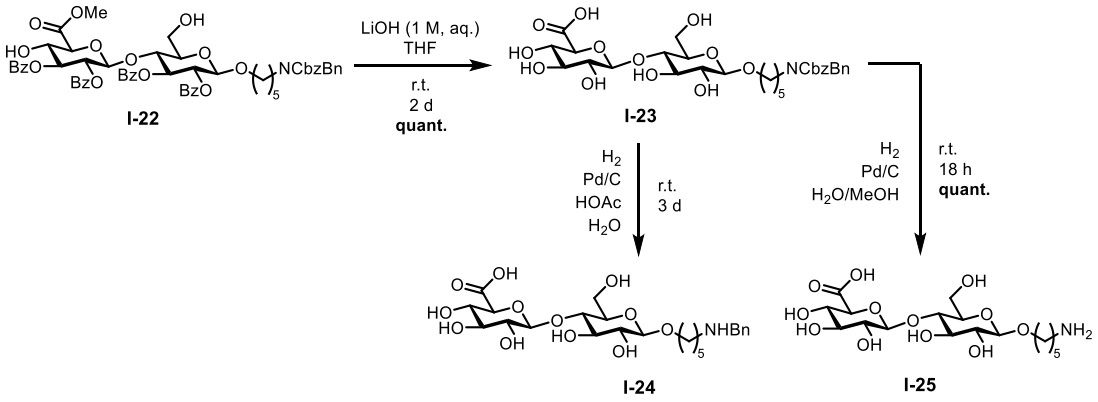

Figure 3.43: Reaction pathways for the cleavage of protecting groups from oxidized cellobiose **I-22**.

Unexpectedly, hydrogenation in water resulted in selective cleavage of the Cbz group leading to the formation of **I-24**, while the benzyl group on the amine function remained unaffected after days under the same reaction conditions. This finding was confirmed by the proton NMR spectrum showing a broad aromatic signal from 7.41 to 7.52 ppm and a singlet at 4.23 ppm for the methylene group (upper spectrum Figure 3.44). It was assumed that the active concentration of hydrogen in the solution was too low due to low solubility of hydrogen in water.[286] Therefore, a solvent mixture of water and methanol with a ratio of 2:1 was used to enhance the concentration of hydrogen in the reaction mixture. The deprotection of **I-23** was completed in 18 hours, giving the cellobiuronic acid B-cell epitope **I-25** with

quantitative yield after 2 steps. As shown in the lower ^{1}H-NMR spectrum in Figure 3.44, no signals referring to benzyl or Cbz group were detected.

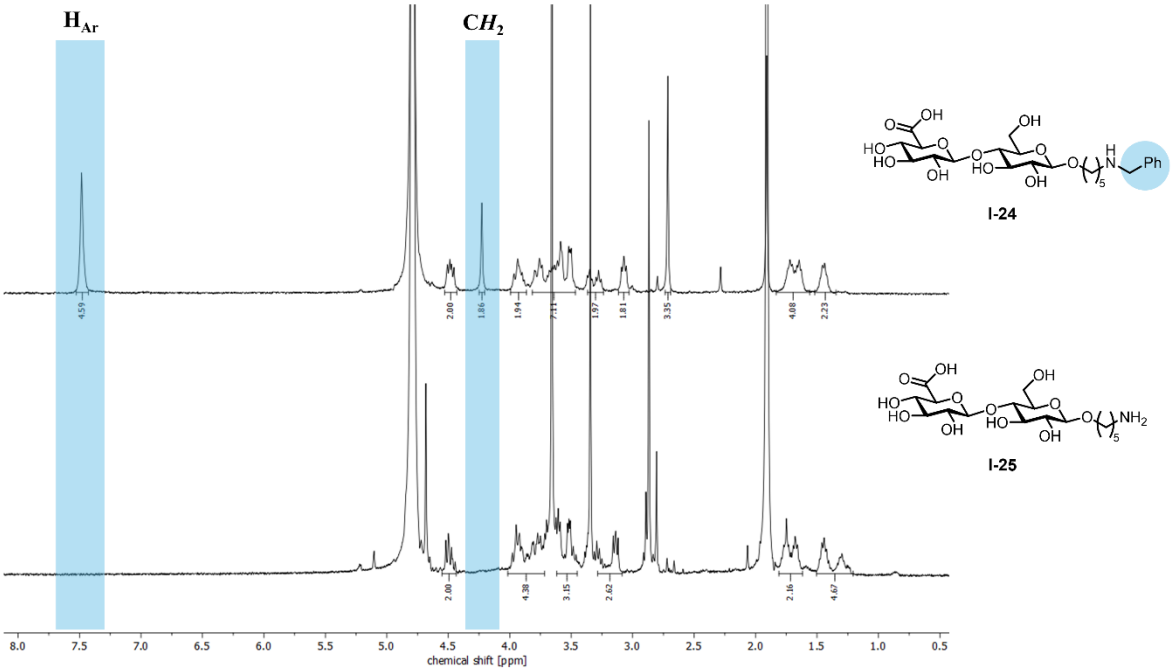

Figure 3.44: ^{1}H-NMR spectra of products after hydrogenation of **I-23** to obtain **I-25**.

For the synthesis of B-cell epitope Glc-β-(1→4)-GlcA, the acid labile benzylidene group was first substituted by two benzoyl groups (Figure 3.45). The reaction was performed using the diol **I-20** under the same conditions as the perbenzoylation for the synthesis of the thioglycoside **I-5** and **I-6**. Since the positions O-4' and O-6' are less sterically crowded, only 5.0 eq. of BzCl was used in combination with DMAP as catalyst. After purification via flash chromatography, fully protected cellobioside **I-26** was obtained with a yield of 65%. According to the previous findings in this section, the cleavage of TBDPS group was conducted using HF-pyridine complex in a solvent combination of pyridine and THF to prevent side reactions that may occur under alkaline conditions. The cellobioside **I-27** with free hydroxyl group on position O-6 was isolated with a yield of 89%.

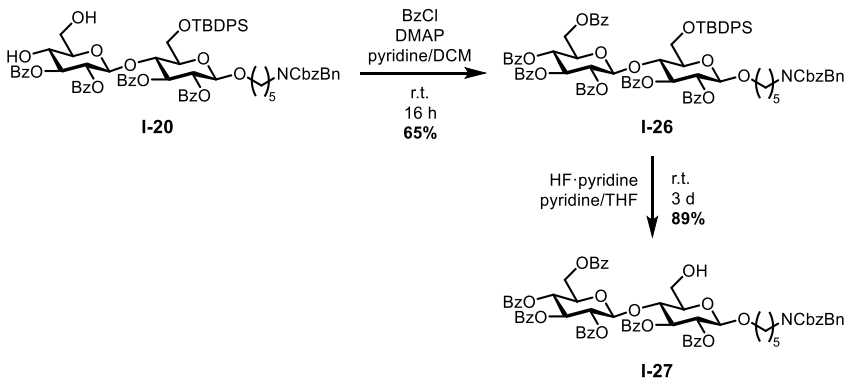

Figure 3.45: Benzoylation of O-4' and O-6' as well as cleavage of TBDPS protecting group from O-6.

In accordance with the previous method, oxidation of the primary alcohol was conducted using TEMPO as an oxidative catalyst with BAIB as co-oxidant. The resulting carboxylic acid was methylated using TMS-diazomethane, giving the antigen precursor **I-28** with a yield of 66% after 2 steps. Full deprotection of the saccharide was performed through alkaline hydrolysis of the methyl and benzoyl groups, followed by a hydrogenation of **I-29** using the optimized method with a water-methanol solvent mixture. The second B-cell epitope **I-30** was successfully isolated with quantitative yield after 2 steps.

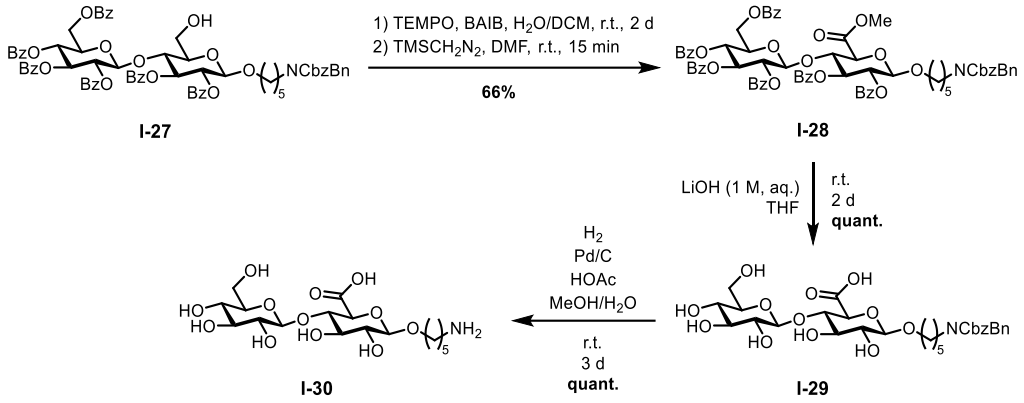

Figure 3.46: Oxidation of O-6 position and subsequent cleavage of the remaining protecting groups to obtain the second B-cell epitope **I-30**.

3.2.5 Regioselective O-3' Protection and Deprotection of Cellobiose

To prepare B-cell epitopes against serotype 3 *S. pneumoniae* with longer carbohydrate sequences, a cellobiose building block is required that allows oligomerization through β-(1→3')-glycosylation. Therefore, different strategies for site-selective functionalization of position O-3' with protecting groups orthogonal to the rest of the groups used for the carbohydrate are discussed in the current section. Based on present knowledges, there are two main challenges related to regioselective installation of protecting groups to O-3' of cellobiose: selectivity between O-2/O-3 within a glucose building block and selectivity between O-3/O-3' when working with a disaccharide. Though, an indication is given in section 3.2.2 (in relation to the benzoylation reaction) that the usage of a bulky TBDPS group on position O-6 can lead to certain regioselectivity by blocking the position O-3 due to steric hindrance. Furthermore, the building block with orthogonal protecting groups on position O-6 and O-6' enables the modification of the resulting carbohydrates into antigens with sequences consisting of alternating glucose and glucuronic acid units. Accordingly, the O-6 TBDPS protected disaccharide **I-17** is used as a starting material for site-selective functionalization.

Considering a protecting group that is orthogonal to benzylidene acetal (acid labile), TBDPS group (fluoride labile) and possibly to benzoyl group (alkaline hydrolysis), 2-naphthylmethyl group (Nap) presents one possibility for a temporary protecting group, which is frequently used for synthesis of monosaccharide building blocks.[127] The cleavage of Nap group is induced by oxidation using 2,3-dichloro-5,6-dicyano-1,4-benzoquinone (DDQ) in a buffered solution that will not affect the other protecting groups.[287,288] Direct functionalization of the saccharide with 2-naphthylmethylbromide (NapBr) requires a strong base, typically sodium hydride, which will lead to low regioselectivity. One method to introduce Nap group with site-selectivity is organotin-mediated alkylation that involves formation of a stannylene acetal intermediate by treatment of the diol with organotin compounds.[289,290] The regioselectivity is proposed to be influenced by stereoelectronic effects of the parent saccharide structure and is a result of selective Sn-O bond cleavage in the presence of halide salts.[290]

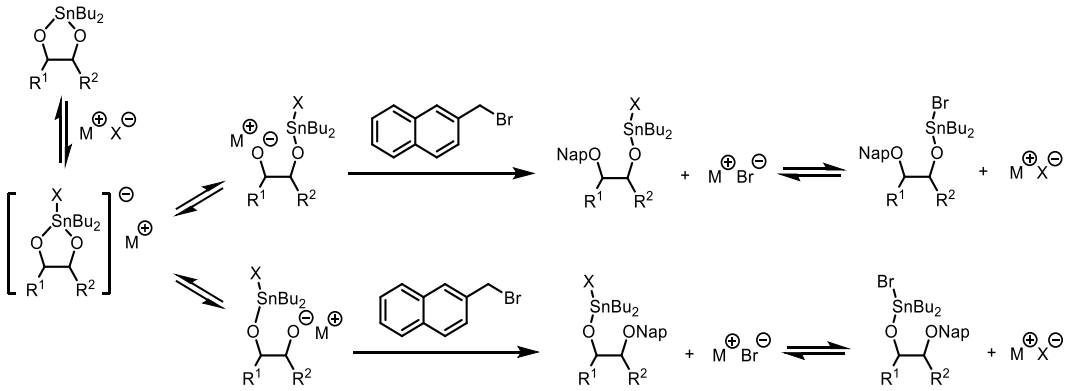

Figure 3.47: Proposed mechanism for the activation of tin intermediates by halides. X = F, Cl, Br, I.[290]

As shown in Figure 3.47, the coordination of halide X^- to the stannylene acetal results in the formation of a pentacoordinated tin compound and promotes selective Sn-O bond cleavage that leads to a reactive alkoxide with M^+ as counter ion, which is converted into the 2-naphthylmethyl ether in the presence of NapBr. Halide anions that form stronger Sn-X bond show higher activation ability for alkylation following the order: $F^- > Cl^- > Br^- > I^-$.[290] Preferentially, the Sn-O cleavage leads to a tetracoordinated tin atom with less sterically hindered environment, which can be used for the protection of the ethyl thioglycoside **I-17**, since O-3' experiences stronger steric hindrance than O-2' due to adjacent benzylidene group and position O-3 is less accessible for the formation of stannylene acetal. The reaction was conducted with either tetrabutylammonium iodide (TBAI)[290] or cesium fluoride (CsF)[291] as halide source (Figure 3.48). In both methods, dibutyltin oxide was used for the formation of stannylene acetal. While the reaction with an iodide salt showed no significant conversion of the starting material after 5 days, the reaction in presence of fluoride clearly showed conversion after 20 hours, confirming the activation ability of different halide anions reported in literature.

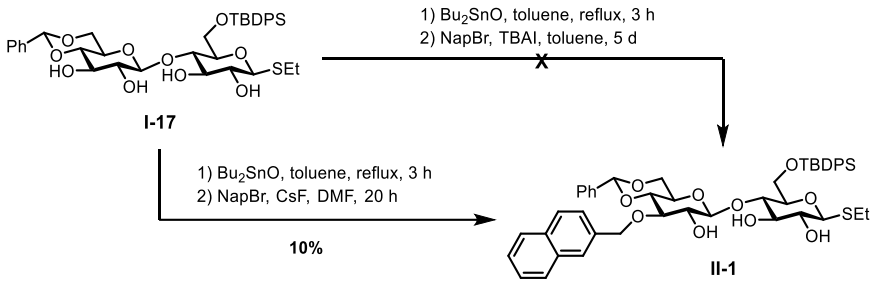

Figure 3.48: Protection of position O-3' with naphthylmethyl group using dibutyltin oxide mediated alkylation.

The mechanism for the reaction with CsF according to Zhou et al.[290] is shown in Figure 3.49. Due to the bulkiness of the TBDPS group on position O-6 and thus reduced accessibility of position O-3, the reaction of partially protected thioglycoside **I-17** was expected to only form stannylene acetal on position O-2'/O-3'. In the presence of CsF, the fluoride binds strongly to the tin atom, resulting in its pentacoordination. Since the hydroxyl group on O-2' is generally more reactive[292] and position O-3' is sterically more hindered due to the neighboring benzylidene group, Sn-O bond cleavage opens the stannylene acetal and gives the reactive alkoxide on position O-3', which performs a subsequent nucleophilic attack to naphthylmethyl bromide forming the corresponding ether.

The hypothesis concerning the regioselectivity for ether formation on O-3' was approved in the experiment. Even CsF was used for the activation of hydroxyl groups, only the formation of O-3' protected product was observed significantly. However, the reaction was slow (due to steric effects), so that the desired product **II-1** was only obtained with a yield of 10% after 20 h reaction time and purification via flash chromatography, while the starting material was almost fully recovered.

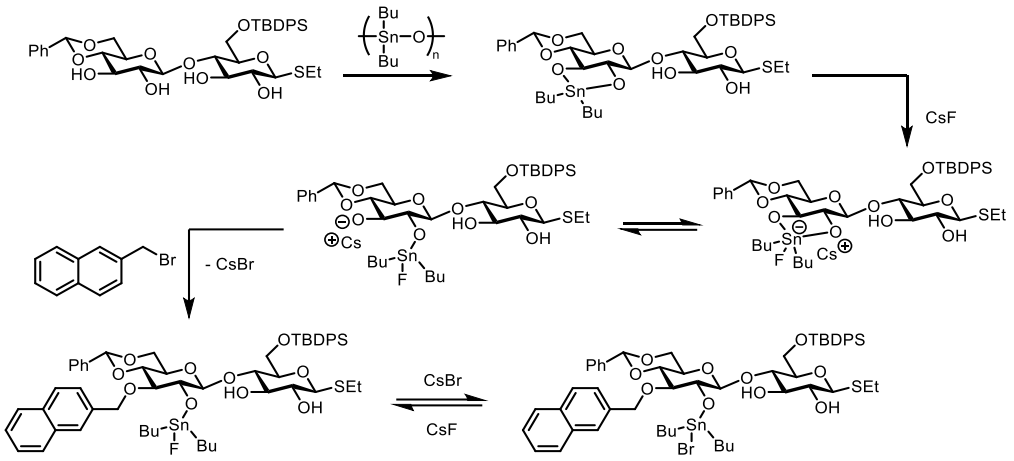

Figure 3.49: Mechanism proposed by Zhou et al. for dibutylstannylene acetyl-mediated alkylation under activation with CsF.

By analyzing the molecular structure of the isolated saccharide via NMR experiments, the 2-naphthylmethyl group was found to be covalently linked to the position O-3' as desired. A fragment of the HMBC spectrum is shown in Figure 3.50 displaying a correlation between the protons of the Nap methylene group and the carbon C-3' from the disaccharide.

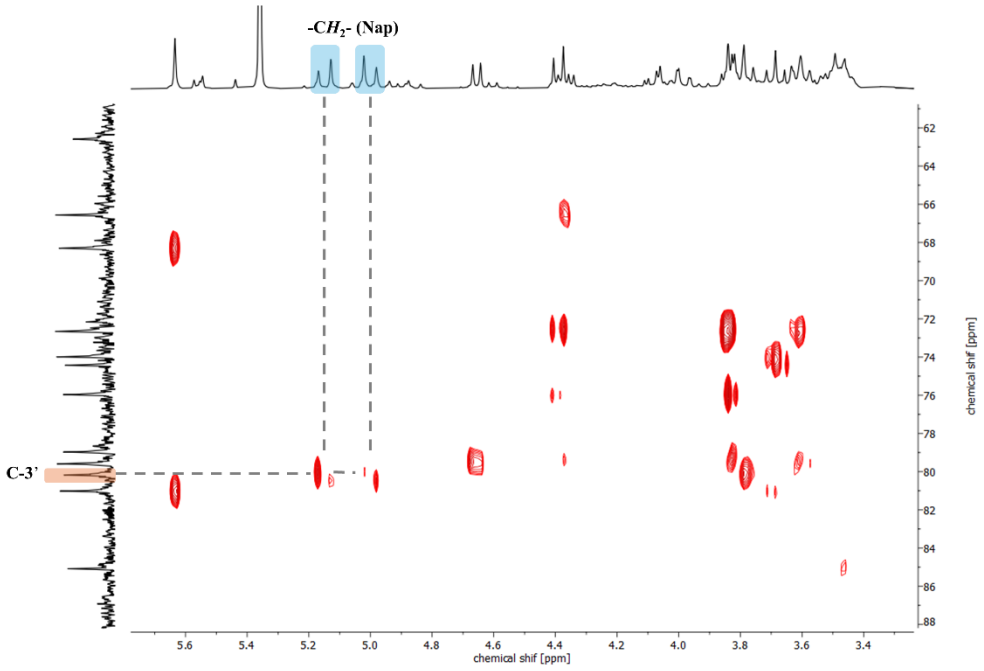

Figure 3.50: Fragment of HMBC spectrum of O-3' Nap-protected thioglycoside **II-1**.

In the next approach, a regioselective installation of a fluorenylmethoxycarbonyl (Fmoc) group was conducted following the procedure by Despras et al. for the synthesis of a lactose building block.[293] This method uses fluorenylmethoxycarbonyl chloride (FmocCl) as a reagent in the presence of *sym*-collidine as a base (Figure 3.51). The choice of *sym*-collidine as a base has two advantages: it has a pk_a value around 7.4 which is slightly more basic than pyridine that is more effective in the abstraction of the proton (or HCl) released during the reaction and can thus better protect the acid labile benzylidene

group. In addition, the nitrogen of *sym*-collidine is sterically more hindered than in pyridine, so that it helps to introduce the Fmoc group to a position that is sterically less demanded. Unfortunately, no conversion of the educt was observed after days of reaction time, which can be explained by the steric hindrance caused by the bulky TBDPS group, so that none of the remaining hydroxyl group could be attacked by the reagent, considering Fmoc itself is also a bulky protecting group.

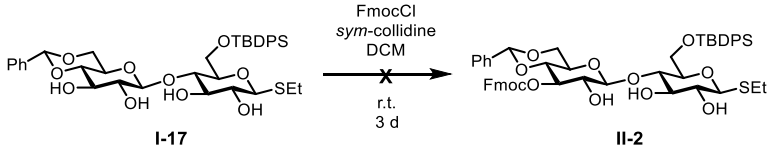

Figure 3.51: Approach for the regioselective O-3' protection of **I-17** with Fmoc-group.

A method for site-selective acylation of *trans*-1,2-diols in *O*-glycosides using a pair of chiral benzotetramisole (BTM) catalyst (chemical structure of the (*R*)-enantiomer shown in Figure 3.52A) was reported by Tang et al. in 2017.[294] During the reaction, an cationic acylation reagent is formed from a anhydride and BTM (one example using acetic anhydride and (*R*)-BTM is shown in Figure 3.52B). Based on density functional theory (DFT) calculations, the interaction between the cationic catalyst and the lone pair of the anchor oxygen (cation-*n* interaction) was recognized to be one of the determining factors for the regioselectivity. In case of a α-*O*-glucoside with a O-4/O-6 benzylidene group, the reaction using (*R*)- or (*S*)-BTM catalyst leads to selective C-3 and C-2 acylation, respectively. The favored cation-*n* interactions are shown in Figure 3.52C, the anchor oxygens for cation-*n* interactions are marked in red and the favored positions of acylation in blue.

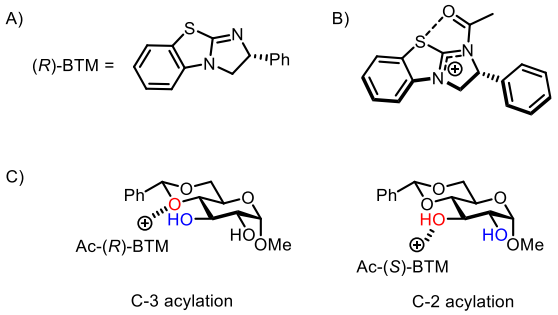

Figure 3.52: A) Chemical structure of (*R*)-BTM. B) Active cationic acylation reagent. C) (*R*) and (*S*)-BTM catalyzed acylation of α-O-glucosides with anchor oxygen in red and favored position for acylation in blue.

The concept and application of this chiral catalyst was later extended by the same research group for selective acylation of thioglycosides.[295] When the anomeric center is protected with adamantanethiol, the acylation is directed by the favorable interaction between the adamantyl C-H bonds and the π system of the acylated catalyst, leading to an O-2 selectivity. At the same time, when a benzylidene group is present on position O-4/O-6, the transition state for O-3 acylation is stabilized through π-π-interactions between the benzylidene group and the (*R*)-BTM catalyst (Figure 3.53). This implicates that a site-

selective O-3 acylation is possible, if the thioglycoside is designed with a group on the anomeric center that is less hydrophobic to suppress the interactions with the π-system of BTM.

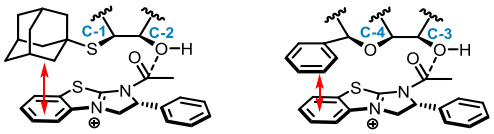

Figure 3.53: Most stable transition state of C-2 acylation (left) and C-3 acylation (right) of a thioglycoside.

Based on these findings, a new ethyl thioglycoside was synthesized from **I-15** with an O-4'/O-6' benzylidene protection, and the position O-6 is functionalized with a *tert*-butyldimethylsilyl group (TBDMS) to avoid additional π-π-interactions (Figure 3.54). The synthesis was carried out in a one-pot reaction starting with the introduction of benzylidene group under the same conditions as in section 3.2.2 using BDMA as reagent and a catalyst combination consisting of HOTf and $Mg(OTf)_2$. The following TBDMS protection was performed according to the procedure by Porto et al. using *tert*-butyldimethylsilyl chloride (TBDMSCl) and imidazole.[296] Compared to TBDPS group, the functionalization with TBDMSCl is less regioselective due to the smaller size, so that products with multiple TBDMS groups were found, which led to loss of the starting material. The desired product **II-3** was obtained with 37% yield after purification via normal phase and reversed phase chromatography.

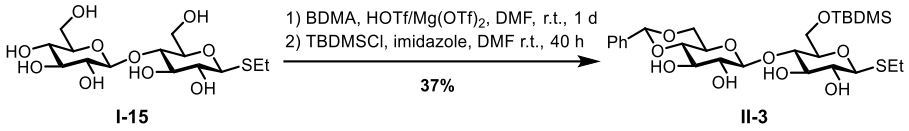

Figure 3.54: One-pot reaction for the protection at O-4' and O-6' of ethyl thioglycoside **I-15** with benzylidene acetal and position O-6 with TBDMS group.

For the orthogonality to benzylidene, TBDMS and benzoyl groups, a protection with levulinoyl ester was chosen that is cleavable using a hydrazine solution, whereas other esters are not affected.[297,298] Since levulinic anhydride is not commercially available and the synthesis is considered complicated, the first approach for (*R*)-BTM catalyzed acylation was carried out using in situ synthesized levulinic chloride (Figure 3.55).

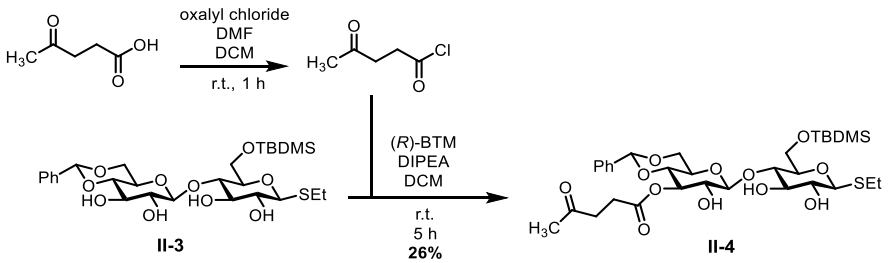

Figure 3.55: Regioselective introduction of levulinoyl group to position O-3' using levulinic chloride and (*R*)-BTM.

Levulinic chloride is first synthesized using levulinic acid as starting material, oxalyl chloride as reagent and DMF as catalyst.[299] After 1 hour of reaction, the acid chloride was easily obtained after removing the reagent, catalyst and solvent by simple evaporation. Levulinic chloride was then used as an acylation reagent in combination with (*R*)-BTM as catalyst and diisopropylethylamine (DIPEA) as a base. The starting material was fully converted after 5 hours, but the desired product **II-4** was obtained with 26% yield after purification via normal phase and subsequent reversed phase flash chromatography.

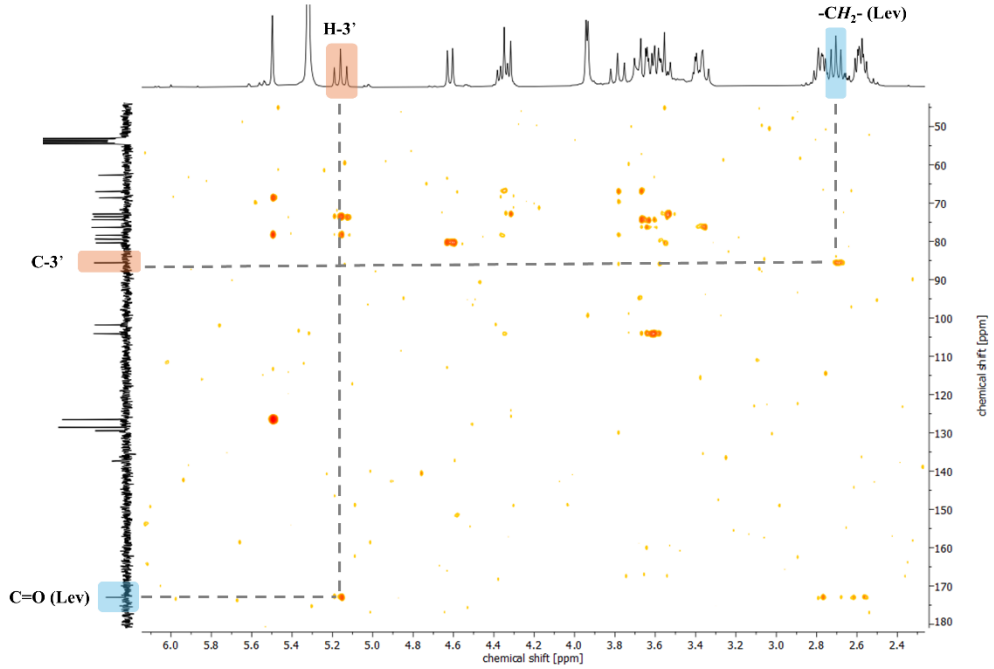

Figure 3.56: Fragment of HMBC spectrum of O-3' levulinoyl protected cellobioside **II-4**.

The site-selective levulinoyl protection of position O-3' was confirmed by the HMBC measurement, demonstrating coupling between H-3' proton (pseudo triplet at 5.16 ppm) and the carbonyl carbon of Lev group (173.0 ppm) as well as correlation between the Lev methylene group (2.72 ppm) and the C-3' carbon at (74.4 ppm) from the saccharide. However, the test reaction was performed with 50 mg starting material, and the reaction outcome was not reproducible in the scale-up experiment, which led to formation of multiple side products and complications in the isolation process. An indication of side reactions was given by the color switch of the solution from yellowish to deep brown when adding the base to the reaction mixture even under ice-cooling. Since an α-proton is present in levulinic acid, the acid chloride can be converted in the presence of an amine base into a ketene **II-5** due to elimination of HCl (Figure 3.57A). Ketenes are considered as highly reactive species[300], which can undergo dimerization or reactions with hydroxyl groups to form esters without any regioselectivity. Another side reaction could be the formation of pseudo esters.[301] With traces of water in the reaction mixture, the enolic form of levulinic chloride can be formed as an intermediate, leading to an intramolecular esterification. The enolic form of the lactone can be further converted into the pseudo ester **II-6** (Figure 3.57B).

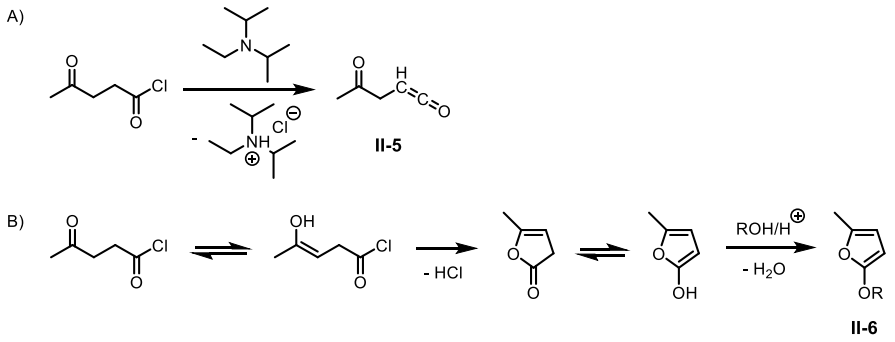

Figure 3.57: Side reactions expected in the regioselective O-3' acylation using levulinic chloride.

In the publication of Tang et al.[295], a strategy using an in-situ synthesized mixed anhydride of levulinic and pivalic acid was suggested for the acylation. Compared to levulinic ester, a pivalic ester exhibit much more bulkiness, making it more difficult to use as a protecting group, especially in the presence of other bulky protecting groups. To verify this assumption, the partially protecter thioglcoside was subjected to a reaction using pivalic anhydride as acylation reagent and (*R*)-BTM as catalyst (Figure 3.58). After 3 days of reaction time under ambient temperatures, no conversion of the starting material was observed, leading to the conclusion that pivaloyl group is too bulky for the present case to access any of the remaining free hydroxyl groups.

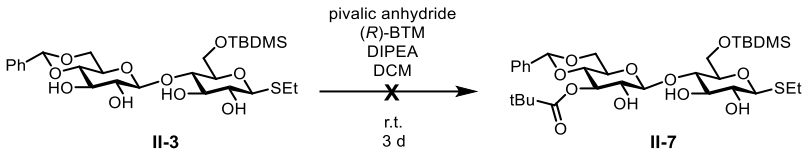

Figure 3.58: Approach for the regioselective O-3' protection with using pivalic anhydride, (*R*)-BTM and DIPEA.

Mixed anhydride was prepared from levulinic acid and pivalic anhydride and used in combination with (*R*)-BTM and DIPEA for the site-selective acylation of **II-3** (Figure 3.59). The O-3' protected thioglycoside **II-4** was obtained with a yield of 49%, showing increased formation of the desired product comparing to the previous method with levulinic chloride. By analyzing the fractions after the flash chromatography, products with levulinoyl groups on other positions were also found in smaller amounts (< 5% each). This implies that the acylation reagent is reactive to access distinct positions, but with a well-established regioselectivity for O-3'.

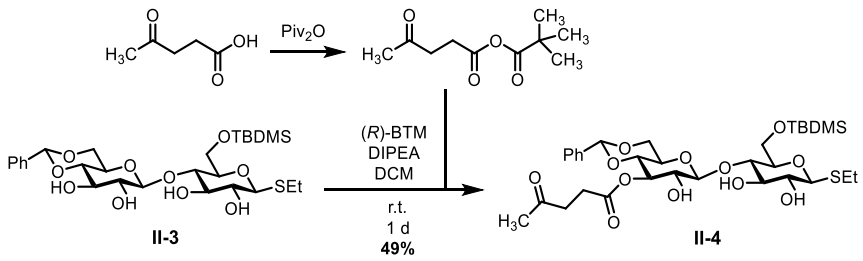

Figure 3.59: Regioselective O-3' protection with levulinoyl group using mixed anhydride, (*R*)-BTM and DIPEA.

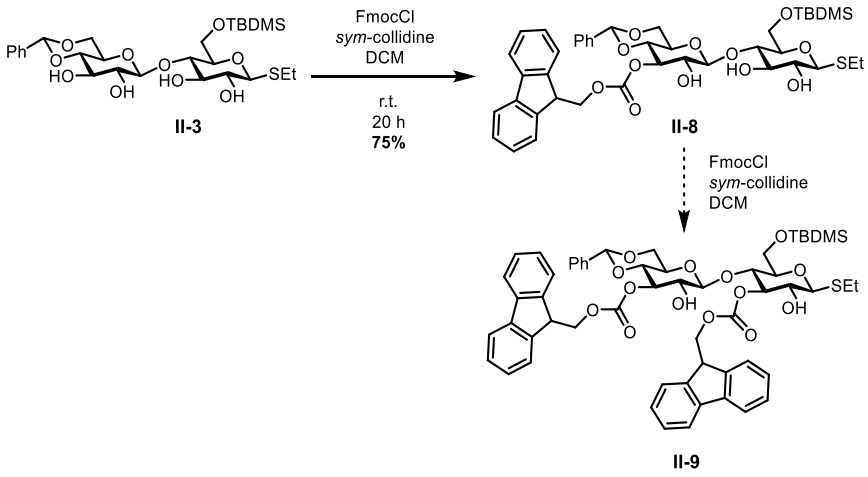

Figure 3.60: Regioselective installation of Fmoc group on position O-3' and subsequent protection of O-3.

The last approach for the regioselective functionalization involves an installation of Fmoc group to the thioglycoside with a less bulky TBDMS group on O-6. The reaction was conducted under the same conditions as previously discussed for the TBDPS protected thioglycoside **I-17** with FmocCl as reagent and *sym*-collidine as a base (Figure 3.60). Using this method, O-3' protected thioglycoside **II-8** was synthesized with high regioselectivity due to steric hindrance given by the silyl group, while only one side product carrying Fmoc groups on positions O-3 and O-3' (**II-9**) was formed in a follow-up reaction. However, the polarities of both products showed significant differences, so that the desired product **II-8** was able to be isolated simply with a yield of 75%. A proof for the regioselective protection with Fmoc group was given by the HMBC measurement, showing a correlation between the proton signal of H-3' at 5.19 ppm and the carbonyl carbon at 154.6 ppm (Figure 3.61).

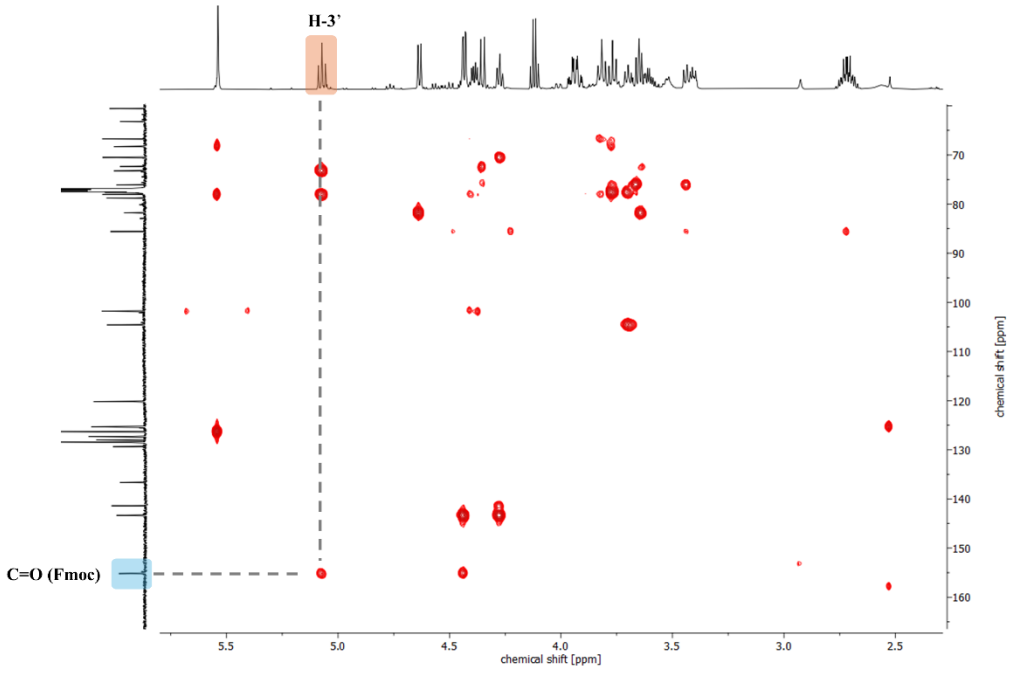

Figure 3.61: Fragment of HMBC spectrum from Fmoc protected thioglycoside **II-8**.

All approaches for the regioselective O-3' functionalization are summarized in Table 3.2 in terms of the educt selected, protecting group (PG) installed, reaction condition as well as reaction time, yield, and side reactions. Generally, functionalization of the thioglycoside **I-17** led to low conversion of the starting material resulting from bulkiness of TBDPS group and thus poor accessibility of the hydroxyl groups. Even though no formation of side reactions were observed during the Nap protection of **I-17** using CsF as a halide source, the regioselective method is not recommended due to slow progress of the reaction. Using chiral (*R*)-BTM catalyst, site-selective O-3' functionalization of **II-3** with levulinoyl group was achieved in combination with either levulinic chloride or mixed anhydride of levulinic and pivalic acid as an acylation reagent. However, acylation of other free hydroxyl groups (O-2/O-3/O-3') caused by reactive acylation reagents was also observed, resulting in formation of various side products carrying one or multiple levulinoyl groups and complications in the isolation process. In comparison, Fmoc protection using FmocCl and *sym*-collidine of **II-3** led to successful formation of O-3' protected products with high regioselectivity that is also easy to isolate, making this reaction a promising method for O-3' protection of cellobioside.

Table 3.2: Summary of different approaches for regioselective O-3' functionalization of a cellobioside building block.

Educt	PG	Reaction condition/time	Yield	Side reaction(s)
I-17	Nap	1) Bu_2SnO, toluene, reflux, 3h 2) NapBr, TBAI, toluene, r.t., 5 d	-	-
I-17	Nap	1) Bu_2SnO, toluene, reflux, 3h 2) NapBr, CsF, DMF, r.t., 20 h	**10%**	-
I-17	Fmoc	FmocCl, sym-collidine, DCM, r.t., 3 d	**-**	-
II-3	Lev	LevCl, (*R*)-BTM, DIPEA, DCM, r.t., 5 h	**26%**	Ketene formation and protection of O-2/O-3/O-2'
II-3	Lev	LevOH, Piv_2O, (*R*)-BTM, DIPEA, DCM, r.t., 1 d	**49%**	Protection of O-2/O-3/O-2'
II-3	Fmoc	FmocCl, sym-collidine, DCM, r.t., 20 h	**75%**	Protection of O-3

Subsequently, Fmoc protected thioglycoside **II-8** was fully protected with benzoyl groups using the optimized procedure discussed in section 3.2.2. After purification via flash chromatography, the thioglycoside donor **II-9** with orthogonal protecting groups on position O-6, O-3' and O-6' was obtained with a yield of 97%.

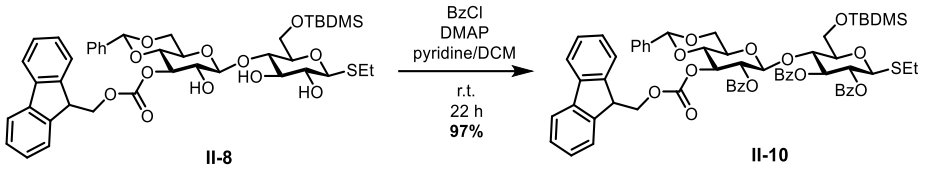

Figure 3.62: Benzoylation of the remaining hydroxyl group of **II-8**.

The glycosylation was conducted following the same preactivation method discussed in section 3.2.3 (Figure 3.63). Glycosyl donor **II-10** and acceptor **I-4** were dried separately via co-evaporation with anhydrous toluene. Promotor DMTST was synthesized by mixing methyl disulfide and methyl triflate in a ratio of 1:2 and added to the donor solution. After the donor was fully activated, the glycosyl acceptor was added to the reaction mixture. The glycosylation was completed already after 1 hour, implying a higher donor reactivity compared to the donor **I-6** for the synthesis of disaccharide antigens. This is expected for the donor carrying a less bulky TBDMS protecting group on position O-6 that provides higher accessibility of the anomeric center. The desired β-glycosylation product **II-11** was obtained with a yield of 40%.

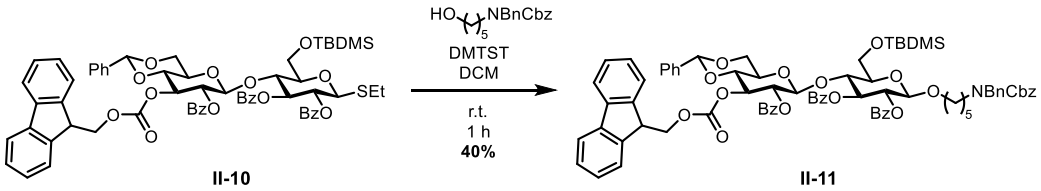

Figure 3.63: Glycosylation of spacer **I-4** with ethyl thioglycoside **II-10** using DMTST as promotor.

To prepare the glycosyl acceptor for β-(1→3')-glycosylation, selective cleavage of the Fmoc group was tested using a 5% piperidine solution in DMF (Figure 3.64). The reaction was completed within 30 minutes. According to the reaction control via TLC, only one new spot assignable to carbohydrate compounds was found, which was isolated via flash chromatography and analyzed through a combination of different NMR methods. Surprisingly, two saccharide molecules with a ratio of 3:10 were found in the NMR spectra that both have exact the same molecular weight and polarity.

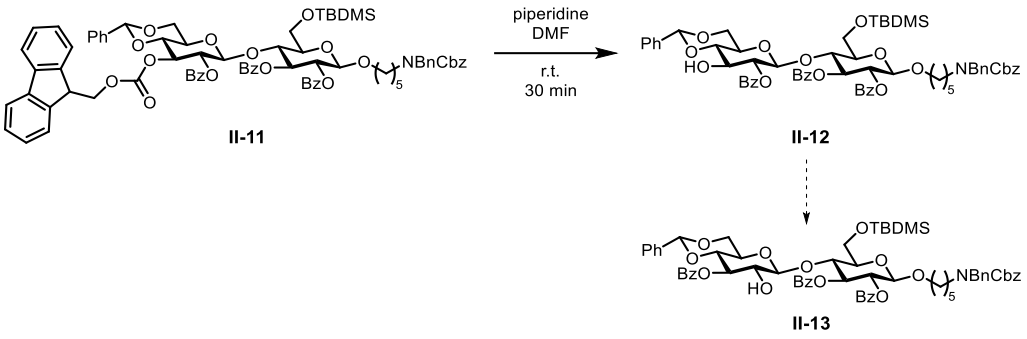

Figure 3.64: Cleavage of Fmoc group from cellobioside **II-11** to obtain the glycosyl acceptor **II-12** and subsequent conversion into acceptor **II-13**.

Therefore, correlation spectroscopy (COSY) was used to encode the exact structures of those molecules. As shown in Figure 3.65, the major compound of the reaction was found to be the desired product **II-12** with a free hydroxyl group on position C-3', since the proton H-3' is not downfield shifted (a downfield shift of the ring proton is typically one of the indications for acylation of the hydroxyl groups on the same position). The minor compound **II-13** exhibit a free hydroxyl group on position C-2' instead of C-3' unexpectedly, which implicates an acyl migration from O-2' to O-3' by intramolecular transesterification. This type of reaction has been reported to occur in 1,2- or 1,3-diols (especially *cis*-diols) through formation of cyclic or orthoester-type intermediates catalyzed by acidic or basic reagents, whereas it is less expected for pivaloyl and benzoyl groups.[289,302–304] Since the products before and after the benzoyl migration have very similar polarity, it is difficult to isolate the desired product. When increasing the reaction time, the ratio of both products changes gradually towards higher molar fraction of **II-13**, showing that C-3' benzoyl protected saccharide is the thermodynamically favored product.

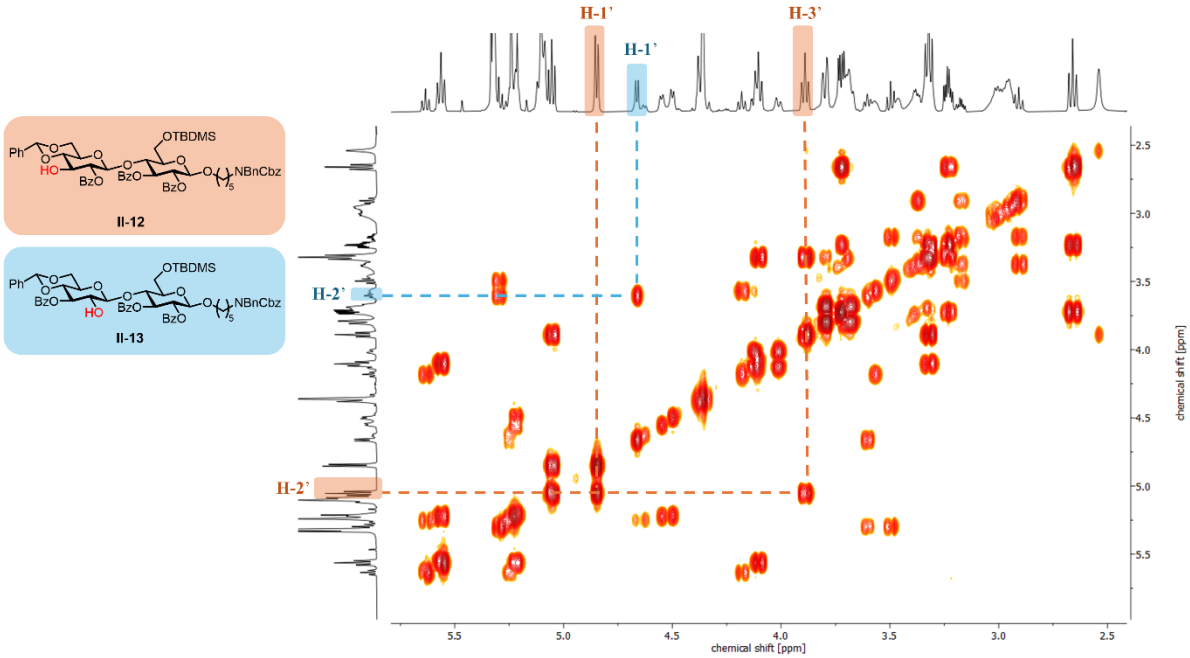

Figure 3.65: Fragment of COSY spectrum of the products isolated from Fmoc deprotection of **II-11**.

To successfully synthesize the glycosyl acceptor, selective cleavage of Fmoc group in the presence of benzoyl groups needs to be further studied in terms of reaction conditions and duration as well as kinetics of the benzoyl migration. Optimized reaction condition can be implemented into oligomerization of the cellobiose building block **II-9** in glycosylation reactions either in solution or with solid-phase support. As demonstrated in Figure 3.66, oligomerization of **II-9** in a solid-phase synthesis involves repeated cycle of glycosylation and Fmoc cleavage reactions. When using a resin carrying photochemically cleavable spacer (**II-14**), the conditions for the cleavage of the carbohydrate oligomers will leave the protecting groups unaffected. Due to further modification via selective deprotecting and oxidation, B-cell epitopes containing alternating glucose and glucuronic acid building blocks can be obtained.

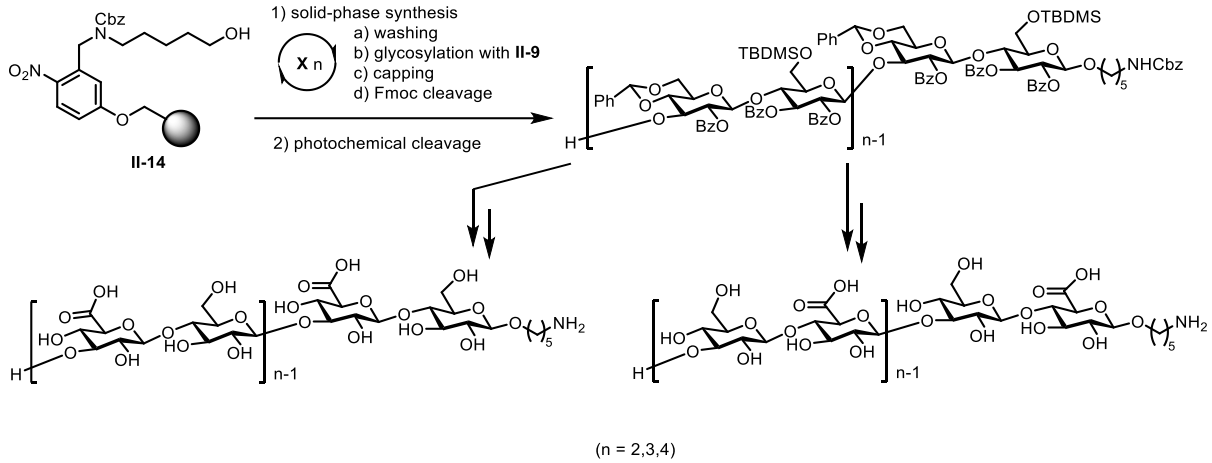

Figure 3.66: Solid-phase supported oligomerization of cellobiose building block **II-9** and subsequent modification into *S. pneumoniae* serotype 3 antigens.

For the glycosylation reactions, it has to be considered that the reactivity of a carbohydrate acceptor with a free secondary hydroxyl group is lower than a small molecule spacer with a primary hydroxyl group. Especially glycosyl acceptors with a 4',6'-benzylidene group exhibit lower reactivity due to reduced torsional freedom.[269] In order to gain insights into the reactivity of the glycosyl acceptor, a simplified glycosyl donor **II-15** was synthesized from partially protected thioglycoside **II-3** by benzoylation of the remaining hydroxyl groups (Figure 3.67). The low yield of 27% was a result of poor solubility of the fully protected thioglycoside **II-15** in majority of the solvents, making it difficult to isolate via normal or reversed phase flash chromatography.

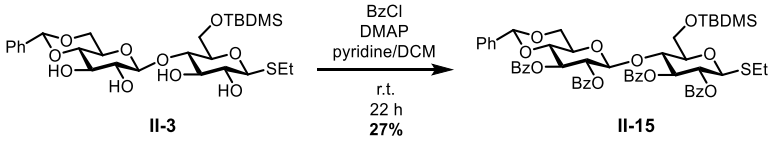

Figure 3.67: Benzoylation of partially protected thioglycoside **II-3** to obtain **II-15**.

The fully protecter thioglycoside **II-15** was subjected to a glycosylation reaction using the acceptor **II-12** that includes smaller amounts of **II-13** as impurities. Even though the reaction was performed following the donor preactivation protocol, no conversion of the glycosyl acceptor into the tetrasaccharide was observed after 2 days. This implies that harsher conditions for donor activation are required for the β-(1→3')-glycosylation.

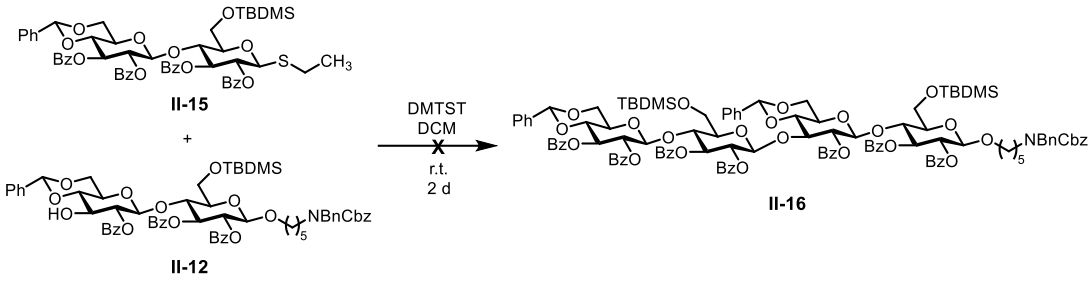

Figure 3.68: Glycosylation reaction using donor **II-15** and acceptor **II-12** with DMTST as promotor.

Besides, electron withdrawing groups (benzylidene and benzoyl groups) can also lower the donor reactivity and hamper the glycosylation with sterically hindered acceptors. Therefore, it might be a better option to introduce electron donating groups[271] to the saccharide building block **II-9**. An example is shown in Figure 3.69, the donor reactivity can be enhanced by selective TBDMS cleavage and oxidation of the free hydroxyl group on position C-6 into a carboxylic acid. After benzylation of the acid, the new saccharide donor **II-17** can be used in oligomerization reactions.

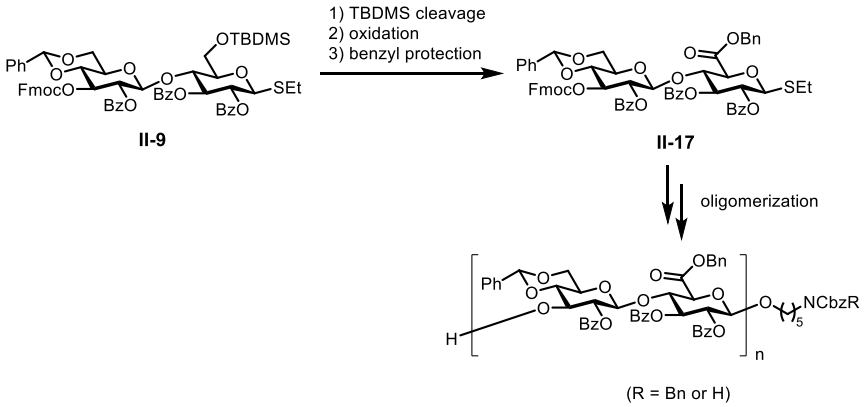

Figure 3.69: Reaction pathways for the synthesis of cellobiuronic acid oligomers.

3.3 Conclusion

Despite the development of various polysaccharide and conjugate vaccines, the human pathogenic bacteria *S. pneumoniae* are considered as a significant cause for worldwide epidemiology. Based on the structure of the capsular polysaccharides (CPS), the bacteria are differentiated into over 100 serotypes. In case of serotype 3, the CPS structure consists of cellobiuronic acid monomers that are bond through 1,3'-β-glycosidic linkages, whereas cellobiuronic acid itself has been proven to be the smallest antigenic unit.

In the present study, a bottom-up strategy for the synthesis of *S. pneumoniae* serotype 3 antigens is established. Using cellobiose as starting material, two thioglycosides with a TBDPS group on position O-6 and a benzylidene group on position O-4'/O-6' have been designed and synthesized as donor components for the glycosylation of an amine-carrying spacer. The glycosylation conditions have been studied to achieve stereoselective outcome, and the product has been used as a common intermediate for the modification into disaccharide antigens GlcA-β-(1→4)-Glc and Glc-β-(1→4)-GlcA by selective deprotection, oxidation of position C-6 or C-6' and global deprotection.

Furthermore, different approaches for site-selective O-3' functionalization of cellobiose have been investigated. As a result, a thioglycoside donor building block with an additional orthogonal protecting group on position O-3' has been successfully synthesized, that is aimed to be used as monomer unit for the synthesis of longer serotype 3 oligosaccharide antigens. The oligomerization can be carried out through reactions in solutions or with solid-phase support, whereas the crucial steps, selective deprotection of position O-3' and subsequent β-(1→3')-glycosylation, remain challenging and require further optimization.

After successful synthesis, the oligosaccharides carrying glucose or glucuronic acid as terminal unit and an aminopentyl spacer on the reducing terminus can be conjugated to the C_2-symmetric monomer to obtain a B-cell epitope presenting monomer. By mixing with other structural and functional monomers, supramolecular multivalent vaccines can be formulated that include B-cell and T-cell recognition motives as well as immune stimulants. The modular vaccine approach is expected to induce antibody production and immunoprotection against *S. pneumoniae* stereotype 3, which needs to be verified through immunological studies.

4 Cucurbit[8]uril Mediated Supramolecular Interpenetrating Network Formation for 3D-Bioprinting

Most of the results in this chapter have been published.[305]

4.1 Motivation and Concept

In the past decades, the precise printing of biologically active constructs across various length scales has become an important part of tissue engineering and biomedical research.[158] Researchers have achieved advancements in both improving printing techniques and formulating suitable biomaterials for the application as extracellular matrices.[159,160] In case of extrusion-based bioprinting, a cell-laden construct is created through extrusion of the so-called biomaterial ink through a nozzle and stacking of layers of the filaments. The development of a suitable aqueous biomaterial ink must fulfill the requirements in terms of its physical, chemical, and biochemical properties such as cytocompatibility, viscoelasticity, shear-thinning and self-healing behavior as well as shape fidelity, which remains a huge challenge.[184]

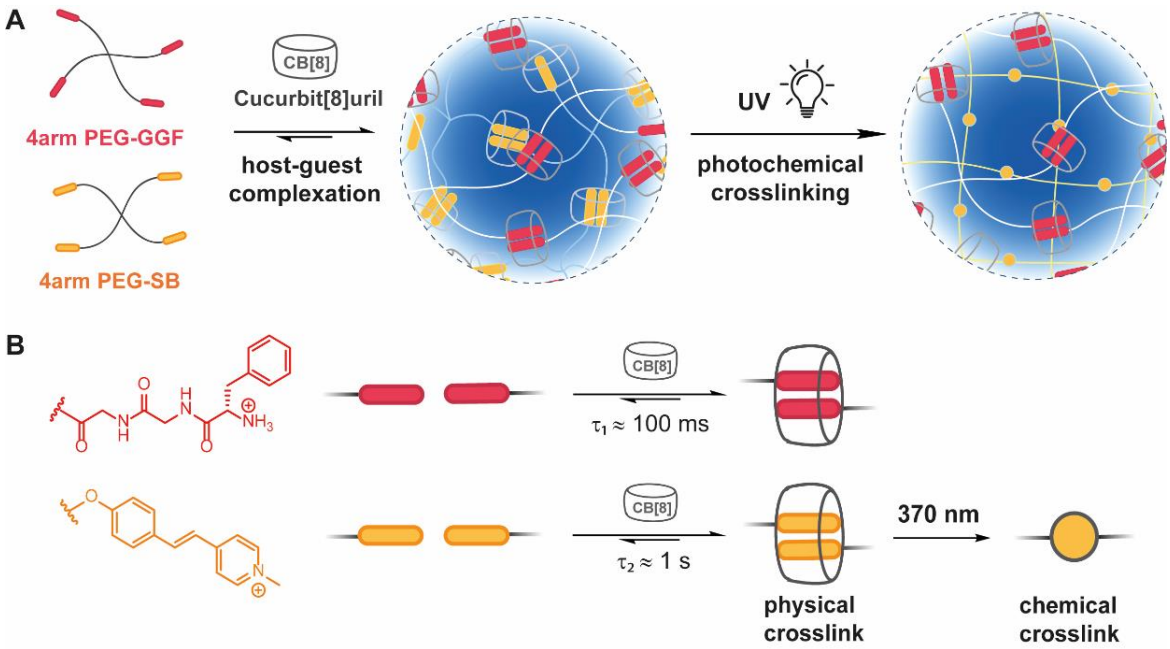

Figure 4.1: Schematic representation of hydrogel formation utilizing functionalized 4arm poly(ethylene glycol), PEG-FGG (red) and PEG-SB (yellow). Irradiation with a light source with the wavelength of 370 nm leads to selective transition of the physical network based on PEG-SB into a covalent chemical network. B) Molecular structure of the guest molecules Phe-Gly-Gly tripeptide (red) and stilbazolium iodide (SB). Both of them are able to form host-guest complexes by mixing with CB[8] in aqueous media. The physical crosslink formed by stilbazolium iodide and CB[8] can be transformed into a chemical crosslink by the application of an 370 nm light source.

In the present study, a novel approach utilizing supramolecular interpenetrating network hydrogels (IPN) with tunable physical and chemical crosslink densities is developed. Therefore, star-shaped poly(ethylene glycol) (PEG) is functionalized with either tripeptide phenylalanine-glycine-glycine (FGG) or stilbazolium iodide (SB) to obtain polymers PEG-FGG and PEG-SB as network components. Both end groups (FGG and SB) can undergo supramolecular homoternary host-guest complexation with

cucurbit[8]uril (CB[8]), leading to the formation of three-dimensional single networks (SN) by mixing the functionalized polymers and CB[8] in aqueous media (Figure 4.1A).[157,306,307] Upon irradiation, the physical network consisting of PEG-SB and CB[8] can be rapidly and selectively transformed into a chemical network due to photochemical [2+2]-cycloaddition of stilbazolium (Figure 4.1B).[308] The combination of the individual networks enables the fine tuning of the homogeneous network structure and especially the ratio between the supramolecular and covalent networks. With this, it is possible to control the properties such as network stress relaxation, shape fidelity, shear-thinning and self-healing behavior, making the system a potential candidate as extracellular matrix and biomaterial ink in the application of 3D-bioprinting and bone tissue regeneration (Figure 4.2). The printed disc with encapsulated stem cells can be implanted to a defect site of a bone. Subsequently, the cell differentiation can be activated to form functional tissues that leads to healing of the defect bone.

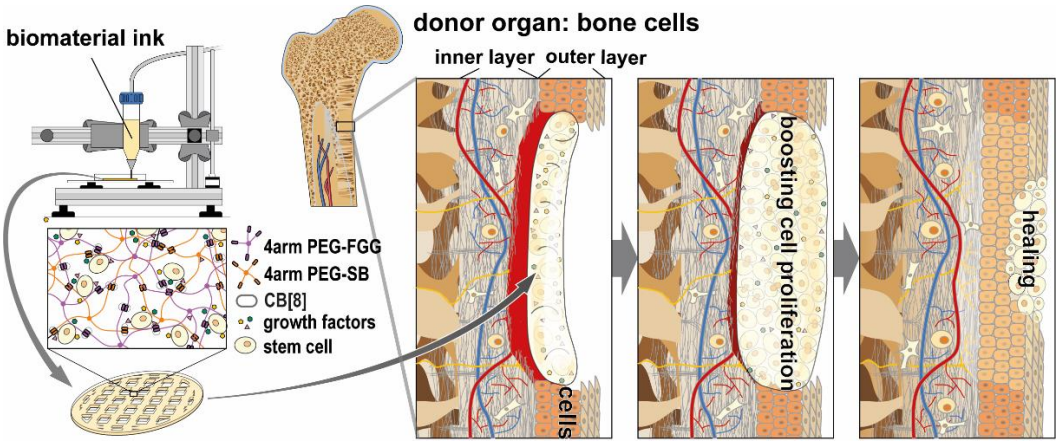

Figure 4.2: Application of the interpenetrating network hydrogels as biomaterial ink in 3D-bioprinting and in bone tissue regeneration. The printed disc including stem cells can be implanted into a bone defect and support cell proliferation and differentiation, thus promoting bone regeneration.

4.2 Results and Discussion

4.2.1 Network Building Block Design and Synthesis

In order to create 3-dimensional interpenetrating network hydrogels with chemically defined network structures, star-shaped 4arm poly(ethylene glycol) (4arm-PEG-OH, *M*w = 20 kDa, Đ = 1.02) was end-functionalized with molecules that can undergo host-guest complexation with cucurbit[8]uril (CB[8]) and the polymer obtained were used as network monomers. To minimize the interactions between the networks, guest molecules with the capability to form homoternary complexes with CB[8] without the potential to cross-interact with another guest molecules (as reported in literature) were chosen for the following studies: tripeptides phenylalanine-glycine-glycine (FGG) and stilbazolium iodide (SB).

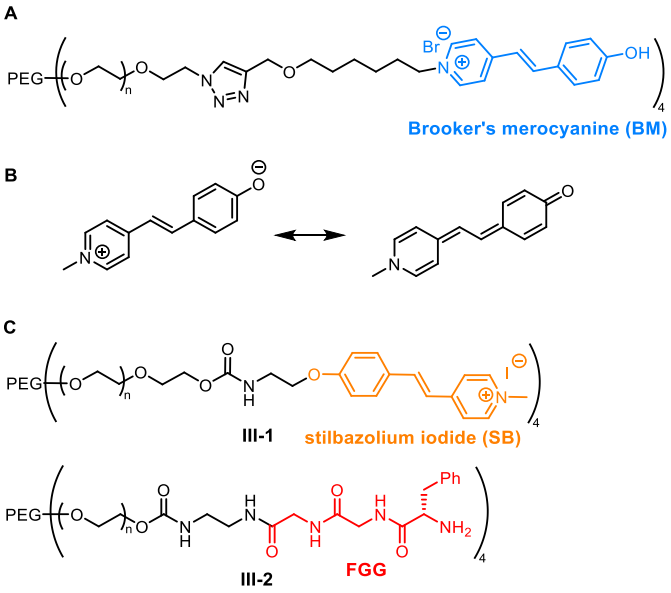

Figure 4.3: A) Structure of 4arm PEG macromer functionalized with Brooker's merocyanine reported by Zou et al.[308] B) Two resonance structures of Brooker's merocyanine. C) Structure of 4arm PEG macromer studied in this work.

According to the publication of Zou et al., CB[8] can catalyze reversible photodimerization of *trans*-Brooker's merocyanine (BM, also known as stilbazolium) and effectively transform physical crosslinking into chemical crosslinks in hydrogel networks when BM is introduced as end groups of the 4arm PEG macromer.[308] The structure of the macromer reported is shown in Figure 4.3A. Brooker's merocyanine is alkylated by an aliphatic spacer and attached to the 4arm PEG via copper-catalyzed click chemistry. Due to the resonance structures of BM (Figure 4.3B), one zwitterionic and one neutral structure, BM is known for its solvatochromic properties.[309] Depending on the polarity of the solvent, either the zwitterionic or the neutral structure is more dominant, leading to varying colors of the solution from yellow to red to blue with decreasing polarity of the solvent. When considering the complexation with CB[8], BM leaves the polar aqueous media and is trapped the hydrophobic cavity leading to a blue shift of the absorption spectrum, which was observed by Kaliappan et al.[157] This implies that BM exists in the neutral form, when the complexation takes place, leading to poorer reactivity in the dimerization

event. To minimize this effect, BM is introduced as a phenolic ether as end group in this work (**III-1** in Figure 4.3C) and named as stilbazolium (SB) for the rest of the chapter. This reduces the +M-effect of the oxygen atom in the original structure and forces the molecule to remain in its zwitterionic form even after the complexation with the hydrophobic CB[8], leading to higher reactivity in the photodimerization.

The conjugation chemistry used to incorporate guest molecules as polymer end-groups was inspired by the work of Tang et al.[310] The free hydroxyl end-groups of 4arm PEG-OH can be converted into *p*-nitrophenyl carbonates in the first step. The resulting polymers can be further subjected to reactions with amine-functionalized molecules to achieve the formation of carbamate linkages (final structures are shown in Figure 4.3C). To this end, FGG and SB guest molecules with amine-functionalized spacer were designed and synthesized.

As shown in Figure 4.4, the Fmoc-protected tripeptide Fmoc-Phe-Gly-Gly-OH (**III-3**) was synthesized according to Merrifield via solid phase peptide synthesis (SPPS) using 2-chlorotrityl chloride resin. After the first Fmoc-protected amino acid was laden to the resin over the *C*-terminus in an esterification reaction using diisopropylethylamine (DIPEA) as a base, the remaining reactive trityl groups were capped with methanol. Each coupling step started with the cleavage of the Fmoc-group from the *N*-terminus using a 20% solution of piperidine in dimethylformamide (DMF). Subsequently, the Fmoc-protected amino acid was coupled to the reactive amine using the reagent mixture containing 2-(1*H*-benzotriazol-1-yl)-1,1,3,3-tetramethyluronium hexafluorophosphate (HBTU), hydroxybenzotriazole (HOBt) and DIPEA. After the last coupling step, the Fmoc-protected peptide Fmoc-Phe-Gly-Gly-OH was cleaved from the resin using a solution consisting of trifluoroacetic acid (TFA), triisopropylsilane (TIS) and water. The peptide **III-3** was obtained without further purification with a quantitative yield. In the next step, functionalization of the free *C*-terminus was achieved in a amidation with *N*-Boc-ethylenediamine using the same reagent mixture HBTU/HOBt/DIPEA as in the solid phase synthesis giving desired product **III-4** with a yield of 64%. Finally, the butyloxycarbonyl (Boc) group was cleaved off by using a 10% TFA solution in dichloromethane (DCM) to obtain **III-5** in a quantitative yield.

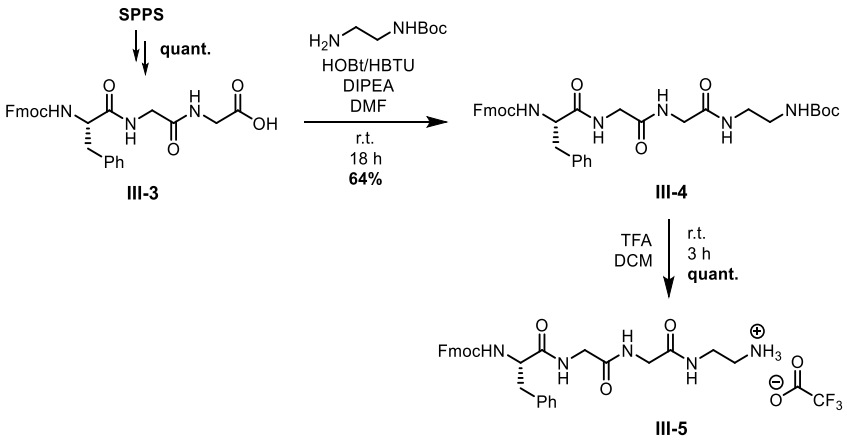

Figure 4.4: Synthetic route for the preparation of tripeptide FGG with amine carrying spacer.

In a 4-step synthesis that was developed in collaboration, stilbazolium iodide functionalized with an amine carrying spacer was prepared (see Figure 4.5). Boc-protected 2-aminoethanol (**III-6**) was synthesized using 2-aminoethanol and di-*tert*-butyl dicarbonate (Boc_2O) with a yield of 93%. The product was converted with *p*-hydroxybenzaldehyde in a Mitsunobu reaction to form the corresponding phenolic ether **III-7**. By conducting the reaction with triphenylphosphine (PPh_3) and diethyl azodicarboxylate (DEAD) in tetrahydrofuran (THF), a yield of 67% was achieved after purification via flash chromatography. Subsequently, stilbazolium iodide **III-8** was formed with a yield of 61% in a Knoevenagel condensation using the benzaldehyde **III-7** and 1,4-dimethylpyridinium iodide with piperidine as a base. After cleaving the Boc-group, **III-9** was obtained in a yield of 91%.

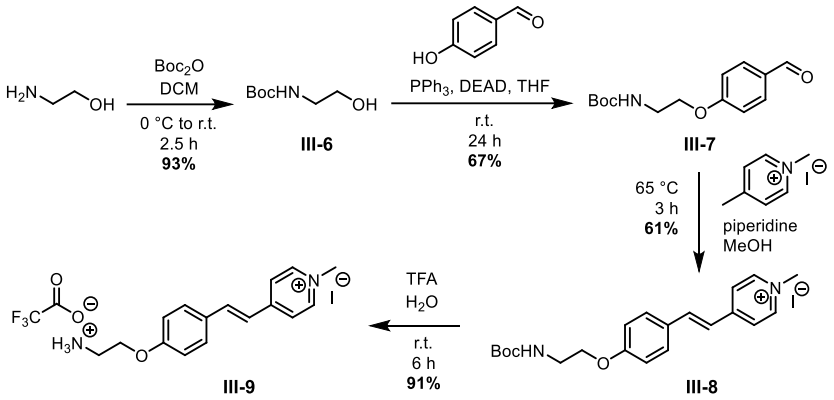

Figure 4.5: Synthetic route for the preparation of stilbazolium iodide with amine carrying spacer.

As shown in Figure 4.6, the conversion of the free hydroxyl-groups of 4arm PEG-OH into *p*-nitrophenyl carbonates was conducted using *p*-nitrophenyl chloroformate in the presence of pyridine in dichloromethane (DCM) at ambient temperature yielding 88% 4arm PEG-carbonate **III-10** after purification via precipitation.

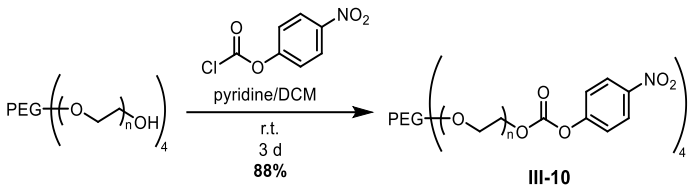

Figure 4.6: Synthetic routes for functionalization of 20k 4arm PEG-OH with *p*-nitrophenyl chloroformate.

The degree of functionalization was calculated in ^{1}H-NMR spectrum (Figure 4.7A) by comparing the aromatic signals of the p-nitrophenyl groups (in orange) to the broad signal associated with the PEG back bone (in blue). Following this calculation, 90% of the PEG end groups were functionalized.

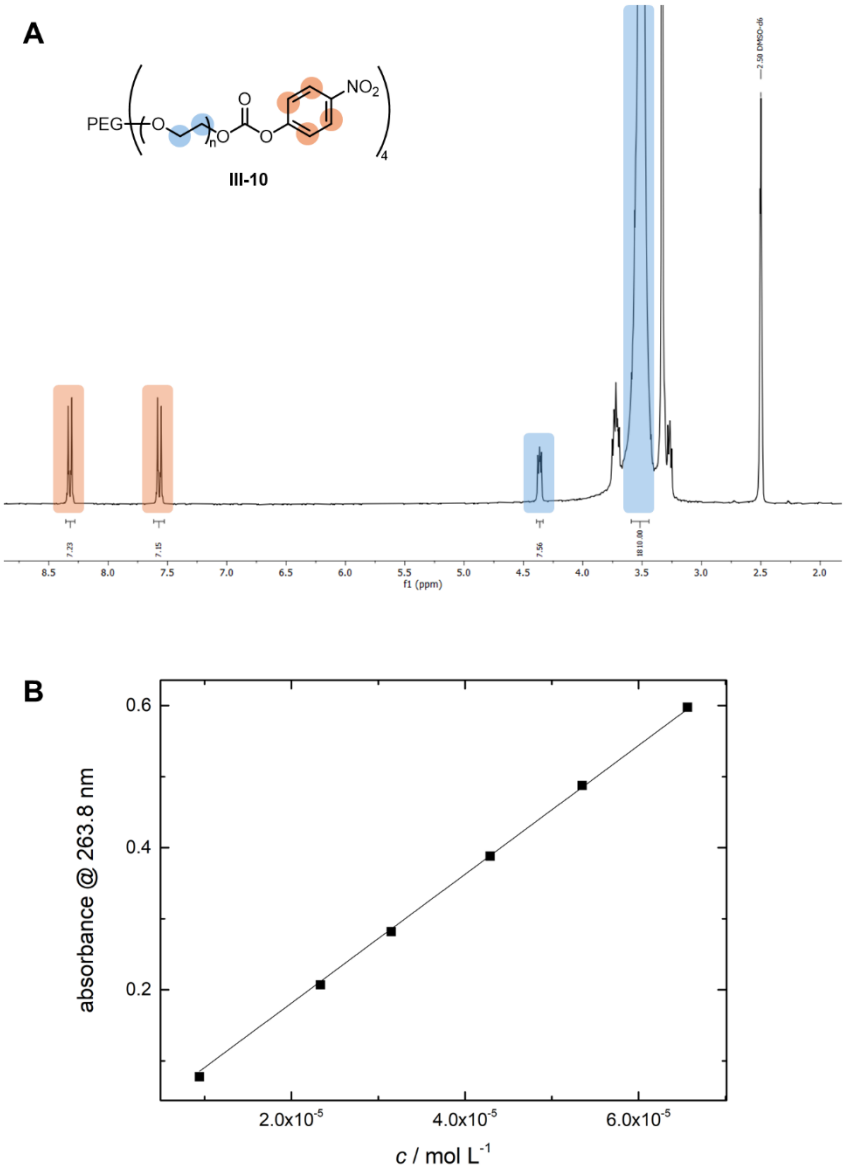

Figure 4.7: A: ^{1}H-NMR spectrum of **III-10** measured in dmso-d_6 showing proton signals of the aromatic group (in orange) and PEG backbone (in blue). B: UV-Vis calibration curve of p-nitrophenyl chloroformate calculated by applying the absorbance at 263.8 nm against the concentration of the reagent.

To prove the accuracy of the NMR calculation method, additional photometric measurements of the end group and the functionalized polymer were conducted. From a 100 µM stock solution of *p*-nitrophenyl chloroformate in chloroform, solutions with higher dilution (c = 10, 20, 30, 40, 50 and 60 µM) were prepared (the exact mass of stock solution and solvent were determined to calculate the final concentrations). From those solutions, UV-Vis spectra were recorded and the UV-Vis absorbance A at absorption maximum (263.8 nm) was applied against the exact concentration c under linear regression (see Figure 4.7B). The following calibration curve was obtained:

$$A = (9065 \pm 45) \cdot \frac{c}{\text{mol L}^{-1}}$$

In order to determine the degree of functionalization, the UV-Vis spectrum of a 10 µM solution of functionalized PEG in chloroform was measured. The concentration of *p*-nitrophenyl group was calculated by inserting the measured absorbance at 263.8 nm giving a degree of functionalization of 92% which is comparable to the result from the NMR method.

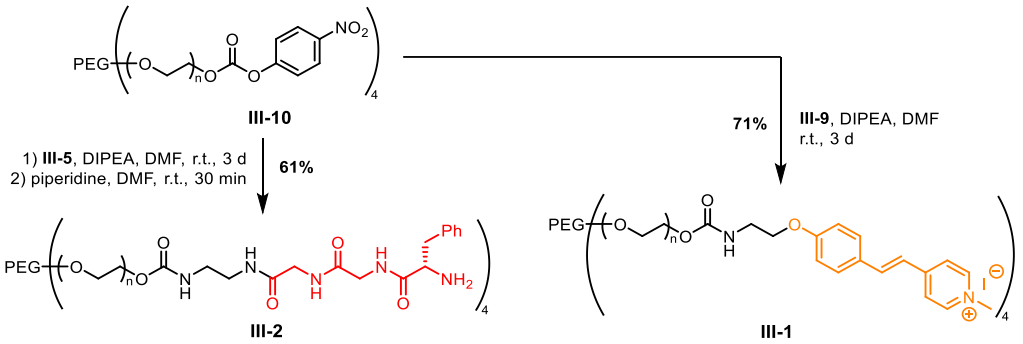

Figure 4.8: Synthetic routes for functionalization of 20k 4arm PEG-carbonate **III-10** with tripeptide FGG **III-5** or stilbazolium iodide **III-9** yielding the network building blocks **III-1** and **III-2**.

Subsequently, 4arm PEG-carbonate was allowed to react with amine carrying FGG tripeptide **III-5** or stilbazolium iodide **III-9** in DMF with DIPEA as a base leading to formation of the corresponding carbamate. For the synthesis of peptide-functionalized PEG, an additional step involving Fmoc-deprotection was conducted using a 20% piperidine solution in DMF. Finally, the polymers **III-1** and **III-2** were purified via dialysis and obtained with a degree of functionalization of around 80% (via ^{1}H-NMR).

For the studies of stilbazolium dimerization kinetics, stilbazolium iodide **III-11** was synthesized as a small molecule without spacer (Figure 4.9). This was achieved in a Knoevenagel condensation using 4-hydroxybenzaldehyde and 1,4-dimethylpyridinium iodide in methanol with piperidine as a base. The desired product **III-11** was obtained in a yield of 66% after precipitation.

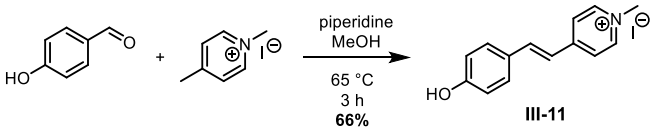

Figure 4.9: Synthesis of stilbazolium iodide **III-11**.

4.2.2 Stilbazolium Dimerization Kinetics

Since stilbazolium iodide has a carbon-carbon double bond that bridges the two aromatic units, two photochemical processes were expected: thermally reversible *cis-trans*-isomerization[311] and irreversible dimerization[157] (Figure 4.10). The absorption of a photon leads to the excitation from the singlet ground state S_0 into the excited singlet state S_1. Besides relaxation via internal conversion and fluorescence, the excited singlet state can undergo intersystem crossing into the triplet state T_1 that allows *cis-trans*-isomerization and [2+2]-cycloaddition to take place.[312] Following the principles of reaction kinetics, the reaction rate of the monomolecular *cis-trans*-isomerization is less concentration-dependent than the dimerization which is a bimolecular process. Translating this into a hydrogel system with stilbazolium introduced as an end group, the local stilbazolium concentration is low and the diffusion is limited when stilbazolium is covalently linked to polymer chains, leading to the assumption that the isomerization can take place spontaneously, but the dimerization is rather slow.

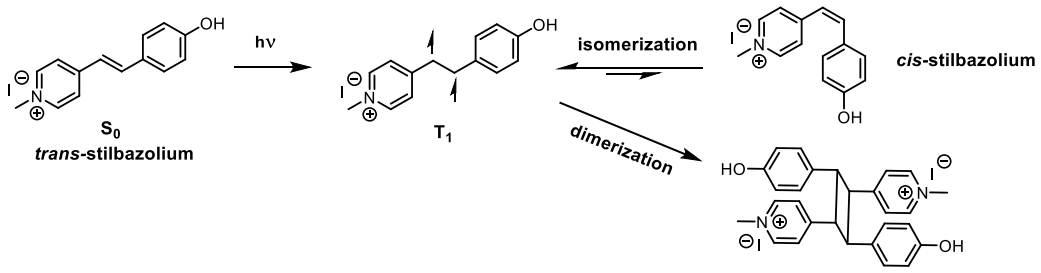

Figure 4.10: Photochemical reactions of stilbazolium iodide.

To explore the role of CB[8] in the photodimerization kinetics, UV-Vis spectroscopic measurements and NMR measurements were carried out using the stilbazolium **III-11**. The UV-Vis absorption spectrum revealed an absorption maximum of stilbazolium iodide at 370 nm which was determined as the wavelength of the external light source. The molecular structures during the irradiation process were identified via ^{1}H-NMR spectroscopy. A solution of stilbazolium iodide **III-11** in D_2O was irradiated with a 370 nm LED and proton NMR spectra were measured after different irradiation durations (0, 5, 10, 30, 60, 90, 120 and 180 min). The spectra including the range of aromatic and double bond signals are shown in Figure 4.11. It is notable that the intensity of signals from the *trans*-stilbazolium isomer that can be clearly identified in the 0 min spectrum decrease with increasing irradiation periods. At the same time, new signals associated with the *cis*-isomer can be recognized already after 5 minutes irradiation. The signal intensity increases in the initial period of the irradiation process but decreases again after longer times of irradiation. In the proton NMR spectrum after 10 min irradiation, signals assignable to the dimer species appear and the intensity increases constantly with the irradiation duration. After 3 hours of irradiation, double bond signals can hardly be recognized which means that stilbazolium is almost fully converted into the dimer.

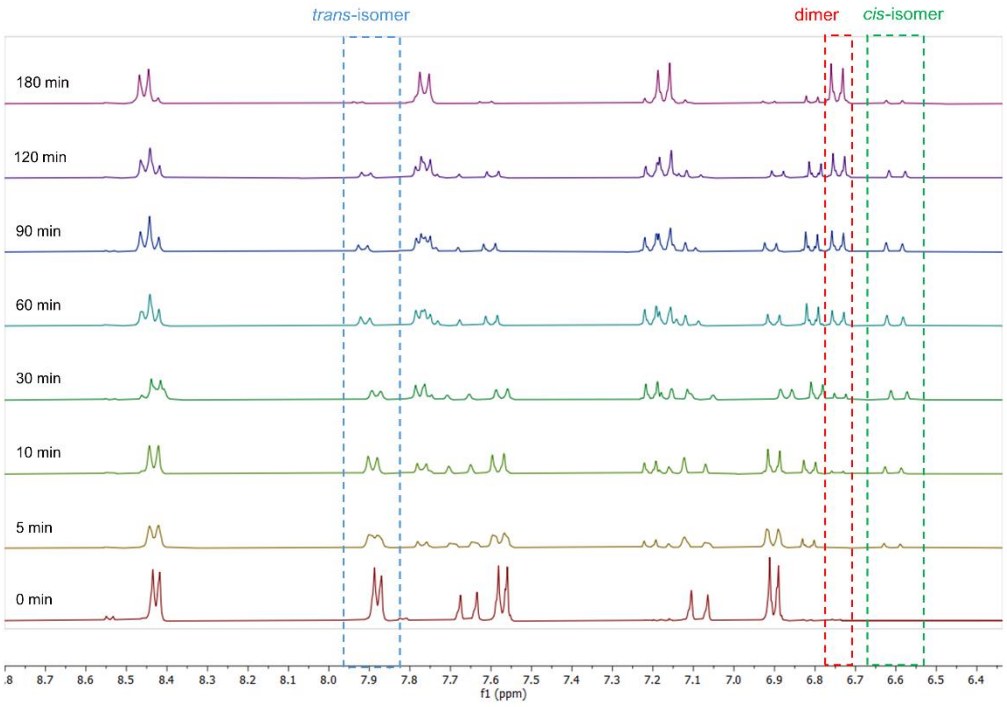

Figure 4.11: NMR studies on the isomerization and dimerization of stilbazolium iodide in D_2O in the absence of CB[8]. The solution was irradiated with a 370 nm LED and the proton NMR spectra were recorded after 0, 5, 10, 30, 60, 90, 120 and 180 min irradiation.

For the UV-Vis studies, aqueous solutions of stilbazolium iodide with and without addition of CB[8] were prepared with a stilbazolium **III-11** concentration of $c = 6 \cdot 10^{-5}$ mol L^{-1}. To one of the solutions was added CB[8] to reach a molar ratio of SB:CB[8] = 2:1. The solutions were irradiated with a 370 nm LED and the absorption spectra recorded after different irradiation periods are shown in Figure 4.12.

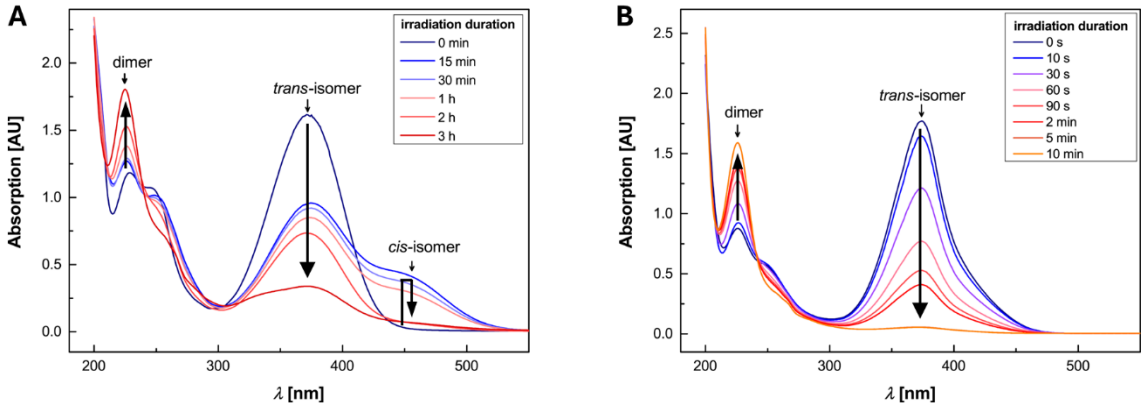

Figure 4.12: A) UV-Vis absorption spectra of an aqueous solution containing stilbazolium ($c = 6 \cdot 10^{-5}$ mol L^{-1}) after different irradiation duration. B) UV-Vis absorption spectra of an aqueous solution containing stilbazolium ($c = 6 \cdot 10^{-5}$ mol L^{-1}) and CB[8] (0.5 molar equivalent) after different irradiation durations.

In the absence of CB[8] (Figure 4.12A), the absorption band of the *trans*-isomer at 370 nm decreases with longer irradiation duration. At the beginning of irradiation, the decrease of the *trans*-isomer concentration was accompanied by the formation of the *cis*-isomer that shows an absorption band with its maximum at 450 nm. Upon longer irradiation, the absorption band of the cis-isomer decreases, while

there is a constant increase of a new absorption band at 229 nm which is associated with the dimer. These findings are in line with the observations from the NMR measurements indicating the occurrence of both photochemical reactions that are expected.

In contrast, the sample with addition of CB[8] shows surprising results (Figure 4.12B). Upon irradiation, the *trans*-isomer absorption band at 370 nm decreases, there is only an increase in the intensity of the absorption band at 229 nm which relates to the dimer formation. Unlike the case without CB[8], no *cis-trans*-isomerization was observed. It seems that the photoisomerization is fully suppressed as a result of the host-guest complexation. Moreover, the conversion of the trans-isomer into the dimer was fully completed after 10 min which is much faster than the case without CB[8] (no full conversion after 3 h). Apparently, the introduction of CB[8] accelerates the dimerization reaction due to the pre-organization of the reactive pair. Since CB[8] has to be used in an equimolar ratio to stilbazolium, it doesn't function as a catalyst but a reaction template. The homoternary complexation of stilbazolium in CB[8] results in high local concentration that benefits the bimolecular quenching of the triplet state T_1, enabling fast dimerization events.

It is imaginable that this phenomenon can be applied in polymeric gel systems as an efficient crosslinking method generating homogeneous network structures. When stilbazolium is introduced as an functional group at the end of a polymer arm (in case of star-shaped polymers) or a side chain (in case of grafted polymers), the host-guest complexation with CB[8] will pre-arrange the chain ends which perform the network junctions. Once the polymer network is irradiated, the dynamic physical crosslink will be rapidly transformed into a covalent crosslink, leading to drastic changes of the mechanical properties.

4.2.3 Mechanical Properties of Single Network Hydrogels

To investigate the mechanical properties of the single networks and photochemical transformation of the physical PEG-SB network into the chemical network, different hydrogel samples were prepared and studied using oscillatory rheology. Details to sample composition and irradiation durations are summarized in Table 4.1. The sample coding includes information on the polymer concentration, type of network (SN for single network), component in the mixture and irradiation duration (* for 10 min, ** for 1 h irradiation with a 370 nm LED). For example, 5% SN(SB:CB[8])* refers to a sample containing 5 wt% 4arm PEG-SB and CB[8] in a molar ratio of 2:1 with respect to the SB end group, whereas the gel is irradiated for 10 min.

Table 4.1: Sample composition of single network hydrogels containing PEG-FGG, PEG-SB and CB[8], and irradiation durations of each hydrogel using a 370 nm LED.

Sample	Polymer concentration	Molar fraction PEG-FGG	Molar fraction PEG-SB	Addition CB[8]	Irradiation duration
5% SN(FGG:CB[8])	50 mg mL^{-1}	1	0	+	-
5% SN(SB:CB[8])	50 mg mL^{-1}	0	1	+	-
5% SN(SB:CB[8])*	50 mg mL^{-1}	0	1	+	10 min
5% SN(SB:CB[8])**	50 mg mL^{-1}	0	1	+	1 h
5% SN(SB)*	50 mg mL^{-1}	0	1	-	10 min
5% SN(SB)**	50 mg mL^{-1}	0	1	-	1 h

As published in literature, both Phe-Gly-Gly tripeptide with free *N*-terminus (FGG) and stilbazolium iodide (SB) can undergo homoternary host-guest complexation with CB[8] in aqueous media. To assess the ability of FGG and SB decorated 4arm PEG to form hydrogel networks in the presence of CB[8] and the mechanical properties, 5 wt% (50 mg L^{-1}) solutions of 4arm PEG-FGG **III-2** and PEG-SB **III-3** were prepared in PBS buffer (Figure 4.13A and B). Even though the solutions contained star-shaped PEG with a concentration above the critical overlap concentration (c^* = 38 mg L^{-1})[313], no gelation process was observed based on physical entanglements among polymer chains. After the addition of CB[8] (in a molar ratio of 2:1 for FGG:CB[8] or SB:CB[8]) and equilibration at 40 °C, hydrogels with viscous liquid-like behavior (Figure 4.13C) and higher stiffness (Figure 4.13D) were formed. It should be mentioned that no gelation was observed, when the polymer solution was equilibrated at room temperature with the presence of CB[8] due to its poor solubility in water. The gelation is only initiated at higher temperatures by either repeating heating (up to 80 °C) and cooling cycles or continuous equilibration at 40 °C. This can be explained by the higher solubility of CB[8] at increased water

temperature.[314] Once the host-guest complexation takes place, CB[8] is dissolved due to the high solubility of the PEG-chains in water.

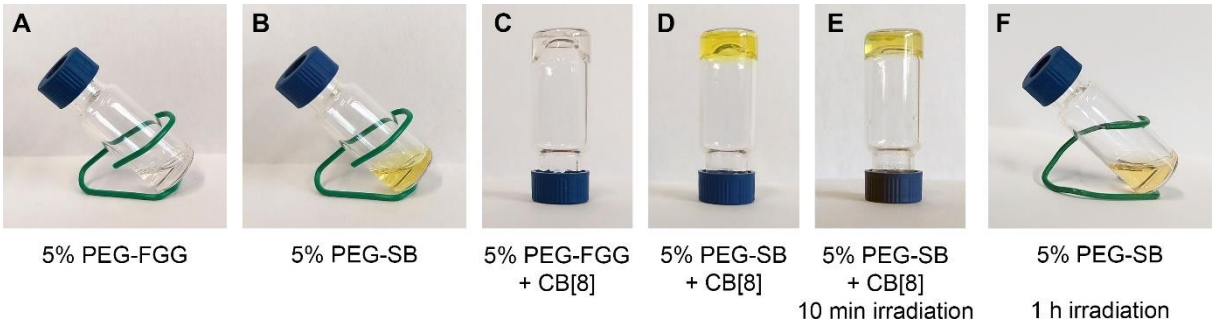

Figure 4.13: Photos of solutions or hydrogels. A) 5 wt% PEG-FGG solution; B) 5 wt% PEG-SB solution; C) hydrogel of 5 wt% PEG-FGG crosslinked with CB[8] (5% SN(FGG:CB[8])); D) hydrogel of 5 wt% PEG-SB crosslinked with CB[8] (5% SN(FGG:CB[8])); E) hydrogel of 5 wt% PEG-SB crosslinked with CB[8] after 10 min irradiation; F) hydrogel of 5 wt% PEG-SB without CB[8] after 1 h irradiation with a 370 nm LED.

Notably, the hydrogels consisting of PEG-FGG and PEG-SB feature different mechanical properties (Figure 4.14A), one behaves more like a viscous liquid (5% SN(FGG:CB[8]) in blue) and the other a viscoelastic solid (5% SN(SB:CB[8]) in red). Since the binding constants reported for homodimers with CB[8] are $\log(K_{eq}) = 11.17$ for FGG tripeptide[307] and $\log(K_{eq}) = 8.00$ in case of stilbazolium iodide[306], a higher thermodynamic stability of the homoternary complex between FGG and CB[8] and thus a higher stiffness of the hydrogel are expected in the first place. Surprisingly, the oscillatory rheological data reveals a higher crossover frequency for the hydrogel based on PEG-FGG and CB[8], which is related to faster network relaxation.[224]

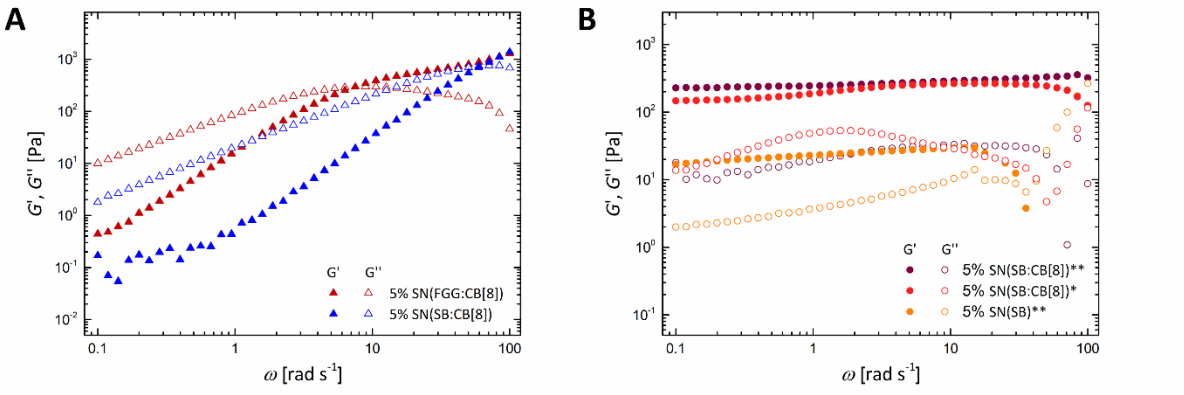

Figure 4.14: Rheological properties of 5% single network hydrogels. A) Frequency sweeps of 5 wt% single network hydrogels using PEG-FGG (dark blue) or PEG-SB (red) with CB[8] in a molar ratio of 2:1 relating to the end group and CB[8]. B) Frequency sweeps of 5 wt% covalent networks composed of PEG-SB in the presence of CB[8] after irradiation of 1 h (brown) or 10 min (red) and in the absence of CB[8] after irradiation for 1 h (orange).

Using oscillatory shear rheology, viscoelastic behavior of the sample can be investigated by measuring the storage modulus G' and the loss modulus G'' at varying frequency f (in s^{-1}). The storage modulus describes the solid contribution of the material related to the energy stored due to network deformation,

while the loss modulus measures the relaxation of the network similar to a fluid property. According to the Maxwell model that illustrates a viscoelastic material as a serial combination of a purely solid spring (Hooke's law) and a purely viscous damper (Newtonian fluid), the storage and loss modulus can be described with a single relaxation rate β and the plateau modulus G_0 as follows[224]:

$$G' = G_0 \left(\frac{f}{\beta}\right)^2 / (1 + \left(\frac{f}{\beta}\right)^2)$$

$$G'' = G_0 \left(\frac{f}{\beta}\right) / (1 + \left(\frac{f}{\beta}\right)^2)$$

The Maxwell model can be used to analyze networks that fit into the terminal flow regime in the rheological master curve. A characteristic measure is the crossover frequency ω_0 (in rad s^{-1}) where $G' = G''$, which relates to the time scale of network relaxation from a solid to a liquid. When $G' = G''$, the network relaxation rate β and crossover frequency ω_0 are in the following relationship:

$$\beta = f = \frac{\omega_0}{2\pi}$$

The relaxation time τ of the network can be calculated as:

$$\tau = \frac{1}{\beta}$$

Following this model, the network relaxation times τ = 97 ms for the PEG-FGG network and τ = 838 ms for the PEG-SB network are determined, respectively. The network relaxation time is dependent on the crosslink density and exchange rate of transient interactions such as metal-ligand complexes, physical entanglement, and host-guest complexes specifically in this work. Since the number of functional end groups are comparable, the crosslink densities in both gels should be similar. The relaxation times therefore disclose the higher exchange rate of the host-guest complex formed by FGG and CB[8] in terms of the dissociation and association kinetics[224], resulting in liquid-like properties of the hydrogel.

Concerning the application in cell culture, the viscoelasticity of extracellular matrix (ECM) plays an important role in affecting cell spreading, proliferation and differentiation.[223,315] Hydrogels exhibiting rapid stress relaxation (independent of substrate stiffness) have been proven to be great candidates for encapsulation of cells.[316,317] Based on the rheological measurements, it is thinkable that the network consisting of PEG-FGG and CB[8] is very dynamic and will perform fast stress relaxation. The hydrogel is therefore excellent for the application as a synthetic ECM (more data to hydrogel biocompatibility are shown and discussed in section 4.2.6). However, high viscous contribution of the single physical network also leads to a lack of shape fidelity that makes it less suitable for bioprinting experiments.

In order to improve the stiffness and form stability of the hydrogel, a second network consisting of 4arm PEG-SB and CB[8] is introduced. Following the UV-Vis studies discussed in section 4.2.2, the physical network of PEG-SB and CB[8] can be rapidly and selectively transformed into a chemical network by applying an external light trigger due to pre-installed network junctions. To verify the outcomes of the UV-Vis studies, 5 wt% solutions of PEG-SB in the absence of CB[8] and single network hydrogels containing 5 wt% PEG-SB physically crosslinked with CB[8] were prepared and analyzed via oscillatory shear rheology after different irradiation durations.

In the presence of CB[8], the mechanical properties of the hydrogel shows significant difference after 10 min irradiation with a 370 nm LED than the pre-irradiation state. Before the irradiation, the physically crosslinked hydrogel 5% SN(SB:CB[8]) exhibit viscous flow behavior that can be observed both in the inverted vial test (Figure 4.13D) and the frequency sweep (red data points in Figure 4.14A), typical for a dynamic physically crosslinked hydrogel. After irradiation for 10 min (5% SN(SB:CB[8])*), a stiffer solid hydrogel is formed due to dimerization of stilbazolium end groups (Figure 4.13E) and the frequency sweep also demonstrates that the storage modulus G' is about one order of magnitude higher than the loss modulus G'' over the entire frequency test window, which is related to a static hydrogel. When the same physical hydrogel is irradiated for 1 h with the 370 nm LED (5% SN(SB:CB[8])** in Figure 4.14B), the mechanical properties measured in rheology is very similar to 5% SN(SB:CB[8])* after 10 min irradiation. This indicates that the photochemical crosslinking process is completed already after 10 min irradiation, which matches to the finding from the UV-Vis studies. When CB[8] is absent, no hydrogel formation is observed after 10 min irradiation. If the solution is irradiated for 1 h, it seems that a static hydrogel is form when analyzing the rheological data (5% SN(SB)** in Figure 4.14B), since G' is higher than G''. The sample itself however does not show solid gel properties but remains a solution that contains parts of solid domains. Comparing the moduli measured in the frequency sweeps, the solid contribution of 5% SN(SB)** after 1 h irradiation with a storage modulus G' around 10 Pa is much lower than 5% SN(SB:CB[8])* which has a storage modulus around 100 Pa after 10 min irradiation. Evidently, the pre-organization of the stilbazolium end group by host-guest complexation with CB[8] provides a promising method for efficient photochemical crosslinking.

4.2.4 Interpenetrating Network Formation

For the successful design of biomaterial inks, different requirements such as biocompatibility, viscoelasticity, shear-thinning and self-healing behavior as well as post-printing shape fidelity have to be fulfilled. Since it is challenging to achieve all the (bio-)mechanical properties just by using one single synthetic material, formation of interpenetrating networks provides an opportunity to combine networks featuring different structures and to obtain hydrogel materials with complex properties. To this end, the single networks discussed in section 4.2.3 are mixed to create interpenetrating network (IPN) hydrogels with tunable physical and chemical crosslink densities (due to varying molar fractions of PEG-FGG and PEG-SB), leading to materials with adjustable mechanical properties. Information on sample composition of single and interpenetrating network hydrogels with only supramolecular crosslinks are summarized in Table 4.2 and the frequency sweeps measured are shown in Figure 4.15. The sample coding includes information on polymer concentration, type of network (SN for single network and IPN for interpenetrating network) and molar fractions of both polymers. For example, 5% IPN(75:25) refers to an interpenetrating network hydrogel containing 5 wt% polymer with 75% PEG-FGG and 25% PEG-SB. The sample is crosslinked using CB[8] with a molar ratio of 2:1 with respect to the polymer end groups.

Table 4.2: Sample composition of physical interpenetrating network hydrogels containing PEG-FGG, PEG-SB and CB[8].

Sample	Polymer concentration	Molar fraction PEG-FGG	Molar fraction PEG-SB	Addition CB[8]
5% SN(FGG:CB[8])	50 mg mL^{-1}	1	0	+
5% SN(SB:CB[8])	50 mg mL^{-1}	0	1	+
5% IPN(75:25)	50 mg mL^{-1}	0.75	0.25	+
5% IPN(50:50)	50 mg mL^{-1}	0.5	0.5	+
5% IPN(25:75)	50 mg mL^{-1}	0.25	0.75	+

All hydrogels exhibit similar viscoelastic liquid-like behavior due to the fact that all samples contain only supramolecular crosslinks formed by homoternary host-gust complexation between the polymer end groups FGG or SB with CB[8]. With increasing amount of PEG-SB, the frequency sweeps show a slight shift of the crossover frequency from 50 rad s^{-1} to around 10 rad s^{-1}, which is expected due to the higher fraction of the SB-CB[8] complexes featuring slower exchange kinetics. It is also noticeable that the IPN hydrogels tend to be less stiff (lower plateau storage modulus G_0) than the single network hydrogels, indicating a certain competitive behavior between the FGG and SB end groups in terms of binding to CB[8]. When a CB[8] host is occupied by a FGG guest molecule in the 5% IPN(50:50), it is unlikely that a SB guest molecule will enter the cavity of CB[8]. Since the total concentration of FGG

end group is only 50% of the 5% SN(FGG:CB[8]), it is less probable to find the next binding partner. Once the CB[8] is free due to dissociation of the 1:1 inclusion complex between FGG and CB[8], a SB molecule close to the CB[8] can bind to it, so that no FGG molecule can enter the cavity. Since the critical overlap concentration is reached, the polymers have contact to their neighbors, so that the competition can take place within the entire network, leading to decreased stiffness of the resulting hydrogel. Evidently, the formation of heteroternary complexes by FGG, SB and CB[8] in an 1:1:1 ratio is not possible or at least less favored than the homoternary complex formation so that it is negligible.

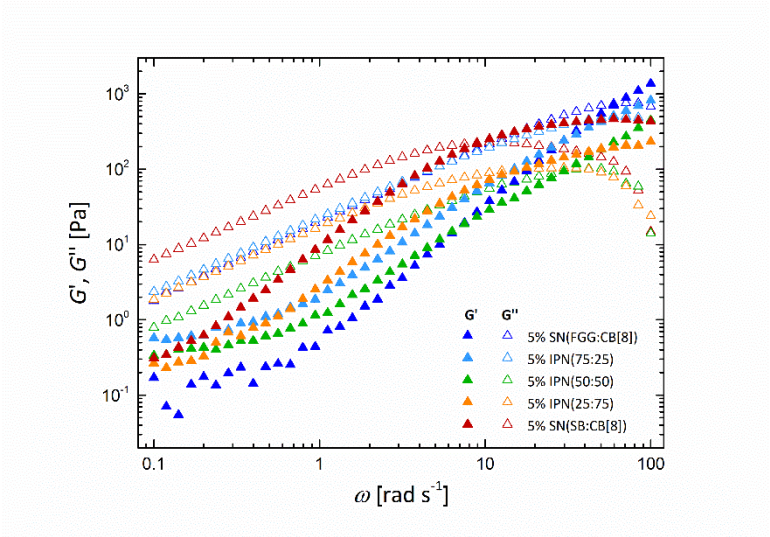

Figure 4.15: Frequency sweeps of 5 wt% interpenetrating network hydrogels with 0%, 25%, 50%, 75% and 100% PEG-SB pre-irradiation at 20 °C.

However, the competitive binding affects the total network crosslink density and thus leads to undesired decrease of the mechanical stiffness of the physical hydrogels. It is therefore thinkable that the physical and chemical network density after the irradiation is less controllable. To reduce the gel weakening effect by the competitive binding events and to make sure that both networks only have limited interaction (no physical entanglements) with each other, hydrogels were prepared with a polymer concentration of c = 35 mg L^{-1}, which is slightly below the critical overlap concentration (c^* = 38 mg L^{-1}) reported in literature.[313] Details to sample composition and irradiation durations are summarized in Table 4.3. The sample coding includes information on polymer concentration, type of network (SN for single network and IPN for interpenetrating network), molar fractions of both polymers and irradiation duration (* for 10 min). For example, 3.5% IPN(75:25)* refers to a sample containing in total 3.5 wt% polymer with 75% PEG-FGG and 25% PEG-SB. The sample is crosslinked using CB[8] with a molar ratio of 2:1 with respect to the polymer end groups and the gel is irradiated for 10 min.

Table 4.3: Sample composition of interpenetrating network hydrogels containing PEG-FGG, PEG-SB and CB[8], and irradiation durations of each hydrogel using a 370 nm LED.

Sample	Polymer concentration	Molar fraction PEG-FGG	Molar fraction PEG-SB	Addition CB[8]	Irradiation duration
3.5% SN(FGG:CB[8])	35 mg mL^{-1}	1	0	+	-
3.5% SN(FGG:CB[8])*	35 mg mL^{-1}	1	0	+	10 min
3.5% SN(SB:CB[8])	35 mg mL^{-1}	0	1	+	-
3.5% SN(SB:CB[8])*	35 mg mL^{-1}	0	1	+	10 min
3.5% IPN(75:25)	35 mg mL^{-1}	0.75	0.25	+	-
3.5% IPN(50:50)	35 mg mL^{-1}	0.5	0.5	+	-
3.5% IPN(25:75)	35 mg mL^{-1}	0.25	0.75	+	-
3.5% IPN(75:25)*	35 mg mL^{-1}	0.75	0.25	+	10 min
3.5% IPN(50:50)*	35 mg mL^{-1}	0.5	0.5	+	10 min
3.5% IPN(25:75)*	35 mg mL^{-1}	0.25	0.75	+	10 min

All samples (with varying amount of PEG-SB) were analyzed using oscillatory shear rheology in frequency sweep measurements at both 20 and 37 °C to monitor the mechanical properties at the preparation temperature and according to the post-printing incubation conditions.

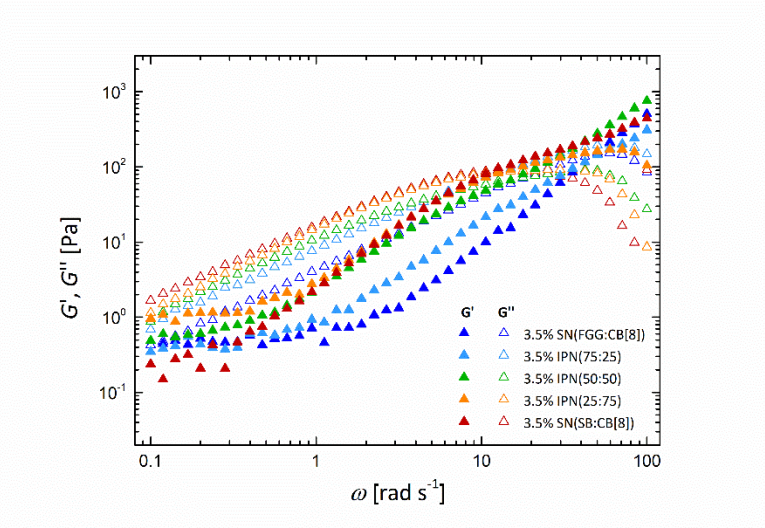

Figure 4.16: Frequency sweeps of 3.5 wt% interpenetrating network hydrogels with 0%, 25%, 50%, 75% and 100% PEG-SB pre-irradiation at 20 °C.

Frequency sweeps measured at 20 °C (Figure 4.16) show viscoelastic liquid-like gel behavior for all pre-irradiation hydrogels. As already seen in the 5 wt% hydrogels, the crossover frequency shifts to lower frequency regime with increasing amount of PEG-SB. Since the polymer concentration is lower,

the total crosslink density within the networks is lower, resulting in hydrogels with decreased mechanical properties (lower plateau storage modulus than the 5% hydrogels). At a concentration below the critical overlap concentration, there is no overlap of the polymer coils. This leads to decreased probability for two chain ends to meet each other. Therefore, no large effect of the competitive binding can be observed, and the total crosslink densities of each gel are comparable.

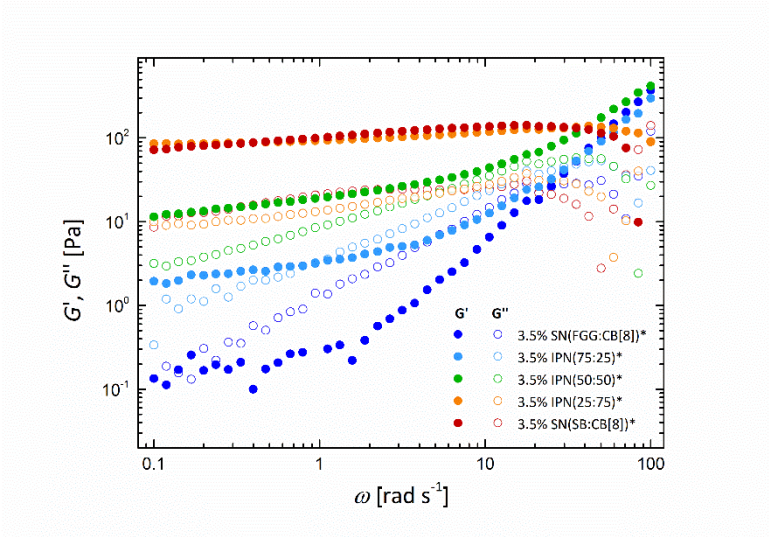

Figure 4.17: Frequency sweeps of 3.5 wt% interpenetrating network hydrogels with 0%, 25%, 50%, 75% and 100% PEG-SB post-irradiation at 20 °C.

Upon irradiation with a 370 nm LED, the hydrogels exhibit drastic changes in their mechanical properties due to photochemical transformation of the PEG-SB network. Frequency sweeps of the 3.5% SN and IPN hydrogels post-irradiation are shown in Figure 4.17. In case of 3.5% SN(FGG:CB[8])*, the mechanical properties are exactly the same pre- and post-irradiation, indicating that the FGG:CB complex is not affected by light. The hydrogel containing 25% PEG-SB (3.5% IPN(75:25)*) shows similar viscoelastic liquid-like behavior as the pure physical network with a slight increase of the storage modulus G' in the lower frequency regime (G' higher than G'' at angular frequencies below 1 rad s^{-1}). This comes from the small solid-like gel contribution of the chemical network which is formed by dimerization of stilbazolium end groups within CB[8]. This contribution becomes more pronounced with higher amount of PEG-SB. The properties of 3.5% IPN(25:75)* is therefore dominated by the chemical network, resulting in a solid-like material (storage modulus G' higher than loss modulus G'') over the entire frequency spectrum that is very similar to the photochemically crosslinked SN hydrogel 3.5% SN(SB:CB[8])*. Interestingly, the hydrogel comprising both polymers in a ratio of 1:1 displays an intermediate state demonstrating solid-like attributes and viscoelastic behavior at the same time. At low frequencies, the hydrogel exhibits characteristics of the chemical network, whereas features of the transient physical network are demonstrated in the higher frequency regime. This is indicative for the improvement of the hydrogel form stability through formation of a covalent network, while the dynamic nature related to the supramolecular host-guest complexation is maintained.

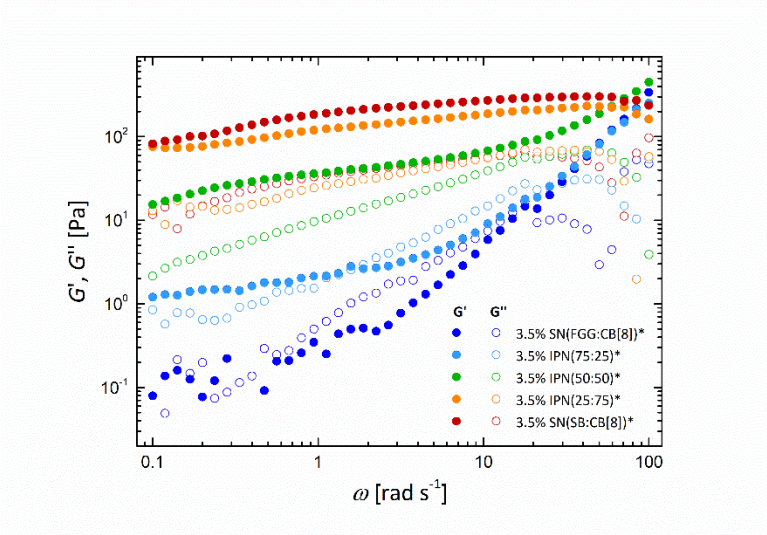

Figure 4.18: Frequency sweeps of 3.5 wt% interpenetrating network hydrogels with 0%, 25%, 50%, 75% and 100% PEG-SB post-irradiation at 37 °C.

Frequency sweeps at 37 °C of the irradiated hydrogels were measured to assess the mechanical properties at the operation temperature for cell culture experiments (Figure 4.18). Comparing to the measurements at 20 °C, the hydrogels exhibit similar mechanical properties at increased temperatures, implying that the hydrogels are stable enough to be used in cell culture experiments. It seems like the hydrogels show an increase of the hydrogel stiffness, which can rather be explained by water evaporation at higher measuring temperatures, that is common for rheological experiments even though a solvent trap is applied to avoid drying effects. Considering the working conditions for cell culture, the biomaterial ink including cells and hydrogel material are usually covered in aqueous cell culture medium after the printing process. Therefore, loss of water content in the hydrogels is less likely in the bioprinting application.

4.2.5 Comparison of SN and IPN hydrogels

In the context of bioprinting, both mechanical support and dynamics within the biomaterial inks are significant not only in terms of their extrudability[184] but also play an important role on influencing cell behavior[186,187]. Due to the requirements for successful bio-ink development, the material should feature viscoelastic, self-healing properties and post-printing shape fidelity. Since the interpenetrating network hydrogel with a composition of 50% supramolecular and 50% chemical crosslink shows form stability without being entirely static, further investigations of dynamic (bio-)mechanical properties (including stress relaxation, flow behavior, self-healing, and compression tests) focus on the hydrogel 3.5% IPN(50:50) pre- and post-irradiation as well as the comparison to single network hydrogels with pure physical or chemical crosslinks.

When applying a constant shear strain to a sample, a certain stress is induced within the material. Depending on the type of material, the sample exhibit different relaxation modulus $E(t)$ or normalized shear stress over time. A purely elastic sample (solid) will completely store the deformation energy and show a constant stress proportional to the shear strain following Hooke's law (normalized shear stress equals 1). In contrast, an ideal fluid shows an abrupt increase of the stress which instantly decreases to zero due to energy dissipation. In case of a viscoelastic materials (most biological tissues belong to this category), the initial strain leads to an increase of the stress that gradually decreases over time. Part of the deformation energy is stored due to the elastic contribution, whereas the rest is dissipated as heat resulting from the viscous contribution. The larger the solid-like contribution of the material given by less dynamic crosslinking, the slower is the stress relaxation, as shown by Krieg et al. in their investigation of DNA-crosslinked hydrogels with various lengths of overlap domains (Figure 4.19A).[220] The viscoelastic behavior of the extracellular matrix has been shown to have a large impact on cellar processes, including growth, spreading and differentiation.[223] Therefore, it is important to design bioinks featuring stress relaxation on a similar time scale as biological tissues.

Comparing the single and interpenetrating network hydrogels pre- and post-irradiation in this work, different relaxation behavior were observed upon application of a constant strain of 10% (Figure 4.19B). Due to the reversibility of supramolecular host-guest complexes, SN and IPN hydrogels pre-irradiation (3.5% SN(FGG:CB[8]), SN(SB:CB[8]) and IPN(50:50)) show rapid and full relaxation of the initial stress within 1 s. When the hydrogels experience a shear strain, the deformation energy is dissipated by dissociation of the host-guest complexes due to its fast kinetics, showing large liquid-like contribution of the material which is in line with the findings from the frequency sweeps discussed earlier. When the network is crosslinked by only covalent interactions (3.5% SN(SB:CB[8])*), the energy dissipation is caused by rearrangement of the polymer chains between network junctions, leading to a stress-relaxation time of $t_{1/2}$ = 20 s. This behavior is comparable to a rubber comprised of a chemical network with a low crosslink density. In case of 3.5% IPN(50:50)*, the network contains 50% supramolecular and 50% covalent crosslinks. The reduction of the initial stress results from both mechanisms, leading to

intermediate stress-relaxation time of $t_{1/2}$ = 2 s compared to fully physical or fully covalent networks, closely resembling that found in biological tissues.[223] It is possible to further adjust the network relaxation behavior by changing the polymer concentration or the size of the PEG macromer. With increasing amounts of the polymer, the crosslink density increases and additional interactions between network components are imaginable (for example physical entanglements of the polymer chains), resulting in slower stress relaxation. When using smaller 4arm PEG macromers for hydrogel formation at the same concentration, the total crosslink density will be higher which can also lead to higher solid-like contribution similar to stiff thermosets in the extreme case.

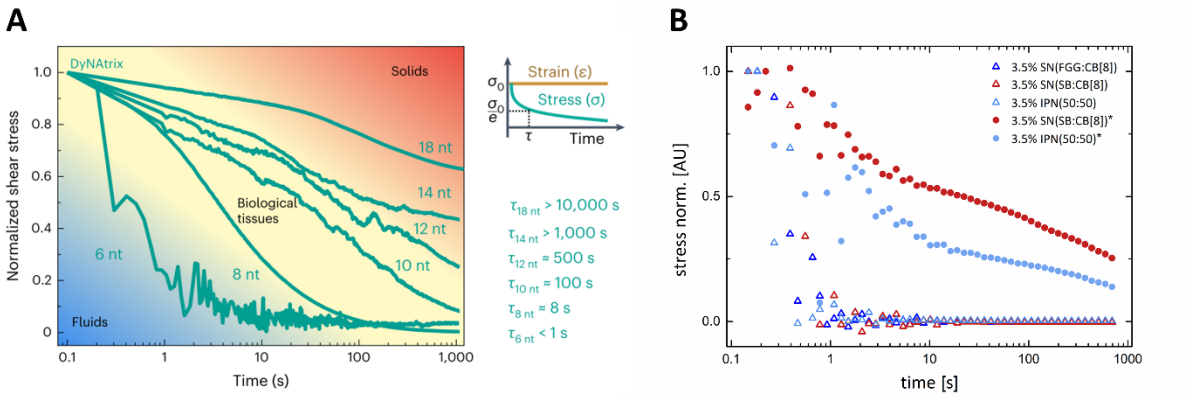

Figure 4.19: A) Normalized stress-relaxation curves of dynamic matrices crosslinked via DNA crosslinker various lengths of overlap domains (6 to 18 nt) covering the typical range of biological tissues.[223] Reproduced with permission.[220] Copyright 2023, Springer Nature. B) Stress relaxation of 3.5% hydrogels composed of single network (SN) or interpenetrating network (IPN) crosslinked with CB[8] before and after 10 min irradiation with an external light source of 370 nm. The measurements were performed at a constant strain of 10%.

To investigate the printability of the hydrogels, flow curves with increasing shear rates from 0.01 to 1000 s^{-1} were measured for different single and interpenetrating network hydrogels (Figure 4.20A). Among the physically crosslinked hydrogels (3.5% SN(FGG:CB[8]), 3.5% SN(SB:CB[8]) and 3.5% IPN(50:50)), the initial viscosity is around 10^4 mPa s for each. Interestingly, the yielding appears at different shear rates. For the hydrogel with fast exchange kinetics (3.5% SN(FGG:CB[8])), a shear-thinning behavior can be observed across the whole measuring window, but a rupture of the network is first seen at a shear rate 110 s^{-1}, while the other two physical networks show yielding at around 10 s^{-1}. The IPN network 3.5% IPN(50:50)* features an initial viscosity about one order of magnitude higher than the pure physical gels, while that of 3.5% SN(SB:CB[8])* is even higher (10^8 mPa s) which can be attributed to the higher fraction of chemical network density. The yielding is observed at 0.1 s^{-1} and 0.5 s^{-1} for the networks with 100% and 50% chemical crosslinks, respectively. Evidently, the shear rate, at which the yielding point is reached depends on the network dynamics. In case of fast exchange rates in terms of formation of network junctions, the network recovers rapidly from its disassembly and retains the initial viscosity. Once the dissociation rate is higher than the association rate of the crosslinks, the viscosity starts to decrease dramatically, which can be observed as yielding. Since the macromers in 3.5% SN(SB:CB[8])* are only crosslinked covalently, the gel is not able to recover from the rupture

caused by deformation, resulting in an early yielding point. The hydrogel 3.5% IPN(50:50)* again presents an intermediate case with constant viscosity from 0.01 to 1 s^{-1} but an earlier yielding than the purely physical gels according to the reduced fraction of supramolecular crosslinks.

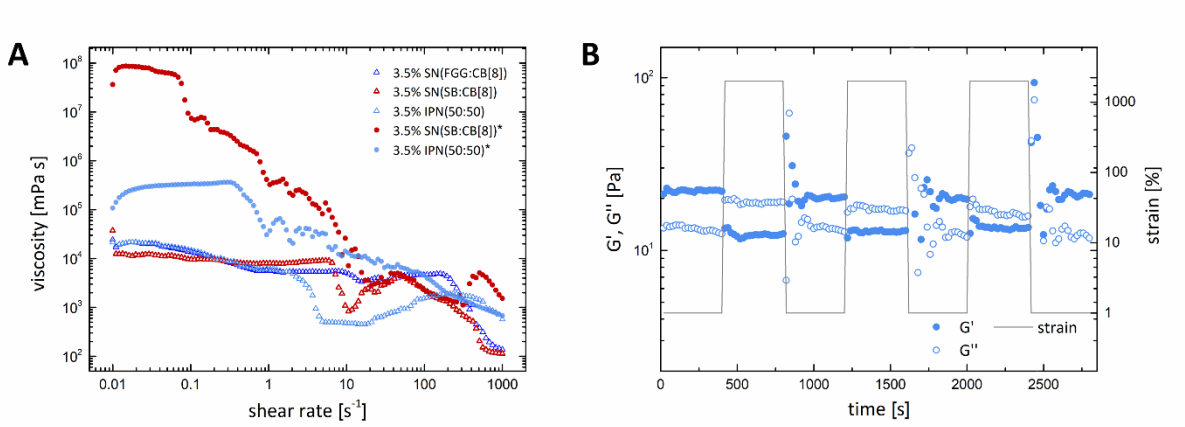

Figure 4.20: Investigation of hydrogel printability. A) Flow curves of 3.5% single and double network hydrogels pre- and post-irradiation. B) Step-strain measurement of 3.5% IPN(50:50)* with alternating strain between 1% and 2000%.

In addition, a step-strain measurement with alternating strain between 1% and 2000% was performed for the interpenetrating network hydrogel 3.5% IPN(50:50)* to study the shear-thinning and self-healing behavior (Figure 4.20B). The hydrogel shows attributes of a solid-like material at low shear strain ($G' > G''$) but becomes a liquid at high shear strain ($G' < G''$). The alteration of the shear strain between 1% and 1000% was repeated several times to show that the liquid gel at high shear strain can self-heal and solidify rapidly, when the shear strain decreases. This is achieved by the reversible formation of host-guest complexes between FGG and CB[8]. The mechanical properties after the self-healing process are almost the same as before, implying that the shear-thinning effect is only caused by dissociation of the host-guest complexes, while the covalent gel network is unaffected by application of large shear strains. In terms of bioprinting applications, the IPN hydrogel can be transformed into a liquid by pressure-controlled extrusion through a thin nozzle due to its shear-thinning properties. After the printing process, the self-healing hydrogel is able to restore its original stiffness.

One further property that needs to be studied is the behavior towards compression. When a bio-active, cell-laden construct is successfully printed that supports different cellular processes in the cultivation, the next crucial step will be the implantation of the construct into the defect site of living tissues. Therefore, it is crucial that the construct is stable with respect to compressive loading and will not generate too much stress for cells during the operation.[318] To this end, compression tests were carried out for different single and interpenetrating network hydrogels. For preparative reasons, the compression testing was only performed with post-irradiated gels with at least 50% chemical crosslinks.

The test was conducted by placing cylindrical samples with 10 mm diameter and 2.5 mm thickness between the upper and lower measuring plates of the rheometer and compressing the sample with a

velocity of 0.05 mm s^{-1}. The resulting stress-strain curves are shown in Figure 4.21. Along with the compression, the sample volume decreases, which leads to higher density of the material. The normal stress shows a linear proportionality to the strain when the deformation is minimal, while the relationship between normal stress and strain tends to be exponential of higher degree of deformation, since the material becomes less compressible. An important measure for the compressibility of a material is the compression modulus E_{comp} that can be determined using the slope of the initial linear regime from the stress-strain curve. For 3.5% hydrogels with 50%, 75% and 100% PEG-SB, the compression modulus slightly increases from (1.14 ± 0.04) kPa to (1.24 ± 0.03) kPa, then to (2.34 + 0.95) kPa with increasing fraction of chemical crosslinks, since the chemical network is less flexible in rearranging itself during a deformation process. By changing the polymer concentration from 3.5% to 5%, the compression modulus significantly increases to (9.46 ± 0.58) kPa. The normal stress at 80% deformation is also about five orders of magnitude higher when increasing the polymer concentration from 3.5% to 5%, indicating that the polymer concentration has a higher influence on the compressive properties of the hydrogels than the type of crosslink.

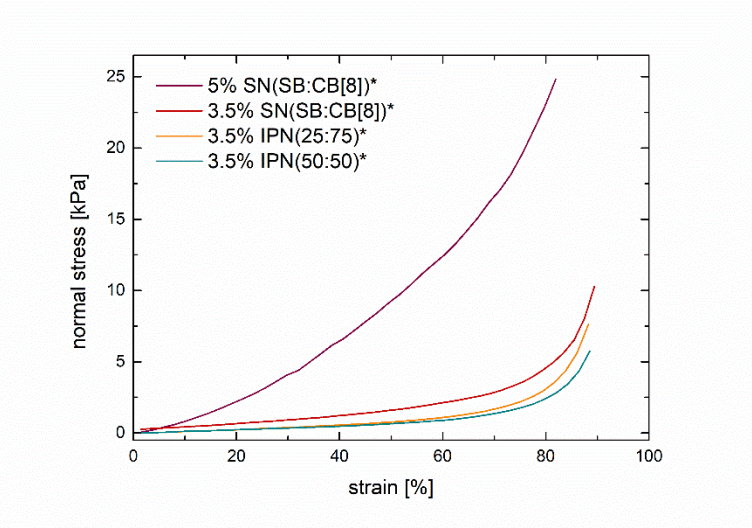

Figure 4.21: Compressive properties of single and double network hydrogels post-irradiation.

Results from frequency sweeps (network relaxation time and plateau storage modulus) and compression experiments (compressive modulus as well as normal stress at 80% deformation) for all hydrogels mentioned are summarized in Table 4.4.

Table 4.4: Relaxation time, plateau storage modulus, compression modulus and compression stress at 80% strain of different samples.

Sample	Frequency sweep (20 °C)		Compression test	
	Relaxation time τ [ms]	**Plateau modulus G_0 [Pa]**	**Compression modulus E_{comp} [kPa]**	**Stress at 80% stain [kPa]**
5% SN(FGG:CB[8])	97	1400	-	-
5% SN(SB:CB[8])	838	600	-	-
5% SN(SB:CB[8])*	-	263	9.46 ± 0.58	23.9 ± 1.0
5% SN(SB:CB[8])**	-	354	10.03 ± 0.69	24.2 ± 0.8
5% SN(SB)*	-	No gel formation	-	-
5% SN(SB)**	-	29	-	-
5% IPN(75:25)	150	900	-	-
5% IPN(50:50)	242	390	-	-
5% IPN(25:75)	349	130	-	-
3.5% SN(FGG:CB[8])	126	509	-	-
3.5% SN(FGG:CB[8])*	250	380	-	-
3.5% SN(SB:CB[8])	483	441	-	-
3.5% SN(SB:CB[8])*	-	114	2.43 ± 0.95	4.3 ± 0.5
3.5% IPN(75:25)	556	315	-	-
3.5% IPN(50:50)	419	721	-	-
3.5% IPN(25:75)	465	168	-	-
3.5% IPN(75:25)*	209	302	-	-
3.5% IPN(50:50)*	-	430	1.14 ± 0.04	2.4 ± 0.1
3.5% IPN(25:75)*	-	138	1.24 ± 0.03	3.4 ± 0.4

4.2.6 Biocompatibility and Application of IPN hydrogel in 3D-Bioprinting

Based on the results from the previous sections, the interpenetrating network hydrogel 3.5% IPN(50:50)* exhibit viscoelastic properties due to reversible supramolecular crosslinks (dynamic component that supports cellular processes) and matrix stiffness given by the covalent crosslinks after photochemical network transformation (static component offering structural stability). Both properties are important in terms of the bio-ink processability and impact on cell behavior. In this section, those features are further studied in the context of cell culture and bioprinting by performing cell viability assays in suspensions and in gels as well as bioprinting experiments using osteoblastic SaOS-2 cell line.

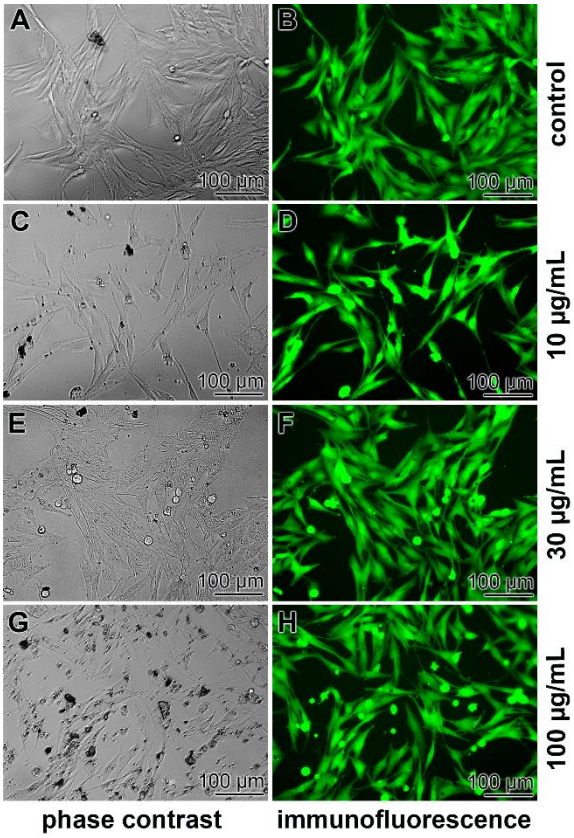

Figure 4.22: Cell viability assay of physically crosslinked hydrogel 3.5% SN(FGG:CB[8]). Calcein-AM stain was added after 3 days cultivation of SaOS-2 cells to assess the viability. The images were recorded in phase contrast (left) and fluorescence channel (right) for cell suspensions with various amount of the hydrogel: A) and B) 0 µL mL^{-1}; C) and D) 10 µL mL^{-1}; E) and F) 30 µL mL^{-1}; G) and H) 100 µL mL^{-1}.

Cell viability assay was carried out using osteoblastic SaOS-2 cell line to assess the cytocompatibility of 3.5% SN(FGG:CB[8]) as a dynamic component of the IPN hydrogels. The culture medium was mixed with different amounts of the hydrogel (0, 10, 30, 100 µL mL^{-1}) and cultivated for three days. After addition of membrane penetrating calcein-AM stain[319], images in phase contrast and in fluorescence channel (495 nm excitation and 511 nm emission with cells detected in green) were recorded (shown in Figure 4.22) to examine the cell viability by comparing the images to the control experiment (with 0 µL addition of gel). The results reveal that the single network hydrogel with only physical crosslinks is non-toxic and cytocompatible.

In the next step, the SaOS-2 cell growth was monitored after direct injection of cell suspension (cells in culture medium that contains nutrients) into hydrogels with different compositions. Therefore, 3.5% SN(FGG:CB[8]) was prepared without additional component, with addition of chondroitin sulfate (CS) which is a sulfated glycosaminoglycan that can promote cell adhesion and act as a growth factor, or with extra cell culture medium that is pre-mixed into the hydrogel matrix. Concurrently, cultivation was also performed in cell culture medium as a positive control experiment. Calcein-AM staining solution was used to assess the cell viability. Images in phase contrast and in fluorescence channel (495 nm excitation and 511 nm emission) recorded are shown in Figure 4.23.

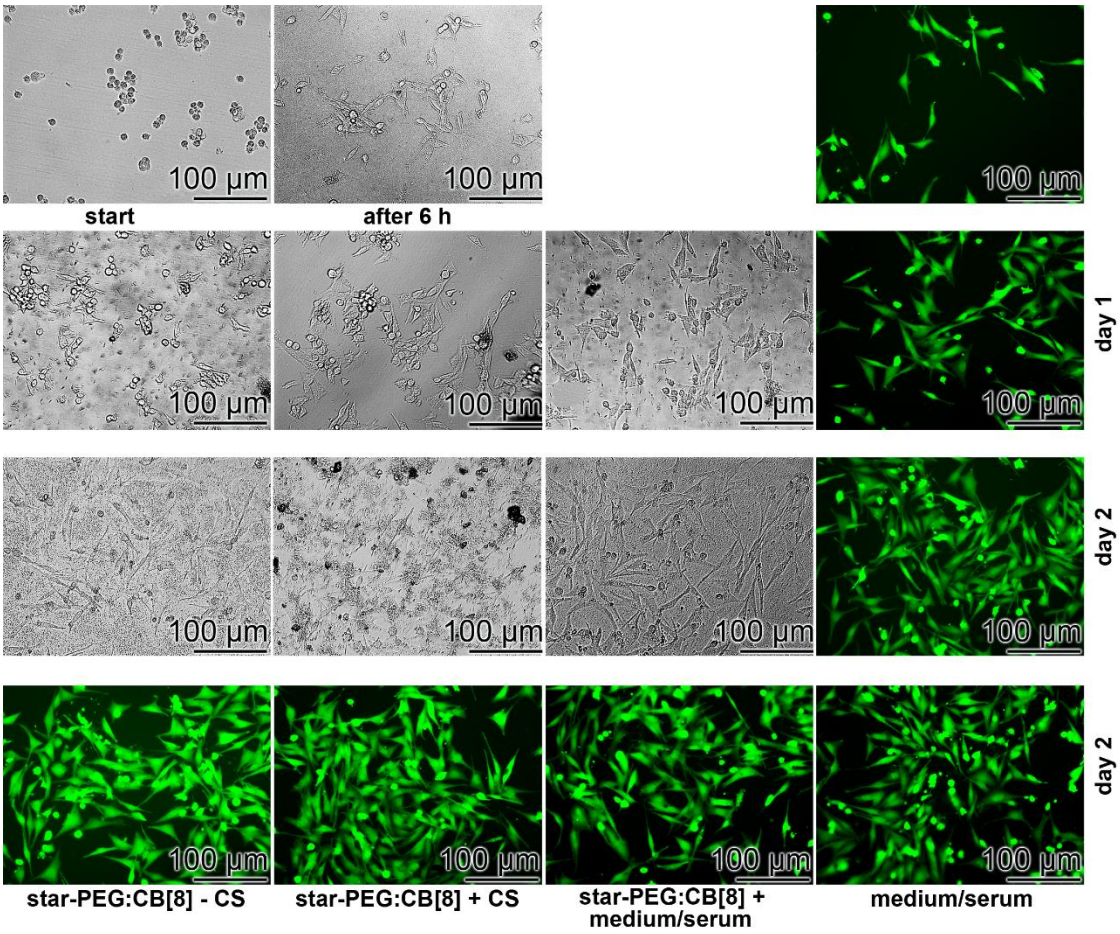

Figure 4.23: Viability of cells after injection of the cell suspension into hydrogels with different compositions.

Typically, in a cell culture experiment, the cells are transferred in roundish shape to new medium. Once the cells are placed into the well plate, they can start to proliferate. Due to adhesion of cells on the bottom of the well plate, an elongated morphology can be observed showing that the cells can interconnect with each other. [320] After injection of the cell suspension into the hydrogel without additional components, the cells featured rounded shape (top left image), whereas the number of cells increased, and the morphology of cells changed with time. After 1 day of cultivation, part of the cells started to adapt elongated morphology which indicates cell adhesion, but a larger part of the cells still had the rounded morphology that can be explained by the spatial constraint given by the surrounding

gel matrix. However, the cells were able to fully adapt the elongated morphology after 3 days of cultivation owing to the dynamic nature of the hydrogel. When chondroitin sulfate was added to the hydrogel, a transition of the morphology from roundish to elongated could already be observed after 6 hours of incubation, implying that CS was able to promote cell adhesion. The same effect was also found in the hydrogel with additional cell culture medium pre-mixed into the gel matrix, resulting in better adhesion and distribution of cells. Comparing these three cases, the overall results of cell adhesion and proliferation after 3 days of incubation were similar, confirming the compatibility of the hydrogel 3.5% SN(FGG:CB[8]) as a dynamic extracellular matrix (ECM) component for the application in cell culture experiments.

Besides the viscoelasticity and stress relaxation behavior of the hydrogel, shape fidelity after the printing process is also crucial for the success of bioprinting experiments. In most approaches, post-printing processing of the hydrogel is necessary to increase stiffness of the material, via photochemical crosslinking for example.[160] In this work, the mechanical stiffness was improved by the formation of interpenetrating network consisting of a physical and a chemical network. To explore the potential of 3.5% IPN(50:50) for the usage as a biomaterial ink, IPN hydrogel pre-loaded with cell suspension was prepared and subjected to extrusion-based bioprinting experiments. In a pressure-controlled mode, robust 2-layer porous cylindrical scaffolds with different sizes were able to be created (one with a 50 mm diameter and 320 µm layer thickness is shown in Figure 4.24A).

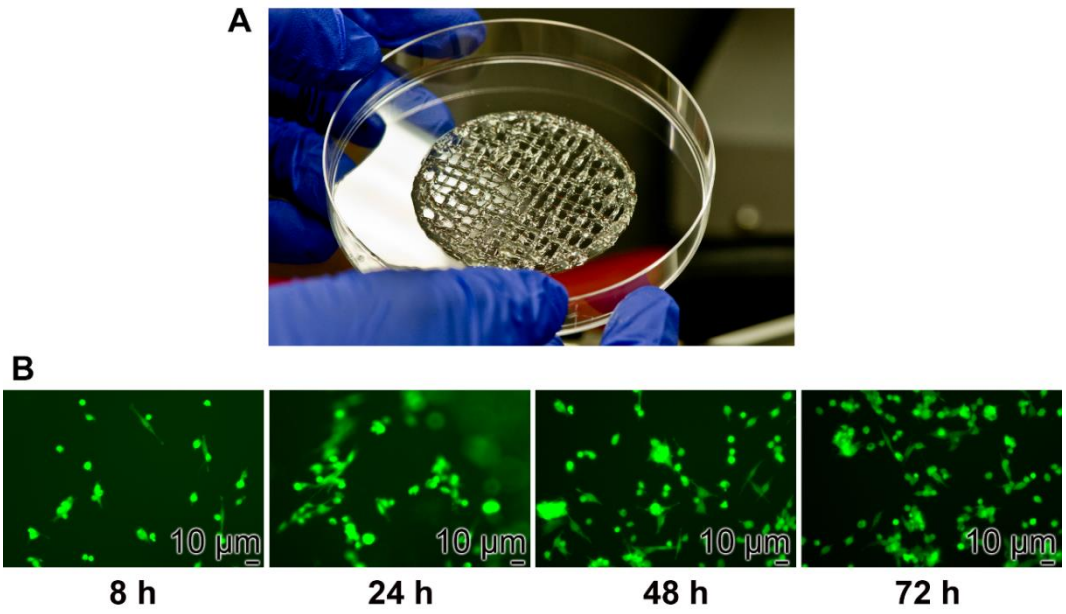

Figure 4.24: A) Cylindrical disc printed with cell-laden 3.5 wt% pre-crosslinked hydrogel. B) Cell viability was evaluated to 8, 24, 48, and 72 hours post-extrusion utilizing calcein-AM stain. The images were recorded in the fluorescence mode using excitation wavelength of 495 nm and emission wavelength of 511 nm.

The constructs obtained were covered by cell culture medium and the cell viability was evaluated after different incubation times (8, 24, 48 and 72 hours). Calcein-AM was again used as a staining reagent. Cell images recorded in fluorescence channel (495 nm excitation and 511 nm emission) after addition

of the staining solution are shown in Figure 4.24B. Noticeably, the transition of rounded into elongated morphology is much slower compared to purely physical hydrogels (Figure 4.23). This is expected as a result of the chemical network that is less dynamic, the cells experience more constant spatial constraint and therefore needs more time to interconnect with each other. Nevertheless, the cell density shows a continuous increase over time.

Since vital and dead cells cannot be differentiated when using calcein-AM stain, the cell viability was further investigated utilizing a reagent mixture containing NucBlue (staining nuclei of all cells) and propidium iodide (stains only nuclei of dead cells) directly after seeding and after 2 or 6 days of incubation. Images from fluorescence channel (excitation 360 nm/emission 469 nm for NucBlue, excitation 535 nm/emission 617 nm for propidium iodide) were recorded and the fluorescence intensities were analyzed (Figure 4.25A). The cell density within the gel matrix exhibits a progressive increase over time without any significant increase of the number of dead cells. By overlapping images from both fluorescence channels, the total cell numbers and the number of dead cells can be compared (Figure 4.25B). The results show that the interpenetrating network hydrogel used in the printing experiment is cell-friendly and supports cell proliferation and growth post-extrusion.

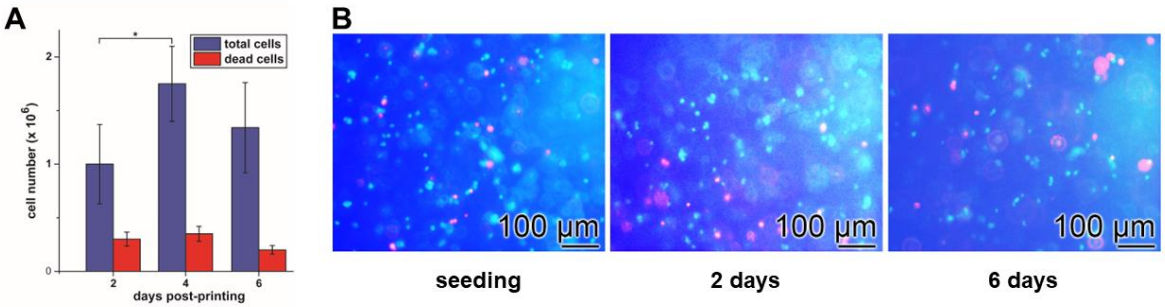

Figure 4.25: Cell viability was evaluated directly after seeding as well as to 2, 4 and 6 days post-extrusion utilizing a reagent mixture containing NucBlue (for staining of all the cells, the cells appear blue) and propidium iodide (for the staining of dead cells, the cells appear red). A) Cell numbers counted 2, 4, and 6 days post-extrusion. The blue columns demonstrate the total cell number, and the red columns show dead cell numbers. B) Fluorescence images of the cells directly after seeding as well as 2 and 6 days post-extrusion, using NucBlue (excitation at 360 nm, emission at 469 nm) and propidium iodide (excitation at 535 nm, emission at 617 nm).

Post-printing form stability of the constructs obtained was examined over several days under wet conditions. Therefore, photos of printed discs were taken directly after seeding and after 1 or 2 days of incubation. It seems that the filaments remain over days with slight dissociation of the hydrogel, which is caused by the dynamic, liquid-like contribution of the physical network. Slight degradation of the bio-ink is desirable, since the bio-ink should not be entirely static, so that the cells are able to move within the hydrogel. Furthermore, the cells should be able to move to the surface of the hydrogel to cover the construct, in order to interconnect with each other and form functional tissues.

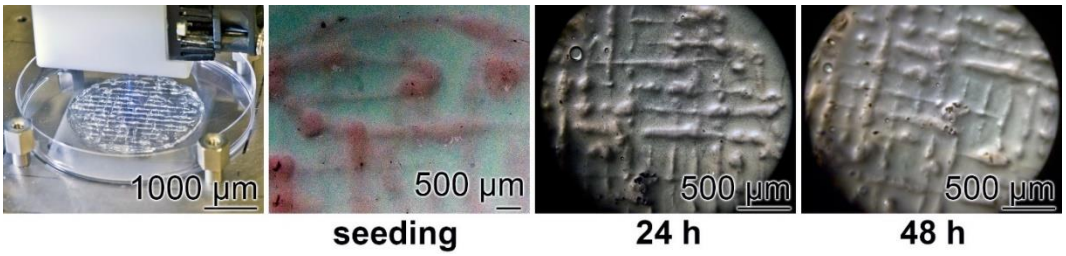

Figure 4.26: Photos of the bio-printed construct directly after seeding as well as 24, 48 hours of incubation at 37 °C in cell culture medium.

Finally, the ability of SaOS-2 cells towards differentiation after the printing process was tested through in vitro mineralization assay (Figure 4.27). To this end, an activation cocktail containing β-glycerophosphate, L-(+)-ascorbic acid and dexamethasone[321] was added to cell culture medium that was used to cover printed discs. By addition of this mixture, the cells were able to differentiate into bone cells and the formation of hydroxyapatite is stimulated. At the same time, a negative control experiment was performed without the activation cocktail. After 2, 4 and 6 days of incubation, staining reagent was added to detect hydroxyapatite particles deposited on the cell surface.[322] The samples incubated with addition of activation cocktail showed fluorescent staining at each time point (lower panel in Figure 4.27), confirming the ability of SaoS-2 cells to differentiate in the given interpenetrating network gel matrix after the printing event.

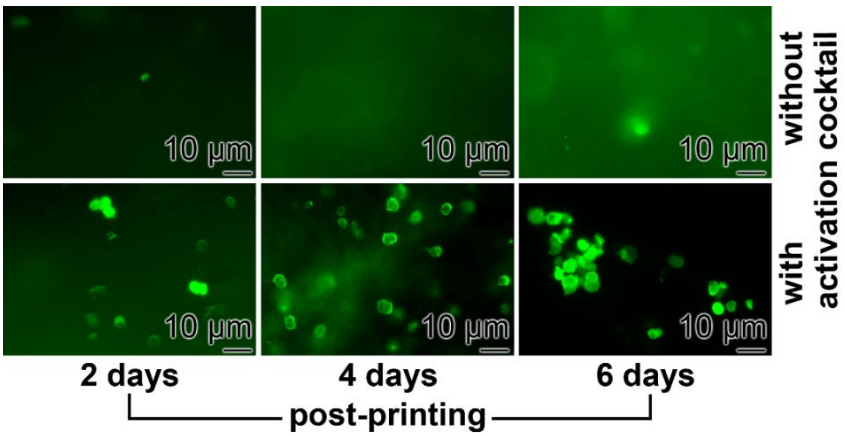

Figure 4.27: The differentiation of the SaoS-2 cells post-printing was assessed using a mineralization assay. Printed discs were cultivated in parallel with and without the activation cocktail. The mineral depositions on the cell surface were stained after 2, 4, and 6 days post-printing. The images were recorded in the fluorescence mode using excitation wavelength of 492 nm and emission wavelength of 520 nm.

4.3 Conclusion

In the past decades, the ability of creating 3-dimensional biologically active constructs has gained increasing interest in the field of biomaterial research. Development of hydrogel materials suitable for the application of 3D-bioprinting remains a challenging task since multifaceted demands in terms of processability and cytocompatibility have to be fulfilled. In this work, a novel interpenetrating network (IPN) hydrogel design with tunable physical and chemical crosslink density is demonstrated that displays complex, dynamic properties.

As network monomers, star-shaped 4arm poly(ethylene glycol) (4arm PEG) has been functionalized with end groups Phe-Gly-Gly tripeptide (FGG) and stilbazolium iodide (SB) through carbonate conjugation chemistry. Both end groups can undergo host-guest complexation with cucurbit[8]uril (CB[8]) in aqueous media. NMR and UV-Vis studies of stilbazolium regarding its photochemical reaction kinetics have yielded compelling insights, revealing the role of CB[8] as a reaction template which can drastically enhance the reaction rate comparing to the case without pre-complexation with CB[8].

The formation of interpenetrating networks is achieved by supramolecular hydrogelation based on CB[8]-mediated host-guest complexation with FGG or SB end groups and subsequent photochemical transformation of the network composed of PEG-SB and CB[8] via templated stilbazolium dimerization event. By using this approach, the mechanical properties of the physical and chemical networks can be successfully combined to create tunable hydrogel materials that are shear-thinning, self-healing, viscoelastic and display post-printing form stability.

Furthermore, the hydrogel constructs exhibit high cytocompatibility and support cellular processes such as proliferation and differentiation. Due to the modular design of those networks, the mechanical properties can be simply adjusted by changing the polymer concentration or the ratio between physical and chemical network densities. It is also possible to incorporate additional recognition motifs to the hydrogel by supramolecular or covalent linkage, leading to materials with complex biological functions, which open up new design opportunities for biomaterial inks.

5 Solute Diffusion in Associative Supramolecular Networks

5.1 Motivation and Concept

Diffusion of solutes in gels play important roles in different technical and biological processes. Understanding of the solute diffusion behavior is therefore essential for the design of smart and biomimetic gel networks.[323] How fast the diffusion process takes place is typically characterized using the diffusion coefficient *D* that measures the mean squared displacement of the solute per time unit, which is affected by the architecture and dynamics of the gel networks as well as the size of the solute molecule.[324,325] Besides, the molecular mobility can be further influenced by association of the solute molecule to the network matrix itself, which is often observed in biological systems.[326]

Fluorescence recovery after photobleaching (FRAP) has been used frequently to assess diffusion behavior of molecules in solutions, gels and complex biological environments. In a typical experiment, fluorescent molecules in the sample within a region of interest (ROI) are bleached using a high intensity laser. The fluorescence then recovers due to the diffusion of unbleached dye molecules into the ROI and reflects solute diffusion behavior.[326]

Herein, the diffusion behavior of dye molecules within a supramolecular associative network of star-shaped 4-arm poly(ethylene glycol) end-functionalized with tripeptide phenylalanine-glycine-glycine (4arm PEG-FGG) and crosslinked through cucurbit[8]uril (CB[8]) host-guest complexation is measured by FRAP on a confocal laser scanning microscope (CLSM). For the comparison of size-controlled diffusivities, a small molecule dye sulfo-cyanine3 (Cy3) and a protein mCitrine are used as free diffusing, fluorescent species. In addition, both dye molecules are functionalized with the associative FGG motif to investigate the influence of association and dissociation kinetics on molecular diffusion (Figure 5.1).

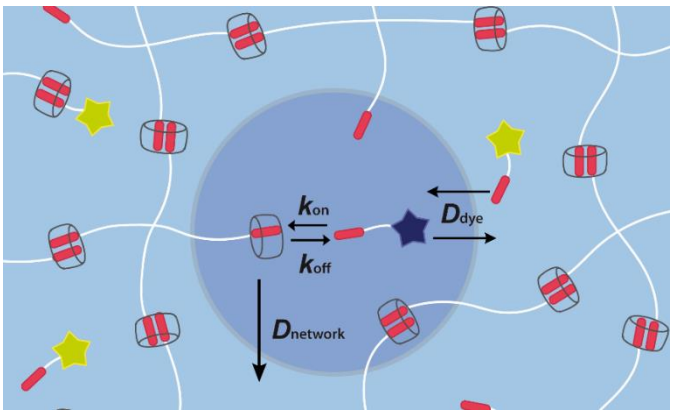

Figure 5.1: Schematic representation of the FRAP experiment in a hydrogel consisting of CB[8] crosslinked 4arm PEG-FGG and dye molecules attached to FGG tripeptide. The recovery of the fluorescence within the ROI (circle in dark blue) is driven by diffusion of the fluorescent dyes and the association kinetic of the host-guest complexes.

5.2 Results and Discussion

5.2.1 Dye Functionalization with Associative Motif

In order to investigate solute diffusion through fluorescence recovery after photobleaching (FRAP) experiments, different dye molecules were prepared. The small molecule dye carrying the associative FGG tripeptide was synthesized in an amidation of sulfo-cyanine3 *N*-hydroxysuccinimide ester (Cy3 NHS ester) with **III-5** using DIPEA as a base (Figure 5.2). The product **III-12** was obtained with 25% yield after purification via semi-preparative HPLC. In a subsequent reaction, a Fmoc deprotection of the peptide was carried out using a 20v% piperidine solution in DMF, giving peptide conjugated Cy3 (Cy3-FGG, **III-13**) with quantitative yield after purification via semi-preparative HPLC. Through the tripeptide FGG, the dye molecule **III-13** is able to bind CB[8] through host-guest complexation.

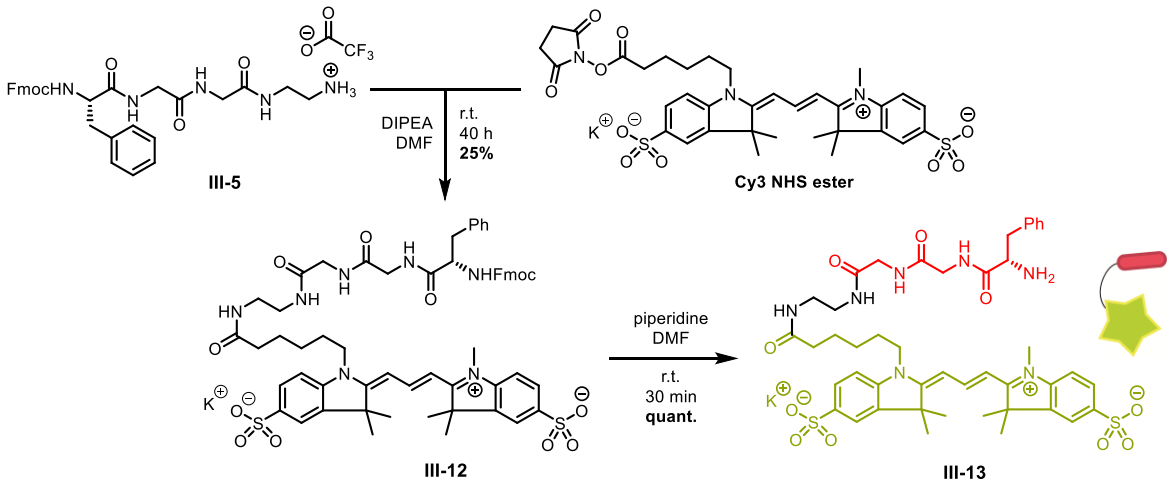

Figure 5.2: Synthesis of FGG functionalized sulfo-cyanine3 **III-13**.

As free diffusing small molecule dye, a commercially available sulfo-cyanine3 azide (Cy3-N_3) was used. Yellow fluorescent proteins mCitrine carrying either non-associating MGG or associative FGG tripeptide on the *N*-terminus (mCitrine-MGG and mCitrine-FGG) were obtained by protein expression following literature known procedures[327] in collaboration from the Institute of Molecular Biology (IMB) Mainz. The proteins were concentrated to 400 µM solutions in an aqueous buffer containing 20 mM Hepes-NaOH (pH = 7.4), 150 mm sodium chloride, 1 mM tris(2-carboxyethyl)phosphine and 10% glycerol. As shown in Figure 5.3, the fluorescent protein mCitrine-FGG is able to undergo host-guest complexation with CB[8] through the tripeptide FGG on the *N*-terminus to be involved in the associative network, while the other protein mCitrine-MGG cannot bind CB[8] and functions therefore as a free diffusing protein.

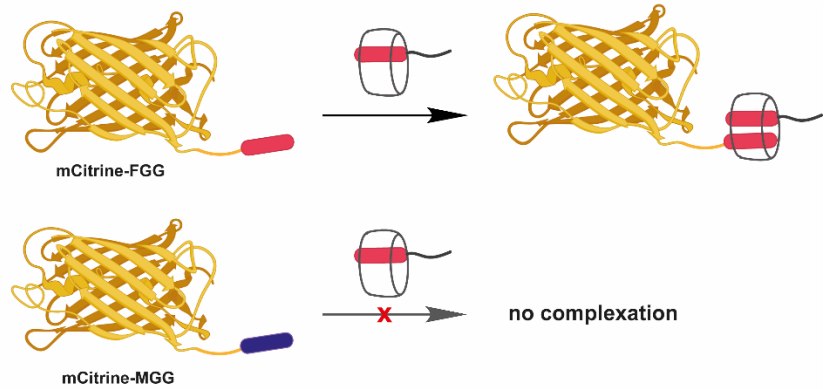

Figure 5.3: The fluorescent protein mCitrine-FGG is able to undergo host-guest complexation with CB[8] through the tripeptide FGG on the *N*-terminus, while the other protein mCitrine-MGG cannot bind CB[8].

5.2.2 Effect of Sample Preparation

Using a library of dye molecules (Cy3-N_3, Cy3-FGG, mCitrine-MGG and mCitrine-FGG), 3.5 wt% hydrogels consisting of CB[8] crosslinked 4arm PEG-FGG (**III-2**) and 0.5 μM of small molecule dye or 5 μM fluorescent protein were formed. Therefore, stock solutions of the polymer and small molecule dyes were prepared, including a 35 mg mL^{-1} 4arm PEG-FGG solution in water, 5 mg mL^{-1} Cy3-N_3 solution in DMSO and a 0.2 mg mL^{-1} Cy3-FGG solution in DMSO. The protein solutions were used as obtained. The concentrations of dye molecules within the samples were chosen for the optimal fluorescence intensity of the images and are below 0.1% molar fraction with respect to the polymer end groups, so that the effect of dye molecules carrying the associative FGG motif to the network association is negligible.

Due to poor solubility of CB[8] in water, preparation of hydrogels with homogeneous dye distribution was challenging for the cases, when a dye attached to a FGG motif was used. Since the stock solutions of the small molecule dyes were both prepared in dimethyl sulfoxide (DMSO) that affects the formation of host-guest complexes between CB[8] and FGG tripeptide, the solvent had to be removed before gelation. In the first method (method **a**), the dye was lyophilized and mixed with the stock solution of 4arm PEG-FGG (35 g L^{-1} in water) to form a homogeneous mixture. By addition of CB[8] as a solid, the hydrogel was formed after shaking at 37 °C over night. In the second method (method **b**), dye (as stock solution in DMSO) and the same polymer stock solution were mixed with CB[8]. After lyophilization, the solid mixture is redissolved in water. It was observed that the gelation was much faster using method **b**. For both procedures, the excess of CB[8] that remained undissolved over night was removed by centrifugation before transferring the hydrogels to microscopy slides.

In Figure 5.4, confocal microscopy images of samples containing either Cy3-N_3 or Cy3-FGG are shown. Images A and D were recorded from the sample containing Cy3-N_3 prepared following method **a**. In this case, a homogeneous distribution of the dye molecule throughout the entire sample was achieved. In the contrary, the images of samples containing Cy3-FGG (B, C, E, F) show less homogeneous samples with spots of higher fluorescence intensity than their surrounding. This can be explained by the poor solubility of CB[8] in water and therefore its tendency to form larger particles in the hydrogel network. When the dye molecule is decorated with the FGG tripeptide, it can also bind to CB[8] through host-guest complexation, forming bright spots with high local fluorescence intensity. While the images B and E are assigned to a sample prepared using method **a**, image C and F belong to the sample prepared using method **b**. By comparing image E and F, it seems that pre-mixing of all component in a water-DMSO solvent mixture promotes the formation of CB[8] particles that are stabilized within the hydrogel network, that are not able to be removed by simple centrifugation. The presence of those fluorescent spots can falsify the results of FRAP experiments, since the CB[8] particles are also able to diffuse through the probe and strongly influence the fluorescence intensity within the region of interest (ROI).

Therefore, the preparation method **a** was chosen for the preparation protocol and used for the subsequent experiments.

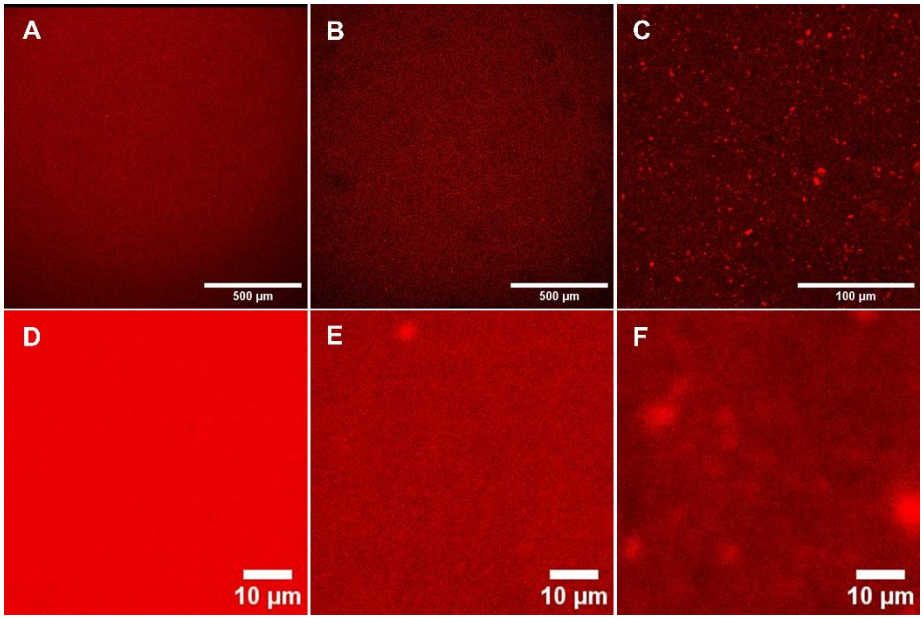

Figure 5.4: Confocal microscopy images of hydrogel samples containing small molecule dyes Cy3-N_3 (A, D) and Cy3-FGG using the method **a** (B, E) or method **b** (C, F).

In case of the samples with fluorescent proteins, the proteins mCitrine-MGG and mCitrine-FGG were added as 400 µM aqueous stock solutions to the polymer solution to form a homogeneous mixture. After addition of CB[8] in a ratio of 1:2 with respect to the polymer end groups, the samples were shaken 40 hours at 37 °C to equilibrate. The samples were again centrifuged to remove excess of CB[8] solid particles. The fluorescent images of both samples in Figure 5.5 show similar homogeneous distribution of the dye proteins.

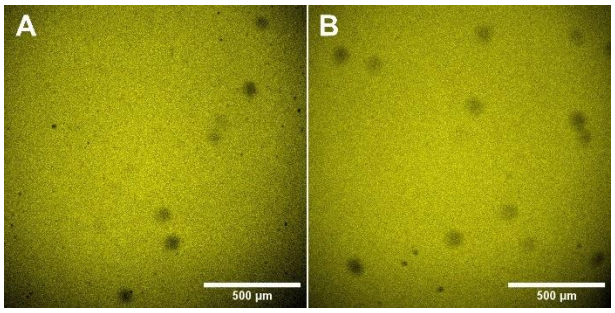

Figure 5.5: Fluorescent images of samples including fluorescent proteins mCitrine-MGG (A) and mCitrine-FGG (B).

5.2.3 Qualitative Observation of Diffusive Behavior

In order to study the effect of size and association kinetics on the solute diffusion behavior, FRAP experiments were conducted on a confocal laser scanning microscope using the point-bleaching method. In this case, an objective lens with low z-resolution was chosen to generate a cylindrical bleach area rather than a plane. With this, the diffusion from z-direction is avoided and a two-dimensional diffusion process is expected. The size of ROI is considered so small, that the concentration of fluorescent dyes throughout the entire sample is assumed to remain constant after the bleaching process. As shown in Figure 5.6, bleaching with high intensity laser results in a local decrease of the fluorescence intensity within the ROI (comparison of the pre-bleach image A and post-bleach image B). Directly after the bleaching event (t = 0 s), the image shows the lowest total fluorescence intensity. Over time, bleached fluorophores can diffuse out of the ROI, while unbleached fluorescent dyes can diffuse into the bleached area leading to recovery of the initial fluorescence intensity (image C and D).

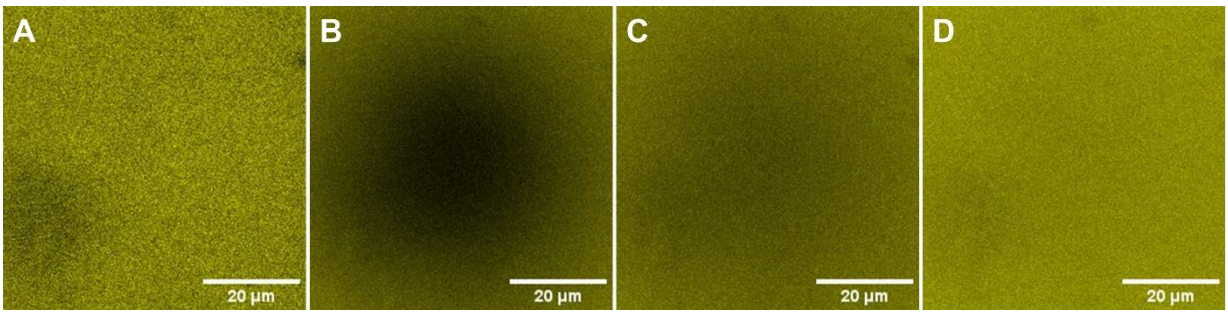

Figure 5.6: Confocal pre- and post-bleach images of the hydrogel sample containing mCitrine-MGG from a FRAP experiment using a point bleach method with a ROI size of 20 µm diameter: A) pre-bleach image; B) 0 s post-bleach image; C) 10 s post-bleach image; D) 50 s post-bleach image.

Notably, the bleaching process does not create a bleached area with a sharply defined geometry, instead, the fluorescence intensity exhibits a smooth gradient, which has two reasons. First, it is impossible to create a bleach area in the shape of a plane with clear boundary due to the spatial extension of the laser beam. Second, the bleaching process is not done instantaneously, so that the diffusion of molecules can already take place during the bleaching event, which leads to a broader distribution of the fluorescence intensity. The second effect is even stronger for fast diffusing species, which leads to large deviation of the bleached area from the theoretical ROI. It should also be noted that effective bleaching takes longer time for larger theoretical ROIs.[326]

For direct comparison, each of the samples was bleached with an initial ROI of 20 µm in diameter for 300 frames (0.261 s per frame) and the sample area was then scanned with a speed of 1 frame per second. Since the amounts of dye in the samples were different, the brightness of the images were normalized based on the average brightness of the corresponding pre-bleach images, which was recorded 10 times before bleaching. The recovery curves are shown in Figure 5.7A. Samples containing small molecule dyes (in pink) demonstrate rapid recovery of fluorescence intensity. As expected, the initial normalized

brightness of the image for the sample containing Cy3-N_3 (pink dashed line) is only around 83% due to fast diffusion of the dye molecules, so that the bleached fluorophores within the ROI can be immediately replaced. The recovery of the fluorescence intensity was fully completed after 2 s. In case of the sample containing Cy3-FGG (pink solid line), the initial normalized brightness is around 72%, about 10% lower than the first sample. The recovery is slightly slower than in the first case, indicating that the association of Cy3-FGG to CB[8] slows down the diffusion. Apparently, the fluorescence of the sample containing Cy3-FGG doesn't recover back to 100% of the pre-bleach intensity, but only to 90%, implying a strong interaction of dye molecules to immobile binding sites. This part of the dye molecules is also called immobile fraction.[326] The presence of an immobile fraction of around 10% can be explained by Cy3-FGG binding to solid CB[8] particles that are less dynamic. In general, the fluorophore concentration outside of the ROI is estimated as constant during the FRAP experiment, but in reality, it doesn't have to be the case. Since the concentration of Cy3-FGG was not able to be accurately determined, the total concentration of fluorescent species in the sample could be lower than desired, so that the total active fluorophore concentration before and after the bleaching process are not comparable, thus leading to decreased fluorescence intensity. In case of samples containing fluorescent proteins (in green), the initial brightness after bleaching is around 65% for both samples as a result of more effective bleaching. The fluorescence recovery takes place on similar time scale, whereas a plateau value around 100% in only reached after 10 min.

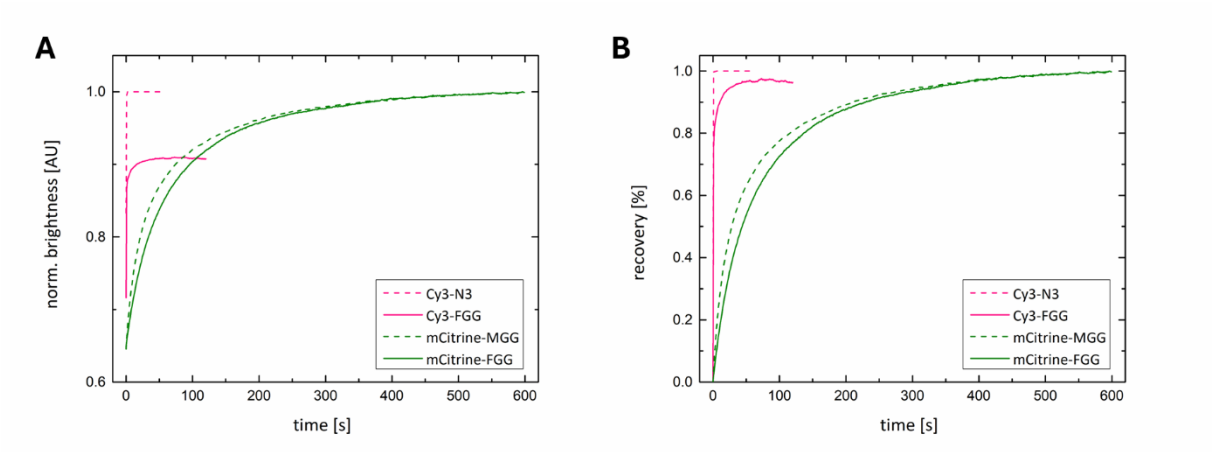

Figure 5.7: Fluorescence recovery curves after photobleaching for samples including different dye species at 20 °C. A) Recovery presented as normalized brightness. B) Recovery presented in percentage.

For better representation, the normalized brightness was calibrated into fluorescence recovery in percentage based on the initial brightness (0%) and the plateau value (100%) to subtract the immobile fraction. The resulting curves are shown in Figure 5.7B. The samples containing fluorescent proteins (in green) show generally much slower fluorescence recovery compared to the samples containing small molecule dyes (in pink). This implies a stronger size-dependency of the diffusion behavior in the current system, though the association of the FGG motif to CB[8] also contributes to a slower diffusion due to binding to CB[8], because the effective size of the solutes changes when it is bound to the polymer

network. The association and dissociation kinetics are rather fast compared to the time scale on which the diffusion of a solute with a significant larger size takes place.

5.2.4 Calculation of Diffusion Coefficients and Quantitative Comparison

To quantitatively evaluate FRAP data, different physical and mathematical solutions have been developed over the past decades. While the fluorescence recovery half-time $\tau_{1/2}$ is easy to calculate, which is defined as the time for 50% recovery of the fluorescence intensity related to the initial intensity as 0% and plateau intensity as 100%[328–330], it is strongly dependent on the geometry and size of the ROI as well as the bleaching duration. It is only suitable for simple comparison within a set of experiments but not over different studies. Since the diffusion coefficient D is an absolute measure to characterize diffusion behavior, it is more meaningful to determine diffusion coefficients from different experiments. One solution has been developed for two-dimensional, pure isotropic diffusion processes with a circular bleaching spot.[331,332] The diffusion coefficient D_r can be calculated from the experimentally defined bleaching radius r_n and the fluorescence recovery half-time $\tau_{1/2}$ as follows:

$$D_r = 0.224 \cdot \frac{r_n^2}{\tau_{1/2}}$$

For samples containing each of the dye species, FRAP experiments were conducted three times at 20 °C with a circular ROI of 20 µm diameter (r_n = 10 µm). The recovery half-times $\tau_{1/2}$ for each experiment were directly extracted from the FRAP recovery curves and the mean value for each sample was determined. In case of the sample containing Cy3-N_3 and Cy3-FGG, more than 80% of the fluorescence intensity was recovered after 1 s, so a linear slope of the recovery curve was estimated between 0 and 1 s to calculate the recovery half-time. The fluorescence recovery half-time $\tau_{1/2}$ and diffusion coefficients D_r obtained from the calculations are listed in Table 5.1. In accordance with the recovery curves discussed in the previous section, the fluorescent proteins exhibit diffusion coefficients about one order of magnitude smaller than the small molecule dyes and the association of the dye molecules through interaction between the FGG tripeptide and CB[8] lowers the diffusivity in addition.

Table 5.1: Fluorescence recovery half-time $\tau_{1/2}$ and diffusion coefficients D_r for different samples from FRAP experiments with a circular ROI of 20 µm diameter at 20 °C.

Dye	$\tau_{1/2}$ [s]	D_r [µm^2 s^{-1}]
Cy3-N_3	0.5	44.80
Cy3-FGG	0.9	23.83
mCitrine-MGG	28.7	0.78
mCitrine-FGG	44.3	0.51

Due to long photobleaching time in the FRAP experiments and diffusion during this period, the size of bleached area may differ from the experimentally defined size of ROI. Especially for fast diffusing species, the actual size of the bleached area can be multiple times larger, leading to underestimation of the diffusion coefficients. In order to take the effect of diffusion during bleaching into account, another simplified equation has been developed to obtain diffusion coefficient D_e by adding the effective radius r_e, which is influenced by both the nominal radius r_n and the bleaching protocol[324]:

$$D_e = \frac{r_n^2 + r_e^2}{8\tau_{1/2}}$$

If the bleaching process takes place instantaneously, $r_e = r_n$ and a diffusion coefficient similar to the previous method can be obtained:

$$D_e = 0.25 \cdot \frac{r_n^2}{\tau_{1/2}} \approx D_r$$

For simplicity, the post-bleaching profile can be described using a Gaussian function and the effective radius of bleached area can be calculated from the standard deviation of the Gaussian profile as $r_e = 2\sigma$. For the sample containing Cy3-FGG as solute dye, FRAP experiments were carried out with varying sizes of ROI (d_{ROI} = 20, 30, 50 and 100 μm) and 50 s bleaching time. The first post-bleach image of each measurement was fitted using a 2D Gaussian function giving two standard deviations σ_x and σ_y. The effective radius r_e was calculated as:

$$r_e = 2\sqrt{\frac{\sigma_x^2 + \sigma_y^2}{2}}$$

The resulting values for effective radius r_e and the nominal radius r_n as well as the ratio of both r_e/r_n are summarized in Table 5.2. Noticeably, the effective radius after the bleaching process is much larger than nominal radius set up for the experiments. Using the same sample with fast diffusing solute dye, the deviation of the actual ROI size increases with increasing nominal size of the bleaching spot. The diffusion might be therefore strongly underestimated when assuming an instantaneous bleaching process. On the other hand, the accuracy of the r_e determination might be lower for larger nominal ROI, since the effective ROI could be larger than the recorded confocal images.

Table 5.2: Diameter d_{ROI} and radius r_n of the experimentally defined ROI as well as the effective radius r_e of ROI calculated from the fluorescence intensity profile after 50 s photobleaching.

d_{ROI} [µm]	r_n [µm]	r_e [µm]	r_e/r_n
20	10	24.56	2.45
30	15	40.08	2.67
50	25	48.42	1.94
100	50	169.24	3.38

Concurrently, the diffusion from the z-dimension should not be ignored, since it can also affect the fluorescence intensity within the ROI. Especially for large ROI sizes, the recovery through diffusion of fluorophores from z-direction can be faster than the one within the confocal plane, leading to a much faster recovery of the fluorescence intensity. For the samples containing Cy3-FGG, mCitrine-MGG and mCitrine-FGG, the first post-bleach image after 300 frames of bleaching (d_{ROI} = 20 µm) was fitted using a 2D Gaussian function to calculate the effective radius r_e and the diffusion coefficient D_e. In case of Cy3-N_3 as solute dye, the diffusion process is too fast, and it is not possible to fit the first image using the 2D Gaussian function. As shown in Table 5.3, the deviation of the effective radius r_e from the experimentally defined radius r_n after the same bleaching duration is larger for fast diffusing species. For the sample containing Cy3-FGG, the effective radius is even almost 15 times larger than the nominal radius. In comparison to direct calculation using the recovery half-time $\tau_{1/2}$ and the nominal radius r_n, inclusion of the effective radius r_e yields diffusion coefficients D_e around one order of magnitude higher than D_r for each dye species.

Table 5.3: Fluorescence recovery half-time $\tau_{1/2}$, nominal radius r_n and effective radius r_e of the ROI and the diffusion coefficient D_e measured for different samples through FRAP experiments at 20 °C.

Dye	$\tau_{1/2}$ [s]	r_n [µm]	r_e [µm]	D_e [µm^2 s^{-1}]
Cy3-FGG	24.0	10	148.26	115.01
mCitrine-MGG	28.7	10	45.72	9.54
mCitrine-FGG	44.3	10	35.49	3.83

Alternatively, each of the post-bleach images can be individually fitted using an inverted Gaussian function. For the one-dimensional case, the intensity profile I of the ROI can be described as a function of the coordinate x and the time t [333,334]:

$$I(x,t) = I_0 - \frac{M}{2(\pi D_t t)^{1/2}} \cdot \exp\left(\frac{-x^2}{4D_t t}\right) = I_0 - A(t) \cdot \exp\left(\frac{-x^2}{2\sigma^2}\right)$$

Herein, I_0 represents the constant background fluorescence intensity for unbleached area. D_t stands for the translational diffusion coefficient and M is defined as the amount of diffusing species per length. By adjusting the equation, the fluorescence intensity $I(x,t)$ can be described by an amplitude $A(t)$ and the standard deviation σ of the Gaussian profile. For the sample containing mCitrine-FGG, the fluorescence intensity profiles were extracted from the post-bleach images and fitted using the 1D Gaussian function (1, 5 and 15 s post-bleaching profiles are shown as examples in Figure 5.8). With increasing time, the amplitude of the curves decreases, while the Gaussian distribution becomes broader, which is shown by the increasing standard deviation σ from 19.67 to 21.01 to 29.90 µm.

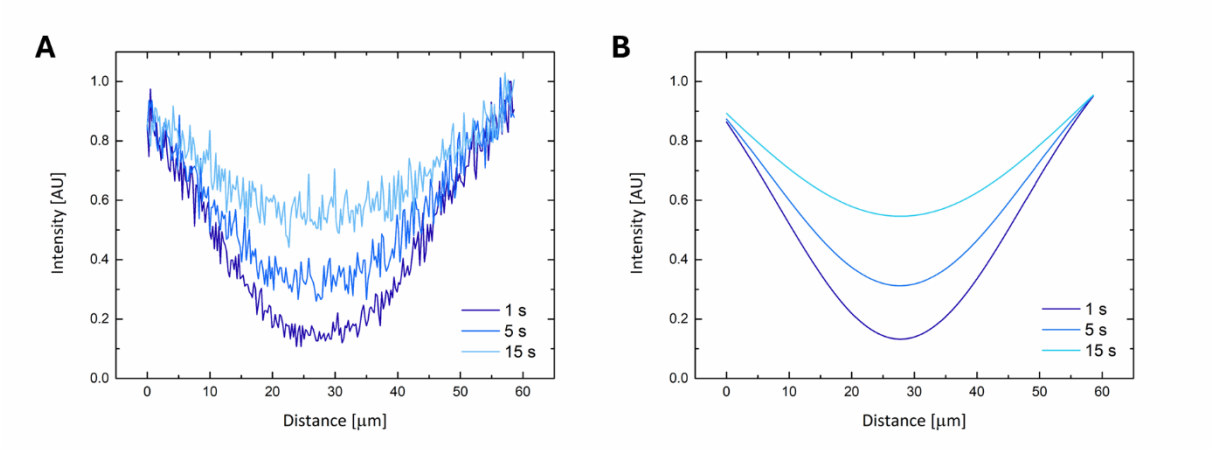

Figure 5.8: Fluorescence intensity profiles (A) and corresponding gauss fit curves (B) from different post-bleaching images (1, 5, and 15 s post-bleaching) of the sample containing mCitrine-FGG.

By plotting σ^2 against time t, a function describing the mean squared displacement of the diffusing species per time unit (Einstein-Smoluchowski equation) can be obtained. This equation also includes the dimensionality d of the diffusion process and an additional scaling exponent α.

$$\sigma^2 = 2dD_t t^{\alpha}$$

When the solute display normal or Fickian diffusion behavior through Brownian motion, a linear scaling of σ^2 against time t can be observed ($\alpha = 1$). There are two cases for anomalous diffusion: subdiffusion ($\alpha < 1$) that is observed when particle displacement is hindered, and superdiffusion ($\alpha > 1$) which occurs when an active transport takes place and the particle motion is faster than expected.[227]

Though the 1D Gaussian plot works well for the post-bleach images of samples containing fluorescent proteins, the fit is rather challenging for the samples with Cy3-FGG, since the actual size of ROI might be much larger than the image itself. In addition, due to presence of solid CB[8] particles that form favored binding spots for Cy3-FGG, the post-bleach images display low signal-to-noise ratios. As shown in Figure 5.9A, the first post-bleach image exhibits a dark spot due to photobleaching. When a line profile is extracted through the horizontal yellow line, the data point demonstrate strong noise compared

to the signal itself. With increasing time, the signal-to-noise ratio decreases due to recovery of the fluorescence intensity, which complicates the precise data fitting using a 1D Gaussian function.

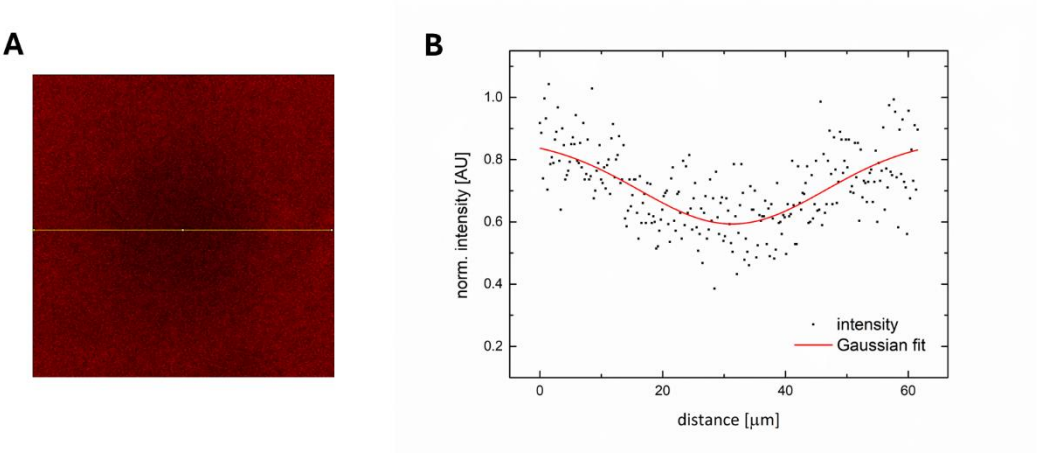

Figure 5.9: Post-bleach fluorescence image of the sample containing Cy3-FGG (A) and the corresponding Gaussian fit (B).

For higher accuracy of the results, the data were fitted using a 2D Gaussian function, giving two standard deviations σ_x and σ_y, from which σ^2 was calculated:

$$\sigma^2 = \frac{\sigma_x^2 + \sigma_y^2}{2}$$

By plotting σ^2 obtained against time t, curves presenting the mean squared displacement per time unit are obtained (Figure 5.10A and B). Surprisingly, all dye molecules show anomalous diffusion ($\alpha \neq 1$). While Cy3-FGG exhibits superdiffusion ($\alpha > 1$), the fluorescent proteins both demonstrate subdiffusive behavior ($\alpha < 1$). In case of Cy3-FGG, the super-diffusion can be a result of the fast interconversion between two different states (free diffusion or association to the network) with different diffusivities.[227] It is possible, that diffusion is not spatially uniform in the presence of association dynamics, leading to acceleration of the diffusion process similar to active transport in cellular events. In contrast, the subdiffusion of the fluorescent proteins is attributed to molecular crowding due to larger molecular size of the proteins than the mash size of the network. As a result, the proteins are not able to freely diffuse through the gel medium. When the fluorescent protein is decorated with the FGG binding motif on the *N*-terminus, an additional deceleration effect is caused by association of the fluorescent proteins to CB[8].

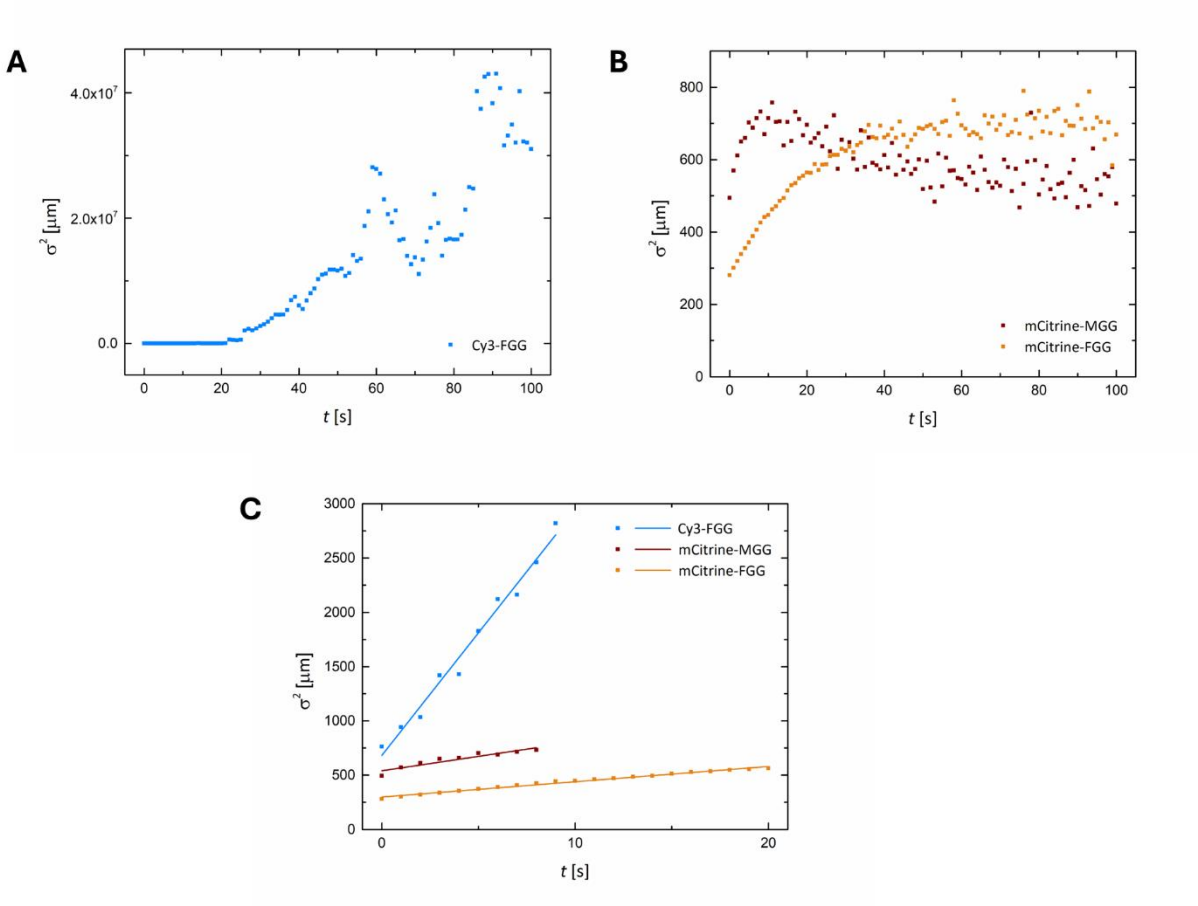

Figure 5.10: Plots of squared standard deviation σ^2 against time t for the sample containing Cy3-FGG (A) or mCitrine-MGG and mCitrine-FGG (B) as well as plots of the linear section of the diffusion curves (C).

The initial linear regime of the curves were used to calculate the diffusion coefficient D_t from the slope b with $D_t = b/2$ (Figure 5.10C). Since each experiment was carried out three times, the mean values and standard deviations of D_t were determined. The results obtained are summarized in Table 5.4 in comparison to the previously calculated D_r and D_e.

Table 5.4: Diffusion coefficients D_r, D_e and D_t for different dye species at 20 °C.

Dye	D_r [µm² s⁻¹]	D_e [µm² s⁻¹]	D_t [µm² s⁻¹]
Cy3-N_3	44.80	-	-
Cy3-FGG	23.83	115.01	$(4.21 \pm 2.24) \cdot 10^5$
mCitrine-MGG	0.78	9.54	17.28 ± 7.46
mCitrine-FGG	0.51	3.83	7.92 ± 2.23

Using this method, diffusion coefficients D_t within the same range as D_e are obtained for the fluorescent proteins. Unexpectedly, the diffusion coefficient D_t for Cy3-FGG is around factor 1000 higher than previously determined, which is too high for diffusion in solution or gel systems. Evidently, the last

methods suffers from difficulties in correctly fitting the 2D Gaussian distribution, which might also be the reason for unexpected decrease of σ^2 for mCitrine-MGG in Figure 5.10B (recovery time < 20 s). Due to the diffusion process, the boundary in terms of fluorescence intensity between ROI and the surrounding gel medium becomes less sharp, so that it becomes more difficult to fit the Gaussian profile. Moreover, recording of the post-bleach images can cause additional photobleaching within the entire area of the image. This can be possibly optimized through adjustment of the image size with respect to the ROI, in order to achieve a clearer definition of the unbleached background intensity over time. For fast diffusion processes, a higher initial frame rate can be used to better track the diffusion directly after the bleaching event, whereas the frame rate can be reduced for longer time scales to reduce photo damage of the samples.

5.3 Conclusion

Understanding of diffusion processes is crucial for designing smart and functional (bio-)materials. Fluorescence recovery after photobleaching (FRAP) has been frequently used as a method to gain insights into the dynamics of the diffusing species in materials and in biological systems, revealing size- and reaction-dependent diffusion behavior.

In the present study, the diffusion of small molecule dyes and fluorescent proteins were investigated in a supramolecular gel network that is crosslinked by cucurbit[8]uril host-guest complexes. By functionalizing the dye species with the associative FGG tripeptide, they are able to bind to the network through the same supramolecular complexation. Results from FRAP measurements of samples including different dye species were evaluated to show that the size-dependency is the more dominant factor in the present network compared to the host-guest complexation kinetics. By plotting intensity data of post-bleach images using 2D Gaussian functions, insights into the mean squared displacement per time unit and thus the type of diffusion were revealed for different dye species. While fluorescent proteins undergo subdiffusion due to molecular crowding within the hydrogel networks, the small molecule dye carrying an associative motif displays superdiffusive behavior caused by association and dissociation dynamics.

In case of fast diffusing species, it has been challenging to measure the diffusion within the time scale accessible by the experiment. Therefore, the bleaching and scanning protocol require optimization. Alternatively, the diffusion of small molecule through the hydrogels can be studied using other dye molecules that can be bleached more effectively than Cy3. To further understand the dynamics of associative networks crosslinked through host-guest complexation, diffusion of the polymers (self-diffusion, tracer diffusion and multivalent binding) can be investigated using 4arm-PEG with both FGG functionalization and dye-labeling.

Since the deviation of the results from different calculation methods are large in some cases, FRAP experiments can be carried out using various ROI shapes, so that the fluorescence intensity can be evaluated according to different mathematical models. Hence, the usage of complementary techniques such as fluorescence correlation spectroscopy (FCS), single-particle tracking (SPT) or forced Rayleigh scattering (FRS) can also help to verify the results from FRAP experiments.

6 Summary

Along with various advancements within synthetic and supramolecular chemistry over the past decades, numerous synthetic, functional materials with biological and biochemical relevance have been developed. Compared to biotechnological isolation processes of biological recognition motifs, the usage of synthetic bottom-up approaches provide access to building blocks that are structurally more defined. Using reversible, non-covalent interactions, formation of dynamic and complex self-assembling systems carrying biologically active motifs can be achieved and tailored for the desired application.

In the first part of the thesis (chapter 3), synthetic methods to produce carbohydrate epitopes for the usage in supramolecular antibacterial vaccines against *S. pneumoniae* were developed. Based on the knowledge of cellobiuronic acid being the smallest antigen unit of serotype 3 *S. pneumoniae* bacteria, synthetic routes to obtain serotype 3 antigens with different lengths and terminal units were designed. The synthesis started with the disaccharide cellobiose and underwent several steps for the conversion into thioglycosides and orthogonal protection of the free hydroxyl groups, leading to glycosyl donors (**I-5** and **I-6**) that were conjugated to an amine-carrying spacer component **I-4** through chemical glycosylation. Due to orthogonal protecting groups installed on position 6 and 6', subsequent selective deprotection and oxidation were performed on one of the primary hydroxyl groups to obtain antigens GlcA-β-(1→4)-Glc (**I-25**) and Glc-β-(1→4)-GlcA (**I-30**) that can be attached to the supramolecular vaccine carrier[38] through the free amine group. Since the cellobiuronic acid monomers in the bacterial polysaccharide capsule are connected through 1,3'-β glycosidic linkages, methods for site-selective functionalization of position O-3' were required. By exploiting steric and electronic effects as well as usage of bulky or chiral reagents and catalysts, different methods for site-selective O-3' protection of cellobiose were successfully developed to prepare monomer building blocks for the synthesis of cellobiuronic acid oligomers, which can be achieved through glycosylations in solution or automated solid-phase carbohydrate synthesis. Using antigens with different lengths and terminal units, the relationship between antigen structure and supramolecular vaccine efficacy can be further studied.

In the second part of the thesis, supramolecular hydrogels crosslinked through cucurbit[8]uril (CB[8]) host-guest complexation were formed and studied in terms of their mechanical properties and their application in 3D-bioprinting (chapter 4). Star-shaped poly(ethylene glycol) (PEG) was decorated with stilbazolium groups (SB) or tripeptide phenylalanine-glycine-glycine (FGG) to obtain network macromers PEG-SB (**III-1**) and PEG-FGG (**III-2**), which can both undergo host-guest complexation with CB[8] individually to form three-dimensional physical hydrogel networks. The mechanical properties of the hydrogels were studied via rheology, showing networks exhibiting fast stress relaxation and shear thinning as well as self-healing behavior. Upon irradiation with UV light, the network based on **III-1** can be rapidly transformed into a chemical network due to fast dimerization of stilbazolium. According to the UV-Vis and NMR measurements, the stilbazolium dimerization can be drastically

accelerated through the pre-rearrangement within the CB[8] cavity. By combining the physical PEG-FGG and chemical PEG-SB single networks, interpenetrating network (IPN) hydrogels were formed that showed improved form stability while the viscoelastic features of the physical network were maintained. Within cell culture and bioprinting experiments using SaOS-2 cell line, cytocompatibility, bioprintability as well as post-printing stability of the IPN hydrogels were assessed, showing excellent viability of the cells before and after the printing process.

Furthermore, solute diffusion within the associative networks composed of PEG-FGG and CB[8] was investigated through fluorescence recovery after photobleaching (FRAP) experiments (chapter 5). Therefore, small molecule dyes (Cy3 and Cy3-FGG) and fluorescent proteins (mCitrine-MGG and mCitrine-FGG) were each incorporated into the hydrogel network to study their individual diffusion behavior. While the size dependency was studied by comparing the non-associating small molecule dye Cy3 and fluorescent protein mCitrine-MGG, the decoration of both dye species with the CB[8] binding motif FGG tripeptide provided insight into the impact of binding kinetics on the diffusion process. Using different mathematical models, diffusion coefficients of each dye species were obtained quantitatively, showing that the size of the solute molecule had a higher impact (at least one order of magnitude) on the diffusion behavior in the present system, whereas the binding of solute molecules to the associative network through host-guest complexation also contributed to a slower diffusion (with a factor of 2 to 3).

In conclusion, different building blocks for supramolecular vaccines and biomaterial inks were designed and successfully synthesized. While a primary focus of the supramolecular vaccine project was on the synthesis of desired carbohydrate epitopes, the supramolecular hydrogels crosslinked through CB[8] host-guest complexation were also studied in terms of their cytocompatibility, bioprintability and solute diffusion behavior. Overall, the findings provide synthetic methods and functional material designs that open up possibilities for future biomedical applications.

7 Experimental Section

7.1 Materials

Chemicals and (anhydrous) solvents were obtained from commercial sources and used without further purification. All reactions were conducted in oven dried laboratory glass ware. Reaction conditions such as vacuum and argon atmosphere were achieved by the usage of a Schlenk line. Water used for reactions, sample preparation and high performance liquid chromatography was purified utilizing a *Veolia PURELAB flex 4* (Paris, France) water purification system. Acetonitrile for high performance liquid chromatography was purchased commercially in HPLC grade. Column chromatography was carried out using silica gel with a particle size of 35–70 µm and a pore size 60 Å by *Acros Organics* (New Hersey, USA). *Spectra/por* biotech cellulose ester dialysis membranes (VWR, diameter = 20 mm, MWCO = 0.1 – 0.5 kDa) were purchased from VWR and used as received.

For cell culture, McCoy's medium and fetal calf serum (FCS) were purchased from *Biochrom-Seromed* (Berlin, Germany) and calcein-AM solution (Sigma-Aldrich) was used as staining reagent for cell viability evaluations.

Fluorescence dyes sulfo-Cyanine3 azide and sulfo-Cyanine3 NHS ester for confocal microscopy were purchased from *Lumiprobe GmbH* (Hannover, Germany).

7.2 Instrumentation

7.2.1 Solid phase peptide synthesis (SPPS)

Solid phase peptide synthesis was performed on a *CS136XT Peptide Synthesizer* by *CS Bio Co.* (Menlo Park, USA) following a modified version of the standard Fmoc-protocol reported by *Atherton* and *Sheppard*.[335] Peptide grade solvents and reagents were used. 2-chlorotrityl chloride resin was chosen for Fmoc-protected amino acid loading.

7.2.2 Thin layer chromatography (TLC)

For thin layer chromatography, *ALUGRAM® Xtra SIL G UV$_{254}$ plates* with fluorescence indicator by *Macherey-Nagel* (Düren, Germany) were used. The compounds were detected using the following methods:

- UV-absorption at λ= 254 nm.
- Sugar staining reagent: A mixture of 50 mL ethanol with 2.7 mL conc. H_2SO_4 and 50 mL ethanol with 0.1 mL *m*-methoxyphenol. Upon heating, the spots turn orange/red/brown.

- Vanilin staining reagent: A solution of 3 g vanillin in 100 mL ethanol with 0.5 mL H_2SO_4. The spots turn brown upon heating.
- Seebach staining reagent: A solution of 0.5 g $Ce(NH_4)_2(NO_3)_6$ and 24.0 g $(NH_4)_6Mo_7O_{24}\cdot 4H_2O$ with 28 mL conc. H_2SO_4. The spots turn into dark blue colors upon heating.
- Potassium permanganate staining reagent: 0.75 g $KMnO_4$ and 2.50 g $NaHCO_3$ in 200 mL H_2O. The spots appear dark brown.

7.2.3 Flash chromatography

Preparative chromotographic purification was performed on a *Sepacore® Easy Purification System* by *Büchi* (Flawil, Switzerland) equipped with a *UV-Photometer C-640* and a *Büchi Fraction Collector C-660* was used. The silica gel utilized for normal phase separation was obtained from *Acros Organics* (Geel, Belgium) and had an average particle size of 35-70 µm and a. pore size of 60 Å. For reversed phase purification, a prepacked CHROMABOND® Flash RS 40 C18 column from *Macherey-Nagel* (Düren, Germany) was used.

7.2.4 High performance liquid chromatography (HPLC)

Analytical and semi-preparative HPLC was carried out on a *JASCO LC-400* (Tokyo, Japan) system consisting of a binary pump, an in-line degasser, mixer, an AS-4050 HPLC autosampler, a MD-4015 PDA detector and an *Advantec MFC Inc. CHF122SC* (Dublin, USA) fraction collector. Signals were detected at wavelengths of 210 nm, 254 nm, 400 nm and 550 nm depending on the compound. The software *ChromNAV* was used for method controlling and data analysis.

Analytical HPLC was conducted using the following columns with a flow rate of 1.5 mL/min:

- Luna C18 (2), 250 mm × 4.6 mm, 5 µm, 100 Å, *Phenomenex* (Torrence, USA)
- Chromolith RP-C18e, 100 mm × 4.6 mm, 150 Å, *Merck KGaA* (Darmstadt, Germany)
- Nucleodur C18 Pyramid, 50 mm × 4.6 mm, 1.8 µm, 110 Å, *Mancherey-Nagel* (Düren, Germany)

Semi-preparative HPLC was carried out on the following columns with a flow rate of 18.9 mL/min:

- Luna C18 (2), 250 mm × 21.2 mm, 10 µm, 100 Å, *Phenomenex* (Torrence, USA)
- Nucleodur C18 Pyramid, 250 mm × 21.2 mm, 5 µm, 110 Å, *Mancherey-Nagel* (Düren, Germany)

7.2.5 NMR spectroscopy

NMR Spectroscopy was performed on the following spectrometers by Brucker (Rheinstätten, Germany):

- Bruker Avance III HD 300 (300 MHz ^{1}H-NMR, 75 MHz ^{13}C-NMR)
- Bruker Avance II 400 (400 MHz ^{1}H-NMR, 101 MHz ^{13}C-NMR)
- Bruker Avance III HD 400 (400 MHz ^{1}H-NMR, 101 MHz ^{13}C-NMR)
- Bruker Avance III 600 (600 MHz ^{1}H-NMR, 151 MHz ^{13}C-NMR)

All samples were prepared by dissolving the compound in deuterated solvents from *Deutero* (Kastellaun, Germany) for the measurements. The spectra recorded were evaluated using *MestReNova 14.1.0* by *Mestrelab Research S.L.* (Santiago de Compostela, Spain). The chemical shifts (δ) are given in ppm relating to the solvent signal and the coupling constants (J) were measured in Hz. The signal multiplicity are given as follows: s (singlet), d (doublet), t (triplet), dd (doublet of doublet), m (multiplet).

The anomeric ratios of the oligosaccharide compounds were calculated using the integrals in the ^{1}H-NMR-spectra.

7.2.6 Mass spectrometry

Mass spectra were recorded on an *Agilent 6545 Q-Tof-MS9* (Santa Clara, US) high resolution mass spectrometer through electron spray ionization (ESI) and on an *Autoflex maX MALDI-TOF/TOF* from *Bruker* (Bremen, Germany) mass spectrometer using matrix-assisted laser desorption/ionization (MALDI).

7.2.7 Optical rotation

The optical rotation of chiral compounds were determined using either a *Perkin-Elmer* 241 apparatus (Waltham, Massachusetts, USA) or a Polarimeter MCP by *Anton Paar* (Graz, Austria) at room temperature (20 °C). The cuvettes were either 10 cm long with a inner volume of 1 mL or 10 mm long with a volume of 0.2 mL. The samples were prepared in chloroform or methanol with a concentration of c = 1 g/100 mL. All the measurements were conducted at a wavelength of λ = 589 nm.

7.2.8 UV/Vis-spectrometry

UV/Vis spectra were recorded on a *PerkinElmer Lamda 365+* (Waltham, USA) UV/Vis spectrometer utilizing a tungsten-halogen and a deuterium lamp at 20 °C.

7.2.9 Rheology

Rheological properties of the hydrogel pre- and post-irradiation were studied using a stress-controlled *MCR 302e* rheometer from *Anton Paar* (Ostfildern-Scharnhausen, Germany) with a 10 mm diameter parallel-plate measuring system on a silica glass plate (0.05 mm gap).

7.2.10 Confocal microscopy for fluorescence recovery after photobleaching (FRAP)

For fluorescence recovery after photobleaching (FRAP) experiments, a TCS SP5 confocal fluorescence microscope from *Leica* (Wetzlar, Germany) was used. The microscope was equipped with a motorized xy-table, four lasers for excitation (405 nm, argon (458/476/488/495/514 nm), 561 nm and 633 nm) and the following objectives: 10x/0.3 dry, 20x/0.7 dry, 40x/1.3 oil, 63x/1.2 water, 63x/1.4 oil. Fluorescence emission within the range from 400 to 800 nm was able to be detected by four photomultiplier tubes.

7.3 General Procedures

7.3.1 Solid phase peptide synthesis

Loading of the resin: the first amino acid (2.0 eq.) was dissolved in DCM (10 mL/g resin) and a slight amount of DMF. The resulting solution was added to the reaction vessel containing the resin followed by the addition of DIPEA (2.0 eq.). After shaking for 5 min, another portion of DIPEA (3.0 eq.) was added and the reaction vessel was shaken for 1 h. Subsequently, MeOH (1 mL/g resin) was added and the mixture shaken for further 15 min. Afterwards, the vessel was drained and the resin consecutively washes with DCM, DMF, DCM and MeOH.

For each coupling step: the resin was swollen in DCM for 10 min while shaking the reaction vessel. After draining, a 20% piperidine solution in DMF was added and the mixture shaken for 20 min to cleave off the Fmoc protecting group followed by washing steps using DMF and DCM. To couple the next amino acid, a solution containing the corresponding Fmoc-protected amino acid (4.0 eq.), HBTU (4.0 eq.), HOBt (4.0 eq.) and DIPEA (6.0 eq.) in DMF (48 mL/g resin) was added and the reaction vessel shaken for 1 h. After removal of the solution, the resin was washed with DMF. This procedure was repeated for each amino acid. After the last coupling step, the resin was washed with DCM.

Cleavage of peptide: the *N*-terminus protected peptide was cleaved off by addition of a mixture containing TFA:H_2O:TIS = 38:1:1. (30 mL). After shaking for 1 h, the solution was drained. This step was repeated three times.

7.3.2 UV/Vis studies of stilbazolium iodide

Without CB[8]: 1.0 mg (*E*)-4-(4-hydroxystyryl)-1-methylpyridin-1-ium iodide (**III-11**) was dissolved in 50 mL water ($c = 6 \cdot 10^{-5}$ mol L^{-1}) and shaken thoroughly. 20 mL were transferred into a glass vial equipped with a magnetic stirrer for good mixing. The sample was irradiated using the same 370 nm LED mentioned above. The UV/Vis absorption spectra from 200 to 500 nm were recorded after irradiation duration of 0 min, 15 min, 30 min, 1 h, 2 h and 3 h.

With CB[8]: 1.0 mg (*E*)-4-(4-hydroxystyryl)-1-methylpyridin-1-ium iodide (**III-11**) was dissolved in 50 mL water ($c = 6 \cdot 10^{-5}$ mol L^{-1}) and 1.8 mg (0.5 eq.) CB[8] were added. The mixture was shaken thoroughly and irradiated with ultrasonic radiation for one minute. Each measurement was performed with a different sample, containing 5 mL of the mixture. The sample was irradiated using the same 370 nm LED. The UV/Vis absorption spectra from 200 to 500 nm were recorded after irradiation duration of 0 s, 10 s, 30 s, 60 s, 90 s, 3 min, 5 min and 10 min.

7.3.3 Sample preparation for NMR time plots

Without complexation: 5 mg (*E*)-4-(4-hydroxystyryl)-1-methylpyridin-1-ium iodide (**III-11**) was dissolved in 0.6 mL D_2O, shaken for one minute and transferred in an NMR tube.

With complexation: 5.0 mg (*E*)-4-(4-hydroxystyryl)-1-methylpyridin-1-ium iodide (**III-11**) was dissolved in 0.6 mL D_2O and 9.1 mg (0.5 eq) of CB[8] was added. The mixture was shaken for one minute and exposed to ultrasonic irradiation for 1 minute to support the complexation process before transferring into the NMR tube.

The samples were irradiated using a 370 nm LED and ^{1}H-NMR spectra were recorded after different time period of irradiation.

7.3.4 Hydrogel preparation

Stock solutions of polymers **III-1** and **III-2** with a concentration of 35 mg mL^{-1} were prepared by dissolving the polymer in PBS buffer. Respective amounts of the stock solutions were mixed in mass vials to obtain 60 µL solutions containing 0%, 25%, 50%, 75% and 100% PEG-SB. After the addition of CB[8] (1 mg), the samples were vortexed and shaken at 40 °C overnight under exclusion of light.

7.3.5 Rheological measurements

Oscillatory frequency sweeps (0.01–100 rad/s at a fixed strain of 2%) were performed at 20 and 37 °C to measure storage (*G*') and loss modulus (*G*") of the hydrogel and to determine the crosslink lifetime of associative network from the crossover frequency ω using the equation $\tau = 1/\beta = 2\pi/\omega$ (β as the network relaxation rate).[224] Amplitude sweeps (0.01–100% strain at a constant angular frequency of 5 rad s^{-1}) were measured at 20 °C to characterize the non-linear viscoelastic properties.

The stress relaxation of individual hydrogels was investigated at a fixed strain of 10%. Flow curves were performed with increasing shear rate $\dot{\gamma}$ = 0.01 – 1000 s^{-1}. Step-strain experiments were carried out to show shear-thinning and self-healing behavior by alternating the strain between 1% and 2000% at an angular frequency of 1 rad s^{-1}.

To investigate the mechanical properties under compression, cylindrical hydrogel samples with 10 mm diameter and a thickness between 2.3 and 2.5 mm were prepared in vials following the hydrogel preparation procedure. After photochemical crosslinking using a 370 nm LED (10 min irradiation), the sample was compressed with a velocity of 0.05 mm s^{-1}. The compression modulus (E_{comp}) was calculated using the initial slope of the stress-strain curve. For each sample composition, the experiment was performed three times and the average values as well as standard deviations are reported.

7.3.6 Photochemical crosslinking of PEG-SB network

In transparent Eppendorf 1.5 mL safe-lock tubes, 60 µL gel samples containing 0%, 25%, 50%, 75% and 100% component **III-2** were prepared following the procedure above. The hydrogels were each irradiated for 10 min using a *Kessil PR160L-370 nm* (Richmond, Canada) LED under the maximal intensity of 399 mW/cm^2 in 1 cm distance for photochemical crosslinking of network with **III-2**. Each sample was placed 10 cm relative to the lamp and irradiated for 10 min.

7.3.7 FRAP sample preparation

For the FRAP measurements, following stock solutions from polymer and dye molecules were prepared:

1: 4arm PEG-FGG (**III-1**): 35 mg mL^{-1} in PBS buffer

2: Cy3-azide: 0.5 mg mL^{-1} in H_2O:DMSO (9:1)

3: Cy3-FGG (**III-13**): 1 mg mL^{-1} in DMSO

4: mCitrine-MGG: 400 µM in an aqueous buffer containing 20 mM Hepes-NaOH (pH = 7.4), 150 mM sodium chloride, 1 mM tris(2-carboxyethyl)phosphine and 10% glycerol

5: mCitrine-FGG: 400 μM in an aqueous buffer containing 20 mM Hepes-NaOH (pH = 7.4), 150 mM sodium chloride, 1 mM tris(2-carboxyethyl)phosphine and 10% glycerol

In case of hydrogels including small molecule dyes: 0.5 μL of solution **2** or 1 μL of solution **3** was placed in a transparent Eppendorf 1.5 mL safe-lock tube and lyophilized. After addition of 90 μL of solution **1**, CB[8] was added (0.6 mg). The samples were vortexed and shaken at 37 °C for 40 h.

For hydrogels including mCitrine-MGG or mCitrine-FGG: in transparent Eppendorf 1.5 mL safe-lock tubes, 90 μL of solution **1** was mixed with 1 μL of solution **4** or **5**. After the addition of CB[8] (0.6 mg), the samples were vortexed and shaken at 37 °C for 40 h.

7.3.8 FRAP measurements

For the FRAP experiments, the samples were placed in an ibiTreat μ-slide 18 well chambered coverslip (ibidi GmbH, Gräfelfing, Germany). The measurements were performed with Leica FRAP Booster Beam Expander with an image size of 256x256 and 25x zoom in a scan speed of 1000 Hz. A z-plane of approximately 50 μm above the coverslip surface was chosen. The sample was excited using a 561 nm (Cy3) or 514 nm (mCitrine) laser with 5% laser intensity. Fluorescence was collected using a HC PL FLUOTAR 10.0×0.30 dry objective in the range of 572 – 670 nm (Cy3) or 525 – 625 nm (mCitrine). For pre- and post-bleach images, 5% laser intensity was used. For the bleaching process, 100% laser intensity was applied. With an acquisition speed of 1 s/frame, 10 pre-bleach frames were recorded, followed by 300 bleach frames recorded with 0.261 s/frame and then 600 postbleach frames were recorded at 1 s/frame.

7.4 Chemical Synthesis

7.4.1 Synthesis of disaccharide antigens

_N_-Benzyl (5-hydroxypentyl)carbamate (I-1)

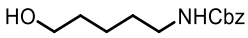

5-aminopentanol (4.600 g, 44.59 mmol, 1.0 eq.) was dissolved in $NaHCO_3(_{aq})$ (50 mL, 3 M) and a solution of benzyl chloroformate (9.4 mL, 11.410 g, 66.88 mmol, 1.5 eq.) in THF (20 mL) was added dropwise at under ice-cooling. The reaction mixture was stirred at ambient temperature overnight and diluted with ethyl acetate (100 mL). The organic layer was washed with brine (30 mL), dried over Na_2SO_4 and concentrated *in vacuo*. The residue was triturated with *n*-hexane. The resulting solid was filtrated, washed with diethyl ether and dried under vacuum.

Yield: 10.040 g, 95% (42.31 mmol); colorless solid.

MF $C_{13}H_{19}NO_3$ MW 237.2990 [237.1365]

R_F = 0.24 (SiO_2, CH:EA = 1:1).

HR-QTOF-MS (ESI, pos.), *m/z*: 260.1263 $[M+Na]^+$, (calc. 260.1257).

^{1}H-NMR, COSY, HSQC, HMBC (300 MHz, $CDCl_3$, 298 K): δ [ppm] = 7.30 – 7.26 (m, 3H, H_{Ar}), 7.25 – 7.17 (m, 2H, H_{Ar}), 5.00 (s, 2H, -C*H*$_2$Ph), 4.60 (s, 1H, -N*H*), 3.53 (t, $^3J_{\text{-}C\mathbf{H_2}\text{OH},\text{-}C\mathbf{H_2}\text{CH}_2\text{OH}}$ = 6.4 Hz, 2H, -C*H*$_2$OH), 3.10 (m, 2H, -C*H*$_2$NH-), 1.46 (m, 4H, -(C*H*$_2$)$_2$CH$_2$OH), 1.29 (m, 2H, -C*H*$_2$CH$_2$NH-).

^{13}C-NMR, HSQC, HMBC (75 MHz, $CDCl_3$, 298 K): δ [ppm] = 156.6 (*C*=O), 136.7 (C_{Ar}), 128.6 (C_{Ar}), 128.6 (C_{Ar}), 128.2 (C_{Ar}), 128.2 (C_{Ar}) 127.1 (C_{Ar}), 66.7 (-*C*H$_2$Ph), 62.7 (-*C*H$_2$OH), 41.0 (-*C*H$_2$NH-), 32.3 (-CH$_2$(*C*H$_2$)$_2$OH), 29.8 (-CH$_2$(*C*H$_2$)$_2$OH), 23.0 (-*C*H$_2$CH$_2$NH-).

_N_-Benzyl-(5-oxytrityl)carbamate (I-2)

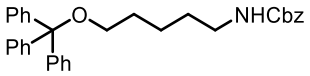

Benzyl-(5-hydroxypentyl)carbamate **I-1** (10.000 g, 42.14 mmol, 1.0 eq.) was dissolved in pyridine (35 mL) and trityl chloride (12.920 g, 46.36 mmol, 1.1 eq.) was added at 0 °C. After stirring the reaction mixture overnight at room temperature, 40 mL water were added and the solution was extracted with CH_2Cl_2 (3×40 mL). Consecutively, the organic layer was washed with saturated $NaHCO_{3(aq.)}$ (40 mL) and brine (40 mL), dried over MgSO4 and concentrated. The product was purified by flash chromatography (SiO_2, gradient: 0% → 20% EA in CH).

Yield: 5.340 g (11.13 mmol), 26%; colorless solid.

MF $C_{32}H_{33}NO_3$ MW 479.6200 [479.2460]

R_F = 0.26 (SiO_2, CH:EA = 10:1).

HR-QTOF-MS (ESI, pos.), *m/z*: 502.2345 $[M+Na]^+$, (calc. 502.2345).

^{1}H-NMR, COSY, TOCSY, HSQC, HMBC (300 MHz, $CDCl_3$): δ [ppm] = 7.44 – 7.36 (m, 5H, H_{Ar}), 7.34 – 7.30 (m, 4H, H_{Ar}), 7.30 – 7.26 (m, 4H, H_{Ar}), 7.26 – 7.16 (m, 7H, H_{Ar}), 5.06 (s, 2H, -CH_2Ph), 3.23 – 3.09 (m, 2H, -CH_2OH), 3.02 (t, $^3J_{\text{-CH}_2\text{NH-,-CH}_2\text{CH}_2\text{NH-}}$ = 6.4 Hz, 2H, -CH_2NH-), 1.65 – 1.43 (m, 4H, -(CH_2)$_2$CH$_2$OH), 1.36 (m, 2H, -CH_2CH$_2$NH-).

^{13}C-NMR, HSQC, HMBC (75 MHz, $CDCl_3$): δ [ppm] = 156.5 (*C*=O), 147.0 (C_{Ar}), 144.5 (C_{Ar}), 144.5 (C_{Ar}), 144.5 (C_{Ar}), 136.8 (C_{Ar}), 128.8 (C_{Ar}), 128.8 (C_{Ar}), 128.8 (C_{Ar}), 128.8 (C_{Ar}), 128.7 (C_{Ar}), 128.7 (C_{Ar}), 128.3 (C_{Ar}), 128.2 (C_{Ar}), 128.1 (C_{Ar}), 128.1 (C_{Ar}), 128.1 (C_{Ar}), 127.9 (C_{Ar}), 127.9 (C_{Ar}), 127.9 (C_{Ar}), 127.9 (C_{Ar}), 127.4 (C_{Ar}), 127.0 (C_{Ar}), 127.0 (C_{Ar}), 127.0 (C_{Ar}), 86.5 (-*C*(Ph)$_3$), 66.7 (-*C*H$_2$Ph), 63.4 (-*C*H$_2$O-), 41.1 (-*C*H$_2$NH-), 29.9 (-*C*H$_2$CH$_2$O-), 29.8 (-CH$_2$(*C*H$_2$)$_2$OH), 27.1 (-CH$_2$(*C*H$_2$)$_2$OH), 23.6 (-*C*H$_2$CH$_2$NH-).

_N_-(Benzyl)-benzyloxycarbonyl-5-aminopentan-1-ol (I-4)

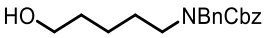

N-Benzyl-(5-oxytrityl)carbamate **I-2** (5.300 g, 11.05 mmol, 1.00 eq.) was dissolved in dry DMF (40 mL), sodium hydride (60% dispersion in paraffin oil) (0.530 g, 13.26 mmol, 1.20 eq.) was added at 0 ˚C and the reaction mixture was stirred for 10 min. Successively, benzyl bromide (1.5 mL, 2.160 g, 12.71 mmol, 1.15 eq.) was added to the reaction mixture, which was then stirred at room temperature for 2 h. After quenching the remaining sodium hydride with cold water, the aqueous layer was extracted with ethyl acetate (2×20 mL), the organic layer was dried over $MgSO_4$ and the solvent was removed under reduced pressure. The residue was redissolved in a mixture of CH_2Cl_2 and methanol (1:1, 20 mL). Portions of *p*-toluenesulfonic acid were added until a pH value of 3 was reached. The resulting reaction mixture was stirred at ambient temperature for 2 days. After removing the solvent, the residue was dissolved in DCM (100 mL), washed with saturated $NaHCO_{3\ aq.}$ (50 mL) and brine (30 mL), dried over $MgSO_4$, filtered and concentrated *in vacuo*. The product was purified using flash chromatography (SiO_2, gradient: 0% → 80% EA in CH).

Yield: 1.575 g (4.81 mmol), 44% after 2 steps, colorless oil.

MF $C_{20}H_{25}NO_3$ MW 327.4240 [327.1834]

R_F = 0.22 (SiO_2, CH:EA = 2:1).

HR-QTOF-MS (ESI, pos.), *m/z*: 350.1728 $[M+Na]^+$, (calc. 350.1727).

^{1}H-NMR, COSY, HSQC, HMBC (400 MHz, $CDCl_3$, 298 K): δ [ppm] = 7.46 – 7.03 (m, 10H, H_{Ar}), 5.28 – 5.01 (m, 2H, -C*H*$_2$Ph), 4.60 – 4.35 (m, 2H, -C*H*$_2$Ph), 3.75 – 3.48 (m, 2H, -C*H*$_2$-), 3.31 – 3.15 (m, 2H, -C*H*$_2$-), 1.66 – 1.42 (m, 6H, -C*H*$_2$-), 1.34 (s, 1H, -O*H*).

^{13}C-NMR, HSQC, HMBC (101 MHz, $CDCl_3$, 298 K): δ [ppm] = 128.6 (C_{Ar}), 128.5 (C_{Ar}), 127.9 (C_{Ar}), 127.3 (C_{Ar}), 127.2 (C_{Ar}), 67.2 (-*C*H$_2$Ph), 62.7 (-*C*H$_2$-), 50.5 (-*C*H$_2$Ph), 47.0 (-*C*H$_2$-), 32.3 (-*C*H$_2$-), 27.4 (-*C*H$_2$-), 22.9 (-*C*H$_2$-).

1,2,3,6,2',3',4',6'-Octa-*O*-acetyl-α/β-D-cellobiose (I-7)

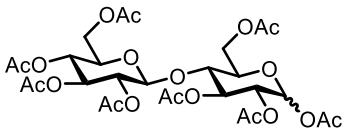

α/β-D-Cellobiose (5.005 g, 14.62 mmol, 1.00 eq.) was suspended in pyridine (30 mL). After the solution was cooled to 0 °C, acetic anhydride (24 mL, 25.920 g, 253.89 mmol, 18.00 eq.) was added dropwise. Subsequently, catalytic amount of 4-Dimethylaminopyridine was added. The reaction mixture was stirred at 40 °C for 3 d. After cooling to ambient temperature, the solution was diluted ethyl acetate (150 ml), washed with 1 M $HCl_{aq.}$ (2×50 mL) and conc. $NaHCO_{3\ aq.}$ (4×50 mL), dried over $MgSO_4$, filtered and concentrated *in vacuo*. The residue was co-evaporated with toluene (4×40 mL). The product was used without further purification.

Yield: 9.750 g (14.37 mmol), 98%; colorless solid; α:β = 20:3 (NMR).

MF $C_{28}H_{38}O_{19}$ MW 678.5930 [678.2007]

R_F = 0.28 (SiO_2, CH:EA = 1:1).

$[\alpha]_D^{20}$ = -0.7° (*c* = 1.00; $CHCl_3$).

HR-QTOF-MS (ESI, pos.), *m/z*: 701.1906 $[M+Na]^+$, (calc. 701.1900).

Signals assignable to β-anomer:

^{1}H-NMR, COSY, TOCSY, HSQC, HSQC no dec., HMBC (600 MHz, $CDCl_3$, 296 K): δ [ppm] = 5.63 (d, $^3J_{H\text{-}1,H\text{-}2}$ = 8.3 Hz, 1H, H-1), 5.19 (dd, $^3J_{H\text{-}3,H\text{-}2}$ = $^3J_{H\text{-}3,H\text{-}4}$ = 9.1 Hz, 1H, H-3), 5.11 (dd, $^3J_{H\text{-}3',H\text{-}2'}$ = $^3J_{H\text{-}3',H\text{-}4'}$ = 9.4 Hz, 1H, H-3'), 5.03 (dd, $^3J_{H\text{-}4',H\text{-}3'}$ = $^3J_{H\text{-}4',H\text{-}5'}$ = 9.1 Hz, 1H, H-4'), 5.01 (dd, $^3J_{H\text{-}2,H\text{-}1}$ = $^3J_{H\text{-}2,H\text{-}3}$ = 9.1 Hz, 1H, H-2), 4.89 (dd, $^3J_{H\text{-}2',H\text{-}3'}$ = 9.4 Hz, $^3J_{H\text{-}2',H\text{-}1'}$ = 8.0 Hz, 1H, H-2'), 4.49 (d, $^3J_{H\text{-}1',H\text{-}2'}$ = 8.0 Hz, 1H, H-1'), 4.45 (dd, $^2J_{H\text{-}6b,H\text{-}6a}$ = 12.2 Hz, $^3J_{H\text{-}6b,H\text{-}5}$ = 2.0 Hz, 1H, H-6b), 4.34 (dd, $^2J_{H\text{-}6a',H\text{-}6b'}$ = 12.5 Hz, $^3J_{H\text{-}6a',H\text{-}5'}$ = 4.5 Hz, 1H, H-6a'), 4.08 (dd, $^2J_{H\text{-}6a,H\text{-}6b}$ = 12.2 Hz, $^3J_{H\text{-}6a,H\text{-}5}$ = 4.8 Hz, 1H, H-6a), 4.01 (dd, $^2J_{H\text{-}6b',H\text{-}6a'}$ = 12.5 Hz, $^3J_{H\text{-}6b',H\text{-}5'}$ = 2.3 Hz, 1H, H-6b'), 3.80 (dd, $^3J_{H\text{-}4',H\text{-}3'}$ = $^3J_{H\text{-}4',H\text{-}5'}$ = 9.4 Hz, 1H, H-4), 3.72 (ddd, $^3J_{H\text{-}5,H\text{-}4}$ = 9.9 Hz, $^3J_{H\text{-}5,H\text{-}6a}$ = 4.9 Hz, $^3J_{H\text{-}5,H\text{-}6b}$ = 2.0 Hz, 1H, H-5), 3.64 (ddd, $^3J_{H\text{-}5',H\text{-}4'}$ = 9.4 Hz, $^3J_{H\text{-}5',H\text{-}6a'}$ = 4.5 Hz, $^3J_{H\text{-}5',H\text{-}6b'}$ = 2.3 Hz, 1H, H-5'), 2.09 (s, 3H, -COCH_3), 2.06 (s, 3H, -COCH_3), 2.06 (s, 3H, -COCH_3), 2.00 (s, 3H, -COCH_3), 1.99 (6H, -COCH_3), 1.98 (s, 3H, -COCH_3), 1.95 (s, 3H, -COCH_3).

^{13}C-NMR, HSQC, HSQC no dec., HMBC (151 MHz, $CDCl_3$, 296 K): δ [ppm] = 170.6 (-*C*OCH_3), 170.4 (-*C*OCH_3), 170.3 (-*C*OCH_3), 169.8 (-*C*OCH_3), 169.6 (-*C*OCH_3), 169.4 (-*C*OCH_3), 169.1 (-*C*OCH_3), 168.9 (-*C*OCH_3), 100.7 (C-1'), 91.6 (C-1), 75.9 (C-4), 73.6 (C-5), 72.9 (C-3'), 72.4 (C-3), 72.0 (C-5'),

71.6 (C-2'), 70.4 (C-4'), 67.8 (C-2), 61.7 (C-6), 61.6 (C-6'), 20.9 (-CO*C*H$_3$), 20.9 (-CO*C*H$_3$), 20.7 (-CO*C*H$_3$), 20.7 (-CO*C*H$_3$), 20.6 (-CO*C*H$_3$), 20.6 (-CO*C*H$_3$), 20.6 (-CO*C*H$_3$), 20.6 (-CO*C*H$_3$).

2,3,6,2',3',4',6'-Hepta-*O*-acetyl-1-bromo-α-D-cellobioside (I-8)

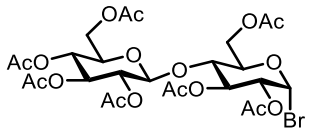

1,2,3,6,2',3',4',6'-Octa-*O*-acetyl-α/β-D-cellobiose (**I-7**) (9.659 g, 14.2 mmol, 1.00 eq.) was dissolved in 70 mL dry CH_2Cl_2 in a round-bottom flask. After the solution was cooled to 0 °C, a solution with 33% HBr in HOAc (12 mL) was added dropwise under stirring. The mixture was allowed to warm to ambient temperature and was stirred for 24 h under light exclusion. The solution was diluted with CH_2Cl_2 (200 mL), washed with water (2×150 mL), 1% $NaHCO_{3\ aq.}$ (150 mL), saturated $NaHCO_{3\ aq.}$ (150 mL) and with conc. $NaCl_{\ aq.}$ (150 mL) and dried over Na_2SO_4. The organic layer was filtered and the solvent was removed *in vacuo*. The product was used without further purification.

Yield: 9.753 g (13.94 mmol), 98%; colorless solid; 100% α (NMR).

MF $C_{26}H_{35}BrO_{17}$ MW 698.4530 [698.1058]

R_F = 0.40 (SiO_2, CH:EA = 1:1).

$[\alpha]_D^{22}$ = -87.5 (*c* = 1.00; $CHCl_3$); Lit: $[\alpha]_D^{22}$ = -94.5 (*c* = 1.00; $CHCl_3$). [336]

HR-QTOF-MS (ESI, pos.), *m/z*: 721.0949 $[M+Na]^+$, (calc. 721.0950).

^{1}H-NMR, COSY, TOCSY, HSQC, HSQC no dec., HMBC (600 MHz, $CDCl_3$, 296 K): δ [ppm] = 6.52 (d, $^3J_{H\text{-}1,H\text{-}2}$ = 4.1 Hz, 1H, H-1), 5.53 (dd, $^3J_{H\text{-}3,H\text{-}2}$ = $^3J_{H\text{-}3,H\text{-}4}$ = 9.7 Hz, 1H, H-3), 5.15 (dd, $^3J_{H\text{-}3',H\text{-}2'}$ = $^3J_{H\text{-}3',H\text{-}4'}$ = 9.4 Hz, 1H, H-3'), 5.08 (dd, $^3J_{H\text{-}4',H\text{-}3'}$ = $^3J_{H\text{-}4',H\text{-}5'}$ = 9.4 Hz, 1H, H-4'), 4.94 (dd, $^3J_{H\text{-}2',H\text{-}3'}$ = 9.4 Hz, $^3J_{H\text{-}2',H\text{-}1'}$ = 8.0 Hz, 1H, H-2'), 4.76 (dd, $^3J_{H\text{-}2,H\text{-}3}$ = 9.7 Hz, $^3J_{H\text{-}2,H\text{-}1}$ = 4.1 Hz, 1H, H-2), 4.54 (d, $^3J_{H\text{-}1',H\text{-}2'}$ = 8.0 Hz, 1H, H-1'), 4.54 – 4.51 (m, 1H, H-6a), 4.37 (dd, $^2J_{H\text{-}6a',H\text{-}6b'}$ = 12.5 Hz, $^3J_{H\text{-}6a',H\text{-}5'}$ = 4.4 Hz, 1H, H-6a'), 4.22 – 4.13 (2H, H-5, H-6b), 4.05 (dd, $^2J_{H\text{-}6b',H\text{-}6a'}$ = 12.5 Hz, $^3J_{H\text{-}6b',H\text{-}5'}$ = 2.3 Hz, 1H, H-6b'), 3.83 (dd, $^3J_{H\text{-}4,H\text{-}3}$ = $^3J_{H\text{-}4,H\text{-}5}$ = 9.7 Hz, 1H, H-4), 3.67 (ddd, $^3J_{H\text{-}5',H\text{-}4'}$ = 9.4 Hz, $^3J_{H\text{-}5',H\text{-}6a'}$ = 4.4 Hz, $^3J_{H\text{-}5',H\text{-}6b'}$ = 2.3 Hz, 1H, H-5'), 2.14 (s, 3H, -COC*H*$_3$), 2.09 (6H, -COC*H*$_3$), 2.04 (6H, -COC*H*$_3$), 2.01 (s, 3H, -COC*H*$_3$), 1.99 (s, 3H, -COC*H*$_3$).

^{13}C-NMR, HSQC, HSQC no dec., HMBC (151 MHz, $CDCl_3$, 296 K): δ [ppm] = 170.7 (-*C*OCH$_3$), 170.4 (-*C*OCH$_3$), 170.3 (-*C*OCH$_3$), 170.2 (-*C*OCH$_3$), 169.5 (-*C*OCH$_3$), 169.4 (-*C*OCH$_3$), 169.1 (-*C*OCH$_3$), 100.7 (C-1'), 86.5 (C-1), 75.4 (C-4), 73.1 (C-5), 73.1 (C-3'), 72.2 (C-5'), 71.7 (C-2'), 70.9 (C-2), 69.5

(C-3), 67.8 (C-4'), 61.7 (C-6'), 61.0 (C-6), 21.0 (-CO*C*H$_3$), 20.9 (-CO*C*H$_3$), 20.8 (-CO*C*H$_3$), 20.7 (-CO*C*H$_3$).

_p_-Tolyl 2,3,6,2',3',4',6'-hepta-_O_-acetyl-1-thio-β-D-cellobioside (I-9)

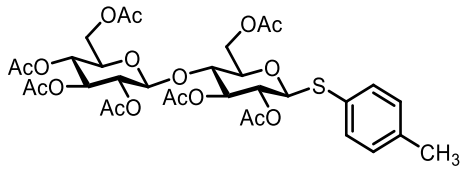

2,3,6,2',3',4',6'-Hepta-*O*-acetyl-1-bromo-α-D-cellobioside (**I-8**) (3.000 g, 4.29 mmol, 1.00 eq.) was dissolved in anhydrous acetonitrile (25 mL). After the solution was cooled to 0 °C, 4-methylbenzenethiol (0.586 g, 4.72 mmol, 1.10 eq.) and triethylamine (1.19 mL, 0.868 g, 8.58 mmol, 2.00 eq.) were added. The reaction mixture was allowed to warm to ambient temperature and was stirred for 3 h. Subsequently, the solution was diluted with CH_2Cl_2 (100 mL) and washed with water (3×100 mL). The aqueous layer was extracted with CH_2Cl_2 (50 mL). The organic extracts were combined, dried over $MgSO_4$, filtered and the solution was concentrated *in vacuo*. The product was recrystallized from ethanol.

Yield: 2.261 g (3.04 mmol), 71%; colorless solid; 100% β (NMR).

MF $C_{33}H_{42}O_{17}S$ MW 742.7420 [742.2143]

R_F = 0.55 (SiO_2, CH:EA = 1:1).

$[\alpha]_D^{22}$ = -14.9 (c = 1.00; $CHCl_3$); Lit: $[\alpha]_D^{22}$ = -28.0 (c = 1.00; $CHCl_3$).[337]

HR-QTOF-MS (ESI, pos.), *m/z*: 765.2016 $[M+Na]^+$, (calc. 765.2033).

^{1}H-NMR, COSY, TOCSY, HSQC, HSQC no dec., HMBC (600 MHz, $CDCl_3$, 296 K): δ [ppm] = 7.38 – 7.33 (m, 2H, H_{Ar}), 7.13 – 7.08 (m, 2H, H_{Ar}), 5.17 (dd, $^3J_{H\text{-}3,H\text{-}2}$ = $^3J_{H\text{-}3,H\text{-}4}$ = 9.3 Hz, 1H, H-3), 5.12 (dd, $^3J_{H\text{-}3',H\text{-}2'}$ = $^3J_{H\text{-}3',H\text{-}4'}$ = 9.4 Hz, 1H, H-3'), 5.05 (dd, $^3J_{H\text{-}4',H\text{-}3'}$ = $^3J_{H\text{-}4',H\text{-}5'}$ = 9.4 Hz, 1H, H-4'), 4.91 (dd, $^3J_{H\text{-}2',H\text{-}3'}$ = 9.4 Hz, $^3J_{H\text{-}2',H\text{-}1'}$ = 8.0 Hz, 1H, H-2'), 4.86 (dd, $^3J_{H\text{-}2,H\text{-}1}$ = 9.8 Hz, $^3J_{H\text{-}2,H\text{-}3}$ = 9.3 Hz, 1H, H-2), 4.58 (d, $^3J_{H\text{-}1,H\text{-}2}$ = 9.8 Hz, 1H, H-1), 4.55 (dd, $^2J_{H\text{-}6b,H\text{-}6a}$ = 12.0 Hz, $^3J_{H\text{-}6b,H\text{-}5}$ = 2.1 Hz, 1H, H-6b), 4.48 (d, $^3J_{H\text{-}1',H\text{-}2'}$ = 8.0 Hz, 1H, H-1'), 4.37 (dd, $^2J_{H\text{-}6a',H\text{-}6b'}$ = 12.5 Hz, $^3J_{H\text{-}6a',H\text{-}5'}$ = 4.3 Hz, 1H, H-6a'), 4.07 (dd, $^2J_{H\text{-}6a,H\text{-}6b}$ = 11.9 Hz, $^3J_{H\text{-}6a,H\text{-}5}$ = 5.4 Hz, 1H, H-6a), 4.01 (dd, $^2J_{H\text{-}6b',H\text{-}6a'}$ = 12.5 Hz, $^3J_{H\text{-}6b',H\text{-}5'}$ = 2.2 Hz, 1H, H-6b'), 3.70 (dd, $^3J_{H\text{-}4,H\text{-}3}$ = $^3J_{H\text{-}4,H\text{-}5}$ = 9.3 Hz, 1H, H-4), 3.63 (ddd, $^3J_{H\text{-}5',H\text{-}4'}$ = 9.4 Hz, $^3J_{H\text{-}5',H\text{-}6a'}$ = 4.3 Hz, $^3J_{H\text{-}5',H\text{-}6b'}$ = 2.2 Hz, 1H, H-5'), 3.59 (ddd, $^3J_{H\text{-}5,H\text{-}4}$ = 9.3 Hz, $^3J_{H\text{-}5,H\text{-}6a}$ = 5.4 Hz, $^3J_{H\text{-}5,H\text{-}6b}$ = 2.0 Hz, 1H, H-5), 2.33 (s, 3H, Ar-C*H*$_3$), 2.11 (s, 3H, -COC*H*$_3$), 2.08 (s, 3H, -COC*H*$_3$), 2.06 (s, 3H, -COC*H*$_3$), 2.01 (s, 3H, -COC*H*$_3$), 2.00 (s, 3H, -COC*H*$_3$), 1.99 (s, 3H, -COC*H*$_3$), 1.97 (s, 3H, -COC*H*$_3$).

^{13}C-NMR, HSQC, HSQC no dec., HMBC (151 MHz, $CDCl_3$, 296 K): δ [ppm] = 170.6 (-*C*OCH$_3$), 170.4 (-*C*OCH$_3$), 170.4 (-*C*OCH$_3$), 169.9 (-*C*OCH$_3$), 169.7 (-*C*OCH$_3$), 169.4 (-*C*OCH$_3$), 169.2 (-*C*OCH$_3$), 138.8 (C_{Ar}), 133.9 (C_{Ar}), 129.8 (C_{Ar}), 127.8 (C_{Ar}), 100.9 (C-1'), 85.8 (C-1), 76.8 (C-5), 76.5 (C-4), 73.7 (C-3), 73.0 (C-3'), 72.1 (C-5'), 71.7 (C-2'), 70.2 (C-2), 67.8 (C-4'), 62.1 (C-6), 61.6 (C-6'), 21.3 (Ar-*C*H$_3$), 21.0 (-CO*C*H$_3$), 21.0 (-CO*C*H$_3$), 20.8 (-CO*C*H$_3$), 20.7 (-CO*C*H$_3$), 20.7 (-CO*C*H$_3$), 20.7 (-CO*C*H$_3$), 20.7 (-CO*C*H$_3$).

_p_-Tolyl 1-thio-β-D-cellobioside (I-10)

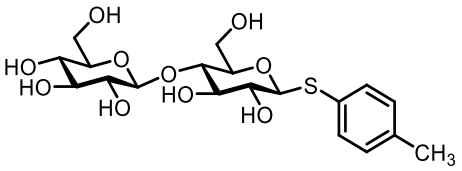

To a solution of *p*-Tolyl 2,3,6,2',3',4',6'-hepta-*O*-acetyl-1-thio-β-D-cellobioside (**I-9**) (0.650 g, 0.88 mmol, 1.00 eq.) in methanol (16 mL), sodium methoxide was added portionwise, until pH of 9 was reached. The mixture was stirred for 16 h. Subsequently, the solution was acidified with the Amberlyst 15-resin (hydrogen form) until a pH of 4 was reached. After filtration through a pad of celite, the solvent was removed *in vacuo*. The product was used without further purification.

Yield: 0.400 g (0.88 mmol), quant.; colorless solid; 100% β (NMR).

MF $C_{19}H_{28}O_{10}S$ MW 448.4830 [448.1403]

R_F = 0.12 (SiO_2, CH_2Cl_2:MeOH = 9:1).

$[\alpha]_D^{22}$ = -47.0 (*c* = 1.00; MeOH).

HR-QTOF-MS (ESI, pos.), *m/z*: 471.1299 $[M+Na]^+$, (calc. 471.1295).

^{1}H-NMR, COSY, TOCSY, HSQC, HSQC no dec., HMBC (400 MHz, methanol-d_4, 296 K): δ [ppm] = 7.46 (m, 2H, H_{Ar}), 7.13 (m, 2H, H_{Ar}), 4.52 (d, $^3J_{H\text{-}1,H\text{-}2}$ = 9.8 Hz, 1H, H-1), 4.40 (d, $^3J_{H\text{-}1',H\text{-}2'}$ = 7.9 Hz, 1H, H-1'), 3.91 – 3.81 (3H, H-6a, H-6b, H-6b'), 3.64 (dd, $^2J_{H\text{-}6a',H\text{-}6b'}$ = 11.8 Hz, $^3J_{H\text{-}6a',H\text{-}5'}$ = 5.5 Hz, 1H, H-6a'), 3.55 (dd, $^3J_{H\text{-}4,H\text{-}3} = {}^3J_{H\text{-}4,H\text{-}5}$ = 8.8 Hz, 1H, H-4), 3.51 (dd, $^3J_{H\text{-}3,H\text{-}2} = {}^3J_{H\text{-}3,H\text{-}4}$ = 8.7 Hz, 1H, H-3), 3.40 (ddd, $^3J_{H\text{-}5,H\text{-}4}$ = 8.8 Hz, $^3J_{H\text{-}5,H\text{-}6a}$ = 3.7 Hz, $^3J_{H\text{-}5,H\text{-}6b}$ = 2.3 Hz, 1H, H-5), 3.35 (dd, $^3J_{H\text{-}3',H\text{-}2'} = {}^3J_{H\text{-}3',H\text{-}4'}$ = 4.5 Hz, 1H, H-3'), 3.33 – 3.29 (2H,H-4', H-5'), 3.31 – 3.21 (m, 1H, H-2), 3.21 (dd, $^3J_{H\text{-}2',H\text{-}3'}$ = 9.2 Hz, $^3J_{H\text{-}2',H\text{-}1'}$ = 7.9 Hz, 1H, H-2'), 2.31 (s, 3H, Ar-CH_3).

^{13}C-NMR, HSQC, HSQC no dec., HMBC (101 MHz, methanol-d_4, 296 K): δ [ppm] = 138.9 (C_{Ar}), 133.8 (C_{Ar}), 130.9 (C_{Ar}), 130.5 (C_{Ar}), 104.5 (C-1'), 89.4 (C-1), 80.5 (C-5), 80.2 (C-4), 78.1 (C-5'), 78.0 (C-3), 77.8 (C-3'), 74.9 (C-2'), 73.4 (C-2), 71.4 (C-4'), 62.4 (C-6'), 61.9 (C-6), 21.1 (SPh-*C*H$_3$).

_p_-Tolyl 4',6'-_O_-benzylidene-1-thio-β-D-cellobioside (I-11)

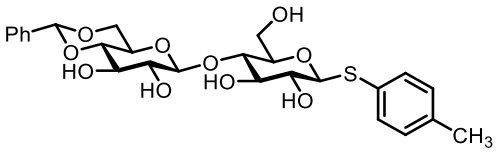

_p_-Tolyl 1-thio-β-D-cellobioside (**I-10**) (1.000 g, 2.23 mmol, 1.00 eq.) was dissolved in dry DMF (12 mL). Subsequently, benzaldehyde dimethyl acetal (0.37 mL, 0.373 g, 2.45 mmol, 1.10 eq.) and _p_-toluenesulfonic acid monohydrate (0.380 g, 0.22 mmol, 0.10 eq.) were added. The reaction mixture was warmed up to 60 °C and was stirred under 200 mbar. After every two hours, an additional portion of benzaldehyde dimethyl acetal (0.15 mL, 0.152 g, 1.00 mmol, 0.44 eq.) was added (four times in total). The reaction was monitored _via_ TLC and was completed after 8 h. After the solvent was removed _in vacuo_, the crude product was subjected to flash chromatography (SiO_2, gradient: 0% → 10% MeOH in CH_2Cl_2). The product containing fractions were combined and the solvent was removed _in vacuo_.

Yield: 0.372 g (0.69 mmol), 31%; colorless solid; 100% β (NMR).

MF $C_{26}H_{32}O_{10}S$ MW 536.5920 [536.1716]

R_F = 0.64 (SiO_2, CH_2Cl_2:MeOH = 19:1).

$[\alpha]_D^{22}$ = -63.2 (c = 1.00; MeOH).

HR-QTOF-MS (ESI, pos.), _m/z_: 559.1611 $[M+H]^+$, (calc. 559.1608).

^{1}H-NMR, COSY, TOCSY, HSQC, HSQC no dec., HMBC (400 MHz, methanol-d_4/CD_2Cl_2, 296 K): δ [ppm] = 7.65 – 7.54 (4H, H_{Ar}), 7.50 – 7.42 (3H, H_{Ar}), 7.25 (m, 2H, H_{Ar}), 5.68 (s, 1H, (-O)$_2$C_H_Ph), 4.66 (d, $^3J_{H\text{-}1',H\text{-}2'}$ = 7.9 Hz, 1H, H-1'), 4.65 (d, $^3J_{H\text{-}1,H\text{-}2}$ = 9.8 Hz, 1H, H-1), 4.42 (dd, $^2J_{H\text{-}6a',H\text{-}6b'}$ = 10.4 Hz, $^3J_{H\text{-}6a',H\text{-}5'}$ = 4.0 Hz, 1H, H-6a'), 4.01 (dd, $^2J_{H\text{-}6b,H\text{-}6a}$ = 12.3 Hz, $^3J_{H\text{-}6b,H\text{-}5}$ = 2.7 Hz, 1H, H-6b), 3.96 (dd, $^2J_{H\text{-}6a,H\text{-}6b}$ = 12.3 Hz, $^3J_{H\text{-}6a,H\text{-}5}$ = 4.0 Hz, 1H, H-6a), 3.92 – 3.85 (m, 1H, H-6b'), 3.78 (dd, $^3J_{H\text{-}2',H\text{-}3'}$ = $^3J_{H\text{-}3',H\text{-}4'}$ = 9.0 Hz, 1H, H-3'), 3.70 (dd, $^3J_{H\text{-}4,H\text{-}3}$ = $^3J_{H\text{-}4,H\text{-}5}$ = 9.0 Hz, 1H, H-4), 3.67 – 3.59 (3H, H-3, H-4', H-5'), 3.54 (ddd, $^3J_{H\text{-}5,H\text{-}4}$ = 9.0 Hz, $^3J_{H\text{-}5,H\text{-}6a}$ = 4.0 Hz, $^3J_{H\text{-}5,H\text{-}6b}$ = 2.6 Hz, 1H, H-5), 3.47 (dd, $^3J_{H\text{-}2',H\text{-}3'}$ = 9.0 Hz, $^3J_{H\text{-}2',H\text{-}1'}$ = 7.9 Hz, 1H, H-2'), 3.39 (dd, $^3J_{H\text{-}2,H\text{-}1}$ = 9.8 Hz, $^3J_{H\text{-}2,H\text{-}3}$ = 8.3 Hz, 1H, H-2), 2.44 (s, 3H, -SPh-C_H_$_3$).

^{13}C-NMR, HSQC, HSQC no dec., HMBC (101 MHz, methanol-d_4/CD_2Cl_2, 296 K): δ [ppm] = 138.8 (C_{Ar}), 138.5 (C_{Ar}), 133.5 (C_{Ar}), 130.4 (C_{Ar}), 129.8 (C_{Ar}), 128.9 (C_{Ar}), 127.2 (C_{Ar}), 104.9 (C-1'), 102.7 ((-O)$_2$_C_HPh), 89.2 (C-1), 81.6 (C-5'), 80.5 (C-4), 80.0 (C-5), 77.3 (C-3), 75.5 (C-2'), 74.2 (C-3'), 73.1 (C-2), 69.2 (C-6'), 67.5 (C-4'), 61.8 (C-6), 21.2 (SPh-_C_H$_3$).

***p*-Tolyl 6-*O*-(tert-butyldiphenylsilyl)-4',6'-*O*-benzylidene-1-thio-β-D-cellobioside (I-12)**

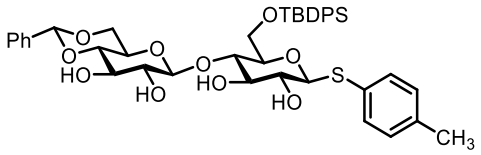

Method a:

p-Tolyl 4',6'-*O*-benzylidene-1-thio-β-D-cellobioside (**I-11**, 0.140 g, 0.261 mmol, 1.00 eq.) was dissolved in dry DMF (12 mL). After cooling to 0 °C, *tert*-butyldiphenylsilyl chloride (0.09 mL, 0.093 g, 0.339 mmol, 1.30 eq.) and imidazole (0.046 g, 0.678 mmol, 2.60 eq.) were added. The reaction mixture was allowed to warm to ambient temperature and was stirred for 40 h. The reaction was quenched by the addition of cold water (3 mL) and the mixture was extracted with CH_2Cl_2 (3×20 mL). The organic extracts were combined and washed with conc. $(NH_4)_2SO_{4\,aq.}$ (20 mL). The organic layer was dried over $MgSO_4$, filtered and concentrated *in vacuo*. The crude product was subjected to flash chromatography (SiO_2, gradient: 0% → 10% MeOH in CH_2Cl_2). The product containing fractions were combined and the solvent was removed *in vacuo*.

Yield: 0.61 g (0.078 mmol), 30%; colorless solid; 100% β (NMR).

Method b:

p-Tolyl 1-thio-β-D-cellobioside (**I-10**, 3.500 g, 7.804 mmol, 1.00 eq.) was dissolved in dry DMF (25 mL). After cooling to 0 °C, benzylidene dimethyl acetal (3.5 mL, 3.563 g, 23.412 mmol, 3.00 eq.) and magnesium triflate (0.126 g, 0.390 mmol, 0.05 eq.) were added. Subsequently, trifluoromethanesulfonic acid (0.34 mL, 0.586 g, 3.902 mmol, 0.50 eq.) was added dropwise. The reaction mixture was allowed to warm to ambient temperature and was stirred for 40 h. After adding 1 mL triethylamine, the mixture was concentrated *in vacuo*. The crude product was re-dissolved in dry DMF (25 mL) and imidazole (3.700 g, 54.346 mmol, 6.00 eq.) was added. *tert*-butyldiphenylsilyl chloride (9.40 mL, 9.958 g, 36.231 mmol, 4.00 eq.) was added dropwise under ice-cooling. After stirring for 17 h, the reaction was quenched by addition of cold water (10 mL) and the mixture was extracted with CH_2Cl_2 (3×50 mL). The organic extracts were combined and washed with conc. $(NH_4)_2SO_{4\,aq.}$ (50 mL). The organic layer was dried over $MgSO_4$, filtered and concentrated *in vacuo*. The crude product was subjected to flash chromatography (SiO_2, gradient: 0% → 10% MeOH in CH_2Cl_2). The product containing fractions were combined and the solvent was removed *in vacuo*.

Yield: 1.266 g (0.77 mmol), 77%; colorless solid; 100% β (NMR).

MF $C_{42}H_{50}O_{10}SSi$ MW 774.9970 [774.2894]

R_F = 0.31 (SiO_2, CH_2Cl_2:MeOH = 19:1).

$[\alpha]_D^{22}$ = -59.8 (c = 1.00; MeOH).

HR-QTOF-MS (ESI, pos.), *m/z*: 797.2781 $[M+Na]^+$, (calc. 797.2786).

^{1}H-NMR, COSY, TOCSY, HSQC, HSQC no dec., HMBC (600 MHz, CD_2Cl_2/MeOD, 298K): δ [ppm] = 7.82 – 7.75 (m, 4H, H_{Ar}), 7.49 – 7.35 (m, 13H, H_{Ar}), 7.07 – 7.03 (m, 2H, H_{Ar}), 5.49 (s, 1H, $(RO)_2CHPh$), 4.57 (d, $^3J_{H\text{-}1',H\text{-}2'}$ = 7.9 Hz, 1H, H-1'), 4.50 (d, $^3J_{H\text{-}1,H\text{-}2}$ = 9.8 Hz, 1H, H-1), 4.26 (dd, $^2J_{H\text{-}6a',H\text{-}6b'}$ = 10.4 Hz, $^3J_{H\text{-}6a',H\text{-}5'}$ = 5.0 Hz, 1H, H-6a'), 4.07 – 4.00 (m, 2H, H-6a, H-6b), 3.83 (s, 1H, -OH), 3.80 – 3.65 (m, 3H, H-4, H-3', H-6'), 3.59 (d, $^3J_{H\text{-}3,H\text{-}2}$ = $^3J_{H\text{-}3,H\text{-}4}$ = 8.8 Hz, 1H, H-3), 3.51 (dd, $^3J_{H\text{-}4',H\text{-}3'}$ = $^3J_{H\text{-}4',H\text{-}5'}$ = 9.3 Hz, 1H, H-4'), 3.47 (ddd, $^3J_{H\text{-}5,H\text{-}4}$ = 9.8 Hz, $^3J_{H\text{-}5,H\text{-}6b}$ = 3.4 Hz, $^3J_{H\text{-}5,H\text{-}6b}$ = 2.2 Hz, 1H, H-5), 3.46 – 3.39 (m, 2H, H-2', H-5'), 3.36 (dd, $^3J_{H\text{-}2,H\text{-}1}$ = 9.3 Hz, 1H, H-2), 2.91 (s, 1H, -OH), 2.82 (s, 1H, -OH), 2.80 (s, 1H, -OH), 2.30 (s, 3H, -SPh-CH_3), 1.08 (s, 9H, -Si-C(CH_3)$_3$).

^{13}C-NMR, HSQC, HSQC no dec., HMBC (151 MHz, CD_2Cl_2, 298K): δ [ppm] = 138.8 (C_{Ar}), 137.6 (C_{Ar}), 136.4 (C_{Ar}), 136.2 (C_{Ar}), 134.0 (C_{Ar}), 133.5 (C_{Ar}), 133.5 (C_{Ar}), 130.3 (C_{Ar}), 130.2 (C_{Ar}), 129.8 (C_{Ar}), 128.9 (C_{Ar}), 128.8 (C_{Ar}), 128.3 (C_{Ar}), 128.2 (C_{Ar}), 126.8 (C_{Ar}), 103.7 (C-1'), 102.3 ($(RO)_2CHPh$), 88.3 (C-1), 80.5 (C-4'), 79.6 (C-5), 79.3 (C-4), 76.4 (C-3), 74.7 (C-2'), 73.8 (C-3'), 72.5 (C-2), 68.7 (C-6'), 67.1 (C-5'), 63.1 (C-6), 27.1 ((-Si-C(CH$_3$)$_3$), 21.4 (-SPh-CH$_3$), 19.7 (-Si-C(CH$_3$)$_3$).

_p_-Tolyl 2,3,2',3'-tetra-_O_-benzoyl-6-_O_-(tert-butyldiphenylsilyl)-4',6'-_O_-benzylidene-1-thio-β-D-cellobioside (I-5)

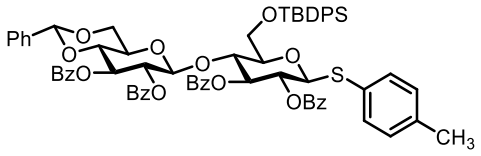

p-Tolyl 6-*O*-(*tert*-butyldiphenylsilyl)-4',6'-*O*-benzylidene-1-thio-β-D-cellobioside (**I-12**, 1.900 g, 2.452 mmol, 1.0 eq.) was dissolved in dry CH_2Cl_2 (16 mL). Pyridine (3.9 mL, 3.878 g, 0.982 mmol, 20.0 eq.), benzoyl chloride (4.6 mL, 5.514 g, 39.266 mmol, 16.0 eq.), and catalytic amount of 4-dimethylaminopyridine were added at under ice-cooling and the reaction mixture was stirred for 2 d at ambient temperature. After quenching the remaining benzoyl chloride with 10 mL cold water, the solution was diluted with CH_2Cl_2 (50 mL) and the organic layer was washed with saturated $NaCl_{(aq)}$ (30 mL), dried over $MgSO_4$ and concentrated *in vacuo*. The crude product was subjected to normal phase flash chromatography (SiO_2, gradient: 0% → 30% EA in CH) and further purified by reversed phase flash chromatography (C_{18}, gradient: 40% → 100% ACN in H_2O).

Yield: 1.233 g (1.035 mmol), 42%; colorless solid; 100% β (NMR).

MF $C_{70}H_{66}O_{14}SSi$ MW 1191.4290 [1190.3943]

R_F = 0.24 (SiO_2, CH:EA = 4:1).

$[\alpha]_D^{22}$ = -15.9 (*c* = 1.00; $CHCl_3$).

HR-QTOF-MS (ESI, pos.), *m/z*: 1213.3784 $[M+Na]^+$, (calc. 1213.3885).

^{1}H-NMR, COSY, TOCSY, HSQC, HSQC no dec., HMBC (400 MHz, CD_2Cl_2, 298K): δ [ppm] = 8.12 – 8.04 (m, 2H, H_{Ar}), 8.02 – 7.95 (m, 2H, H_{Ar}), 7.93 – 7.88 (m, 2H, H_{Ar}), 7.88 – 7.83 (m, 4H, H_{Ar}), 7.69 – 7.54 (m, 7H, H_{Ar}), 7.53 – 7.41 (m, 9H, H_{Ar}), 7.41 – 7.27 (m, 9H, H_{Ar}), 7.24 – 7.16 (m, 2H, H_{Ar}), 7.05 – 6.94 (m, 2H, H_{Ar}), 5.69 – 5.53 (m, 2H, H-3, H-3'), 5.39 – 5.26 (m, 2H, H-2, H-2'), 5.23 (s, 1H, $(RO)_2CHPh$), 5.07 (d, $^3J_{H\text{-}1',H\text{-}2'}$ = 8.0 Hz, 1H, H-1'), 4.82 (d, $^3J_{H\text{-}1,H\text{-}2}$ = 10.0 Hz, 1H, H-1), 4.47 (dd, $^3J_{H\text{-}4,H\text{-}3}$ = $^3J_{H\text{-}4,H\text{-}5}$ = 9.6 Hz, 1H, H-4), 3.96 (dd, *J* = 10.6 Hz, 4.9 Hz, 1H, H-6a'), 3.91 – 3.78 (m, 2H, H-6a, H-6b), 3.59 (t, $^3J_{H\text{-}4',H\text{-}3'}$ = $^3J_{H\text{-}4',H\text{-}5'}$ = 9.5 Hz, 1H, H-4'), 3.48 – 3.30 (m, 2H, H-5, H-5'), 2.83 (m, 1H, H-6b'), 2.28 (s, 3H), 1.18 (s, 9H, -Si-C(CH_3)$_3$).

^{13}C-NMR, HSQC, HSQC no dec., HMBC (101 MHz, CD_2Cl_2, 298K): δ [ppm] = 166.1 (-*C*OPh), 165.9 (-*C*OPh), 165.6 (-*C*OPh), 165.4 (-*C*OPh), 138.9 (C_{Ar}), 137.5 (C_{Ar}), 136.5 (C_{Ar}), 136.1 (C_{Ar}), 134.0 (C_{Ar}), 133.8 (C_{Ar}), 133.6 (C_{Ar}), 132.9 (C_{Ar}), 130.9 (C_{Ar}), 130.8 (C_{Ar}), 130.5 (C_{Ar}), 130.3 (C_{Ar}), 130.3 (C_{Ar}), 130.2 (C_{Ar}), 130.1 (C_{Ar}), 130.1 (C_{Ar}), 129.9 (C_{Ar}), 129.6 (C_{Ar}), 129.2 (C_{Ar}), 129.0 (C_{Ar}), 128.9 (C_{Ar}), 128.8 (C_{Ar}), 128.7 (C_{Ar}), 128.4 (C_{Ar}), 126.6 (C_{Ar}), 101.8 ($(RO)_2CHPh$), 101.0 (C-1'), 86.6 (C-1), 79.7 (C-5), 79.1

(C-4'), 75.1 (C-3'), 74.5 (C-4), 72.9 (C-2), 72.6 (C-3), 71.1 (C-2'), 68.4 (C-6'), 67.0 (C-5'), 61.7 (C-6), 27.3 ((-Si-C(CH$_3$)$_3$), 21.4 (-SPh-CH$_3$), 19.9 (-Si-C(CH$_3$)$_3$).

Ethyl 2,3,6,2',3',4',6'-hepta-*O*-acetyl-1-thio-β-D-cellobioside (I-14)

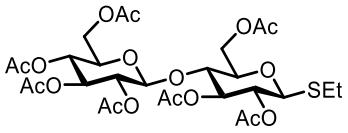

1,2,3,6,2',3',4',6'-Octa-*O*-acetyl-α/β-D-cellobiose **I-7** (10.000 g, 14.74 mmol, 1.0 eq.) was dissolved in dry CH_2Cl_2 (70 mL) and ethanethiol (1.2 mL, 1.007 g, 16.21 mmol, 1.1 eq.) was added. Consecutively, boron trifluoride diethyl etherate (2.1 mL, 2.301 g, 16.21 mmol, 1.1 eq.) were added dropwise at 0°C and the reaction mixture was stirred for 2 h at room temperature. The solution was diluted with 200 mL CH_2Cl_2, washed with saturated $NaHCO_{3(aq)}$ (3x100 mL) and conc. $NaCl_{(aq)}$ (150 mL). The organic layer was dried over $MgSO_4$ and then concentrated under reduced pressure. The resulting solid recrystallized in ethanol and was used without further purification.

Yield: 9.597 g (14.09 mmol), 96%; colorless solid; α:β = 1:40.

MF $C_{28}H_{40}O_{17}S$ MW 680.6710 [680.1986]

R_F = 0.33 (SiO_2, CH:EA = 1:1).

$[\alpha]_D^{20}$ = -12.9° (c = 1.00; $CHCl_3$).

HR-QTOF-MS (ESI, pos), *m/z*: 703.1870 $[M+Na]^+$, (calc. = 703.1878).

Signals assignable to β-anomer:

^{1}H-NMR, COSY, TOCSY, HSQC, HSQC no dec., HMBC (400 MHz, $CDCl_3$, 298 K): δ [ppm] = 5.18 (dd, $^3J_{H\text{-}3,H\text{-}2}$ = $^3J_{H\text{-}3,H\text{-}4}$ = 9.3 Hz, 1H, H-3), 5.13 (dd, $^3J_{H\text{-}3',H\text{-}2'}$ = $^3J_{H\text{-}3',H\text{-}4'}$ = 9.3 Hz, 1H, H-3'), 5.06 (dd, $^3J_{H\text{-}4',H\text{-}3'}$ = $^3J_{H\text{-}4',H\text{-}5'}$ = 9.6 Hz, 1H, H-4'), 4.98 – 4.87 (m, 2H, H-2, H-2'), 4.54 – 4.43 (m, 3H, H-1, H-6a, H-1'), 4.37 (dd, $^2J_{H\text{-}6a',H\text{-}6b'}$ = 12.5 Hz, $^3J_{H\text{-}6a',H\text{-}5'}$ = 4.3 Hz, 1H, H-6a'), 4.08 (dd, $^2J_{H\text{-}6b,H\text{-}6a}$ = 12.0 Hz, $^3J_{H\text{-}6b,H\text{-}5}$ = 5.4 Hz, 1H, H-6b), 4.03 (dd, $^2J_{H\text{-}6b',H\text{-}6a'}$ = 12.5 Hz, $^3J_{H\text{-}6b',H\text{-}5}$ = 2.3 Hz, 1H, H-6b'), 3.75 (dd, $^3J_{H\text{-}4,H\text{-}3}$ = $^3J_{H\text{-}4,H\text{-}5}$ = 9.5 Hz, 1H, H-4), 3.68 – 3.57 (m, 2H, H-5, H-5'), 2.72 – 2.60 (m, 2H, -S-CH_2-CH$_3$), 2.11 (s, 3H, -COCH_3), 2.08 (s, 3H, -COCH_3), 2.04 (s, 3H, -COCH_3), 2.02 (s, 3H, -COCH_3), 2.01 (s, 3H, -COCH_3), 2.00 (s, 3H, -COCH_3), 1.97 (s, 3H, -COCH_3), 1.25 (t, 3H, -S-CH$_2$-CH_3).

^{13}C-NMR, HSQC, HSQC no dec., HMBC (101 MHz, $CDCl_3$, 298 K): δ [ppm] = 170.6 (-COCH$_3$), 170.4 (-COCH$_3$), 170.4 (-COCH$_3$), 169.9 (-COCH$_3$), 169.8 (-COCH$_3$), 169.4 (-COCH$_3$), 169.2 (-COCH$_3$), 101.0 (C-1'), 83.6 (-1), 76.8 (C-5), 76.6 (C-4), 73.7 (C-3), 73.1 (C-3'), 72.1 (C-5'), 71.7 (C-2), 70.3

(C-2'), 67.9 (C-4'), 62.3 (C-6), 61.7 (C-6'), 24.6 (-S-*C*H$_2$-CH$_3$), 21.0 (-CO*C*H$_3$), 20.9 (-CO*C*H$_3$), 20.8 (-CO*C*H$_3$), 20.7 (-CO*C*H$_3$), 15.1 (-S-CH$_2$-*C*H$_3$).

Ethyl 1-thio-β-D-cellobioside (I-15)

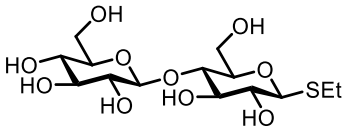

2,3,6,2',3',4',6'-Hepta-*O*-acetyl-1-thioethyl-β-D-cellobioside **I-14** (9.580 g, 14.07 mmol, 1.0 eq.) was suspended in methanol (55 mL) and sodium methoxide was added consecutively until a pH of 9 was reached. After stirring overnight at room temperature, the reaction solution was acidified to a pH of 3 with Amberlyst 15 (hydrogen form) and filtered over a pad of celite. The filtrate was concentrated under reduced pressure and the resulting solid was used without further purification.

Yield: 5.431 g (14.06 mmol), quant. ; colorless solid, α:β = 1:17 (NMR).

MF $C_{14}H_{26}O_{10}S$ MW 386.4120 [386.1247]

R_F = 0.90 (SiO_2, MeOH).

$[\alpha]_D^{20}$ = -16.8° (*c* = 1.00; MeOH).

HR-QTOF-MS (ESI, pos), *m/z* 409.1205 $[M+Na]^+$, (calc. = 409.1238).

Signals assignable to β-anomer:

^{1}H-NMR, COSY, TOCSY, HSQC, HSQC no dec., HMBC (400 MHz, D_2O, 298 K): δ [ppm] = 4.55 (d, $^3J_{H\text{-}1,H\text{-}2}$ = 10.0 Hz, 1H, H-1), 4.50 (d, $^3J_{H\text{-}1',H\text{-}2'}$ = 7.9 Hz, 1H, H-1'), 3.95 (dd, $^2J_{H\text{-}6a,H\text{-}6b}$ = 12.4 Hz, $^3J_{H\text{-}6a,H\text{-}5}$ = 2.0 Hz, 1H, H-6a), 3.90 (dd, $^2J_{H\text{-}6a',H\text{-}6b'}$ = 12.4 Hz, $^3J_{H\text{-}6a',H\text{-}5'}$ = 2.1 Hz, 1H, H-6a'), 3.78 (dd, $^2J_{H\text{-}6b,H\text{-}6a}$ = 12.4 Hz, $^3J_{H\text{-}6b,H\text{-}5}$ = 4.8 Hz, 1H, H-6b), 3.72 (dd, $^3J_{H\text{-}6b',H\text{-}6a'}$ = 12.4 Hz, $^3J_{H\text{-}6b',H\text{-}5'}$ = 5.6 Hz, 1H, H-6b'), 3.67 – 3.57 (m, 3H, H-3, H-4, H-5), 3.53 – 3.35 (m, 4H, H-3', H-4', H-5', H-2), 3.30 (dd, $^3J_{H\text{-}2',H\text{-}3'}$ = 9.3 Hz, $^3J_{H\text{-}2',H\text{-}1'}$ = 7.9 Hz, 1H, H-2'), 2.90 – 2.46 (m, 2H, -S-C*H*$_2$-CH$_3$), 1.42 – 0.91 (m, 3H, -S-CH$_2$-C*H*$_3$).

^{13}C-NMR, HSQC, HSQC no dec., HMBC (101 MHz, D_2O, 298 K): δ [ppm] = 102.5 (C-1'), 84.9 (C-1), 78.6 (C-5), 78.4 (C-4), 76.0 (C-5'), 75.7 (C-3), 75.4 (C-3'), 73.1 (C-2'), 72.0 (C-2), 69.4 (C-4'), 60.5 (C-6'), 60.1 (C-6), 24.1 (-S-*C*H$_2$-CH$_3$), 14.5 (-S-CH$_2$-*C*H$_3$).

Ethyl 4',6'-*O*-benzylidene-1-thio-β-D-cellobioside (I-16)

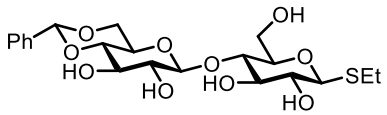

1-Thioethyl-α/β-cellobioside **I-15** (3.000 g, 7.76 mmol, 1.00 eq.) was dissolved in dry DMF, magnesium triflate (0.100 g, 0.31 mmol, 0.04 eq.) and benzaldehyde dimethyl acetal (2.9 mL, 2.95 g, 19.41 mmol, 2.50 eq.) were added. Successively, trifluoromethanesulfonic acid (0.27 mL, 0.466 g, 3.11 mmol, 0.40 eq.) was added dropwise at 0 ˚C to the reaction mixture. After stirring for 5 hours, another portion of benzaldehyde dimethyl acetal (1.5 mL, 1.515 g, 9.95 mmol, 1.28 eq.) was added. The reaction mixture was allowed to stir at ambient temperature for 20 h, then alkalized with triethylamine and concentrated *in vacuo*. The residue was purified by flash chromatography (SiO_2, gradient: 0% → 10% MeOH in CH_2Cl_2).

Yield: 3.272 g (6.90 mmol), 88%; colorless solid, 100% β (NMR).

MF $C_{21}H_{30}O_{10}S$ MW 474.5210 [474.1560]

R_F = 0.42 (SiO_2, CH_2Cl_2:MeOH = 10:1).

$[\alpha]_D^{20}$ = -30.8° (c = 1.00; MeOH).

HR-QTOF-MS (ESI, pos), *m/z:* 497.1462 $[M+Na]^+$, (calc. = 497.1452).

^{1}H-NMR, COSY, TOCSY, HSQC, HSQC no dec., HMBC (600 MHz, CD_2Cl_2, 298 K): δ [ppm] = 7.52 – 7.43 (m, 2H, H_{Ar}), 7.39 – 7.26 (m, 3H, H_{Ar}), 5.52 (s, 1H, $(RO)_2CH$Ph), 4.50 (d, $^3J_{H\text{-}1',H\text{-}2'}$ = 7.8 Hz, 1H, H-1'), 4.36 (d, $^3J_{H\text{-}1,H\text{-}2}$ = 9.8 Hz, 1H, H-1), 4.31 – 4.24 (m, 1H, H-6a'), 3.83 – 3.80 (m, 2H, H-6a, H-6b), 3.75 (m, 1H, H-6b'), 3.66 (dd, $^3J_{H\text{-}3',H\text{-}2'} = {}^3J_{H\text{-}3',H\text{-}4'}$ = 9.0 Hz, 1H, H-3'), 3.57 (dd, $^3J_{H\text{-}4,H\text{-}3} = {}^3J_{H\text{-}4,H\text{-}5}$ = 9.3 Hz, 1H, H-4), 3.53 – 3.48 (m, 3H, H-3, H-4', H-5'), 3.42 – 3.34 (m, 2H, H-5, H-2'), 3.32 – 3.26 (m, 1H, H-2), 2.86 – 2.51 (m, 2H, -S-CH_2-CH_3), 1.40 – 1.11 (m, 3H, -S-CH_2-CH_3).

^{13}C-NMR, HSQC, HSQC no dec., HMBC (151 MHz, CD_2Cl_2, 298 K): δ [ppm] = 137.8 (C_{Ar}), 129.7 (C_{Ar}), 128.8 (C_{Ar}), 126.8 (C_{Ar}), 104.7 (C-1'), 102.4 ($(RO)_2C$HPh), 86.2 (C-1), 81.0 (C-4), 81.0 (C-3), 79.3 (C-5), 76.7 (C-4'), 74.9 (C-2'), 73.7 (C-3'), 73.1 (C-2), 68.8 (C-6'), 67.2 (C-5'), 61.8 (C-6), 24.9 (-S-CH_2-CH_3), 15.4 (-S-CH_2-CH_3).

Ethyl 6-*O*-(*tert*-butyldiphenylsilyl)-4',6'-*O*-benzylidene-1-thio-β-D-cellobioside (I-17)

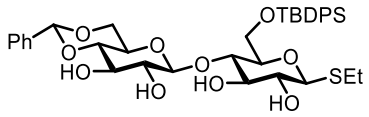

Ethyl 4',6'-O-benzylidene-1-thio-β-D-cellobioside **I-16** (0.950 g, 1.77 mmol, 1.0 eq.) was dissolved in DMF (6 mL). Imidazole (0.301 g, 4.43 mmol, 2.5 eq.) and tert-butyl diphenyl chlorosilane (0.60 mL, 0.633 g, 2.30 mmol, 1.3 eq.) were added to the solution. After stirring for 16 h, the reaction was quenched with cold water. The aqueous layer was extracted with CH_2Cl_2 (3x20 mL) and the organic layer was washed with saturated $(NH_4)_2SO_{2(aq)}$ (20 mL), dried over $MgSO_4$, and concentrated. The residue was purified by flash chromatography (SiO_2, gradient: 0% → 8% MeOH in CH_2Cl_2).

Yield: 1.123 g (1.58 mmol), 89%; colorless solid, 100% β (NMR).

MF $C_{37}H_{48}O_{10}SSi$ MW 712.9260 [712.2737]

R_F = 0.65 (SiO_2, DCM:MeOH = 10:1).

$[\alpha]_D^{20}$ = -41.8° (*c* = 1.00; $CHCl_3$).

HR-QTOF-MS (ESI, pos), *m/z:* 735.2623 $[M+Na]^+$, (calc. = 735.2330).

^{1}H-NMR, COSY, TOCSY, HSQC, HSQC no dec., HMBC (400 MHz, CD_2Cl_2, 298 K): δ [ppm] = 7.88 – 7.58 (m, 4H, H_{Ar}), 7.55 – 7.15 (m, 11H, H_{Ar}), 5.52 (s, 1H, $(RO)_2CHPh$), 4.62 (d, $^3J_{H\text{-}1',H\text{-}2'}$ = 7.8 Hz, 1H, H-1'), 4.35 (d, $^3J_{H\text{-}1,H\text{-}2}$ = 9.6 Hz, 1H, H-1), 4.30 (dd, $^2J_{H\text{-}6a',H\text{-}6b'}$ = 10.4 Hz, $^3J_{H\text{-}6a',H\text{-}5'}$ = 4.9 Hz, 1H, H-6a'), 4.04 (dd, $^2J_{H\text{-}6a,H\text{-}6b}$ = 11.6 Hz, $^3J_{H\text{-}6a,H\text{-}5}$ = 3.7 Hz, 1H, H-6a), 3.98 (dd, $^2J_{H\text{-}6b,H\text{-}6a}$ = 11.6 Hz, $^3J_{H\text{-}6b,H\text{-}5}$ = 2.1 Hz, 1H, H-6b), 3.84 – 3.68 (m, 3H, H-4, H-3', H-6b'), 3.56 (m, 2H, H-3, H-4), 3.51 – 3.40 (m, 4H, H-2, H-5, H-2', H-5'), 2.79 – 2.65 (m, 2H, -S-CH_2-CH_3), 1.29 (m, 3H, -S-CH_2-CH_3), 1.06 (s, 9H, -SiC(CH_3)$_3$).

^{13}C-NMR, HSQC, HSQC no dec., HMBC (101 MHz, CD_2Cl_2, 298 K): δ [ppm] = 136.4 (C_{Ar}), 136.2 (C_{Ar}), 130.3 (C_{Ar}), 129.8 (C_{Ar}), 128.8 (C_{Ar}), 128.3 (C_{Ar}), 128.2 (C_{Ar}), 126.8 (C_{Ar}), 104.0 (C-1'), 102.3 ($(RO)_2CHPh$), 85.7 (C-1), 80.6 (C-4'), 80.1 (C-4), 79.5 (C-5), 76.5 (C-3), 74.8 (C-2'), 73.9 (C-3'), 73.2 (C-2), 68.8 (C-6'), 67.2 (C-5'), 63.4 (C-6), 27.1((-Si-C(CH_3)$_3$), 24.4 (-S-CH_2-CH_3), 19.7 (-Si-C(CH_3)$_3$), 15.7 (-S-CH_2-CH_3).

Ethyl 2,3,2',3'-tetra-*O*-benzoyl-6-*O*-(*tert*-butyldiphenylsilyl)-4',6'-*O*-benzylidene-1-thio-β-D-cellobioside (I-6)

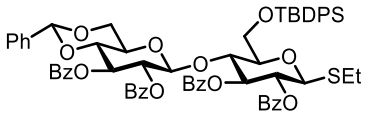

6-*O*-(tert-Butyldiphenylsilyl)-4',6'-*O*-benzylidene-1-thioethyl-β-D-cellobioside **I-17** (0.670 g, 0.94 mmol, 1.0 eq.) was dissolved in dry CH_2Cl_2. Pyridine (1.5 mL, 1.487 g, 18.80 mmol, 20.0 eq.), benzoyl chloride (1,7 mL, 2.114 g, 15.04 mmol, 16.0 eq.), and catalytic amount of 4-dimethylaminopyridine were added at 0 ˚C and the reaction mixture was stirred for 18 h at ambient temperature. After quenching the remaining benzoyl chloride with 10 mL cold water, the solution was diluted with CH_2Cl_2 (50 mL) and the organic layer was washed with saturated $NaCl_{(aq)}$ (2x30 mL), dried over $MgSO_4$ and concentrated *in vacuo*. The crude product was subjected to normal phase flash chromatography (SiO_2, gradient: 0% → 10% EA in CH) and further purified by reversed phase flash chromatography (C_{18}, gradient: 40% → 100% ACN in H_2O).

Yield: 0.969 g (0.86 mmol), 91%; colorless solid, 100% β (NMR).

MF $C_{65}H_{64}O_{14}SSi$ MW 1129.3580 [1128.3786]

R_F = 0.52 (SiO_2, CH:EA = 3:1).

$[\alpha]_D^{20}$ = 19.1° (c = 1.00; $CHCl_3$).

HR-QTOF-MS (ESI, pos), *m/z:* 1063.5334 $[M+Na]^+$, (calc. = 1063.3365).

^{1}H-NMR, COSY, TOCSY, HSQC, HSQC no dec., HMBC (400 MHz, CD_2Cl_2, 298K): δ [ppm] = 8.12 – 8.04 (m, 2H, H_{Ar}), 8.02 – 7.95 (m, 2H, H_{Ar}), 7.93 – 7.88 (m, 2H, H_{Ar}), 7.88 – 7.83 (m, 4H, H_{Ar}), 7.69 – 7.54 (m, 7H, H_{Ar}), 7.53 – 7.41 (m, 9H, H_{Ar}), 7.41 – 7.27 (m, 9H, H_{Ar}), 7.24 – 7.16 (m, 2H, H_{Ar}), 7.05 – 6.94 (m, 2H, H_{Ar}), 5.69 – 5.53 (m, 2H, H-3, H-3'), 5.39 – 5.26 (m, 2H, H-2, H-2'), 5.23 (s, 1H, $(RO)_2CHPh$), 5.07 (d, $^3J_{H\text{-}1',H\text{-}2'}$ = 8.0 Hz, 1H, H-1'), 4.82 (d, $^3J_{H\text{-}1,H\text{-}2}$ = 10.0 Hz, 1H, H-1), 4.47 (dd, $^3J_{H\text{-}4,H\text{-}3}$ = $^3J_{H\text{-}4,H\text{-}5}$ = 9.6 Hz, 1H, H-4), 3.96 (dd, $^2J_{H\text{-}6a',H\text{-}6b'}$ = 10.6 Hz, $^3J_{H\text{-}6a',H\text{-}5}$ = 4.9 Hz, 1H, H-6a'), 3.91 – 3.78 (m, 2H, H-6a, H-6b), 3.59 (t, $^3J_{H\text{-}4',H\text{-}3'}$ = $^3J_{H\text{-}4',H\text{-}5'}$ = 9.5 Hz, 1H, H-4'), 3.48 – 3.30 (m, 2H, H-5, H-5'), 2.83 (m, 1H, H-6b'), 2.28 (s, 3H), 1.18 (s, 9H, -Si-C(CH_3)$_3$).

^{13}C-NMR, HSQC, HSQC no dec., HMBC (101 MHz, CD_2Cl_2, 298K): δ [ppm] = 166.1 (-*C*OPh), 165.9 (-*C*OPh), 165.6 (-*C*OPh), 165.4 (-*C*OPh), 138.9 (C_{Ar}), 137.5 (C_{Ar}), 136.5 (C_{Ar}), 136.1 (C_{Ar}), 134.0 (C_{Ar}), 133.8 (C_{Ar}), 133.6 (C_{Ar}), 132.9 (C_{Ar}), 130.9 (C_{Ar}), 130.8 (C_{Ar}), 130.5 (C_{Ar}), 130.3 (C_{Ar}), 130.3 (C_{Ar}), 130.2 (C_{Ar}), 130.1 (C_{Ar}), 130.1 (C_{Ar}), 129.9 (C_{Ar}), 129.6 (C_{Ar}), 129.2 (C_{Ar}), 129.0 (C_{Ar}), 128.9 (C_{Ar}), 128.8 (C_{Ar}), 128.7 (C_{Ar}), 128.4 (C_{Ar}), 126.6 (C_{Ar}), 101.8 ($(RO)_2CHPh$), 101.0 (C-1'), 86.6 (C-1), 79.7 (C-5), 79.1

(C-4'), 75.1 (C-3'), 74.5 (C-4), 72.9 (C-2), 72.6 (C-3), 71.1 (C-2'), 68.4 (C-6'), 67.0 (C-5'), 61.7 (C-6), 27.3 ((-Si-C(CH$_3$)$_3$), 21.4 (-SPh-CH$_3$), 19.9 (-Si-C(CH$_3$)$_3$).

N-Benzyl(benzyloxy)carbonyl-5-aminopentyl 2,3,2',3'-tetra-O-benzoyl-6-O-(*tert*-butyldiphenyl-silyl)-4',6'-O-benzylidene-β-D-cellobioside (I-18)

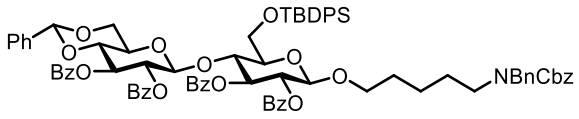

Disaccharide **I-6** (0.850 g, 0.75 mmol, 1.0 eq.) and *N*-(Benzyl)-benzyloxycarbonyl-5-aminopentan-1-ol **I-4** (0.271 g, 0.83 mmol, 1.1 eq.) were co-evaporated with toluene, dried under vacuum, dissolved in dry CH_2Cl_2 (8 mL) and stirred over freshly activated 4 Å molecular sieve powder for 1.5 h. Dimethyl disulfide (0.20 mL, 0.213 g, 2.26 mmol, 3.0 eq.) and methyl trifluoromethanesulfonate (0.49 mL, 0.741 g, 4.52 mmol, 6.0 eq.) were dissolved in dry CH_2Cl_2 (2 mL) to form the promotor. After stirring for 1.5 h, the promotor solution was added to the reaction mixture, which was stirred at ambient temperature for 20 h. After the addition of triethyl amine, the reaction mixture was filtered through a pad of celite and concentrated *in vacuo*. The crude product was subjected to normal phase flash chromatography (SiO_2, gradient: 0% → 40% EA in CH) and further purified by reversed phase flash chromatography (C_{18}, gradient: 50% → 100% ACN in H_2O).

Yield: 0.448 g (0.34 mmol), 44%; colorless solid, 100% β (NMR).

MF $C_{83}H_{83}NO_{17}Si$ MW 1394.6520 [1393.5430]

R_F = 0.28 (SiO_2, CH:EA = 4:1).

$[\alpha]_D^{20}$ = 11.0° (c = 1.00; $CHCl_3$).

HR-QTOF-MS (ESI, pos), *m/z:* 1416.5340 $[M+Na]^+$, (calc. = 1416.5322).

^{1}H-NMR, COSY, HSQC, HMBC (300 MHz, CD_2Cl_2, 298K): δ [ppm] 8.14 – 8.06 (m, 2H, H_{Ar}), 7.96 – 7.89 (m, 4H, H_{Ar}), 7.86 – 7.81 (m, 4H, H_{Ar}), 7.76 – 7.69 (m, 2H, H_{Ar}), 7.65 – 7.55 (m, 4H, H_{Ar}), 7.55 – 7.39 (m, 9H, H_{Ar}), 7.38 – 7.18 (m, 20H, H_{Ar}), 5.77 – 5.57 (m, 2H, H-3, H-3'), 5.42 – 5.34 (m, 2H, H-2, H-2'), 5.25 (s, 1H, (RO)$_2$CHPh), 5.18 – 5.09 (m, 3H, -CH_2Ph, H-1'), 4.62 – 4.52 (m, 1H, H-1), 4.47 (dd, $^3J_{H\text{-}3,H\text{-}4} = {}^3J_{H\text{-}4,H\text{-}5}$ = 9.5 Hz, 1H, H-4), 4.38 (s, 2H, -CH_2Ph), 3.98 (dd, $^2J_{H\text{-}6a',H\text{-}6b'}$ = 10.6 Hz, $^3J_{H\text{-}6a',H\text{-}5'}$ = 4.9 Hz, 1H, H-6a'), 3.90 – 3.74 (m, 3H, H-6b, -CH_2-), 3.64 (dd, $^3J_{H\text{-}3',H\text{-}4'} = {}^3J_{H\text{-}4',H\text{-}5'}$ = 9.5 Hz, 1H, H-4'), 3.51 – 3.40 (m, 1H, H-5'), 3.39 – 3.28 (m, 2H, H-5, H-6a), 3.10 – 2.93 (m, 2H, -CH_2-), 2.86 (m, 1H, H-6b'), 1.57 – 1.31 (m, 6H, -CH_2-), 1.17 (s, 9H, -Si-C(CH_3)$_3$).

^{13}C-NMR, HSQC, HMBC (75 MHz, CD_2Cl_2, 298K): δ [ppm] = 165.9 (*C*=O), 165.8 (*C*=O), 165.5 (*C*=O), 165.2 (*C*=O), 138.7 (C_{Ar}), 137.3 (C_{Ar}), 136.4 (C_{Ar}), 135.9 (C_{Ar}), 133.6 (C_{Ar}), 132.9 (C_{Ar}), 130.7 (C_{Ar}), 130.6 (C_{Ar}), 130.3 (C_{Ar}), 130.2 (C_{Ar}), 130.0 (C_{Ar}), 129.9 (C_{Ar}), 129.4 (C_{Ar}), 129.1 (C_{Ar}), 128.8 (C_{Ar}), 128.8 (C_{Ar}), 128.5 (C_{Ar}), 128.5 (C_{Ar}), 127.5 (C_{Ar}), 126.4 (C_{Ar}), 101.6 ($(RO)_2$*C*HPh), 101.0 (C-1, C-1'), 78.9 (C-4'), 75.4 (C-5), 75.0 (C-4), 73.6 (C-3), 72.8 (C-2'), 72.4 (C-2), 72.3 (C-3'), 69.7 (C-6), 68.3 (C-6'), 67.2 (-*C*H_2Ph), 66.8 (C-5'), 61.5 (-*C*H_2-), 50.4 (-*C*H_2Ph), 46.6 (-*C*H_2-), 29.4 (-*C*H_2-), 27.1 (-*C*H_2-), 23.4 (-C(*C*H_3)$_3$), 19.8 (-*C*(CH_3)$_3$).

_N_-Benzyl(benzyloxy)carbonyl-5-aminopentyl 2,3,2',3'-tetra-_O_-benzoyl-6-_O_-(_tert_-butyldiphenyl-silyl)-β-D-cellobioside (I-20)

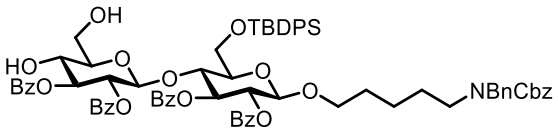

Disaccharide **I-18** (0.395 g, 0.28 mmol, 1.0 eq.) was dissolved in DCM (12 mL). Subsequently, 4 mL of a 90% aqueous TFA solution were added. After stirring at ambient temperature for 3 h, the solvent was removed under reduced pressure and the residue co-evaporated twice with 5 mL toluene. The product was purified using flash chromatography (SiO_2, gradient: 0% → 50% EA in CH).

Yield: 0.222 g (0.17 mmol), 60%; colorless oil, 100% β (NMR).

MF $C_{76}H_{79}NO_{17}Si$ MW 1306.5430 [1305.5117]

R_F = 0.18 (SiO_2, CH:EA = 3:1).

$[\alpha]_D^{20}$ = 6.0° (c = 1.00; $CHCl_3$).

HR-QTOF-MS (ESI, pos), *m/z:* 1328.4989 $[M+Na]^+$, (calc. = 1328.5009).

^{1}H-NMR, COSY, TOCSY, HSQC, HSQC no dec., HMBC (600 MHz, $CDCl_3$, 298 K): δ [ppm] = 8.16 – 8.06 (m, 2H, H_{Ar}), 7.99 – 7.89 (m, 4H, H_{Ar}), 7.86 – 7.79 (m, 4H, H_{Ar}), 7.77 – 7.67 (m, 2H, H_{Ar}), 7.62 – 7.50 (m, 5H, H_{Ar}), 7.50 – 7.36 (m, 9H, H_{Ar}), 7.36 – 7.24 (m, 11H, H_{Ar}), 7.24 – 7.17 (m, 2H, H_{Ar}), 7.16 – 7.08 (m, 1H, H_{Ar}), 5.63 (dd, $^3J_{H\text{-}3,H\text{-}2}$ = $^3J_{H\text{-}3,H\text{-}4}$ = 9.6 Hz, 1H, H-3), 5.47 – 5.38 (m, 1H, H-2), 5.39 – 5.22 (m, 2H, H-2', H-3'), 5.18 – 5.11 (m, 2H, -CH_2Ph), 5.06 (d, $^3J_{H\text{-}1',H\text{-}2'}$ = 7.6 Hz, 1H, H-1'), 4.61 – 4.48 (m, 1H, H-1), 4.43 (dd, $^3J_{H\text{-}4,H\text{-}3}$ = $^3J_{H\text{-}4,H\text{-}5}$ = 9.5 Hz, 1H, H-4), 4.42 – 4.33 (m, 2H, -CH_2Ph), 3.95 – 3.76 (m, 3H, H-6a', -CH_2-), 3.71 (dd, $^3J_{H\text{-}4',H\text{-}3'}$ = $^3J_{H\text{-}4',H\text{-}5'}$ = 9.0 Hz, 1H, H-4'), 3.55 – 3.50 (m, 1H, H-6a'), 3.40 – 3.26 (m, 4H, H-5, H-6b, H-5', H-6b'), 3.09 – 2.91 (m, 2H, -CH_2-), 1.45 – 1.31 (m, 4H, -CH_2-), 1.15 (s, 9H, -Si-C(CH_3)$_3$), 1.13 – 1.07 (m, 2H, -CH_2-).

^{13}C-NMR, HSQC, HSQC no dec., HMBC (151 MHz, $CDCl_3$, 298 K): δ [ppm] = 167.2 (*C*=O), 165.3 (*C*=O), 164.8 (*C*=O), 136.1 (C_{Ar}), 135.6 (C_{Ar}), 133.6 (C_{Ar}), 133.5 (C_{Ar}), 133.3 (C_{Ar}), 133.2 (C_{Ar}), 132.4 (C_{Ar}), 130.4 (C_{Ar}), 130.0 (C_{Ar}), 129.8 (C_{Ar}), 129.7 (C_{Ar}), 129.6 (C_{Ar}), 129.0 (C_{Ar}), 128.9 (C_{Ar}), 128.8 (C_{Ar}), 128.6 (C_{Ar}), 128.6 (C_{Ar}), 128.5 (C_{Ar}), 128.4 (C_{Ar}), 128.3 (C_{Ar}), 128.2 (C_{Ar}), 128.0 (C_{Ar}), 127.9 (C_{Ar}), 127.9 (C_{Ar}), 127.4 (C_{Ar}), 127.3 (C_{Ar}), 127.2 (C_{Ar}), 100.8 (C-1), 100.1 (C-1'), 76.8 (C-3'), 76.0 (C-5), 75.2 (C-5'), 74.2 (C-4), 73.4 (C-3), 71.9 (C-2), 71.6 (C-2'), 69.2 (C-4'), 69.2 (C-6'), 67.2 (-*C*H$_2$Ph), 61.6 (C-6), 61.1 (-*C*H$_2$-), 50.6 (-*C*H$_2$Ph), 47.1 (-*C*H$_2$-), 29.8 (-*C*H$_2$-), 27.8 (-*C*H$_2$-), 27.1 (-C(*C*H$_3$)$_3$), 22.8 (-*C*H$_2$-), 19.6 (-*C*(CH$_3$)$_3$).

_N_-Benzyl(benzyloxy)carbonyl-5-aminopentyl (methyl 2,3,2',3'-tetra-_O_-benzoyl-6-_O_-(_tert_-butyl-diphenylsilyl)-1-β-D-cellobiuronate) (I-21)

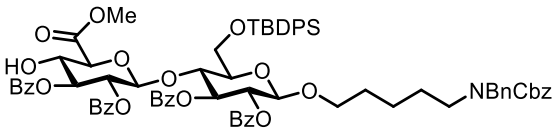

Disaccharide **I-21** (222 mg, 0.170 mmol, 1.0 eq.) was dissolved in CH_2Cl_2 (5 mL) and water (1 mL) followed by the addition of BAIB (66 mg, 0.204 mmol, 1.5 eq.) and TEMPO (13 mg, 0.085 mmol, 0.5 eq.). After stirring for 1 d at ambient temperature, another portion of BAIB (43 mg, 0.136 mmol, 1.0 eq.) and TEMPO (7 mg, 0.051 mmol, 0.3 eq.) were added. The reaction mixture was stirred for 1 d longer and quenched with of a 10% NaS_2O_3 solution (10 mL). The organic layer was separated and the aqueous layer was acidified to pH=1 and extracted with CH_2Cl_2 (2×20 mL). The organic layers were combined, dried over $MgSO_4$ and concentrated. The crude product was redissolved in 5 mL of a CH_2Cl_2/MeOH-mixture (1:1). Subsequently, a solution of trimethylsilyldiazomethane (2M in hexane, 0.25 mL, 58 mg, 0.510 mmol, 3.0 eq.) was added. The reaction mixture was stirred for 20 min and quenched with acetic acid (1 mL). The solution was diluted with CH_2Cl_2 (30 mL), washed with saturated $NaHCO_{3(aq)}$ (20 mL), dried over $MgSO_4$ and concentrated *in vacuo*. The product was purified using flash chromatography (SiO_2, gradient: 0% → 50% EA in CH).

Yield: 169 mg (0.126 mmol), 74%; colorless solid, 100% β (NMR).

MF $C_{77}H_{79}NO_{18}Si$ MW 1334.5530 [1335.5066]

R_F = 0.33 (SiO_2, CH:EA = 2:1).

$[\alpha]_D^{20}$ = 9.0° (c = 1.00; $CHCl_3$).

HR-QTOF-MS (ESI, pos), *m/z:* 1356.4999 $[M+Na]^+$, (calc. = 1356.4959).

^{1}H-NMR, COSY, TOCSY, HSQC, HSQC no dec., HMBC (600 MHz, CD_2Cl_2, 298 K): δ [ppm] = 8.04 – 7.78 (m, 10H, H_{Ar}), 7.75 – 7.68 (m, 2H, H_{Ar}), 7.63 – 7.08 (m, 28H, H_{Ar}), 5.58 (dd, $^3J_{H\text{-}3,H\text{-}2} = {}^3J_{H\text{-}3,H\text{-}4}$ = 9.6 Hz, 1H, H-3), 5.46 – 5.34 (m, 2H, H-2', H-3'), 5.29 – 5.26 (m, 1H, H-2), 5.14 (d, $^3J_{H\text{-}1,H\text{-}2}$ = 7.8 Hz, 1H, H-1), 5.09 (s, 2H, -CH_2Ph), 4.64 – 4.46 (m, 2H, H-1', H-4), 4.36 (s, 2H, CH_2Ph), 4.00 (m, 1H, H-5'), 3.94 – 3.71 (m, 4H, H-4', H-6a, -CH_2-), 3.59 (s, 3H, -COOCH_3), 3.46 – 3.25 (m, 2H, H-5, H-6b), 3.11 – 2.87 (m, 2H, -CH_2-), 1.46 – 1.29 (m, 4H, -CH_2-), 1.17 (s, 9H, -Si-C(CH_3)$_3$), 1.12 – 1.00 (m, 2H, -CH_2-).

^{13}C-NMR, HSQC, HSQC no dec., HMBC (151 MHz, CD_2Cl_2, 298 K): δ [ppm] = 168.3 (*C*OOCH$_3$), 166.1 (*C*=O^{Bz}), 165.8 (*C*=O^{Bz}), 165.1 (*C*=O^{Bz}), 164.7 (*C*=O^{Bz}), 156.44 (*C*=O^{Cbz}), 138.3 (C_{Ar}), 137.2 (C_{Ar}), 136.0 (C_{Ar}), 135.5 (C_{Ar}), 133.6 (C_{Ar}), 133.4 (C_{Ar}), 133.3 (C_{Ar}), 133.2 (C_{Ar}), 132.8 (C_{Ar}), 132.4 (C_{Ar}), 130.2 (C_{Ar}) 130.1 (C_{Ar}), 129.9 (C_{Ar}), 129.7 (C_{Ar}), 129.6 (C_{Ar}), 129.1 (C_{Ar}) 128.8 (C_{Ar}), 128.4 (C_{Ar}), 128.4 (C_{Ar}), 128.3 (C_{Ar}), 128.2 (C_{Ar}), 127.8 (C_{Ar}), 127.6 (C_{Ar}), 127.5 (C_{Ar}), 127.1 (C_{Ar}), 100.7 (C-1'),

100.2 (C-1), 75.1 (C-5), 74.9 (C-3'), 74.5 (C-4'), 73.7 (C-4), 73.1 (C-3), 71.4 (C-2), 70.2 (C-5'), 69.3 (-*C*H$_2$-), 66.9 (-*C*H$_2$Ph), 61.1 (C-6), 52.8 (C-2), 52.7 (-*C*H$_3$), 50.4 (-*C*H$_2$Ph), 47.0 (-*C*H$_2$-), 29.7 (-*C*H$_2$-), 27.8 (-C(*C*H$_3$)$_3$), 26.8 (-*C*H$_2$-), 23.1 (-*C*H$_2$-), 19.4 (-*C*(CH$_3$)$_3$).

_N_-Benzyl(benzyloxy)carbonyl-5-aminopentyl (methyl 2,3,2',3'-tetra-_O_-benzoyl-β-D-cellobiuronate) (I-22)

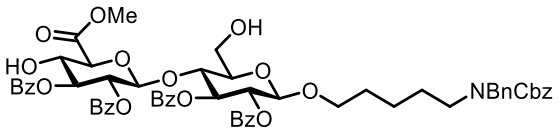

Method a:

To a solution of disaccharide **I-21** (85 mg, 0.064 mmol, 1.0 eq.) in THF (3 mL), a 1 M TBAF solution in THF (0.1 mL, 25 mg, 0.96 mmol, 1.5 eq.) was added. After stirring for 4 h at ambient temperature, the reaction was quenched by addition of water (5 mL) and extracted with CH_2Cl_2 (2×10 mL). The organic layers were combined, dried over $MgSO_4$ and concentrated *in vacuo*. The product was purified using flash chromatography (SiO_2, gradient: 0% → 10% MeOH in CH_2Cl_2).

Yield: 24 mg (0.022 mmol), 33%; colorless solid, 100% β (NMR).

Method b:

To a solution of disaccharide **I-21** (150 mg, 0.112 mmol, 1.0 eq.) in THF (2 mL), pyridine (0.5 mL) and HF-pyridine complex (0.03 mL, 32 mg, 1.120 mmol, 10.0 eq.) were added. After stirring for 22 h at ambient temperature, the reaction was quenched by the addition of sat. $NaHCO_{3(aq)}$ (5 mL), extracted with ethyl acetate (2×20 mL), washed with brine, dried over $MgSO_4$ and concentrated *in vacuo*. The product was purified using flash chromatography (SiO_2, gradient: 0% → 100% EA in CH).

Yield: 103 mg (0.094 mmol), 84%; colorless solid, 100% β (NMR).

MF $C_{61}H_{61}NO_{18}$ MW 1096.1480 [1095.3889]

R_F = 0.17 (SiO_2, CH:EA = 2:1).

$[\alpha]_D^{20}$ = 10.4° (*c* = 1.00; $CHCl_3$).

HR-QTOF-MS (ESI, pos), *m/z:* 1118.3786 $[M+Na]^+$, (calc. = 1118.3781).

^{1}H-NMR, COSY, TOCSY, HSQC, HSQC no dec., HMBC (300 MHz, $CDCl_3$, 298 K): δ [ppm] = 8.17 – 7.79 (m, 8H, H_{Ar}), 7.58 – 7.01 (m, 22H, H_{Ar}), 5.65 (dd, $^{3}J_{H\text{-}3,H\text{-}2} = {}^{3}J_{H\text{-}3,H\text{-}4}$ = 9.5 Hz, 1H, H-3), 5.49 (dd, $^{3}J_{H\text{-}3',H\text{-}2'}$ = 9.8 Hz, $^{3}J_{H\text{-}3',H\text{-}4'}$ = 8.7 Hz, 1H, H-3'), 5.39 (dd, $^{3}J_{H\text{-}2',H\text{-}3'}$ = 9.8 Hz, $^{3}J_{H\text{-}2',H\text{-}1'}$ = 7.8 Hz, 1H, H-2'), 5.34 – 5.23 (m, 1H, H-2), 5.12 (s, 2H, -CH_2Ph), 4.99 (d, $^{3}J_{H\text{-}1',H\text{-}2'}$ = 7.8 Hz, 1H, H-1'), 4.55 (d, $^{3}J_{H\text{-}1,H\text{-}2}$ = 7.9 Hz, 1H, H-1), 4.37 (s, 2H, -CH_2Ph), 4.32 – 4.20 (m, 1H, H-4), 4.05 – 3.87 (m, 2H, H-4', H-5'), 3.77 – 3.70 (m, 3H, H-6a, H-6b, -CH*H*-), 3.43 – 3.37 (m, 5H, H-5, -COOCH_3, -CH*H*-), 3.12 – 2.83 (m, 2H, -CH_2-), 1.55 – 1.35 (m, 4H, -CH_2-), 1.17 – 1.02 (m, 2H, -CH_2-).

^{13}C-NMR, HSQC, HSQC no dec., HMBC (75 MHz, $CDCl_3$, 298 K): δ [ppm] = 168.3 (*C*$OOCH_3$), 166.5 (*C*=O^{Bz}), 165.6 (*C*=O^{Bz}), 165.3 (*C*=O^{Bz}), 164.9 (*C*=O^{Bz}), 156.4 ((*C*=O^{Cbz})) 137.9 (C_{Ar}), 133.4 (C_{Ar}), 133.2 (C_{Ar}), 132.9 (C_{Ar}), 130.0 (C_{Ar}), 129.8 (C_{Ar}), 129.7 (C_{Ar}), 129.4 (C_{Ar}), 129.0 (C_{Ar}), 128.6 (C_{Ar}), 128.4 (C_{Ar}), 128.4 (C_{Ar}), 128.0 (C_{Ar}), 127.9 (C_{Ar}), 127.3 (C_{Ar}), 101.0 (C-1, C-1'), 75.2 (C-4, C-5, C-3'), 74.7 (C-5'), 73.3 (C-3), 72.2 (C-2), 71.5 (C-2'), 70.4 (C-4'), 69.7 (-*C*H_2-), 67.2 (-*C*H_2Ph), 60.5 (C-6), 52.6(-*C*H_3), 50.4 (-*C*H_2Ph), 46.5 (-*C*H_2-), 29.0 (-*C*H_2-), 22.9 (-*C*H_2-).

5-Aminopentyl β-D-cellobiuronic acid (I-25)

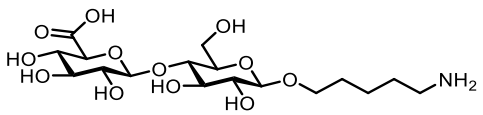

To a solution of disaccharide **I-22** (74 mg, 0.068 mmol, 1.0 eq.) in THF (3 mL), a 1M aqueous solution of LiOH (2 mL) was added. The reaction mixture was stirred for 2 d at ambient temperatures and acidified using Amberlyst 15 (hydrogen form) until pH = 4 was reached. The solution was filtrated, concentrated *in vacuo* and the residue was dissolved in 5 mL H_2O/MeOH mixture (1:1). After addition of Pd/C catalyst (10 mg), the reaction was flushed twice with H_2 and was stirred under H_2 atmosphere for 2 d. To remove the Pd/C catalyst, the reaction mixture was filtered through a pad of celite and the solvent was removed under vacuum.

Yield: 30 mg (0.068 mmol), quant.; colorless solid, 100% β (NMR).

MF $C_{17}H_{31}NO_{12}$ MW 441.4300 [441.1846]

$[\alpha]_D^{20}$ = -7.0° (*c* = 1.00; H_2O).

HR-QTOF-MS (ESI, neg), *m/z:* 500.1987 $[M+CH_3COO]^-$, (calc. = 500.1985).

^{1}H-NMR, COSY, HSQC, HMBC (400 MHz, D_2O, 298 K): δ [ppm] = 4.28 (d, $^3J_{H\text{-}1',H\text{-}2'}$ = 7.9 Hz, 1H, H-1'), 4.19 (d, $^3J_{H\text{-}1,H\text{-}2}$ = 8.1 Hz, 1H, H-1), 3.82 – 3.74 (m, 1H, H-5'), 3.70 – 3.57 (m, 2H, H-4, H-6a), 3.57 – 3.48 (m, 1H, H-6b), 3.43 – 3.23 (m, 6H, C-3, C-5, C-3', C-4', -CH_2-), 3.13 – 3.03 (m, 1H, C-2'), 3.02 – 2.94 (m, 1H, C-2), 2.89 – 2.83 (m, 1H, -CH*H*-), 2.79 – 2.67 (m, 1H, -C*H*H-), 1.53 – 1.32 (m, 4H, -CH_2-), 1.19 – 1.09 (m, 2H, -CH_2-).

^{13}C-NMR, HSQC, HSQC no dec., HMBC (101 MHz, D_2O, 298 K): δ [ppm] = 170.5 (-C-6'), 102.1 (C-1'), 101.9 (C-1), 78.6, 74.8, 74.4, 74.1, 73.8, 72.7, 72.5, 70.9, 69.7 (C-6), 59.7 (-*C*H_2-), 42.5 (-*C*H_2-), 28.0 (-*C*H_2-), 23.5 (-*C*H_2-), 21.9 (-*C*H_2-).

_N_-Benzyl(benzyloxy)carbonyl-5-aminopentyl 2,3,2',3',4',6'-hexa-_O_-benzoyl-6-_O_-(_tert_-butyldiphenylsilyl)-β-D-cellobioside (I-26)

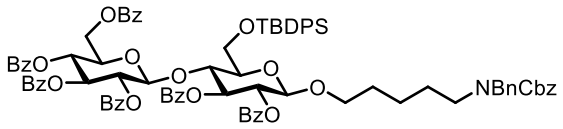

Disaccharide **I-20** (530 mg, 0.41 mmol, 1.0 eq.) was dissolved in dry CH_2Cl_2 (12 mL). After the addition of pyridine (0.39 mL, 385 mg, 4.87 mmol, 12.0 eq.), benzoyl chloride (0.24 mL, 285 mg, 2.03 mmol, 5.0 eq.) and catalytic amount of DMAP, the mixture was stirred at ambient temperatures for 20 h. Subsequently, the reaction mixture was diluted with CH_2Cl_2 (50 mL), washed with saturated $NaHCO_{3(aq)}$ (30 mL) and brine (30 mL), dried over $MgSO_4$ and concentrated *in vacuo*. The crude product was subjected to normal phase flash chromatography (SiO_2, gradient: 0% → 40% EA in CH) and further purified by reversed phase flash chromatography (C_{18}, gradient: 30% → 100% ACN in H_2O).

Yield: 0.400 g (0.26 mmol), 65%; colorless solid, 100% β (NMR).

MF $C_{90}H_{87}NO_{19}Si$ MW 1514.7590 [1513.5642]

R_F = 0.71 (SiO_2, CH:EA = 2:1).

$[\alpha]_D^{20}$ = -5.0° (*c* = 1.00; $CHCl_3$).

HR-QTOF-MS (ESI, pos), *m/z:* 1536.5520 $[M+Na]^+$, (calc. = 1536.5534).

^{1}H-NMR, COSY, TOCSY, HSQC, HSQC no dec., HMBC (400 MHz, $CDCl_3$, 298 K): δ [ppm] = 8.07 – 7.98 (m, 4H, H_{Ar}), 7.93 – 7.76 (m, 10H, H_{Ar}), 7.74 – 7.65 (m, 2H, H_{Ar}), 7.66 – 7.53 (m, 4H, H_{Ar}), 7.51 – 7.45 (m, 3H, H_{Ar}), 7.45 – 7.22 (m, 21H, H_{Ar}), 7.22 – 7.06 (m, 6H, H_{Ar}), 5.78 (dd, $^3J_{H\text{-}3',H\text{-}2'} = {}^3J_{H\text{-}3',H\text{-}4'}$ = 9.7 Hz, 1H, H-3'), 5.71 (dd, $^3J_{H\text{-}3,H\text{-}2} = {}^3J_{H\text{-}3,H\text{-}4}$ = 9.7 Hz, 1H, H-3), 5.51 (dd, $^3J_{H\text{-}2',H\text{-}3'}$ = 9.7 Hz, $^3J_{H\text{-}2',H\text{-}1'}$ = 8.1 Hz, 1H, H-2'), 5.39 (dd, $^3J_{H\text{-}2,H\text{-}1} = {}^3J_{H\text{-}2,H\text{-}3}$ = 8.9 Hz, 1H, H-2), 5.32 – 5.21 (m, 2H, H-1', H-4'), 5.12 (s, 2H, -CH_2Ph), 4.60 – 4.42 (m, 2H, H-1, H-4), 4.41 – 4.33 (m, 2H, -CH_2Ph), 4.30 (dd, $^2J_{H\text{-}6b',H\text{-}6a'}$ = 12.0 Hz, $^3J_{H\text{-}6b',H\text{-}5'}$ = 2.6 Hz, 1H, H-6b'), 4.01 – 3.88 (m, 2H, H-6a, H-5'), 3.86 – 3.74 (m, 2H, H-6b, -CHH-), 3.59 (dd, $^2J_{H\text{-}6a',H\text{-}6b'}$ = 12.0 Hz, $^3J_{H\text{-}6a',H\text{-}5'}$ = 7.3 Hz, 1H, H-6a'), 3.39 – 3.25 (m, 2H, -CHH-, H-5), 3.07 – 2.89 (m, 2H, -CH_2-), 1.56 – 1.27 (m, 4H, -CH_2-), 1.09 (s, 2H, -CH_2-), 1.05 (s, 9H, -SiC(CH_3)$_3$).

^{13}C-NMR, HSQC, HSQC no dec., HMBC (101 MHz, $CDCl_3$, 298 K): δ [ppm] = 166.0 (*C*=O^{Bz}), 165.8 (*C*=O^{Bz}), 165.7 (*C*=O^{Bz}), 165.4 (*C*=O^{Bz}), 164.7 (*C*=O^{Bz}), 138.1 (C_{Ar}), 136.2 (C_{Ar}), 135.6 (C_{Ar}), 133.7 (C_{Ar}), 133.6 (C_{Ar}), 133.4 (C_{Ar}), 133.3 (C_{Ar}), 133.2 (C_{Ar}), 133.1 (C_{Ar}), 132.2 (C_{Ar}), 130.5 (C_{Ar}), 130.1 (C_{Ar}), 130.0 (C_{Ar}), 129.8 (C_{Ar}), 129.8 (C_{Ar}), 129.7 (C_{Ar}), 129.7 (C_{Ar}), 129.0 (C_{Ar}), 128.9 (C_{Ar}), 128.8 (C_{Ar}), 128.7 (C_{Ar}), 128.6 (C_{Ar}), 128.5 (C_{Ar}), 128.4 (C_{Ar}), 128.2 (C_{Ar}), 128.1 (C_{Ar}), 127.9 (C_{Ar}), 127.9 (C_{Ar}), 101.0 (C-1), 100.2 (C-1'), 75.3 (C-5), 74.4 (C-4), 73.1 (C-3'), 72.9 (C-3), 72.7 (C-5'), 72.2 (C-2),

71.9 (C-2'), 69.8 (C-4'), 69.3 (-*C*H_2-), 67.2 (-*C*H_2Ph), 63.2 (C-6'), 61.1 (C-6), 50.7 (-*C*H_2Ph), 46.2 (-*C*H_2-), 29.1 (-*C*H_2-), 27.5, 26.9 (-*C*H_2-), 23.2 (-*C*H_2-), 19.5 (-*C*$(CH_3)_3$).

_N_-Benzyl(benzyloxy)carbonyl-5-aminopentyl 2,3,2',3',4',6'-hexa-_O_-benzoyl-β-D-cellobioside (I-27)

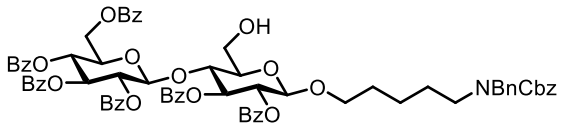

To a solution of disaccharide **I-26** (380 mg, 0.25 mmol, 1.0 eq.) in THF (5 mL), pyridine (1 mL) and HF-pyridine complex (0.10 mL, 108 mg, 3.76 mmol, 15.0 eq.) were added. After stirring for 2 d at ambient temperature, the reaction was quenched by the addition of sat. $NaHCO_{3(aq)}$ (10 mL), extracted with ethyl acetate (2×30 mL), washed with brine (20 mL), dried over $MgSO_4$ and concentrated *in vacuo*. The product was purified using flash chromatography (SiO_2, gradient: 0% → 50% EA in CH).

Yield: 0.285 g (0.22 mmol), 89%; colorless solid, 100% β (NMR).

MF $C_{74}H_{69}NO_{19}$ MW 1276.3540 [1275.4464]

R_F = 0.17 (SiO_2, CH:EA = 2:1).

$[\alpha]_D^{20}$ = -8.0° (c = 1.00; $CHCl_3$).

HR-QTOF-MS (ESI, pos), *m/z:* 1298.4338 $[M+Na]^+$, (calc. = 1298.4356).

^{1}H-NMR, COSY, TOCSY, HSQC, HSQC no dec., HMBC (400 MHz, $CDCl_3$, 298 K): δ [ppm] = 8.01 – 7.84 (m, 9H, H_{Ar}), 7.81 – 7.71 (m, 4H, H_{Ar}), 7.59 – 7.48 (m, 2H, H_{Ar}), 7.47 – 7.36 (m, 7H, H_{Ar}), 7.35 – 7.21 (m, 14H, H_{Ar}), 7.18 – 7.08 (m, 4H, H_{Ar}), 5.81 (dd, $^3J_{H\text{-}3',H\text{-}2'} = {}^3J_{H\text{-}3',H\text{-}4'}$ = 9.7 Hz, 1H, H-3'), 5.70 (dd, $^3J_{H\text{-}3,H\text{-}2} = {}^3J_{H\text{-}3,H\text{-}4}$ = 9.6 Hz, 1H, H-3), 5.50 (dd, $^3J_{H\text{-}2',H\text{-}3'}$ = 9.7 Hz, $^3J_{H\text{-}2',H\text{-}1'}$ = 8.0 Hz, 1H, H-2'), 5.41 (dd, $^3J_{H\text{-}4',H\text{-}3'} = {}^3J_{H\text{-}4',H\text{-}5'}$ = 9.6 Hz, 1H, H-4'), 5.34 – 5.29 (m, 1H, H-2), 5.13 (s, 2H, -CH_2Ph), 5.06 – 5.00 (m, 1H, H-1'), 4.61 – 4.50 (m, 1H, H-1), 4.38 (s, 2H, -CH_2Ph), 4.27 – 4.20 (m, 1H, H-4), 4.06 – 3.93 (m, 2H, H-5', H-6a'), 3.84 (dd, $^3J_{H\text{-}6b',H\text{-}6a'}$ = 11.6 Hz, $^3J_{H\text{-}6b',H\text{-}5'}$ = 4.9 Hz, 1H, H-6b'), 3.80 – 3.68 (m, 3H, H-6a, H-6b, -CHH-), 3.44 – 3.25 (m, 2H, H-5, -CHH-), 3.12 – 2.89 (m, 2H, -CH_2-), 1.51 – 1.28 (m, 6H, -CH_2-).

^{13}C-NMR, HSQC, HSQC no dec., HMBC (101 MHz, $CDCl_3$, 298 K): δ [ppm] = 165.9 (C=O^{Bz}), 165.8 (C=O^{Bz}), 165.6 (C=O^{Bz}), 165.6 (C=O^{Bz}), 165.1 (C=O^{Bz}), 164.8 (C=O^{Bz}), 156.8 (C=O^{Cbz}), 138.0 (C_{Ar}), 133.5 (C_{Ar}), 133.5 (C_{Ar}), 133.3 (C_{Ar}), 133.2 (C_{Ar}), 129.9 (C_{Ar}), 129.8 (C_{Ar}), 129.7 (C_{Ar}), 129.6 (C_{Ar}), 129.5 (C_{Ar}), 129.1 (C_{Ar}), 128.9 (C_{Ar}), 128.7 (C_{Ar}), 128.5 (C_{Ar}), 128.5 (C_{Ar}), 128.4 (C_{Ar}), 128.3 (C_{Ar}), 128.1 (C_{Ar}), 128.0 (C_{Ar}), 127.4 (C_{Ar}), 127.3 (C_{Ar}), 101.2 (C-1), 101.0 (C-1'), 75.4 (C-4), 75.2 (C-5), 73.1 (C-3'), 72.9 (C-3), 72.3 (C-5'), 72.1 (C-2, C-2'), 69.9 (-CH$_2$-), 69.6 (C-4'), 67.3 (-CH$_2$Ph), 62.1 (C-6'), 60.3 (C-6), 50.4 (-CH$_2$Ph), 47.2 (-CH$_2$-), 29.1 (-CH$_2$-), 27.1 (-CH$_2$-), 23.0 (-CH$_2$-).

_N_-Benzyl(benzyloxy)carbonyl-5-aminopentyl 2,3,4,6-tetra-_O_-benzoyl-β-D-glucopyranosyl-(1→4)-(methyl 2,3-di-_O_-benzoyl-β-D-glucopyranosiduronate) (I-28)

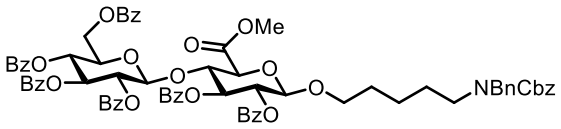

Disaccharide **I-27** (275 mg, 0.210 mmol, 1.0 eq.) was dissolved in CH_2Cl_2 (5 mL) and water (1 mL) followed by the addition of BAIB (86 mg, 0.270 mmol, 1.3 eq.) and TEMPO (16 mg, 0.105 mmol, 0.5 eq.). After stirring for 1 d at ambient temperature, another portion of BAIB (40 mg, 0.124 mmol, 0.6 eq.) and TEMPO (10 mg, 0.064 mmol, 0.3 eq.) were added. The reaction mixture was stirred for 1 d longer and quenched with of a 10% NaS_2O_3 solution (20 mL). The organic layer was separated and the aqueous layer was acidified to pH=1 and extracted with CH_2Cl_2 (2×20 mL). The organic layers were combined, dried over $MgSO_4$ and concentrated. The crude product was redissolved in 5 mL of a CH_2Cl_2/MeOH-mixture (1:1). Subsequently, a solution of trimethylsilyldiazomethane (2 M in hexane, 0.32 mL, 72 mg, 0.631 mmol, 3.0 eq.) was added. The reaction mixture was stirred for 20 min and quenched with acetic acid (1 mL). The solution was diluted with CH_2Cl_2 (20 mL), washed with saturated $NaHCO_{3(aq)}$ (2×10 mL), dried over $MgSO_4$ and concentrated *in vacuo*. The crude product was subjected to normal phase flash chromatography (SiO_2, gradient: 0% → 50% EA in CH) and further purified by reversed phase flash chromatography (C_{18}, gradient: 10% → 100% ACN in H_2O).

Yield: 0.182 g (0.14 mmol), 66%; colorless solid, 100% β (NMR).

MF $C_{75}H_{69}NO_{20}$ MW 1304.3640 [1303.4413]

R_F = 0.29 (SiO_2, CH:EA = 2:1).

$[\alpha]_D^{20}$ = -29.0° (*c* = 1.00; $CHCl_3$).

HR-QTOF-MS (ESI, pos), *m/z:* 1326.4289 $[M+Na]^+$, (calc. = 1326.4305).

^{1}H-NMR, COSY, TOCSY, HSQC, HSQC no dec., HMBC (400 MHz, $CDCl_3$, 298 K): δ [ppm] = 7.98 – 7.83 (m, 8H, H_{Ar}), 7.82 – 7.72 (m, 4H, H_{Ar}), 7.57 – 7.06 (m, 28H, H_{Ar}), 5.81 (dd, $^3J_{H\text{-}3',H\text{-}2'} = {}^3J_{H\text{-}3',H\text{-}4'}$ = 9.7 Hz, 1H, H-3'), 5.74 (dd, $^3J_{H\text{-}3,H\text{-}2} = {}^3J_{H\text{-}3,H\text{-}4}$ = 9.3 Hz, 1H, H-3), 5.45 – 5.27 (m, 3H, H-2, H-2', H.4'), 5.13 (s, 2H, -C*H*$_2$Ph), 5.05 (d, $^3J_{H\text{-}1',H\text{-}2'}$ = 7.9 Hz, 1H, H-1'), 4.71 – 4.56 (m, 1H, H-1), 4.47 – 4.34 (m, 3H, H-4, -C*H*$_2$Ph), 4.03 – 3.90 (m, 3H, H-5. H-5', H-6a'), 3.84 – 3.69 (m, 2H, H-6b', -CH*H*-), 3.39 (s, 3H, -C*H*$_3$), 3.34 – 3.27 (m, 1H, -CH*H*-), 3.09 – 2.86 (m, 2H, -C*H*$_2$-), 1.50 – 1.25 (m, 4H, -C*H*$_2$-), 1.18 – 1.00 (m, 2H, -C*H*$_2$-).

^{13}C-NMR, HSQC, HSQC no dec., HMBC (101 MHz, $CDCl_3$, 298 K): δ [ppm] = 168.1 (*C*=OCH$_3$), 165.9 (*C*=O^{Bz}), 165.8 (*C*=O^{Bz}), 165.5 (*C*=O^{Bz}), 165.1 (*C*=O^{Bz}), 138.1 (C_{Ar}), 133.5 (C_{Ar}), 133.3 (C_{Ar}), 133.2 (C_{Ar}), 129.9 (C_{Ar}), 129.9 (C_{Ar}), 129.8 (C_{Ar}), 129.7 (C_{Ar}), 129.6 (C_{Ar}), 129.6 (C_{Ar}), 129.5 (C_{Ar}), 129.4

(C_{Ar}), 128.8 (C_{Ar}), 128.8 (C_{Ar}), 128.7 (C_{Ar}), 128.5 (C_{Ar}), 128.5 (C_{Ar}), 128.4 (C_{Ar}), 128.4 (C_{Ar}), 128.0 (C_{Ar}), 101.6 (C-1), 101.1 (C-1'), 77.0 (C-4), 74.2 (C-5), 72.9 (C-3), 72.3 (C-3, C-5'), 72.1 (C-2'), 71.8 (C-2), 70.3 (-*C*H_2-), 69.5 (C-4'), 67.2 (-*C*H_2Ph), 62.8 (C-6'), 52.7 (-*C*H_3), 50.6 (-*C*H_2Ph), 47.2 (-*C*H_2-), 29.0 (-*C*H_2-), 27.7 (-*C*H_2-), 23.1 (-*C*H_2-).

5-Aminopentyl β-D-glucopyranosyl-(1→4)-β-D-glucoronic acid (I-30)

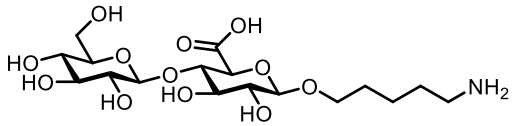

To a solution of disaccharide **I-28** (170 mg, 0.155 mmol, 1.0 eq.) in THF (6 mL), a 1M aqueous solution of LiOH (4 mL) was added. The reaction mixture was stirred for 2 d at ambient temperatures and acidified using Amberlyst 15 (hydrogen form) until pH = 4 was reached. The solution was filtrated, concentrated *in vacuo* and the residue was dissolved in 6 mL H_2O/MeOH mixture (1:1). After addition of Pd/C catalyst (15 mg), the reaction was flushed twice with H_2 and was stirred under H_2 atmosphere for 2 d. To remove the Pd/C catalyst, the reaction mixture was filtered through a pad of celite and the solvent was removed under vacuum.

Yield: 37 mg (0.068 mmol), 65%; colorless solid, 100% β (NMR).

MF $C_{17}H_{31}NO_{12}$ MW 441.4300 [441.1846]

$[\alpha]_D^{20}$ = -26.0° (*c* = 1.00; H_2O).

HR-QTOF-MS (ESI, pos), *m/z:* 442.1922 $[M+H]^+$, (calc. = 442.1919).

^{1}H-NMR, COSY, HSQC, HMBC (400 MHz, D_2O, 298 K): δ [ppm] = 4.45 – 4.37 (m, 2H, H-1, H-1'), 3.91 – 3.70 (m, 3H, H-5, H-6a', -CH*H*-), 3.68 – 3.48 (m, 5H, H-3, H-4, H-4', H-6b', -C*H*H-), 3.45 – 3.15 (m, 4H, H-2, H-2', H-3', H-5'), 3.11 – 2.85 (m, 2H, -CH_2-), 1.68 – 1.49 (m, 4H, -CH_2-), 1.42 – 1.26 (m, 2H, -CH_2-).

^{13}C-NMR, HSQC, HMBC (101 MHz, D_2O, 298 K): δ [ppm] = 175.1 (C-6), 102.2 (C-1'), 102.0 (C-1), 80.2 (C-4), 76.0 (C-5), 75.4 (C-3', C-4'), 74.4 (C-3), 73.2 (C-2'), 72.7 (C-2), 70.0 (C-6'), 69.4 (C-5'), 60.5 (-*C*H_2-), 48.9 (-*C*H_2-), 28.1 (-*C*H_2-), 23.3 (-*C*H_2-), 22.0 (-*C*H_2-).

7.4.2 Synthesis of cellobiose monomer

Ethyl 6-*O*-(*tert*-butyldimethylsilyl)-3'-*O*-methylnaphthyl-4',6'-*O*-benzylidene-1-thio-β-D-cellobioside (II-1)

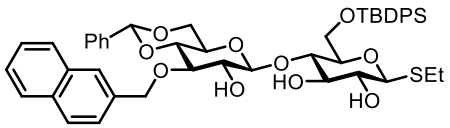

Disaccharide **I-17** (0.200 g, 0.281 mmol, 1.0 eq.) was dissolved in dry toluene (3 mL). After adding dibutyltin oxide (0.093 g, 0.617 mmol, 2.2 eq.), the suspension was heated under reflux for 3 h. Subsequently, the solvent was removed *in vacuo* and the residue was dissolved in dry DMF (3 mL). 2-(Bromomehtyl)naphthalene (0.124 g, 0.561 mmol, 2.0 eq.) and caesium fluoride (0.051 g, 0.337 mmol, 1.2 eq.) were added to the solution. The reaction mixture was stirred at ambient temperature for 24 h and quenched by the addition of water (10 mL), extracted with CH_2Cl_2 (3×15 mL). The organic layers were combined, washed with brine (10 mL), dried over $MgSO_4$ and concentrated *in vacuo*. The crude product was purified via normal phase flash chromatography (SiO_2, gradient: 0% → 5% MeOH in CH_2Cl_2).

Yield: 0.024 g (0.028 mmol), 10%; colorless solid, 100% β (NMR).

MF $C_{48}H_{56}O_{10}SSi$ MW 853.1110 [852.3363]

R_F = 0.38 (SiO_2, CH_2Cl_2:MeOH = 19:1).

^{1}H-NMR (400 MHz, CD_2Cl_2, 298 K): δ [ppm] = 8.05 – 7.65 (m, 10H, H_{Ar}), 7.59 – 7.22 (m, 12H, H_{Ar}), 5.59 (s, 1H, $(RO)_2CH$Ph), 5.11 (m, 1H, -C*H*HNap), 4.97 (m, 1H, -CH*H*Nap), 4.62 (d, $^3J_{H\text{-}1',H\text{-}2'}$ = 7.5 Hz, 1H, H-1'), 4.41 – 4.28 (m, 2H, H-1, H-6a'), 4.05 (dd, $^2J_{H\text{-}6a,H\text{-}6b}$ = 11.6 Hz, $^3J_{H\text{-}6a,H\text{-}5}$ =3.5 Hz, 1H, H-6a), 3.95 (dd, $^2J_{H\text{-}6a,H\text{-}6b}$ = 11.6 Hz, $^3J_{H\text{-}6b,H\text{-}5}$ =1.9 Hz, 1H, H-6b), 3.86 – 3.37 (m, 12H), 2.72 (m, 2H, -S-CH_2-CH_3), 1.30 (t, $^3J_{CH2,CH3}$ = 7.4 Hz, 3H, -S-CH_2-CH_3), 1.01 (s, 9H, -SiC(CH_3)$_3$).

Ethyl 6-*O*-(*tert*-butyldimethylsilyl)-4',6'-*O*-benzylidene-1-thio-β-D-cellobioside (II-3)

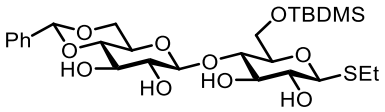

Ethyl 4',6'-*O*-benzylidene-1-thio-β-D-cellobioside **I-15** (1.000 g, 1.86 mmol, 1.0 eq.) was dissolved in dry DMF (10 mL). Subsequently, imidazole (0.317 g, 4.66 mmol, 2.5 eq.) was added to the solution. After cooling the solution to 0 °C, *tert*-butyldimethylsilyl chloride (0.364 g, 2.42 mmol, 1.3 eq.) was added in portions. After stirring for 26 h at ambient temperature, the reaction was quenched by the addition of cold, half saturated $NaHCO_{3\ aq.}$ (40 mL). The mixture was extracted with CH_2Cl_2 (2x 20 mL). The organic extracts were combined and washed with saturated $(NH_4)_2SO_{4\ aq.}$ (20 mL) and water (20 mL). The organic layer was dried over $MgSO_4$, filtered and concentrated under reduced pressure. The crude product was subjected to normal phase flash chromatography (SiO_2, gradient: 0% → 8% MeOH in CH_2Cl_2) and further purified by reverse phase flash chromatography (C_{18}, gradient: 10% → 100% ACN in H_2O).

Yield: 0.767 g (1.30 mmol), 70%; colorless solid, 100% β (NMR).

MF $C_{27}H_{44}O_{10}SSi$ MW 588.7840 [588.2424]

R_F = 0.60 (SiO_2, CH_2Cl_2:MeOH = 10:1).

$[\alpha]_D^{20}$ = -39.7° (*c* = 1.00; MeOH).

HR-QTOF-MS (ESI, pos.), *m*/*z*: 611.2301 $[M+Na]^+$, (calc. 611.2316).

^{1}H-NMR, COSY, TOCSY, HSQC, HSQC no dec., HMBC (400 MHz, CD_2Cl_2, 298 K): δ [ppm] = 7.52 – 7.43 (m, 2H, H_{Ar}), 7.40 – 7.32 (m, 3H, H_{Ar}), 5.53 (s, 1H, $(RO)_2CHPh$), 4.52 (d, $^3J_{H\text{-}1',H\text{-}2'}$ = 7.9 Hz, 1H, H-1'), 4.40 – 4.27 (m, 2H, H-1, H-6a'), 4.01 – 3.87 (m, 2H, H-6a, H-6b), 3.76 (dd, $^2J_{H\text{-}6b',H\text{-}6a'}$ = 10.6 , $^3J_{H\text{-}6b',H\text{-}5'}$ = 9.2 Hz, 1H, H-6b'), 3.67 (dd, $^3J_{H\text{-}3',H\text{-}2'} = {}^3J_{H\text{-}3',H\text{-}4'}$ = 8.8 Hz, 1H, H-3'), 3.60 (dd, $^3J_{H\text{-}4,H\text{-}3} = {}^3J_{H\text{-}4,H\text{-}5}$ = 9.2 Hz, 1H, H-4), 3.54 – 3.43 (m, 3H, H-3, H-4', H-5'), 3.42 – 3.35 (m, 2H, H-5, H-2'), 3.32 (dd, $^3J_{H\text{-}2,H\text{-}1}$ = 9.7 , $^3J_{H\text{-}2,H\text{-}3}$ = 8.6 Hz, 1H, H-2), 2.79 – 2.58 (m, 2H, -S-CH_2-CH$_3$), 1.27 (t, $^3J_{CH2,CH3}$ = 7.4 Hz, 3H, -S-CH$_2$-CH_3), 0.90 (s, 9H, -Si-C(CH_3)$_3$), 0.09 (s, 6H, -Si-CH_3).

^{13}C-NMR, HSQC, HSQC no dec., HMBC (101 MHz, CD_2Cl_2, 298 K): δ [ppm] = 137.6 (C_{Ar}), 129.6 (C_{Ar}), 128.6 (C_{Ar}), 126.6 (C_{Ar}), 104.0 (C-1'), 102.2 ((RO)$_2$*C*HPh), 85.5 (C-1), 80.7 (C-4'), 79.5 (C-4, C-5), 76.4 (C-3), 74.7 (C-2'), 73.5 (C-3'), 72.9 (C-2), 68.7 (C-6'), 67.0 (C-5'), 62.6 (C-6), 26.0 (-SiC(*C*H$_3$)$_3$), 24.2 (-S-*C*H$_2$-CH$_3$), 18.6 (-Si-*C*(CH$_3$)$_3$), 15.5 (-S-CH$_2$-*C*H$_3$), -5.1 (-Si-C*H*$_3$).

Ethyl 6-*O*-(*tert*-butyldimethylsilyl)-3'-*O*-levulinoyl-4',6'-*O*-benzylidene-1-thio-β-D-cellobioside (II-4)

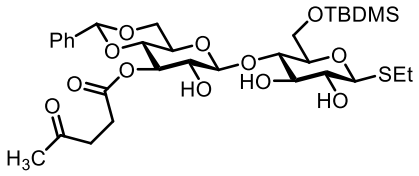

Method a: levulinic chloride as reagent

To a solution of levulinic acid (33 mg, 0.287 mmol, 3.6 eq.) in dry CH_2Cl_2 (2 mL), oxalyl chloride (0.07 mL, 101 mg, 0.798 mmol, 10.0 eq.) and catalytic amount of dry DMF were added. After stirring for 1 h, the solvent was removed *in vacuo*. The residue was redissolved in 1.5 mL dry DCM and 0.5 mL was added dropwise to the reaction mixture containing disaccharide **II-3** (50 mg, 0.080 mmol, 1.0 eq.), (*R*)-BTM (43 mg, 0.160 mmol, 2.0 eq.) and DIPEA (0.06 mL, 44 mg, 0.639 mmol, 4.0 eq.) in DCM (1 mL) under ice-cooling. After stirring for 5 h, 0.5 mL of the levulinic chloride solution was added under ice-cooling, and the rest was added after 20 h stirring at ambient temperatures. The reaction mixture was allowed to stir for another 5 h, quenched by the addition of 1 mL MeOH and concentrated under reduced pressure. The crude product was subject to flash chromatography (SiO_2, gradient: 0% → 4% MeOH in CH_2Cl_2) and further purified by reverse phase HPLC (gradient: 10% → 95% ACN in H_2O).

Yield: 5 mg (0.007 mmol), 9%; colorless solid, 100% β (NMR).

Method b: mixed anhydride as reagent

To a solution of disaccharide **II-3** (40 mg, 0.068 mmol, 1.0 eq.), (*R*)-BTM (2 mg, 0.007 mmol, 0.1 eq.) and DIPEA (0.04 mL, 26 mg, 0.204 mmol, 3.0 eq.) in CH_2Cl_2 (2 mL), levulinic acid (9 mg, 0.075 mmol, 1.1 eq.) and pivalic anhydride (0.02 mL, 14 mg, 0.075 mmol, 1.1 eq.) were added. After stirring for 22 h, the reaction was quenched by the addition of 1 mL MeOH. The solvent was removed under reduced pressure. The crude product was subject to flash chromatography (SiO_2, gradient: 0% → 4% MeOH in CH_2Cl_2) and further purified by reverse phase HPLC (gradient: 10% → 95% ACN in H_2O).

Yield: 23 mg (0.033 mmol), 49%; colorless solid, 100% β (NMR).

MF $C_{32}H_{50}O_{12}SSi$ MW 686.8850 [686.2792]

R_F = 0.30 (SiO_2, CH_2Cl_2:MeOH = 19:1).

$[\alpha]_D^{20}$ = -27.0° (*c* = 1.00; $CHCl_3$).

HR-QTOF-MS (ESI, pos), *m/z:* 709.2674 $[M+Na]^+$, (calc. = 709.2684).

^{1}H-NMR, COSY, HSQC, HMBC (300 MHz, CD_2Cl_2, 298 K): δ [ppm] = 7.62 – 7.26 (m, 5H, H_{Ar}), 5.50 (s, 1H, $(RO)_2CH$Ph), 5.16 (dd, $^3J_{H\text{-}3',H\text{-}2'} = {}^3J_{H\text{-}3',H\text{-}4'} = 9.3$ Hz, 1H, H-3'), 4.62 (d, $^3J_{H\text{-}1',H\text{-}2'} = 7.8$ Hz, 1H, H-1'), 4.49 – 4.26 (m, 2H, H-1, H-6a'), 4.06 – 3.89 (m, 2H, H-6a, H-6b), 3.79 (m, 1H, H-6b'), 3.74 – 3.50 (m, 5H, H-3, H-4, H-5, H-2', H-4'), 3.47 – 3.27 (m, 2H, H-2, H-5'), 2.87 – 2.52 (m, 6H, $-CH_2CH_2-$, $-SCH_2-CH_3$), 2.13 (s, 3H, $-COCH_3$), 1.29 (t, $^3J = 7.4$ Hz, 3H, $-S-CH_2-CH_3$), 0.91 (s, 9H, $-Si-C(CH_3)_3$), 0.10 (s, 6H, $-Si-CH_3$).

^{13}C-NMR, HSQC, HMBC (75 MHz, CD_2Cl_2, 298 K): δ [ppm] = 207.7 (C=OCH_3), 173.0 (O-C=O), 137.4 (C_{Ar}), 129.5 (C_{Ar}), 128.6 (C_{Ar}), 126.6 (C_{Ar}), 104.1 (C-1'), 101.9 ($(RO)_2CHPh$), 85.6 (C-1), 80.4 (C-4), 79.4 (C-5'), 78.4 (C-4'), 76.4 (C-5), 74.4 (C-3'), 73.6 (C-2'), 72.9 (C-2), 68.6 (C-6'), 67.0 (C-3), 62.7 (C-6), 38.8 ($-CH_2CH_2-$), 30.0 ($COCH_3$), 28.5 ($-CH_2CH_2-$), 26.0 ($-Si-C(CH_3)_3$), 24.2 ($-S-CH_2-CH_3$), 18.6 ($-Si-C(CH_3)_3$), 15.6 ($-S-CH_2-CH_3$), -5.8 ($-Si-CH_3$).

Ethyl 6-*O*-(*tert*-butyldimethylsilyl)-3'-*O*-(9-fluorenylmethoxycarbonyl)-4',6'-*O*-benzylidene-1-thio-β-D-cellobioside (II-8)

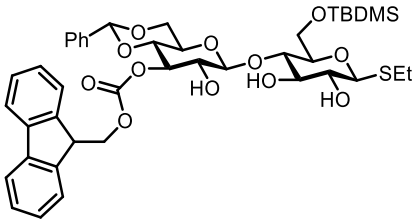

To a solution of disaccharide **II-3** (280 mg, 0.476 mmol, 1.0 eq.) in dry CH_2Cl_2 (4 mL), Fluorenylmethoxycarbonyl chloride (370 mg, 1.427 mmol, 3.0 eq.) and *sym*-collidine (0.38 mL, 346 mg, 2.853 mmol, 6.0 eq.) were added. After stirring for 2 days, the reaction was quenched by addition of methanol (1 mL). The mixture was stirred for 30 min and the solvent was removed *in vacuo*. The crude product was subjected to normal phase flash chromatography (SiO_2, gradient: 0% → 80% EA in CH).

Yield: 232 mg (0.286 mmol), 60%; colorless solid, 100% β (NMR).

MF $C_{42}H_{54}O_{12}SSi$ MW 811.0270 [810.3105]

R_F = 0.39 (SiO_2, CH:EA = 1:1).

$[\alpha]_D^{20}$ = -31.0° (*c* = 1.00; $CHCl_3$).

HR-QTOF-MS (ESI, pos), *m/z:* 833.3002 $[M+Na]^+$, (calc. = 833.2997).

^{1}H-NMR, COSY, HSQC, HSQC no dec., HMBC (600 MHz, $CDCl_3$, 298 K): δ [ppm] = 7.79 – 7.73 (m, 2H, H_{Ar}), 7.61 – 7.56 (m, 2H, H_{Ar}), 7.47 – 7.42 (m, 2H, H_{Ar}), 7.41 – 7.35 (m, 2H, H_{Ar}), 7.34 – 7.31 (m, 3H, H_{Ar}), 7.29 – 7.24 (m, 1H, H_{Ar}), 7.24 – 7.19 (m, 1H, H_{Ar}), 5.54 (s, 1H, $(RO)_2CHPh$), 5.07 (dd, $^3J_{H\text{-}3',H\text{-}2'} = {}^3J_{H\text{-}3',H\text{-}4'}$ = 9.5 Hz, 1H, H-3'), 4.63 (d, $^3J_{H\text{-}1',H\text{-}2'}$ = 7.7 Hz, 1H, H-1'), 4.43 (m, 2H, CH_2^{Fmoc}), 4.39 (dd, $^2J_{H\text{-}6a',H\text{-}6b'}$ = 10.4 Hz, $^3J_{H\text{-}6a',H\text{-}5'}$ = 5.0 Hz, 1H, H-6a'), 4.35 (d, $^3J_{H\text{-}1,H\text{-}2}$ = 9.8 Hz, 1H, H-1), 4.27 (t, ^3J = 7.4 Hz, 1H, CH^{Fmoc}), 3.94 (m, 2H, H-6a, H-6b), 3.82 (m, 1H, H-6b'), 3.77 (dd, $^3J_{H\text{-}4',H\text{-}3'} = {}^3J_{H\text{-}4',H\text{-}5'}$ = 9.6 Hz, 1H, H-4'), 3.73 – 3.67 (m, 1H, H-2'), 3.67 – 3.62 (m, 2H, H-3, H-4), 3.63 – 3.56 (m, 1H, H-5'), 3.45 – 3.42 (m, 1H, H-2), 3.42 – 3.39 (m, 1H, H-5), 2.77 – 2.67 (m, 2H, -S-CH_2-CH_3), 1.31 (t, $^3J_{CH2,CH3}$ = 7.4 Hz, 3H, -S-CH_2-CH_3), 0.89 (s, 9H, -SiC(CH_3)$_3$), 0.10 (s, 3H, -Si-CH_3), 0.09 (s, 3H, -Si-CH_3).

^{13}C-NMR, HSQC, HSQC no dec., HMBC (151 MHz, $CDCl_3$, 298 K): δ [ppm] = 155.2 (C=O), 143.4 (C_{Ar}), 143.3 (C_{Ar}), 141.4 (C_{Ar}) , 141.4 (C_{Ar}), 136.6 (C_{Ar}), 129.4 (C_{Ar}), 128.4 (C_{Ar}), 128.0 (C_{Ar}), 127.3 (C_{Ar}), 126.3 (C_{Ar}), 125.3 (C_{Ar}), 120.2 (C_{Ar}), 104.6 (C-1'), 101.8 ($(RO)_2CHPh$), 85.6 (C-1), 81.8 (C-4), 78.8 (C-5), 78.0 (C-4'), 77.6 (C-3'), 76.1 (C-3), 73.2 (C-2'), 72.3 (C-2), 70.5 (CH_2^{Fmoc}), 68.3 (C-6'), 66.8 (C-5'), 63.2 (C-6), 46.8 (CH^{Fmoc}), 26.0 (-C(CH_3)$_3$), 24.1 (-S-CH_2-CH_3), 18.5 (-C(CH_3)$_3$), 15.5 (-S-CH_2-CH_3), -5.0 (-Si-CH_3), -5.1 (-Si-CH_3).

Ethyl 2,3,2'-tri-*O*-benzoyl-6-*O*-(*tert*-butyldimethylsilyl)-3'-*O*-(9-fluorenylmethoxycarbonyl)-4',6'-*O*-benzylidene-1-thio-β-D-cellobioside (II-10)

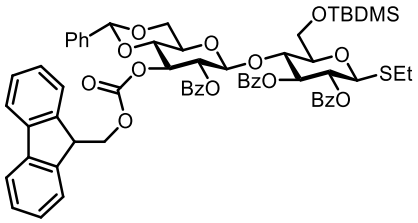

Disaccharide **II-8** (230 mg, 0.284 mmol, 1.0 eq.) was dissolved in dry CH_2Cl_2 (4 mL). Pyridine (0.34 mL, 336 mg, 4.254 mmol, 15.0 eq.), benzoyl chloride (0.26 mL, 319 mg, 2.269 mmol, 8.0 eq.), and catalytic amount of 4-dimethylaminopyridine were added at 0 ˚C and the reaction mixture was stirred for 19 h at ambient temperature. After quenching the remaining benzoyl chloride with 5 mL cold water, the solution was extracted with CH_2Cl_2 (2x 8 mL) and the organic layer was washed with saturated $NaCl_{(aq)}$ (5 mL), dried over $MgSO_4$ and concentrated *in vacuo*. The crude product was subjected to normal phase flash chromatography (SiO_2, gradient: 0% → 30% EA in CH).

Yield: 295 mg (0.263 mmol), 93%; colorless solid, 100% β (NMR).

MF $C_{63}H_{66}O_{15}SSi$ MW 1123.3510 [1122.3892]

R_F = 0.60 (SiO_2, CH:EA = 2:1).

$[\alpha]_D^{20}$ = +18.0° (c = 1.00; $CHCl_3$).

HR-QTOF-MS (ESI, pos), *m/z:* 1140.4224 $[M+NH_4]^+$, (calc. = 1140.4235).

^{1}H-NMR, COSY, TOCSY, HSQC, HSQC no dec., HMBC (600 MHz, $CDCl_3$, 298 K): δ [ppm] = 8.13 – 8.09 (m, 1H, H_{Ar}), 8.06 – 8.02 (m, 2H, H_{Ar}), 8.01 – 7.96 (m, 2H, H_{Ar}), 7.96 – 7.91 (m, 2H, H_{Ar}), 7.69 – 7.66 (m, 1H, H_{Ar}), 7.63 – 7.60 (m, 1H, H_{Ar}), 7.57 – 7.45 (m, 3H, H_{Ar}), 7.45 – 7.41 (m, 5H, H_{Ar}), 7.40 – 7.27 (m, 10H, H_{Ar}), 7.16 – 7.12 (m, 1H, H_{Ar}), 5.64 (dd, $^3J_{H\text{-}3,H\text{-}2}$ = $^3J_{H\text{-}3,H\text{-}4}$ = 9.4 Hz, 1H, H-3), 5.36 (dd, $^3J_{H\text{-}2,H\text{-}1}$ = $^3J_{H\text{-}2,H\text{-}3}$ = 9.7 Hz, 1H, H-2), 5.31 (dd, $^3J_{H\text{-}2',H\text{-}3'}$ = 9.4 Hz, $^3J_{H\text{-}2',H\text{-}1'}$ = 7.8 Hz, 1H, H-2'), 5.24 (s, 1H, $(RO)_2CH$Ph), 5.19 (dd, $^3J_{H\text{-}3',H\text{-}2'}$ = $^3J_{H\text{-}3',H\text{-}4'}$ = 9.6 Hz, 1H, H-3'), 4.92 (d, $^3J_{H\text{-}1',H\text{-}2'}$ = 7.8 Hz, 1H, H-1'), 4.56 (d, $^3J_{H\text{-}1,H\text{-}2}$ = 9.7 Hz, 1H, H-1), 4.17 (m, 3H, H-4, CH_2^{Fmoc}), 3.96 (t, ^3J = 7.7 Hz, 1H, CH^{Fmoc}), 3.77 – 3.71 (m, 2H, H-6a', H-6b'), 3.72 – 3.65 (m, 2H, H-6a, H-6b), 3.57 (dd, $^3J_{H\text{-}4',H\text{-}3'}$ = $^3J_{H\text{-}4',H\text{-}5'}$ = 9.6 Hz, 1H, H-4'), 3.39 – 3.36 (m, 1H, H-5), 3.35 – 3.28 (m, 1H, H-5'), 2.75 – 2.63 (m, 2H, -S-CH_2-CH_3), 1.19 (t, $^3J_{CH2,CH3}$ = 7.5 Hz, 3H, -S-CH_2-CH_3), 0.95 (s, 9H, -SiC(CH_3)$_3$), 0.09 (s, 3H, -Si-CH_3), 0.08 (s, 3H, -Si-CH_3).

^{13}C-NMR, HSQC, HSQC no dec., HMBC (151 MHz, $CDCl_3$, 298 K): δ [ppm] = 165.5 (C=O), 164.8 (C=O), 154.6 (C=O), 143.4 (C_{Ar}), 141.1 (C_{Ar}), 136.7 (C_{Ar}), 133.8 (C_{Ar}), 133.6 (C_{Ar}), 133.4 (C_{Ar}), 133.3 (C_{Ar}), 130.3 (C_{Ar}), 130.0 (C_{Ar}), 129.9 (C_{Ar}), 129.4 (C_{Ar}), 129.3 (C_{Ar}), 129.1 (C_{Ar}), 128.7 (C_{Ar}), 128.6

(C_{Ar}), 128.5 (C_{Ar}), 128.3 (C_{Ar}), 127.8 (C_{Ar}), 126.3 (C_{Ar}), 125.4 (C_{Ar}), 125.2 (C_{Ar}), 120.0 (C_{Ar}), 101.4 ((RO)$_2$*C*HPh), 101.2 (C-1'), 82.9 (C-1), 79.5 (C-5), 78.0 (C-4'), 76.2 (C-3'), 75.6 (C-4), 74.5 (C-3), 72.8 (C-2'), 70.5 (C-2), 70.4 (*C*H$_2^{Fmoc}$), 67.9 (C-6'), 66.2 (C-5'), 61.0 (C-6), 46.5 (*C*H^{Fmoc}), 26.0 (-C(*C*H$_3$)$_3$), 23.4 (-S-*C*H$_2$-CH$_3$), 18.5 (-*C*(CH$_3$)$_3$), 15.0 (-S-CH$_2$-*C*H$_3$), -4.9 (-Si-*C*H$_3$), -5.1 (-Si-*C*H$_3$).

_N_-Benzyl(benzyloxy)carbonyl-5-aminopentyl 2,3,2'-tri-_O_-benzoyl-6-_O_-(_tert_-butyldimethylsilyl)-3'-_O_-(9-fluorenylmethoxycarbonyl)-4',6'-_O_-benzylidene-β-D-cellobioside (II-11)

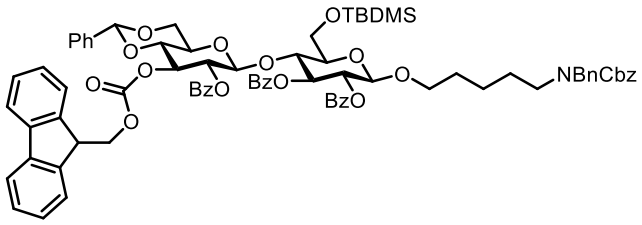

Dissacharide **II-10** (280 mg, 0.249 mmol, 1.0 eq.) and *N*-(Benzyl)-benzyloxycarbonyl-5-aminopentan-1-ol **I-4** (90 mg, 0.274 mmol, 1.1 eq.) were co-evaporated with toluene, dried under vacuum, dissolved in dry CH_2Cl_2 (5 mL) and stirred over freshly activated 4 Å molecular sieve powder for 1 h. Dimethyl disulfide (0.07 mL, 70 mg, 0.748 mmol, 3.0 eq.) and methyl trifluoromethanesulfonate (0.11 mL, 164 mg, 0.997 mmol, 4.0 eq.) were dissolved in dry CH_2Cl_2 (1 mL) to form the promotor. After stirring for 1 h, the promotor solution was added to the reaction mixture. After stirring for 1 h, the reaction mixture was filtered through a pad of celite. The filtrated was diluted with 5 mL CH_2Cl_2, washed with saturated $NaHCO_{3\ aq.}$ (5 mL), dried over $MgSO_4$ and concentrated *in vacuo*. The crude product was subjected to normal phase flash chromatography (SiO_2, gradient: 0% → 30% EA in CH) and further purified by reversed phase flash chromatography (C_{18}, gradient: 30% → 95% ACN in H_2O).

Yield: 40 mg (0.030 mmol), 12%; colorless solid, 100% β (NMR).

MF $C_{81}H_{85}NO_{18}Si$ MW 1388.6450 [1387.5536]

R_F = 0.27 (SiO_2, CH:EA = 4:1).

$[\alpha]_D^{20}$ = +6.0° (*c* = 1.00; $CHCl_3$).

HR-QTOF-MS (ESI, pos), *m/z:* 1426.5166 $[M+K]^+$, (calc. = 1426.5167).

^{1}H-NMR, COSY, TOCSY, HSQC, HSQC no dec., HMBC (600 MHz, CD_2Cl_2, 298 K): δ [ppm] = 8.08 – 8.01 (m, 4H, H_{Ar}), 7.94 – 7.87 (m, 2H, H_{Ar}), 7.74 – 7.67 (m, 2H, H_{Ar}), 7.63 – 7.54 (m, 2H, H_{Ar}), 7.51 – 7.42 (m, 5H, H_{Ar}), 7.41 – 7.37 (m, 2H, H_{Ar}), 7.37 – 7.23 (m, 17H, H_{Ar}), 7.20 – 7.09 (m, 4H, H_{Ar}), 5.61 (dd, $^3J_{H\text{-}3,H\text{-}2} = {}^3J_{H\text{-}3,H\text{-}4}$ = 9.6 Hz, 1H, H-3), 5.28 – 5.22 (m, 3H, (RO)$_2$C*H*Ph, H-2, H-2'), 5.19 (dd, $^3J_{H\text{-}3',H\text{-}2'} = {}^3J_{H\text{-}3',H\text{-}4'}$ = 9.5 Hz, 1H, H-3'), 5.14 – 5.09 (m, 2H, , -C*H*$_2$Ph), 4.93 (d, $^3J_{H\text{-}1',H\text{-}2'}$ = 7.8 Hz, 1H, H-1'), 4.62 – 4.51 (m, 1H, H-1), 4.38 (s, 2H, -C*H*$_2$Ph), 4.26 – 4.09 (m, 3H, H-4, C*H*$_2^{Fmoc}$), 4.00 (t, ^3J = 7.3 Hz, 1H,

C*H*^{Fmoc}), 3.79 – 3.69 (m, 3H, H-6b, H-6a', -C*H*H-), 3.69 – 3.63 (m, 1H, -CH*H*-), 3.58 (dd, $^{3}J_{H\text{-}4',H\text{-}3'}$ = $^{3}J_{H\text{-}4',H\text{-}5'}$ = 9.5 Hz, 1H, H-4'), 3.43 – 3.31 (m, 3H, H-5, H-5', H-6b'), 3.07 – 2.93 (m, 2H, -CH_2-), 2.71 (m, 1H, H-6a), 1.50 – 1.31 (m, 4H, -CH_2-), 1.19 – 1.05 (m, 2H, -CH_2-), 0.97 (s, 9H, -SiC(CH_3)$_3$), 0.10 (s, 6H, -Si-CH_3).

^{13}C-NMR, HSQC, HSQC no dec., HMBC (151 MHz, CD_2Cl_2, 298 K): δ [ppm] = 165.7 (*C*=O), 165.5 (*C*=O), 165.2 (*C*=O), 154.7 (*C*=O), 143.6 (*C*=O), 143.4 (C_{Ar}), 141.4 (C_{Ar}), 141.3 (C_{Ar}), 138.6 (C_{Ar}), 137.2 (C_{Ar}), 133.9 (C_{Ar}), 133.5 (C_{Ar}), 133.5 (C_{Ar}), 130.7 (C_{Ar}), 130.2 (C_{Ar}), 130.1 (C_{Ar}), 129.9 (C_{Ar}), 129.4 (C_{Ar}), 129.3 (C_{Ar}), 128.9 (C_{Ar}), 128.8 (C_{Ar}), 128.7 (C_{Ar}), 128.5 (C_{Ar}), 128.1 (C_{Ar}), 128.0 (C_{Ar}), 127.4 (C_{Ar}), 126.5 (C_{Ar}), 125.3 (C_{Ar}), 125.2 (C_{Ar}), 120.2 (C_{Ar}), 120.2 (C_{Ar}), 101.6 ((RO)$_2$*C*HPh), 101.5 (C-1'), 101.0 (C-1), 78.3 (C-4'), 76.4 (C-3'), 76.1 (C-4), 75.3 (C-5), 73.6 (C-3), 72.9 (C-2'), 72.3 (C-2), 70.4 (*C*H$_2^{Fmoc}$), 70.0 (C-6'), 68.0 (C-6), 67.2 (-*C*H$_2$Ph), 66.4 (C-5'), 61.2 (-*C*H$_2$-), 50.8 (-*C*H$_2$Ph), 46.8 (-*C*H$_2$-), 46.6 (*C*H^{Fmoc}), 29.4 (-*C*H$_2$-), 27.6 (-*C*H$_2$-), 26.1 (-C(*C*H$_3$)$_3$), 23.4 (-*C*H$_2$-), 18.6 (-*C*(CH$_3$)$_3$), -4.9 (-Si-*C*H$_3$), -5.2 (-Si-*C*H$_3$).

_N_-Benzyl(benzyloxy)carbonyl-5-aminopentyl 2,3,2'-tri-_O_-benzoyl-6-_O_-(_tert_-butyldimethylsilyl)-4',6'-_O_-benzylidene-β-D-cellobioside (II-12)

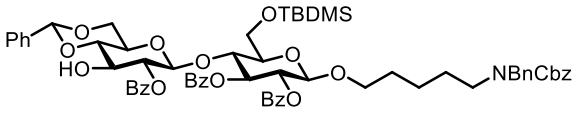

Disaccharide **II-11** (40 mg, 0.030 mmol, 1.0 eq.) was dissolved in a 5% piperidine solution in DCM (5 mL). After stirring for 30 min, the solvent was removed *in vacuo*. The crude product was subjected to normal phase flash chromatography (SiO_2, gradient: 0% → 60% EA in CH).

Yield: 30 mg (0.026 mmol), 86%; colorless solid, 100% β (NMR).

MF $C_{66}H_{75}NO_{16}Si$ MW 1166.4020 [1165.4588]

R_F = 0.35 (SiO_2, CH:EA = 2:1).

$[\alpha]_D^{20}$ = -2.0° (c = 1.00; $CHCl_3$).

HR-QTOF-MS (ESI, pos), *m/z:* 1183.5170 $[M+NH_4]^+$, (calc. = 1183.5193).

^{1}H-NMR, COSY, TOCSY, HSQC, HSQC no dec., HMBC (600 MHz, CD_2Cl_2, 298 K): δ [ppm] = 8.14 – 8.07 (m, 2H, H_{Ar}), 8.05 – 7.99 (m, 3H, H_{Ar}), 7.93 – 7.81 (m, 3H, H_{Ar}), 7.65 – 7.60 (m, 1H, H_{Ar}), 7.60 – 7.54 (m, 1H, H_{Ar}), 7.52 – 7.42 (m, 3H, H_{Ar}), 7.40 – 7.37 (m, 2H, H_{Ar}), 7.35 – 7.21 (m, 14H, H_{Ar}), 7.19 – 7.09 (m, 2H, H_{Ar}), 5.56 (dd, $^3J_{H\text{-}3,H\text{-}2} = {}^3J_{H\text{-}3,H\text{-}4}$ = 9.6 Hz, 1H, H-3), 5.27 – 5.19 (m, 2H, $(RO)_2CH$Ph, H-2), 5.13 – 5.08 (m, 2H, -CH_2Ph), 5.05 (dd, $^3J_{H\text{-}2',H\text{-}3'} = {}^3J_{H\text{-}2',H\text{-}1'}$ = 8.0 Hz, 1H, H-2'), 4.85 (d, $^3J_{H\text{-}1',H\text{-}2'}$ = 8.0 Hz, 1H, H-1'), 4.57 – 4.48 (m, 1H, H-1), 4.36 (s, 2H, -CH_2Ph), 4.10 (dd, $^3J_{H\text{-}4,H\text{-}3} = {}^3J_{H\text{-}4,H\text{-}5}$ = 9.6 Hz, 1H, H-4), 3.89 (dd, $^3J_{H\text{-}3',H\text{-}2'} = {}^3J_{H\text{-}3',H\text{-}4'}$ = 8.0 Hz, 1H, H-3'), 3.83 – 3.77 (m, 1H, H-6a), 3.76 – 3.65 (m, 3H, H-6b, H-6a', -CHH-), 3.43 – 3.37 (m, 1H, -CHH-), 3.35 – 3.29 (m, 2H, H-5, H-4'), 3.23 (ddd, $^3J_{H\text{-}5',H\text{-}4'} = {}^3J_{H\text{-}5',H\text{-}6a'}$ = 9.6 Hz, $^3J_{H\text{-}5',H\text{-}6b'}$ = 4.9 Hz, 1H, H-5'), 3.08 – 2.93 (m, 2H, -CH_2-), 2.66 (m, 1H, H-6b'), 1.16 – 1.04 (m, 4H, -CH_2-), 0.97 (s, 9H, -SiC(CH_3)$_3$), 0.89 – 0.85 (m, 2H, -CH_2-), 0.16 – 0.05 (m, 6H, -Si-CH_3).

^{13}C-NMR, HSQC, HSQC no dec., HMBC (151 MHz, CD_2Cl_2, 298 K): δ [ppm] = 165.7 (C=O), 165.7 (C=O), 165.5 (C=O), 156.8 (C=O), 137.4 (C_{Ar}), 133.9 (C_{Ar}), 133.5 (C_{Ar}), 133.4 (C_{Ar}), 130.1 (C_{Ar}), 130.1 (C_{Ar}), 129.9 (C_{Ar}), 129.0 (C_{Ar}), 128.8 (C_{Ar}), 128.7 (C_{Ar}), 128.5 (C_{Ar}), 128.0 (C_{Ar}), 126.5 (C_{Ar}), 101.8 ($(RO)_2C$HPh), 101.4 (C-1'), 101.1 (C-1), 80.8 (C-4'), 75.9 (C-4), 75.4 (C-5), 74.8 (C-2'), 73.6 (C-3), 72.8 (C-3'), 72.3 (C-2), 69.8 (-CH_2-), 68.1 (C-6'), 67.2 (-CH_2Ph), 66.4 (C-5'), 61.2 (C-6'), 50.8 (-CH_2Ph), 46.6 (-CH_2-), 29.5 (-CH_2-), 28.1 (-CH_2-), 26.1 (-C(CH_3)$_3$), 23.1 (-CH_2-), 18.6 (-C(CH_3)$_3$), -4.8 (-Si-CH_3), -5.2 (-Si-CH_3).

Ethyl 2,3,2',3'-tetra-*O*-benzoyl-6-*O*-(*tert*-butyldimethylsilyl)-4',6'-*O*-benzylidene-1-thio-β-D-cellobioside (II-15)

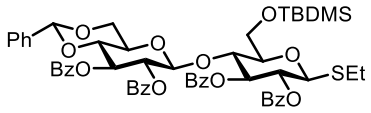

Disaccharide **II-3** (0.760 g, 1.29 mmol, 1.0 eq.) was dissolved in dry CH_2Cl_2 (8 mL). Pyridine (1.6 mL, 1.532 g, 19.36 mmol, 15.0 eq.), benzoyl chloride (1.5 mL, 1.814 g, 12.91 mmol, 10.0 eq.), and catalytic amount of 4-dimethylaminopyridine were added at 0 ˚C and the reaction mixture was stirred for 22 h at ambient temperature. After completion of the reaction, the solution was diluted with CH_2Cl_2 (30 mL) and washed with saturated $NaHCO_{3\,aq.}$ (15 mL) and saturated $NaCl_{(aq)}$ (15 mL), respectively. The organic layer was dried over $MgSO_4$, filtered and concentrated *in vacuo*. The crude product was subjected to normal phase flash chromatography (SiO_2, gradient: 0% → 30% EA in CH) and further purified by reversed phase flash chromatography (C_{18}, gradient: 20% → 95% ACN in H_2O).

Yield: 0.357 g (0.36 mmol), 27%; colorless solid, 100% β (NMR).

MF $C_{55}H_{60}O_{14}SSi$ MW 1005.2160 [1004.3473]

R_F = 0.71 (SiO_2, CH:EA = 2:1).

$[\alpha]_D^{20}$ = +10.0° (c = 1.00; $CHCl_3$).

HR-QTOF-MS (ESI, pos), *m/z:* 1027.3373 $[M+Na]^+$, (calc. = 1027.3365).

^{1}H-NMR, COSY, TOCSY, HSQC, HSQC no dec., HMBC (400 MHz, $CDCl_3$, 298 K): δ [ppm] = 8.09 – 8.00 (m, 2H, H_{Ar}), 7.99 – 7.87 (m, 6H, H_{Ar}), 7.59 – 7.28 (m, 17H, H_{Ar}), 5.70 – 5.55 (m, 2H, H-3, H-3'), 5.46 – 5.32 (m, 2H, H-2, H-2'), 5.20 (s, 1H, $(RO)_2CHPh$), 4.96 (d, $^3J_{H\text{-}1',H\text{-}2'}$ = 7.8 Hz, 1H, H-1'), 4.56 (d, $^3J_{H\text{-}1,H\text{-}2}$ = 10.0 Hz, 1H, H-1), 4.15 (dd, $^3J_{H\text{-}4',H\text{-}3'} = {}^3J_{H\text{-}4',H\text{-}5'}$ = 9.5 Hz, 1H, H-4'), 3.80 – 3.65 (m, 3H, H-6a, H-6a', H-6b'), 3.60 (dd, $^3J_{H\text{-}4,H\text{-}3} = {}^3J_{H\text{-}4,H\text{-}5}$ = 9.5 Hz, 1H, H-4), 3.44 – 3.32 (m, 2H, H-5, H-5'), 2.81 – 2.58 (m, 3H, -S-CH_2-CH_3), 1.20 (t, $^3J_{CH2,CH3}$ = 7.5 Hz, 3H, -S-CH_2-CH_3), 0.97 (s, 9H, -SiC(CH_3)$_3$), 0.10 (s, 3H, -Si-CH_3), 0.10 (s, 3H, -Si-CH_3).

^{13}C-NMR, HSQC, HSQC no dec., HMBC (101 MHz, $CDCl_3$, 298 K): δ [ppm] = 165.7 (C=O^{Bz}), 165.5 (C=O^{Bz}), 164.9 (C=O^{Bz}), 136.8 (C_{Ar}), 133.5 (C_{Ar}), 133.3 (C_{Ar}), 133.2 (C_{Ar}), 133.2 (C_{Ar}), 130.4 (C_{Ar}), 130.0 (C_{Ar}), 129.9 (C_{Ar}), 129.5 (C_{Ar}), 129.5 (C_{Ar}), 129.2 (C_{Ar}), 129.1 (C_{Ar}), 128.6 (C_{Ar}), 128.5 (C_{Ar}), 128.4 (C_{Ar}), 128.3 (C_{Ar}), 126.2 (C_{Ar}), 101.4 (C-1'), 101.3 ($(RO)_2CHPh$), 83.0 (C-1), 80.0 (C-5'), 78.5 (C-4), 75.6 (C-4'), 74.6 (C-3'), 72.7 (C-2'), 72.4 (C-3), 70.6 (C-2), 68.0 (C-6), 66.4 (C-5), 61.0 (C-6'), 26.1 (-C(CH_3)$_3$), 23.4 (-S-CH_2-CH_3), 18.5 (-C(CH_3)$_3$), 15.0 (-S-CH_2-CH_3), -4.9 (-Si-CH_3), -5.1 (-Si-CH_3).

7.4.3 Functionalization of 4arm polyethylene glycol and dye molecules

FmocFGG-OH (III-3)

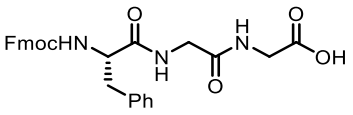

The synthesis was performed on the solid phase peptide synthesizer as described in 7.3.1 using 2.0 g of 2-chlorotrityl chloride resin (1.60 mmol/g). The product was obtained after removing the solvent *in vacuo*, co-evaporation with toluene and lyophilization.

Yield: 1.607 g (3.21 mmol), quant.; colorless solid.

MF $C_{28}H_{27}N_3O_6$ MW 501.5390 [501.1900]

HR-QTOF-MS (ESI, pos), *m/z:* 502.1978 $[M+H]^+$, (calc. = 502.1973).

^{1}H-NMR, COSY, HSQC, HMBC (400 MHz, dmso-d_6, 298 K): δ [ppm] = 8.33 (t, $^3J_{NH,G\text{-}\alpha}$ = 5.8 Hz, 1H, NH^G), 8.12 (t, $^3J_{NH,G\text{-}\alpha}$ = 5.9 Hz, 1H, NH^G), 7.94 – 7.72 (d, J = 7.5 Hz, 2H, H_{Ar}^{Fmoc}), 7.73 – 7.54 (m, 3H, H_{Ar}^{Fmoc}, NH^F), 7.46 – 7.37 (m, 2H, H_{Ar}^{Fmoc}), 7.34 – 7.22 (m, 6H, H_{Ar}^{Fmoc}, H_{Ar}^{F}), 7.20 – 7.17 (m, 1H, H_{Ar}^{F}), 4.36 – 4.20 (m, 1H, F-α), 4.20 – 4.06 (m, 3H, -CH^{Fmoc}, -CH_2^{Fmoc}), 3.79 – 3.76 (m, 4H, 2×G-α), 3.05 (dd, $^2J_{F\text{-}\beta a,F\text{-}\beta b}$ = 13.8 Hz, $^3J_{F\text{-}\beta a,F\text{-}\alpha}$ = 4.0 Hz, 1H, F-βa), 2.78 (dd, $^2J_{F\text{-}\beta b,F\text{-}\beta a}$ = 13.8 Hz, $^3J_{F\text{-}\beta b,F\text{-}\alpha}$ = 10.7 Hz, 1H, F-βb).

^{13}C-NMR, HSQC, HMBC (101 MHz, dmso-d_6, 298 K): δ [ppm] = 172.0 (C=O^{G1}), 171.2 (-COOH^{G2}), 169.2 (C=O^F), 156.0 (C=O^{Fmoc}), 143.8 (C_{Ar}), 140.7 (C_{Ar}), 138.3 (C_{Ar}), 129.3 (C_{Ar}), 128.2 (C_{Ar}), 127.7 (C_{Ar}), 127.2 (C_{Ar}), 126.3 (C_{Ar}), 125.4 (C_{Ar}), 125.4 (C_{Ar}), 120.2 (C_{Ar}), 65.7 (CH$_2^{Fmoc}$), 56.3 (F-α), 46.6 (CH^{Fmoc}), 41.9 (G-α), 40.7 (G-α), 37.4 (F-β).

FmocFGG-C_2-NHBoc (III-4)

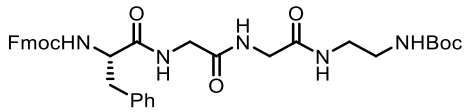

To a solution of Fmoc-FGG-OH (**III-3**, 1.00 g, 1.99 mmol, 1.0 eq.) in DMF (10 mL), HBTU (1.14 g, 2.99 mmol, 1.5 eq.), HOBt (0.40 g, 2.99 mmol, 1.5 eq.) and DIPEA (0.70 mL, 3.99 mmol, 2.0 eq.) were added. After the mixture was stirred for 15 min, *N*-Boc-ethylenediamine (0.63 mL, 0.639 g, 3.99 mmol. 2.0 eq.) was added dropwise. The reaction mixture was stirred for 24 h, diluted with CH_2Cl_2 (50 mL) and washed with brine (30 mL). The organic layer was dried over $MgSO_4$ and the solvent removed *in vacuo*. The residue was subjected to flash chromatography (SiO_2, 0% → 8% MeOH in CH_2Cl_2).

Yield: 0.826 g (1.28 mmol), 64%; yellowish solid.

MF $C_{35}H_{41}N_5O_7$ MW 643.3006 [643.7410]

R_F = 0.14 (SiO_2, CH_2Cl_2:MeOH = 19:1).

HR-QTOF-MS (ESI, pos), *m/z:* 666.2899 $[M+Na]^+$, (calc. = 666.2898).

^{1}H-NMR, COSY, HSQC, HMBC (400 MHz, dmso-d6, 298 K): δ [ppm] = 8.35 (t, $^3J_{NH,G\text{-}\alpha}$ = 5.7 Hz, 1H, N*H*^{G}), 8.07 (t, $^3J_{NH,G\text{-}\alpha}$ = 5.8 Hz, 1H, N*H*^{G}), 7.97 – 7.81 (m, 2H, H_{Ar}), 7.68 (d, $^3J_{NH,F\text{-}\alpha}$ = 8.5 Hz, 1H, N*H*^{F}), 7.67 – 7.57 (m, 2H, H_{Ar}), 7.48 – 7.36 (m, 2H, H_{Ar}), 7.34 – 7.10 (m, 7H, H_{Ar}), 6.82 (t, $^3J_{NHBoc,CH2}$ = 5.7 Hz, 1H, N*H*Boc), 4.39 – 4.23 (m, 1H, -C*H*^{Fmoc}), 4.23 – 4.03 (m, 3H, F-α, F-β), 3.78 (d, $^3J_{G\text{-}\alpha,\ NH}$ = 5.7 Hz, 2H, G-α), 3.69 (d, $^3J_{G\text{-}\alpha,\ NH}$ = 5.8 Hz, 2H, G-α), 3.17 – 3.02 (m, 3H, C*H*$_2^{Fmoc}$-a, -CH_2C*H*$_2$-), 2.98 (m, 2H, -C*H*$_2$$CH_2$-), 2.80 (dd, $^2J_{CH2(Fmoc)\text{-}a,\ CH2(Fmoc)\text{-}b}$ = 13.7 Hz, $^3J_{CH2(Fmoc)\text{-}b,CH(Fmoc)}$ = 10.7 Hz, 1H, C*H*$_2^{Fmoc}$-b), 1.37 (s, 9H, -C(C*H*$_3$)$_3$).

13C-NMR, HSQC, HMBC (101 MHz, dmso-d6, 298 K): δ [ppm] = 172.1 (*C*=O^F), 169.0 (*C*=O^G), 168.7 (*C*=O^G), 155.9 (*C*=O^{Fmoc}), 155.7 (*C*=O^{Boc}), 143.8 (C_{Ar}), 140.7 (C_{Ar}), 138.2 (C_{Ar}), 129.3 (C_{Ar}), 128.1 (C_{Ar}), 127.7 (C_{Ar}), 127.1 (C_{Ar}), 126.3 (C_{Ar}), 125.3 (C_{Ar}), 120.1 (C_{Ar}), 77.8 (-*C*(CH$_3$)$_3$), 65.7 (*C*H$_2^F$), 54.9 (*C*H^{Fmoc}), 46.6 (F-α), 42.1 (2xG-α), 39.2 (*C*H$_2$CH$_2$), 38.7 (CH$_2$*C*H$_2$), 37.3 (*C*H$_2^{Fmoc}$), 28.2 (-C(*C*H$_3$)$_3$).

FmocFGG-C_2-NH_2 (III-5)

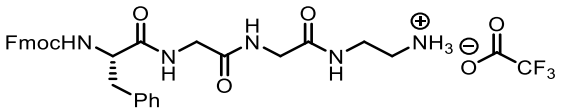

Fmoc-FGG-C_2-NHBoc (**III-4**, 0.82 g, 1.27 mmol, 1.0 eq.) was dissolved in 7 mL of a 10% solution of trifluoroacetic acid in CH_2Cl_2. After stirring for 1 h, the reaction mixture was concentrated *in vacuo* and co-evaporated with toluene.

Yield: 1.01 g (1.28 mmol), quant.; yellowish solid.

MF $C_{32}H_{34}F_3N_5O_7$ MW 657.6472 [657.2410]

R_F = 0.09 (SiO_2, CH_2Cl_2:MeOH = 10:1).

HR-QTOF-MS (ESI, pos), *m/z:* 566,2374 $[M+Na]^+$, (calc. = 566.2374).

^{1}H-NMR, COSY, HSQC, HMBC (400 MHz, dmso-d_6, 298 K): δ [ppm] = 8.36 (t, $^3J_{NH,G\text{-}\alpha}$ = 5.6 Hz, 1H, NH^G), 8.11 (t, $^3J_{NH,G\text{-}\alpha}$ = 5.8 Hz, 1H, NH^G), 8.03 (t, $^3J_{NH,CH2CH2}$ = 5.7 Hz, 1H, NHCH_2CH_2), 7.93 – 7.84 (m, 2H, H_{Ar}), 7.78 (s, 2H, NH_2), 7.68 (d, $^3J_{NH,\ F\text{-}\alpha}$ = 8.5 Hz, 1H, NH^F), 7.66 – 7.58 (m, 3H, H_{Ar}), 7.47 – 7.37 (m, 2H, H_{Ar}), 7.34 – 7.22 (m, 6H, H_{Ar}), 7.18 (m, 1H, H_{Ar}), 4.37 – 4.24 (m, 1H, -CH^{Fmoc}), 4.21 – 4.07 (m, 3H, F-α, F-β), 3.79 (d, $^3J_{G\text{-}\alpha,\ NH}$ = 5.6 Hz, 2H, G-α), 3.73 (d, $^3J_{G\text{-}\alpha,\ NH}$ = 5.7 Hz, 2H, G-α), 3.30 (m, 2H, -CH_2CH_2-), 3.14 – 3.00 (m, 1H, CH_2^{Fmoc}-a), 2.92 – 2.70 (m, 3H, -CH_2CH_2-, CH_2^{Fmoc}-b).

^{13}C-NMR, HSQC, HMBC (101 MHz, dmso-d_6, 298 K): δ [ppm] = 172.1 (C=O^F), 169.6 (C=O^G), 169.1 (C=O^G), 155.9 (C_{Ar}), 143.8 (C_{Ar}), 140.7 (C_{Ar}), 138.2 (C_{Ar}), 129.3 (C_{Ar}), 128.9 (C_{Ar}), 128.2 (C_{Ar}), 127.7 (C_{Ar}), 127.1 (C_{Ar}), 126.3 (C_{Ar}), 125.4 (C_{Ar}), 125.3 (C_{Ar}), 120.1 (C_{Ar}), 65.7 (F-β), 56.2 (CH^{Fmoc}), 46.6 (F-α), 42.2 (2xG-α), 38.6 (CH$_2$CH$_2$), 37.3 (CH$_2^{Fmoc}$), 36.4 (CH$_2C$H$_2$).

***tert*-Butyl (2-hydroxyethyl)carbamate (III-6)**

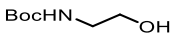

2-Aminoethan-1-ol (3.011 g, 49.30 mmol, 1.0 eq.) was dissolved in CH_2Cl_2 (150 mL) and di-*tert*-butyl dicarbonate (10.725 g, 49.14 mmol, 1.0 eq.) was added dropwise under ice-cooling over a period of 15 min. The reaction mixture was allowed to warm up to room temperature and was stirred for 2.5 h. After removing the solvent under reduced pressure, the product was purified via column chromatography (SiO_2, CH:EA = 3:2).

Yield: 7.391 g (45.85 mmol), 93%; colorless solid.

MF $C_7H_{15}NO_3$ MW 161.2010 [161.1052]

R_F = 0.33 (SiO_2, CH:EA = 1:1).

HR-QTOF-MS (ESI, pos), *m/z:* 184.0942 $[M+Na]^+$, (calc. = 184.0944).

^{1}H-NMR, COSY, HSQC, HMBC (300 MHz, $CDCl_3$, 298 K): δ [ppm] = 4.94 (s, 1H, -N*H*-), 3.70 (m, 2H, -CH_2-), 3.29 (m, 2H, -CH_2-), 2.04 (s, 1H, -O*H*), 1.45 (s, 9H, -C(CH_3)$_3$).

^{13}C-NMR, HSQC, HMBC (75 MHz, $CDCl_3$, 298 K): δ [ppm] = 150.0 (*C*=O), 79.9 (-*C*(CH_3)$_3$), 62.9 (-*C*H_2-), 43.4 (-*C*H_2-), 28.5 (-C(*C*H_3)$_3$).

***tert*-Butyl (2-(4-formylphenoxy)ethyl)carbamate (III-7)**

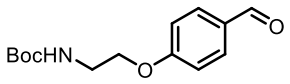

tert-Butyl (2-hydroxyethyl)carbamate **III-6** (6.894 g, 42.77 mmol, 1.0 eq.), 4-hydroxybenzaldehyde (6.270 g, 51.34 mmol, 1.2 eq.) and triphenylphosphine (13.438 g, 51.24 mmol, 1.2 eq.) were dissolved in THF (100 mL) and stirred under ice-cooling. A solution of 40 % solution of diethyl azodicarboxylate in toluene (20.10 mL, 51.20 mmol, 1.2 eq.) was added dropwise and the stirring was continued at room temperature for 14 h. The mixture was poured into water and extracted with ethyl acetate (3×30 mL). The organic layer was washed with brine (3×20 mL) and dried over Na_2SO_4. After filtration and concentration *in vacuo*, the crude product was purified *via* column chromatography (SiO2, gradient 16% → 50% EA in CH).

Yield: 7.546 g (28.46 mmol), 67%; yellowish solid.

MF $C_{14}H_{19}NO_4$ MW 265.3090 [265.1314]

R_F = 0.40 (SiO_2, CH:EA = 3:2).

HR-QTOF-MS (ESI, pos), *m/z:* 288.1207 $[M+Na]^+$, (calc. = 288.1206).

^{1}H-NMR, COSY, HSQC, HMBC (300 MHz, dmso-d_6, 298 K): δ [ppm] = 9.87 (s, 1H, -C*H*O), 7.91 – 7.80 (m, 2H, H_{Ar}), 7.16 – 7.09 (m, 2H, H_{Ar}), 7.09 – 7.00 (m, 1H, N*H*), 4.08 (t, $^3J_{CH2O,CH2NH}$ = 5.7 Hz, 2H, -CH_2O-), 3.38 – 3.24 (m, 2H, -NHCH_2-), 1.38 (s, 9H, -C(CH_3)$_3$).

^{13}C-NMR, HSQC, HMBC (75 MHz, dmso-d_6, 298 K): δ [ppm] = 191.3 (-*C*HO), 163.4 (C_{Ar}), 155.7 (-*C*OO), 131.8 (C_{Ar}), 129.7 (C_{Ar}), 115.0 (C_{Ar}), 77.9 (-*C*(CH_3)$_3$), 66.9 (-*C*H_2O-), 39.7 (-*C*H_2NH-), 28.2 (-C(*C*H_3)$_3$).

(*E*)-4-(4-(2-((*tert*-Butoxycarbonyl)amino)ethoxy)styryl)-1-methylpyridin-1-ium iodide (III-8)

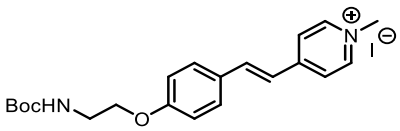

To a solution of *tert*-Butyl (2-(4-formylphenoxy)ethyl)carbamate **III-7** (4.01 g, 15.12 mmol, 1.1 eq.) and 1,4-dimethylpyridin-1-ium iodide (3.22 g, 13.70 mmol, 1.0 eq.) in methanol (250 mL), piperidine (4.10 mL) was added and the reaction mixture was stirred at 65 °C for 3 h. After removing the solvent under reduced pressure, the crude product was purified by precipitation twice in cold diethyl ether.

Yield: 4.013 g (8.32 mmol), 61%; orange solid.

MF $C_{21}H_{27}IN_2O_3$ MW 482.3625 [482.1066]

R_F = 0.22 (SiO_2, DMSO).

HR-QTOF-MS (ESI, pos), *m/z:* 355.2027 $[M+Na]^+$, (calc. = 355.2016).

^{1}H-NMR, COSY, HSQC, HMBC (300 MHz, dmso-d_6, 298 K): δ [ppm] = 8.83 –8.79 (m, 2H, H_{Ar}), 8.18 – 8.13 (m, 2H, H_{Ar}), 7.97 (d, $^3J_{CHCH,CHCH}$ = 16.3 Hz, 1H, -C*H*=CH-), 7.75 – 7.66 (m, 2H, H_{Ar}), 7.37 (d, $^3J_{CHCH,CHCH}$ = 16.3 Hz, 1H, -CH=C*H*-), 7.08 – 7.03 (m, 2H, H_{Ar}), 4.23 (s, 3H, -N-CH_3), 4.03 (t, $^3J_{CH2O,CH2NH}$ = 5.8 Hz, 2H, -CH_2O-), 3.34 – 3.29 (m, 2H, -NHCH_2-), 3.16 (d, $^3J_{NH,NHCH2}$ = 3.8 Hz, 1H, N*H*), 1.38 (s, 9H, -C(CH_3)$_3$).

^{13}C-NMR, HSQC, HMBC (75 MHz, dmso-d_6, 298 K): δ [ppm] = 160.9 (C_{Ar}), 156.2 (-COO), 153.3(C_{Ar}), 145.4 (C_{Ar}), 141.0 (=*C*H-), 130.5 (C_{Ar}), 128.3 (C_{Ar}), 123.5 (C_{Ar}), 121.2 (=*C*H-), 115.6 (*C*$_{Ar}$), 78.3 (-*C*(CH$_3$)$_3$), 67.1 (-*C*H$_2$O-), 47.3 (-N-*C*H$_3$), 39.8 (-*C*H$_2$NH-), 28.7 (-C(*C*H$_3$)$_3$).

(*E*)-4-(4-(2-Ammonioethoxy)styryl)-1-methylpyridin-1-ium trifluoroacetate iodide (III-9)

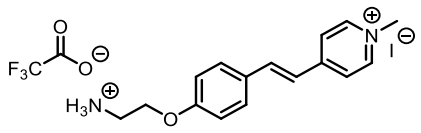

To a mixture of trifluoroacetic acid (18 mL) and water (2 mL) was added (*E*)-4-(4-(2-((tert-butoxycarbonyl)amino)ethoxy)styryl)-1-methylpyridin-1-ium iodide **III-8** (0.82 g, 1.70 mmol, 1.0 eq.). The mixture was stirred for 6 h and the acid was co-evaporated with toluene under reduced pressure. The product was purified *via* reversed phase flash chromatography (C_{18}, gradient: 5% → 100% acetonitrile in water).

Yield: 0.768 g (1.55 mmol), 91%; orange solid.

MF $C_{18}H_{20}F_3IN_2O_3$ MW 496.2687 [496.0471]

R_F = 0.13 (SiO_2, DMSO).

HR-QTOF-MS (ESI, pos), *m/z:* 255.1492 $[M+Na]^+$, (calc. = 255.1492).

^{1}H-NMR, COSY, HSQC, HMBC (400 MHz, D_2O, 298 K): δ [ppm] = 8.50 – 8.41 (m, 2H, H_{Ar}), 7.97 – 7.91 (m, 1H, -C*H*=), 7.97 – 7.91 (m, 2H, H_{Ar}), 7.75 – 7.63 (m, 1H, H_{Ar}), 7.16 (d, $^3J_{CHCH,CHCH}$ = 16.2 Hz, 1H, -CH=), 7.12 – 7.03 (m, 2H, H_{Ar}), 4.38 – 4.31 (m, 2H, -CH_2O-), 4.21 (t, $^3J_{NH,CH2}$ = 8.0 Hz, 2H, -NH_2), 4.19 (s, 3H, -N-CH_3), 3.49 – 3.43 (m, 2H, -C_2NH_2).

^{13}C-NMR, HSQC, HMBC (101 MHz, D_2O, 298 K): δ [ppm] = 159.5 (C_{Ar}), 153.7 (C_{Ar}), 143.1 (C_{Ar}), 140.5 (=CH-), 130.0 (C_{Ar}), 128.7 (C_{Ar}), 123.6 (C_{Ar}), 121.1 (=*C*H-), 115.2 (C_{Ar}), 63.9 (-*C*H2-O-), 46.8 (-*C*H2-NH2), 38.7 (-*C*H3).

4arm PEG-*p*-nitrophenylcarbonate (III-10)

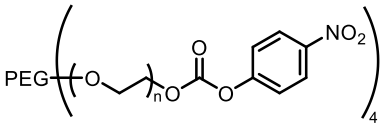

4-arm PEG-OH (1.00 g, 0.050 mmol, M_W = 20000 g mol^{-1}, 1.0 eq) was melted at 60 °C and dried *in vacuo* for 20 h. After cooling down to room temperature, the polymer was dissolved in dry DCM (25 mL). Subsequently, dry pyridine (0.13 mL, 0.127 mg, 1.600 mmol, 32.0 eq.) and *p*-nitrophenyl chloroformate (0.202 g, 1.000 mmol, 20.0 eq.) were added. After stirring at room temperature for 72 h, the reaction mixture was diluted with DCM (100 mL) and brine (150 mL) and extracted two times with DCM (2×200 mL). The organic layer was dried over $MgSO_4$, filtered and concentrated *in vacuo*. The crude product was precipitated in cold diethyl ether. After stirring for 1 h, the product was filtered and dried under vacuum.

Yield: 0.996 g (0.047 mmol), 96%; colorless solid, 93% functionalization (NMR).

^{1}H-NMR (300 MHz, CD_2Cl_2, 296 K): δ/ppm = 8.27 (m, 8H, H_{Ar}), 7.41 (m, 8H, H_{Ar}), 4.44 – 4.39 (m, 8H, PEG), 3.80 – 3.75 (m, 8H, PEG), 3.59 (s, 1796H, PEG).

4arm PEG-SB (III-1)

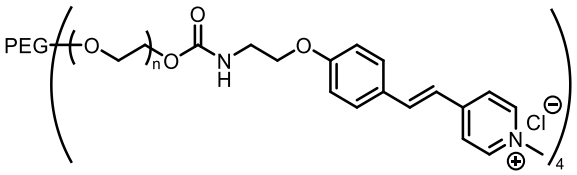

4Arm PEG-*p*-nitrophenylcarbonate **III-10** (0.20 g, 9.62 µmol, 1.0 eq.) was pre-dried *in vacuo* for 1 h and dissolved in dry DMF (5 mL). (*E*)-4-(4-(2-aminoethoxy)styryl)-1-methylpyridin-1-ium iodide **III-9** (0.04 g, 0.18 mmol, 10.0 eq.) and dry *N*,*N*-diisopropylethylamine (0.03 mL, 0.23 mmol, 15.0 eq.) were added to the solution and the reaction mixture was stirred at room temperature for 72 h under exclusion of light. The solvent was removed under reduced pressure and the residue was dissolved in methanol (1 mL), precipitated in ice-cold diethyl ether and stirred for 1 h. After filtration, the crude product was further purified *via* dialysis in water over 5 days under exclusion of light. The product was obtained by lyophilization of the solution.

Yield: 0.191 g (8.83 µmol), 92%; yellow solid, 75% functionalization (NMR).

^{1}H-NMR (400 MHz, dmso-d_6, 296 K): δ/ppm = 8.80 (m, 8H, H_{Ar}), 8.15 (m, 8H, H_{Ar}), 7.96 (m, 4H, =C*H*-), 7.70 (m, 8H, H_{Ar}), 7.36 (m, 4H, =C*H*-), 7.06 (m, 8H, H_{Ar}), 4.23 (s, 12H, -CH_3), 4.10 – 4.02 (m, 16H, -CH_2-), 3.71 – 3.64 (m, 8H, PEG), 3.61 – 3.41 (s, 1796H, PEG).

4arm PEG-FGG (III-2)

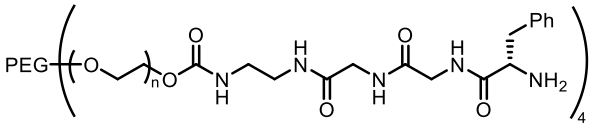

4Arm PEG-*p*-nitrophenylcarbonate **III-10** (0.50 g, 0.024 mmol, 1.0 eq.) was pre-dried *in vacuo* for 1 h and dissolved in dry DMF (2 mL). A solution of FmocHN-FGG-C_2-NH_2 **III-5** (0.26 g, 0.481 mmol, 20.0 eq.) and DIPEA (0.06 mL, 0.047 g, 0.36 mmol, 15.0 eq.) in dry DMF (1 mL) was added, subsequently. After stirring for 3 d, the reaction mixture was diluted with DCM (50 mL) and washed with brine (2×20 mL). The organic layer was dried over $MgSO_4$ and concentrated *in vacuo*. The residue was precipitated in ice-cold diethyl ether. The solid was collected by filtration and redissolved in DMF (8 mL) and piperidine (2 mL). After stirring for 1 h, the solvent was removed *in vacuo*. The product was further purified *via* dialysis in water for 3 d. The product was obtained by lyophilization.

Yield: 0.335 g (0.015 mmol), 65%; colorless solid, 92% functionalization (NMR).

^{1}H NMR (400 MHz, D_2O, 298 K): δ [ppm] = 7.44 – 7.21 (m, 20H, H_{Ar}), 4.19 (m, 8H), 3.95 (m, 4H, F-α), 3.90 – 3.83 (m, 24H, PEG), 3.70 (s, 1812H, PEG, G-α), 3.56 – 3.48 (m, 16H, PEG), 3.34 –3.30 (m, 8H, -C$H_2$$CH_2$-), 3.25 (m, 8H, -$CH_2CH_2$-), 3.07 (m, 8H, F-β).

(*E*)-4-(4-hydroxystyryl)-1-methylpyridin-1-ium iodide (III-11)

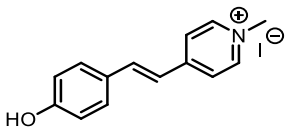

4-Hydroxybenzaldehyde (2.69 g, 22.00 mmol, 1.1 eq.) and 1,4-dimethylpyridin-1-ium iodide (4.70 g, 20.00 mmol, 1.0 eq.) were dissolved in methanol (350 mL) and piperidine (5.6 mL) was added. The reaction mixture was stirred and heated at 65 °C for 3 h. After concentration in vacuo, the crude product was precipitated in 1 L ice-cold diethyl ether and further purified by recrystallization from methanol.

Yield: 4.463 g (13.16 mmol), 66%; red solid.

MF $C_{14}H_{14}INO$ MW 339.1765 [339.0120]

R_F = 0.40 (SiO_2, CH:EA = 3:2).

HR-QTOF-MS (ESI, pos), *m/z:* 288.1207 $[M+Na]^+$, (calc. = 288.1206).

^{1}H-NMR, COSY, HSQC, HMBC (300 MHz, $CDCl_3$, 298 K): δ [ppm] = 8.45 – 8.41 (m, 2H, H_{Ar}), 7.91 – 7.86 (m, 2H, H_{Ar}), 7.65 (d, $^3J_{CH\text{CH,CH}CH}$ = 16.3 Hz, 1H, -C*H*=), 7.59 – 7.55 (m, 2H, H_{Ar}), 7.08 (d, $^3J_{CH\text{CH,CH}CH}$ = 16.3 Hz, 1H, -C*H*=), 6.93 – 6.87 (m, 2H, H_{Ar}), 4.19 (s, 3H, -N-CH_3).

^{13}C-NMR, HSQC, HMBC (75 MHz, $CDCl_3$, 298 K): δ [ppm] = 155.8 (C_{Ar}), 153.8 (C_{Ar}), 144.0 (C_{Ar}), 140.7 (=*C*H-), 130.3 (C_{Ar}), 129.4(C_{Ar}), 123.2 (C_{Ar}), 120.1 (=*C*H-), 116.2 (C_{Ar}), 46.6 (-*C*H_3).

FmocFGG-Cy3 (III-12)

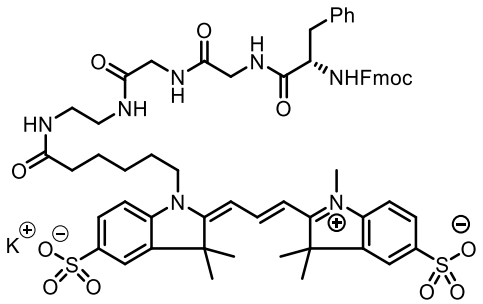

Sulfo-Cyanine3 NHS ester (1 mg, 1.4 µmol, 1.0 eq.) and FmocFGG-C_2-NH_2 (2.3 mg, 3.5 µmol, 2.5 eq.) were dissolved in dry DMF (1 mL). After the addition of DIPEA (1 µL, 0.7 mg, 5.6 µmol, 4.0 eq.), the reaction mixture was stirred at ambient temperature for 40 h. The solvent was removed in vacuo and the crude product was purified via reversed phase HPLC (C_{18} polar endcapped, gradient: 5% → 100% acetonitrile in water with addition of 0.1% trifluoroacetic acid).

Yield: 0.4 mg (0.4 µmol), 25%; red solid.

FGG-Cy3 (III-13)

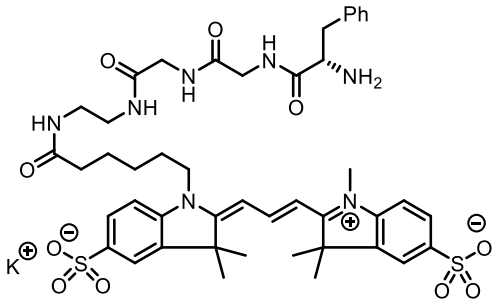

To a solution of FmocFGG-Cy3 (0.4 mg, 0.4 µmol, 1.0 eq.) in DMF (0.5 mL), piperidine (0.1 mL) was added. After stirring for 30 min, the solvent was removed in vacuo and the crude product was purified via reversed phase HPLC (C_{18} polar endcapped, gradient: 5% → 100% acetonitrile in water with addition of 0.1% trifluoroacetic acid).

Yield: 0.4 mg (0.4 µmol), quant.; red solid.

7.5 Biological Experiments

7.5.1 Cell culture conditions

SaOS-2 cells (human osteogenic sarcoma cells) were used for all cell culture experiments. The cells were cultivated in McCoy's medium containing 2 mM L-glutamine, and gentamycin (50 mg ml^{-1}), with addition of 10% fetal bovine serum (FCS) in 25 cm^2 flasks or multi-well plates (*Orange Scientifique*, Brainel'Alleud; Belgium) in a humidified incubator (37 °C and 5% CO_2). The cells were seeded at a starting concentration of 105 cells ml^{-1} in 25 cm^2 flasks. Culture medium/FCS was changed every 3 days.

7.5.2 Cell viability studies

The viability of SaOS-2 cells (human osteogenic sarcoma cells) was evaluated using calcein-AM labeling following the procedure from *Bratosin*.[319] After washing with 10 mL PBS, the cells were detached from the flask by addition of 3 mL Trypsin-EDTA solution. After 6 min incubation at 37 °C, an aliquot was taken and added to fresh McCoy medium with 10% FCS to prepare a cell suspension with a concentration of 10^4 cells mL^{-1}. In a 96 well-plate, 170 µL cell suspension was mixed with 0, 3, 10 and 30 µL of the testing material respectively and filled up with medium to reach a total volume of 200 µL. After incubation for 72 h, the solution was removed, and the cells washed with PBS. After addition of 200 µL of 0.15% calcein-AM stain solution in each well and 15 min incubation, the cell viability was inspected on an *Olympus IX71* fluorescence microscope using the excitation wavelength of 495 nm and emission wavelength of 511 nm. Vital cells were detected in green. For each hydrogel amount, 10 parallel experiments were performed. The results are given as mean values with standard deviation in percentage with respect to the controls.

7.5.3 Bio-ink preparation and bioprinting

Following the protocol in *hydrogel preparation*, 4 mL of 3.5 wt.-% hydrogel with **PEG-FGG:PEG-SB** ratio of 1:1 was prepared and irradiated 10 min using a 370 nm LED for photochemical crosslinking of network **B**. To the pre-crosslinked hydrogel, 200 µL of cell suspension (10^5 cells mL^{-1}) was added and the mixture was loaded to a sterile 30 mL cartridge.

The bioprinting experiments was performed on a computer-controlled 3D-Bioplotter (fourth generation blotter) from *EnvisionTEC GmbH* (Gladbeck, Germany). The cartridge containing the bio-ink was connected with a steel needle and place in a temperated printing head. The printing process was carried out at a temperature of 11 °C with a pressure of 2.0 bar and a printing speed of 8 mm s^{-1}. Cylindrical constructs with diameters of 10 mm or 50 mm diameter and 320 µm layer thickness were directly injected into 94 mm Petri dishes (Greiner Bio-One, Frickenhausen; Germany).

7.5.4 Evaluation of print fidelity

To evaluate the print stability, a 2-layer printed discs was fully covered by McCoy's medium with 10% FCS an incubated at 37 °C.

7.5.5 Cell viability post-extrusion

Printed discs containing SaOS-2 cells were incubated for indicated time periods. The cell viability and growth were assessed using calcein-AM stain as described in section 7.5.2 to 8, 24, 48 and 72 hours post-extrusion. In addition, the total and dead cell numbers directly after seeding as well as 2, 4 and 6 days post-extrusion were quantified using the ReadyProbes Cell Viability Imaging Kit (Thermo Fischer Scientific, Darmstadt, Germany) following the procedure from *Whitehead*.[338] To the cell culture medium, 50 µL mL^{-1} of the reagent mixture containing NucBlue (for staining of all the cells) and propidium iodide (for dead cells) were added. After incubation for 30 min, the cells were inspected on an *Olympus IX71* fluorescence microscope using the excitation wavelength of 360 nm and emission wavelength of 460 nm for the detection of NucBlue (excitation at 360 nm, emission at 469 nm) and propidium iodide (excitation at 535 nm, emission at 617 nm).

7.5.6 Mineralization assay

The differentiation of SaoS-2 cells post-printing was investigated by induction of the inorganic hydroxyapatite formation. Printed discs containing SaOS-2 cells were incubated in petri dishes covered by McCoy's medium with 10% FCS at 37 °C. After 6 h, the medium was replaced by fresh McCoy's medium with 10% FCS containing the activation cocktail (5 mM β-glycerophosphate, 50 mM L(+)-ascorbic acid and 10 nM dexamethasone). After incubation of 2, 4 and 6 days, the mineral depositions on the cell surface were stained using the OsteImage-Mineralization Assay.[322] Fluorescence images were taken with an *Olympus IX71* fluorescence microscope using the excitation wavelength of 492 nm and emission wavelength of 520 nm.

8 References

[1] P. H. Seeberger, *Chem. Rev.* **2020**, *121*, 3598.

[2] B. Pulendran, R. Ahmed, *Nat. Immunol.* **2011**, *12*, 509.

[3] P. M. Moyle, I. Toth, *ChemMedChem* **2013**, *8*, 360.

[4] D. H. Barouch, L. J. Picker, *Nat. Rev. Microbiol.* **2014**, *12*, 765.

[5] G. A. Roth, V. C. T. M. Picece, B. S. Ou, W. Luo, B. Pulendran, E. A. Appel, *Nat. Rev. Mater.* **2022**, *7*, 174.

[6] F. Liang, K. Loré, *Clin. Transl. Immunology* **2016**, *5*, e74.

[7] F. Liang, G. Lindgren, K. J. Sandgren, E. A. Thompson, J. R. Francica, A. Seubert, E. De Gregorio, S. Barnett, D. T. O'hagan, N. J. Sullivan, R. A. Koup, R. A. Seder, K. Loré, *Sci. Transl. Med.* **2017**, *9*, 2094.

[8] D. Sen, L. Forrest, T. B. Kepler, I. Parker, M. D. Cahalan, *PNAS* **2010**, *107*, 8334.

[9] R. L. Coffman, A. Sher, R. A. Seder, *Immunity* **2010**, *33*, 492.

[10] M. M. Steele, A. W. Lund, *J. Immun.* **2021**, *206*, 264.

[11] T. Worbs, S. I. Hammerschmidt, R. Förster, *Nat. Rev. Immunol.* **2017**, *17*, 30.

[12] J. K. Krishnaswamy, U. Gowthaman, B. Zhang, J. Mattsson, L. Szeponik, D. Liu, R. Wu, T. White, S. Calabro, L. Xu, M. A. Collet, M. Yurieva, S. Alsén, P. Fogelstrand, A. Walter, W. R. Heath, S. N. Mueller, U. Yrlid, A. Williams, S. C. Eisenbarth, *Sci. Immunol.* **2017**, *2*, 9169.

[13] I. Gurevich, T. Feferman, I. Milo, O. Tal, O. Golani, I. Drexler, G. Shakhar, *Eur. J. Immunol.* **2017**, *47*, 1802.

[14] S. Crotty, *Immunity* **2019**, *50*, 1132.

[15] S. M. Grant, M. Lou, L. Yao, R. N. Germain, A. J. Radtke, *J. Cell. Sci.* **2020**, *133*, jcs241828.

[16] B. A. Heesters, R. C. Myers, M. C. Carroll, *Nat. Rev. Immunol.* **2014**, *14*, 495.

[17] R. A. Elsner, M. J. Shlomchik, *Immunity* **2020**, *53*, 1136.

[18] E. J. Pone, J. Zhang, T. Mai, C. A. White, G. Li, J. K. Sakakura, P. J. Patel, A. Al-Qahtani, H. Zan, Z. Xu, P. Casali, *Nat. Commun.* **2012**, *3*, 767.

[19] L. Mesin, J. Ersching, G. D. Victora, *Immunity* **2016**, *45*, 471.

[20] M. J. Shlomchik, F. Weisel, *Immunol. Rev.* **2012**, *247*, 52.

[21] R. D. Astronomo, D. R. Burton, *Nat. Rev. Drug. Discov.* **2010**, *9*, 308.

[22] M. Heidelberger, O. T. Avery, *J. Exp. Med.* **1923**, *38*, 73.

[23] M. Heidelberger, F. E. Kendall, *J. Exp. Med.* **1932**, *57*, 373.

[24] E. Malito, B. Bursulaya, C. Chen, P. Lo Surdo, M. Picchianti, E. Balducci, M. Biancucci, A. Brock, F. Berti, M. J. Bottomley, M. Nissum, P. Costantino, R. Rappuoli, G. Spraggon, *PNAS* **2012**, *109*, 5229.

[25] V. Pozsgay, *Curr. Top. Med. Chem.* **2008**, *8*, 126.

[26] S. Lockhart, *Expert Rev. Vaccines* **2003**, *2*, 633.

[27] C. Jones, *An. Acad. Bras. Cienc.* **2005**, *77*, 293.

[28] F. Michon, C. Uitz, A. Sarkar, A. J. D'Ambra, M. Laude-Sharp, S. Moore, P. C. Fusco, *Clin. Vaccine Immunol.* **2006**, *13*, 936.

[29] J. Poolman, C. Frasch, A. Nurkka, H. Käyhty, R. Biemans, L. Schuerman, *Clin. Vaccine Immunol.* **2011**, *18*, 327.

[30] A. S. McKee, P. Marrack, *Curr. Opin. Immunol.* **2017**, *47*, 44.

[31] A. W. Sturgess, K. Rush, R. J. Charbonneau, J. I. Lee, D. J. West, R. D. Sitrin, J. P. Hennessey, *Vaccine* **1999**, *17*, 1169.

[32] N. S. Pujar, N. F. Huang, C. L. Daniels, L. Dieter, M. G. Gayton, A. L. Lee, *Biopolymers* **2004**, *75*, 71.

[33] B. Schumann, H. S. Hahm, S. G. Parameswarappa, K. Reppe, A. Wahlbrink, S. Govindan, P. Kaplonek, L. Pirofski, M. Witzenrath, C. Anish, C. L. Pereira, P. H. Seeberger, *Sci. Transl. Med.* **2017**, *9*, eaaf5347.

[34] M. P. Lisboa, N. Khan, C. Martin, F. F. Xu, K. Reppe, A. Geissner, S. Govindan, M. Witzenrath, C. L. Pereira, P. H. Seeberger, *PNAS* **2017**, *114*, 11063.

[35] B. Schumann, K. Reppe, P. Kaplonek, A. Wahlbrink, C. Anish, M. Witzenrath, C. L. Pereira, P. H. Seeberger, *ACS Cent. Sci.* **2018**, *4*, 357.

[36] R. A. De Silva, Q. Wang, T. Chidley, D. K. Appulage, P. R. Andreana, *J. Am. Chem. Soc.* **2009**, *131*, 9622.

[37] V. Verez-Bencomo, Fernandez-Santana V., E. Hardy, M. E. Toledo, M. C. Rodriguez, L. Heynngnezz, A. Rodriguez, A. Baly, L. Herrera, M. Izquierdo, A. Villar, Y. Valdes, K. Cosme, M. L. Deler, M. Montane, E. Garcia, G. Torano, I. Sosa, I. Hernandez, R. Martinez, A. Muzachio, A. Carmenates, L. Costa, F. Cardoso, C. Campa, M. Diaz, R. Roy, *Science* **2004**, *305*, 522.

[38] D. Straßburger, M. Glaffig, N. Stergiou, S. Bialas, P. Besenius, E. Schmitt, H. Kunz, *ChemBioChem* **2018**, *19*, 1142.

[39] D. Straßburger, N. Stergiou, M. Urschbach, H. Yurugi, D. Spitzer, D. Schollmeyer, E. Schmitt, P. Besenius, *ChemBioChem* **2018**, *19*, 912.

[40] K. A. Geno, G. L. Gilbert, J. Y. Song, I. C. Skovsted, K. P. Klugman, C. Jones, H. B. Konradsen, M. H. Nahm, *Clin. Microbiol. Rev.* **2015**, *28*, 871.

[41] A. G. Auld, *Br. Med. J.* **1897**, *1*, 775.

[42] P. Kaufmann, *Arch. Intern. Med.* **1947**, *79*, 518.

[43] M. Cadoz, *Vaccine* **1998**, *16*, 1391.

[44] E. Kay, J. Cuccui, B. W. Wren, *NPJ Vaccines* **2019**, *4*, 16.

[45] B. Schumann, K. Reppe, P. Kaplonek, A. Wahlbrink, C. Anish, M. Witzenrath, C. L. Pereira, P. H. Seeberger, *ACS Cent. Sci.* **2018**, *4*, 357.

[46] W. C. Gruber, D. A. Scott, E. A. Emini, *Ann. N.Y. Acad. Sci.* **2012**, *1263*, 15.

[47] B. Benaissa-Trouw, D. J. Lefeber, J. P. Kamerling, J. F. G. Vliegenthart, K. Kraaijeveld, H. Snippe, *Infect. Immun.* **2001**, *69*, 4698.

[48] D. J. Lefeber, J. P. Kamerling, J. F. G. Vliegenthart, *Chem. Eur. J.* **2001**, *7*, 4411.

[49] P. H. Seeberger, *Chem. Rev.* **2020**, *121*, 3598.

[50] C. Xiong, S. Feng, Y. Qiao, Z. Guo, G. Gu, *Chem. Eur. J.* **2018**, *24*, 8205.

[51] A. Varki, *Glycobiology* **2017**, *27*, 3.

[52] G. Báti, J. X. He, K. B. Pal, X. W. Liu, *Chem. Soc. Rev.* **2019**, *48*, 4006.

[53] S. Van Der Vorm, T. Hansen, J. M. A. Van Hengst, H. S. Overkleeft, G. A. Van Der Marel, J. D. C. Codeé, *Chem. Soc. Rev.* **2019**, *48*, 4688.

[54] C. S. Chao, C. Y. Lin, S. Mulani, W. C. Hung, K. K. T. Mong, *Chem. Eur. J.* **2011**, *17*, 12193.

[55] D. Crich, *Acc. Chem. Res.* **2010**, *43*, 1144.

[56] E. Juaristi, G. Cuevas, *Tetrahedron* **1992**, *48*, 5019.

[57] J. T. Edward, *Chem. Ind.* **1955**, *3*, 1102.

[58] C. Romers, C. Altona, H. R. Buys, E. Havinga, in *Top Stereochem*, John Wiley And Sons Inc., **1969**, p. 39.

[59] G. Barany, R. B. Merrifield, *J. Am. Chem. Soc.* **1977**, *99*, 7363.

[60] M. Schelhaas, H. Waldmann, *Glycochemical Synthesis: Strategies and Applications* **1996**, *35*, 2056.

[61] B. Ernst, H. G. W., S. P., *Carbohydrates in Chemistry and Biology*, Wiley-VCH Verlag, Weinheim, **2000**.

[62] K. C. Nicolaou, R. E. Dolle, D. P. Papahatjis, R. E. Dolle, *J. Am. Chem. Soc.* **1984**, *106*, 4189.

[63] S. Koto, T. Uchida, S. Zen, *Bull. Chem. Soc. Jpn.* **1973**, *46*, 2520.

[64] V. Dimakos, M. S. Taylor, *Chem. Rev.* **2018**, *118*, 11457.

[65] S. Hanessian, P. Lavallee, *Can. J. Chem.* **1975**, *53*, 2975.

[66] J. Lv, T. Luo, D. Zou, H. Dong, *Eur. J. Org. Chem.* **2019**, *2019*, 6383.

[67] S. K. Chaudhary, O. Hernandez, *Tetrahedron Lett.* **1979**, *2*, 95.

[68] L. Jiang, T.-H. Chan, *J. Org. Chem* **1998**, *63*, 6035.

[69] Y. Zhang, K. Wang, Z. Zhan, Y. Yang, Y. Zhao, *Tetrahedron Lett.* **2011**, *52*, 3154.

[70] H. Tanaka, Y. Tateno, Y. Nishiura, T. Takahashi, *Org. Lett.* **2008**, *10*, 5597.

[71] G. Gu, Y. Du, *J. Chem. Soc. Perkin 1* **2002**, *2*, 2075.

[72] J. Kihlberg, T. Frejd, K. Jansson, G. Magnusson, *Carbohydr Res* **1986**, *152*, 113.

[73] S. Velázquez, M. J. Camarasa, *Tetrahedron Asymmetry* **1994**, *5*, 2141.

[74] M. L. Bohn, M. I. Colombo, P. L. Pisano, C. A. Stortz, E. A. Rúveda, *Carbohydr. Res.* **2007**, *342*, 2522.

[75] E. S. Werstiuk, T. Neilson, J. Can, T. Chem ; Neilson, E. V Wastro-Dowski, R. J. Ibid ; Gregorire, C. B. Ibid ; Reese, R. Sañhill, J. E. Sulston, H. Takaku, T. Nomoto, K. Kamaike, W. T. Markiewicz, M. Wiewioroski, E. Ohtsuka, H. J. Dauben, J. L. R. Honnen, K. M. Harmon, *J. Org. Chem* **1984**, *49*, 51.

[76] P. J. Garegg, *Acta. Chem. Scand.* **1963**, *17*, 1343.

[77] M. Matwiejuk, J. Thiem, *ChemComm* **2011**, *47*, 8379.

[78] D. M. Clode, *Chem. Rev.* **1979**, *79*, 491.

[79] W. A. Bonner, *J. Org. Chem* **1959**, *24*, 1388.

[80] P. J. Duggan, E. M. Tyndall, *J. Chem. Soc. Perkin 1* **2002**, *2*, 1325.

[81] J. M. Lassaletta, M. Meichle, S. Weiler, R. R. Schmidt, *J. Carbohydr. Chem.* **1996**, *15*, 241.

[82] P. J. Garegg, H. Hultberg, S. Wallin, *Carbohydr. Res.* **1982**, *108*, 97.

[83] K. Larsen, C. E. Olsen, M. S. Motawia, *Carbohydr. Res.* **2003**, *338*, 199.

[84] G. Medgyes, G. Jerkovich, J. Kuszmann, *Carbohydr. Res.* **1989**, *186*, 225.

[85] M. Ohlin, R. Johnsson, U. Ellervik, *Carbohydr. Res.* **2011**, *346*, 1358.

[86] A. Liptak, I. Jodal, P. Nanasi, *Carbohydr. Res.* **1975**, *44*, 1.

[87] N. Tanaka, I. Ogawa, S. Yoshigase, J. Nokami, *Carbohydr. Res.* **2008**, *343*, 2675.

[88] F. A. Carey, K. 0 Hodgson, *Carbohydr. Res.* **1970**, *12*, 463.

[89] S. A. Abbas, A. H. Haines, *Carbohydr. Res.* **1975**, *39*, 358.

[90] S. Kim, H. Chang, W. J. Kim, *J. Org. Chem* **1985**, *50*, 1751.

[91] S. Burugupalli, S. Shah, P. L. Van Der Peet, S. Arora, J. M. White, S. J. Williams, *Org Biomol Chem* **2015**, *14*, 97.

[92] M. Wagner, D. Wagner, J. P. H. Verheyden, J. G. Moffatt, *J. Org. Chem* **1974**, *39*.

[93] S. David, S. Handsian, *Tetrahedron* **1985**, *41*, 643.

[94] M. S. Taylor, *Acc. Chem. Res.* **2015**, *48*, 295.

[95] E. Dimitrijević, M. S. Taylor, *ACS Catal.* **2013**, *3*, 945.

[96] J. J. Gridley, H. M. I. Osborn, W. G. Suthers, *Tetrahedron Lett.* **1999**, *40*, 6991.

[97] R. Eby, K. T. Webster, C. Schuerch, *Carbohydr. Res.* **1984**, *129*, 111.

[98] E. V. Evtushenko, *Carbohydr. Res.* **2012**, *359*, 111.

[99] E. Fischer, *Dtsch. Chem. Ges.* **1893**, *26*, 2400.

[100] K. Igarashi, *Adv. Carbohydr. Chem. Biochem.* **1977**, *34*, 243.

[101] R. Schmidt, J. Michel, *Angew. Chem., Int. Ed.* **1980**, *92*, 763.

[102] R. R. Schmidt, J. Michel, *Tetrahedron Lett.* **1984**, *25*, 821.

[103] B. Helferich, J. Goerdeler, *Dtsch. Chem. Ges.* **1940**, *5*, 532.

[104] H. Paulsen, J. P. Hölck, *Carbohydr. Res.* **1982**, *109*, 89.

[105] J. H. Kim, H. Yang, J. Park, G. J. Boons, *J. Am. Chem. Soc.* **2005**, *127*, 12090.

[106] H. Paulsen, O. Lockhoff, *Chem. Ber.* **1981**, *114*, 3079.

[107] H. Paulsen, W. Rauwald, R. Lebuhn, *Carbohydr. Res.* **1985**, *138*, 29.

[108] R. J. Williams, N. W. McGill, J. M. White, S. J. Williams, *J. Carbohydr. Chem.* **2010**, *29*, 236.

[109] M. R. Molla, P. Das, K. Guleria, R. Subramanian, A. Kumar, R. Thakur, *J. Org. Chem* **2020**, *85*, 9955.

[110] K. Le Mai Hoang, X. W. Liu, *Nat. Commun.* **2014**, *5*, 5051.

[111] A. Khanam, P. Kumar Mandal, *Asian J. Org. Chem.* **2021**, *10*, 296.

[112] D. Crich, P. Jayalath, *J. Org. Chem* **2005**, *70*, 7252.

[113] K. Greis, C. Kirschbaum, G. Fittolani, E. Mucha, R. Chang, G. von Helden, G. Meijer, M. Delbianco, P. H. Seeberger, K. Pagel, *Eur. J. Org. Chem* **2022**, *2022*, e202200255.

[114] W. Yang, J. Zhang, C. W. Yang, S. Ramadan, R. Staples, X. Huang, *Org. Lett.* **2021**, *23*, 1153.

[115] P. J. Garegg, P. Konradsson, I. Kvarnström, T. Norberg, S. C. T. Svensson, B. Wigilius, *Acta Chem. Scand., Ser. B* **1985**, *39*, 569.

[116] S. Chatterjee, S. Moon, F. Hentschel, K. Gilmore, P. H. Seeberger, *J. Am. Chem. Soc.* **2018**, *140*, 11942.

[117] T. Bowden, P. J. Garegg, J.-L. Maloisel, P. Konradsson, *Isr. J. Chem.* **2000**, *40*, 271.

[118] N. M. Spijker, C. A. A. van Boeckel, *Angew. Chem. Int. Ed.* **1991**, *30*, 180.

[119] M. T. C. Walvoort, W. De Witte, J. Van Dijk, J. Dinkelaar, G. Lodder, H. S. Overkleeft, J. D. C. Codée, G. A. Van Der Marel, *Org. Lett.* **2011**, *13*, 4360.

[120] M. T. C. Walvoort, G. Lodder, J. Mazurek, H. S. Overkleeft, J. D. C. Codée, G. A. Van Der Marel, *J. Am. Chem. Soc.* **2009**, *131*, 12080.

[121] H. A. Orgueira, A. Bartolozzi, P. Schell, P. H. Seeberger, *Angew. Chem. Int. Ed.* **2002**, *41*, 2128.

[122] G. Anilkumar, M. R. Gilbert, B. Fraser-Reid, *Tetrahedron* **2000**, *56*, 1993.

[123] T. Nokami, R. Hayashi, Y. Saigusa, A. Shimizu, C. Y. Liu, K. K. T. Mong, J. I. Yoshida, *Org. Lett.* **2013**, *15*, 4520.

[124] S. L. Tang, L. B. Linz, B. C. Bonning, N. L. B. Pohl, *J. Org. Chem.* **2015**, *80*, 10482.

[125] N. V. Ganesh, K. Fujikawa, Y. H. Tan, K. J. Stine, A. V. Demchenko, *Org. Lett.* **2012**, *14*, 3036.

[126] H. S. Hahm, M. K. Schlegel, M. Hurevich, S. Eller, F. Schuhmacher, J. Hofmann, K. Pagel, P. H. Seeberger, *PNAS* **2017**, *114*, E3385.

[127] M. Guberman, P. H. Seeberger, *J. Am. Chem. Soc.* **2019**, *141*, 5581.

[128] K. R. Love, P. H. Seeberger, *Angew. Chem. Int. Ed.* **2004**, *43*, 602.

[129] A. R. De Jong, A. G. Volbeda, B. Hagen, H. Van Den Elst, H. S. Overkleeft, G. A. Van Der Marel, J. D. C. Codée, *Eur. J. Org. Chem.* **2013**, 6644.

[130] X. Wu, M. Grathwohl, R. R. Schmidt, *Org. Lett.* **2001**, *3*, 747.

[131] L. Kröck, D. Esposito, B. Castagner, C. C. Wang, P. Bindschädler, P. H. Seeberger, *Chem. Sci.* **2012**, *3*, 1617.

[132] M. Wilsdorf, D. Schmidt, M. P. Bartetzko, P. Dallabernardina, F. Schuhmacher, P. H. Seeberger, F. Pfrengle, *ChemComm* **2016**, *52*, 10187.

[133] S. Eller, M. Collot, J. Yin, H. S. Hahm, P. H. Seeberger, *Angew. Chem. Int. Ed.* **2013**, *52*, 5858.

[134] K. Le Mai Hoang, A. Pardo-Vargas, Y. Zhu, Y. Yu, M. Loria, M. Delbianco, P. H. Seeberger, *J. Am. Chem. Soc.* **2019**, *141*, 9079.

[135] R. Behrend, E. Meyer, F. Rusche, *Justus Liebigs Ann. Chem.* **1905**, *339*, 1.

[136] W. A. Freeman, W. L. Mock, N.-Y. Shih, *J. Am. Chem. Soc.* **1981**, *103*, 7367.

[137] J. Kim, I. S. Jung, S. Y. Kim, E. Lee, J. K. Kang, S. Sakamoto, K. Yamaguchi, K. Kim, *J. Am. Chem. Soc.* **2000**, *122*, 540.

[138] A. Day, A. P. Arnold, R. J. Blanch, B. Snushall, *J. Org. Chem.* **2001**, *66*, 8094.

[139] R. D. Mukhopadhyay, K. Kim, *Nat. Chem.* **2023**, *15*, 438.

[140] S. J. Barrow, S. Kasera, M. J. Rowland, J. Del Barrio, O. A. Scherman, *Chem. Rev.* **2015**, *115*, 12320.

[141] J. Lagona, P. Mukhopadhyay, S. Chakrabarti, L. Isaacs, *Angew. Chem. Int. Ed.* **2005**, *44*, 4844.

[142] L. Barravecchia, A. Blanco-Gómez, I. Neira, R. Skackauskaite, A. Vila, A. Rey-Rico, C. Peinador, M. D. García, *J. Am. Chem. Soc.* **2022**, *144*, 19127.

[143] B. Vinciguerra, L. Cao, J. R. Cannon, P. Y. Zavalij, C. Fenselau, L. Isaacs, *J. Am. Chem. Soc.* **2012**, *134*, 13133.

[144] W. L. Mock, N.-Y. Shih, *J. Org. Chem.* **1986**, *51*, 4440.

[145] M. J. Rowland, M. Atgie, D. Hoogland, O. A. Scherman, *Biomacromolecules* **2015**, *16*, 2436.

[146] E. A. Appel, F. Biedermann, U. Rauwald, S. T. Jones, J. M. Zayed, O. A. Scherman, *J. Am. Chem. Soc.* **2010**, *132*, 14251.

[147] P. Novo, M. D. García, C. Peinador, E. Pazos, *Bioconjug. Chem.* **2021**, *32*, 507.

[148] J. Liu, C. Soo Yun Tan, Y. Lan, O. A. Scherman, *J. Polym. Sci. A Polym. Chem.* **2017**, *55*, 3105.

[149] C. L. Schreiber, B. D. Smith, *Nat. Rev. Chem.* **2019**, *3*, 393.

[150] K. I. Assaf, W. M. Nau, *Chem. Soc. Rev.* **2015**, *44*, 394.

[151] Y. H. Wang, H. Cong, F. F. Zhao, S. F. Xue, Z. Tao, Q. J. Zhu, G. Wei, *Catal. Commun.* **2011**, *12*, 1127.

[152] N. Basilio, L. García-Río, J. A. Moreira, M. Pessêgo, *J. Org. Chem.* **2010**, *75*, 848.

[153] M. Pattabiraman, A. Natarajan, L. S. Kaanumalle, V. Ramamurthy, *Org. Lett.* **2005**, *7*, 529.

[154] B. C. Pemberton, R. K. Singh, A. C. Johnson, S. Jockusch, J. P. Da Silva, A. Ugrinov, N. J. Turro, D. K. Srivastava, J. Sivaguru, *ChemComm* **2011**, *47*, 6323.

[155] W. L. Mock, T. A. Irra, J. P. Wepsiec, T. L. Manimaran, *J. Org. Chem.* **1983**, *48*, 3619.

[156] J. Smitka, A. Lemos, M. Porel, S. Jockusch, T. R. Belderrain, E. Tesařová, J. P. Da Silva, *Photochemical and Photobiological Sciences* **2014**, *13*, 310.

[157] R. Kaliappan, M. V. S. N. Maddipatla, L. S. Kaanumalle, V. Ramamurthy, *Photochem. Photobiol. Sci.* **2007**, *6*, 737.

[158] D. Chimene, K. K. Lennox, R. R. Kaunas, A. K. Gaharwar, *Ann. Biomed. Eng.* **2016**, *44*, 2090.

[159] H. Ravanbakhsh, V. Karamzadeh, G. Bao, L. Mongeau, D. Juncker, Y. S. Zhang, *Adv. Mater.* **2021**, *33*, 2104730.

[160] F. L. C. Morgan, L. Moroni, M. B. Baker, *Adv. Healthc. Mater* .**2020**, *9*, 1901798.

[161] F. L. C. Morgan, L. Moroni, M. B. Baker, *Adv. Healthc. Mater.* **2020**, *9*, 1901798.

[162] J. Jang, H. J. Park, S. W. Kim, H. Kim, J. Y. Park, S. J. Na, H. J. Kim, M. N. Park, S. H. Choi, S. H. Park, S. W. Kim, S. M. Kwon, P. J. Kim, D. W. Cho, *Biomaterials* **2017**, *112*, 264.

[163] N. Ashammakhi, S. Ahadian, C. Xu, H. Montazerian, H. Ko, R. Nasiri, N. Barros, A. Khademhosseini, *Mater. Today Bio.* **2019**, *1*, 100008.

[164] H. Lopez Hernandez, J. W. Souza, E. A. Appel, *Macromol. Biosci.* **2021**, *21*, 2000295.

[165] C. B. Highley, C. B. Rodell, J. A. Burdick, *Adv. Mater.* **2015**, *27*, 5075.

[166] Z. Wang, X. Jin, Z. Tian, F. Menard, J. F. Holzman, K. Kim, *Adv. Healthc. Mater.* **2018**, *7*, 1701249.

[167] S. V. Murphy, A. Atala, *Nat. Biotechnol.* **2014**, *32*, 773.

[168] C. Bader, D. Kolb, J. C. Weaver, S. Sharma, A. Hosny, J. Costa, N. Oxman, *Sci. Adv.* **2018**, *4*, eaas8652.

[169] X. Li, B. Liu, B. Pei, J. Chen, D. Zhou, J. Peng, X. Zhang, W. Jia, T. Xu, *Chem. Rev.* **2020**, *120*, 10793.

[170] P. Serra, A. Piqué, *Adv. Mater. Technol.* **2019**, *4*, 1800099.

[171] E. Davoodi, E. Sarikhani, H. Montazerian, S. Ahadian, M. Costantini, W. Swieszkowski, S. M. Willerth, K. Walus, M. Mofidfar, E. Toyserkani, A. Khademhosseini, N. Ashammakhi, *Adv. Mater. Technol.* **2020**, *5*, 1901044.

[172] C. Yu, J. Schimelman, P. Wang, K. L. Miller, X. Ma, S. You, J. Guan, B. Sun, W. Zhu, S. Chen, *Chem. Rev.* **2020**, *120*, 10695.

[173] W. Li, L. S. Mille, J. A. Robledo, T. Uribe, V. Huerta, Y. S. Zhang, *Adv Healthc Mater* **2020**, *9*, 2000156.

[174] K. S. Lim, B. J. Klotz, G. C. J. Lindberg, F. P. W. Melchels, G. J. Hooper, J. Malda, D. Gawlitta, T. B. F. Woodfield, *Macromol. Biosci.* **2019**, *19*, 1900098.

[175] Y. Chen, J. Zhang, X. Liu, S. Wang, J. Tao, Y. Huang, W. Wu, Y. Li, K. Zhou, X. Wei, S. Chen, X. Li, X. Xu, L. Cardon, Z. Qian, M. Gou, *Sci. Adv.* **2020**, *6*, eaba7406.

[176] L. Y. Zhou, J. Fu, Y. He, *Adv. Funct. Mater.* **2020**, *30*, 2000187.

[177] A. Bandyopadhyay, B. Heer, *Mater. Sci. Eng. R: Rep.* **2018**, *129*, 1.

[178] M. E. Prendergast, J. A. Burdick, *Advanced Materials* **2020**, *32*, 1902516.

[179] W. Liu, Y. S. Zhang, M. A. Heinrich, F. De Ferrari, H. L. Jang, S. M. Bakht, M. M. Alvarez, J. Yang, Y. C. Li, G. Trujillo-de Santiago, A. K. Miri, K. Zhu, P. Khoshakhlagh, G. Prakash, H. Cheng, X. Guan, Z. Zhong, J. Ju, G. H. Zhu, X. Jin, S. R. Shin, M. R. Dokmeci, A. Khademhosseini, *Adv. Mater.* **2017**, *29*, 1604630.

[180] L. Ouyang, J. P. K. Armstrong, Q. Chen, Y. Lin, M. M. Stevens, *Adv. Funct. Mater.* **2020**, *30*, 1908349.

[181] D. Kang, G. Hong, S. An, I. Jang, W. S. Yun, J. H. Shim, S. Jin, *Small* **2020**, *16*, 1905505.

[182] H. Lee, D. W. Cho, *Lab Chip* **2016**, *16*, 2618.

[183] T. Jiang, J. G. Munguia-Lopez, S. Flores-Torres, J. Grant, S. Vijayakumar, A. De Leon-Rodriguez, J. M. Kinsella, *Sci. Rep.* **2017**, *7*, 4575.

[184] M. Hospodiuk, M. Dey, D. Sosnoski, I. T. Ozbolat, *Biotechnol. Adv.* **2017**, *35*, 217.

[185] A. J. Engler, S. Sen, H. L. Sweeney, D. E. Discher, *Cell* **2006**, *126*, 677.

[186] O. Chaudhuri, L. Gu, D. Klumpers, M. Darnell, S. A. Bencherif, J. C. Weaver, N. Huebsch, H. P. Lee, E. Lippens, G. N. Duda, D. J. Mooney, *Nat Mater* **2016**, *15*, 326.

[187] J. Nicolas, S. Magli, L. Rabbachin, S. Sampaolesi, F. Nicotra, L. Russo, *Biomacromolecules* **2020**, *21*, 1968.

[188] M. Diba, S. Spaans, S. I. S. Hendrikse, M. M. C. Bastings, M. J. G. Schotman, J. F. van Sprang, D. J. Wu, F. J. M. Hoeben, H. M. Janssen, P. Y. W. Dankers, *Adv. Mater.* **2021**, *33*, 2008111.

[189] J. Hauptstein, L. Forster, A. Nadernezhad, J. Groll, J. Teßmar, T. Blunk, *Int. J. Mol. Sci.* **2022**, *23*, 924.

[190] N. Kulkarni, S. D. Shinde, G. S. Jadhav, D. R. Adsare, K. Rao, M. Kachhia, M. Maingle, S. P. Patil, N. Arya, B. Sahu, *Bioconjug. Chem.* **2021**, *32*, 448.

[191] C. C. Piras, D. K. Smith, *J. Mater. Chem. B* **2020**, *8*, 8171.

[192] W. Shi, M. Sun, X. Hu, B. Ren, J. Cheng, C. Li, X. Duan, X. Fu, J. Zhang, H. Chen, Y. Ao, *Adv. Mater.* **2017**, *29*, 1701089.

[193] W. J. Kim, C. H. Jang, G. H. Kim, *Nano Lett.* **2019**, *19*, 8612.

[194] C. Li, A. Faulkner-Jones, A. R. Dun, J. Jin, P. Chen, Y. Xing, Z. Yang, Z. Li, W. Shu, D. Liu, R. R. Duncan, *Angew. Chem.* **2015**, *127*, 4029.

[195] M. Müller, J. Becher, M. Schnabelrauch, M. Zenobi-Wong, *Biofabrication* **2015**, *7*, 035006.

[196] Z. Zheng, J. Wu, M. Liu, H. Wang, C. Li, M. J. Rodriguez, G. Li, X. Wang, D. L. Kaplan, *Adv. Healthc. Mater.* **2018**, *7*, 1701026.

[197] M. Kesti, M. Müller, J. Becher, M. Schnabelrauch, M. D'Este, D. Eglin, M. Zenobi-Wong, *Acta Biomater.* **2015**, *11*, 162.

[198] A. M. Navara, Y. S. Kim, Y. Xu, C. L. Crafton, M. Diba, J. L. Guo, A. G. Mikos, *Bioact. Mater.* **2022**, *14*, 302.

[199] L. Hahn, M. Beudert, M. Gutmann, L. Keßler, P. Stahlhut, L. Fischer, E. Karakaya, T. Lorson, I. Thievessen, R. Detsch, T. Lühmann, R. Luxenhofer, *Macromol. Biosci.* **2021**, *21*, 1.

[200] T. Lorson, S. Jaksch, M. M. Lübtow, T. Jüngst, J. Groll, T. Lühmann, R. Luxenhofer, *Biomacromolecules* **2017**, *18*, 2161.

[201] M. Hospodiuk, M. Dey, D. Sosnoski, I. T. Ozbolat, *Biotechnol. Adv.* **2017**, *35*, 217.

[202] U. Hersel, C. Dahmen, H. Kessler, *Biomaterials* **2003**, *24*, 4385.

[203] M. P. Lutolf, J. L. Lauer-Fields, H. G. Schmoekel, A. T. Metters, F. E. Weber, G. B. Fields, J. A. Hubbell, *PNAS* **2003**, *100*, 5413.

[204] G. P. Raeber, M. P. Lutolf, J. A. Hubbell, *Biophys. J.* **2005**, *89*, 1374.

[205] J. H. Y. Chung, S. Naficy, Z. Yue, R. Kapsa, A. Quigley, S. E. Moulton, G. G. Wallace, *Biomater. Sci.* **2013**, *1*, 763.

[206] T. Hu, X. Cui, M. Zhu, M. Wu, Y. Tian, B. Yao, W. Song, Z. Niu, S. Huang, X. Fu, *Bioact Mater* **2020**, *5*, 808.

[207] T. Nonoyama, J. P. Gong, *Proc. Inst. Mech. Eng. H* **2015**, *229*, 853.

[208] S. Hong, D. Sycks, H. F. Chan, S. Lin, G. P. Lopez, F. Guilak, K. W. Leong, X. Zhao, *Adv. Mater.* **2015**, *27*, 4035.

[209] S. Houben, A. A. Aldana, A. S. Huysecom, W. Mpinganzima, R. Cardinaels, M. B. Baker, L. M. Pitet, *ACS Appl. Polym. Mater.* **2023**, *5*, 1819.

[210] J. Zhu, Y. He, Y. Wang, L. H. Cai, *Nat. Commun.* **2024**, *15*, 5902.

[211] M. K. Jaiswal, J. R. Xavier, J. K. Carrow, P. Desai, D. Alge, A. K. Gaharwar, *ACS Nano* **2016**, *10*, 246.

[212] P. Kerativitayanan, J. K. Carrow, A. K. Gaharwar, *Adv. Healthc. Mater.* **2015**, *4*, 1600.

[213] L. Gasperini, J. F. Mano, R. L. Reis, *J. R. Soc. Interface* **2014**, *11*, 20140817.

[214] F. L. C. Morgan, J. Fernández-Pérez, L. Moroni, M. B. Baker, *Adv. Healthc. Mater.* **2022**, *11*, 2101576.

[215] T. Hu, X. Cui, M. Zhu, M. Wu, Y. Tian, B. Yao, W. Song, Z. Niu, S. Huang, X. Fu, *Bioact. Mater.* **2020**, *5*, 808.

[216] Y. Loo, A. Lakshmanan, M. Ni, L. L. Toh, S. Wang, C. A. E. Hauser, *Nano Lett.* **2015**, *15*, 6919.

[217] M. Dai, J. P. Belaïdi, G. Fleury, E. Garanger, M. Rielland, X. Schultze, S. Lecommandoux, *Biomacromolecules* **2021**, *22*, 4956.

[218] Y. Loo, A. Lakshmanan, M. Ni, L. L. Toh, S. Wang, C. A. E. Hauser, *Nano Lett.* **2015**, *15*, 6919.

[219] C. Li, A. Faulkner-Jones, A. R. Dun, J. Jin, P. Chen, Y. Xing, Z. Yang, Z. Li, W. Shu, D. Liu, R. R. Duncan, *Angew. Chem., Int. Ed.* **2015**, *127*, 4029.

[220] Y.-H. Peng, S. K. Hsiao, K. Gupta, A. Ruland, G. K. Auernhammer, M. F. Maitz, S. Boye, J. Lattner, C. Gerri, A. Honigmann, C. Werner, E. Krieg, *Nat. Nanotechnol.* **2023**, *18*, 1463.

[221] K. Zhang, Q. Feng, Z. Fang, L. Gu, L. Bian, *Chem. Rev.* **2021**, *121*, 11149.

[222] G. Stojkov, Z. Niyazov, F. Picchioni, R. K. Bose, *Gels* **2021**, *7*, DOI 10.3390/gels7040255.

[223] O. Chaudhuri, J. Cooper-White, P. A. Janmey, D. J. Mooney, V. B. Shenoy, *Nature* **2020**, *584*, 535.

[224] W. C. Yount, D. M. Loveless, S. L. Craig, *J. Am. Chem. Soc.* **2005**, *127*, 14488.

[225] P. C. Cai, B. Su, L. Zou, M. J. Webber, S. C. Heilshorn, A. J. Spakowitz, *ACS Cent. Sci.* **2022**, *8*, 1318.

[226] A. S. Braegelman, R. C. Ollier, B. Su, C. J. Addonizio, L. Zou, S. L. Cole, M. J. Webber, *ACS Appl. Bio. Mater.* **2022**, *5*, 4589.

[227] S. Tang, M. Wang, B. D. Olsen, *J. Am. Chem. Soc.* **2015**, *137*, 3946.

[228] R. W. Korsmeyer, R. Gurny, E. Doelker, P. Buri, N. A. Peppas, *Int. J. Pharm.* **1983**, *15*, 25.

[229] E. Axpe, D. Chan, G. S. Offeddu, Y. Chang, D. Merida, H. L. Hernandez, E. A. Appel, *Macromolecules* **2019**, *52*, 6889.

[230] N. A. Peppas, B. Narasimhan, *J. Control. Release.* **2014**, *190*, 75.

[231] H. Deschout, K. Raemdonck, J. Demeester, S. C. De Smedt, K. Braeckmans, *Pharm. Res.* **2014**, *31*, 255.

[232] B. L. Sprague, J. G. McNally, *Trends Cell. Biol.* **2005**, *15*, 84.

[233] F. A. Ganaie, J. S. Saad, S. W. Lo, L. McGee, S. D. Bentley, A. J. van Tonder, P. Hawkins, J. D. Keenan, J. J. Calix, M. H. Nahm, *J. Clin. Microbiol.* **2023**, *61*, e0002423.

[234] R. R. Reinert, *Clin. Microbiol. Infect.* **2009**, *15*, 7.

[235] T. Azarian, P. K. Mitchell, M. Georgieva, C. M. Thompson, A. Ghouila, A. J. Pollard, A. von Gottberg, M. du Plessis, M. Antonio, B. A. Kwambana-Adams, S. C. Clarke, D. Everett, J. Cornick, E. Sadowy, W. Hryniewicz, A. Skoczynska, J. C. Moïsi, L. McGee, B. Beall, B. J. Metcalf, R. F. Breiman, P. L. Ho, R. Reid, K. L. O'Brien, R. A. Gladstone, S. D. Bentley, W. P. Hanage, *PLoS Pathog.* **2018**, *14*, e1007438.

[236] D. Straßburger, S. Herziger, K. Huth, M. Urschbach, R. Haag, P. Besenius, *Beilstein J. Org. Chem.* **2021**, *17*, 97.

[237] C. Noti, J. L. De Paz, L. Polito, P. H. Seeberger, *Chem. Eur. J.* **2006**, *12*, 8664.

[238] L. K. Mydock, A. V. Demchenko, *Org. Biomol. Chem.* **2010**, *8*, 497.

[239] G. Báti, J. X. He, K. B. Pal, X. W. Liu, *Chem. Soc. Rev.* **2019**, *48*, 4006.

[240] Y. D. Vankar, P. S. Vankar, M. Behrendt, R. R. Schmidt, *Tetrahedron* **1991**, *47*, 9985.

[241] S. S. Kulkarni, C. C. Wang, N. M. Sabbavarapu, A. R. Podilapu, P. H. Liao, S. C. Hung, *Chem. Rev.* **2018**, *118*, 8025.

[242] S. Xiang, K. L. M. Hoang, J. He, Y. J. Tan, X.-W. Liu, *Angew. Chem.* **2015**, *127*, 614.

[243] J. H. Kim, H. Yang, J. Park, G. J. Boons, *J. Am. Chem. Soc.* **2005**, *127*, 12090.

[244] Y. Wang, Regioselektive Glykosylierung Mit Partiell Geschützter Cellobiose Als Glykosyl-Akzeptor, Johannes Gutenberg University , **2021**.

[245] S. K. Veleti, J. J. Lindenberger, D. R. Ronning, S. J. Sucheck, *Bioorg. Med. Chem.* **2014**, *22*, 1404.

[246] S. A. Mitchell, M. R. Pratt, V. J. Hruby, R. Polt, *J. Org. Chem.* **2001**, *66*, 2327.

[247] M. Karplus, *J. Am. Chem. Soc.* **1963**, *85*, 2870.

[248] Y. E. Tsvetkov, N. É. Byramova, L. V. Backinowsky, *Carbohydr. Res.* **1983**, *115*, 254.

[249] G. Zemplén, A. Kunz, *Eur. J. Inorg. Chem.* **1923**, *54*, 1705.

[250] C. Pezzetta, S. Tshepelevitsh, I. Leito, G. Poli, *Green Chemistry* **2018**, *20*, 2392.

[251] B. Ren, M. Wang, J. Liu, J. Ge, X. Zhang, H. Dong, *Green Chemistry* **2015**, *17*, 1390.

[252] B. Ren, M. Wang, J. Liu, J. Ge, X. Zhang, H. Dong, *Green Chemistry* **2015**, *17*, 1390.

[253] V. Jadhav, C. M. Pedersen, M. Bols, *Org. Biomol. Chem.* **2011**, *9*, 7525.

[254] S. Rubinsztajn, M. Cypryk, J. Chojnowski, *J. Organomet. Chem.* **1989**, *367*, 27.

[255] M. M. Mukherjee, N. Basu, A. Chaudhury, R. Ghosh, *RSC Adv.* **2016**, *6*, 109301.

[256] L. Massi, J. F. Gal, E. Duñach, *Chempluschem* **2022**, *87*, DOI 10.1002/cplu.202200037.

[257] E. J. Corey, K. Shimoji, *Tetrahedron Lett.* **1983**, *24*, 169.

[258] G. Desimoni, G. Faita, A. Mortoni, P. P. Righetti, *Tetrahedron Lett.* **1999**, *40*, 2001.

[259] H. Firouzabadi, N. Iranpoor, S. Sobhani, S. Ghassamipour, *J. Organomet. Chem.* **2004**, *689*, 3197.

[260] H. Paulsen, M. Paal, *Carbohydr. Res.* **1984**, *135*, 53.

[261] T. Ziegler, P. Kováč, C. P. J. Glaudemans, *Liebigs Ann. Chem.* **1990**, *1990*, 613.

[262] T. Ogawa, K. Beppu, S. Nakabayashi, *Carbohydr. Res.* **1981**, *93*, 6.

[263] D. J. Lefeber, J. P. Kamerling, J. F. G. Vliegenthart, *Chem. Eur. J.* **2001**, *7*, 4411.

[264] T. Tomoo, T. Kondo, H. Abe, S. Tsukamoto, M. Isobe, T. Goto, *Carbohydr. Res.* **1996**, *284*, 207.

[265] P. Konradsson, U. E. Udodong, B. Fraser-Reid, *Tetrahedron Lett.* **1990**, *31*, 4313.

[266] G. Lian, X. Zhang, B. Yu, *Carbohydr. Res.* **2015**, *403*, 13.

[267] J. Tatai, P. Fügedi, *Org. Lett.* **2007**, *9*, 4647.

[268] S. C. Ranade, A. V. Demchenko, *J. Carbohydr. Chem.* **2013**, *32*, 1.

[269] N. Verma, Z. Tu, M. S. Lu, S. H. Liu, S. Renata, R. Phang, P. K. Liu, B. Ghosh, C. H. Lin, *J. Org. Chem.* **2021**, *86*, 892.

[270] W. D. Weldu, C.-C. Wang, *J. Org. Chem.* **2021**, *86*, 17906.

[271] Y. Zeng, Z. Wang, D. Whitfield, X. Huang, *J. Org. Chem.* **2008**, *73*, 7952.

[272] Kwan Soo Kim, Jin Hwan Kim, Yong Joo Lee, Yong Jun Lee, J. Park, *J. Am. Chem. Soc.* **2001**, *123*, 8477.

[273] Y. S. Lu, Q. Li, L. H. Zhang, X. S. Ye, *Org. Lett.* **2008**, *10.*, 3445.

[274] C. Xiong, S. Feng, Y. Qiao, Z. Guo, G. Gu, *Chem. Eur. J.* **2018**, *24*, 8205.

[275] N. Mittal, G. M. Nisola, L. B. Malihan, J. G. Seo, S. P. Lee, W. J. Chung, *Korean J. Chem. Eng.* **2014**, *31*, 1362.

[276] L. Yin, J. Zhang, J. Yao, H. Li, *ChemCatChem* **2018**, *10*, 3513.

[277] W. Susanto, K. H. Kong, K. F. Hua, S. H. Wu, Y. Lam, *Tetrahedron Lett.* **2019**, *60*, 288.

[278] A. Presser, A. Hüfner, *Monatsh. Chem.* **2004**, *135*, 1015.

[279] J. D. Liu, Y. C. Chen, G. B. Zhang, Z. Q. Li, P. Chen, J. Y. Du, Y. Q. Tu, C. A. Fan, *Adv. Synth. Catal.* **2011**, *353*, 2721.

[280] D. P. Cox, J. Terpinski, W. Lawrynowicz, *J. Org. Chem.* **1984**, *49*, 3216.

[281] A. Hameed, R. D. Alharthy, J. Iqbal, P. Langer, *Tetrahedron* **2016**, *72*, 2763.

[282] E. J. Corey, A. Venkateswarlu, *J. Am. Chem. Soc* **1972**, *94*, 6190.

[283] Q. Zhang, P. L. Howell, H. S. Overkleeft, D. V. Filippov, G. A. van der Marel, J. D. C. Codée, *Carbohydr. Res.* **2017**, *450*, 12.

[284] E. J. Corey, B. B. Snider, *J. Am. Chem. Soc.* **1972**, *94*, 2549.

[285] I. H. Krouse, P. G. Wenthold, *J. Am. Soc. Mass. Spectrom.* **2005**, *16*, 697.

[286] R. M. Deshpande, R. V Chaudhari, H. Delmas, *J. Chem. Eng. Data* **1996**, *41*, 1414.

[287] J. Xia, C. F. Piskorz, J. L. Alderfer, R. D. Locke, K. L. Matta, *Pergamon Tetrahedron Lett.* **2000**, *41*.

[288] H. Fuwa, S. Fujikawa, K. Tachibana, H. Takakura, M. Sasaki, *Tetrahedron Lett.* **2004**, *45*, 4795.

[289] V. Dimakos, M. S. Taylor, *Chem. Rev.* **2018**, *118*, 11457.

[290] Y. Zhou, J. Li, Y. Zhan, Z. Pei, H. Dong, *Tetrahedron* **2013**, *69*, 2693.

[291] A. R. De Jong, B. Hagen, V. Van Der Ark, H. S. Overkleeft, J. D. C. Codée, G. A. Van Der Marel, *J. Org. Chem.* **2012**, *77*, 108.

[292] M. A. Nashed, L. Anderson, *Tetrahedron Lett.* **1976**, *39*, 3503.

[293] G. Despras, C. Bernard, A. Perrot, L. Cattiaux, A. Prochiantz, H. Lortat-Jacob, J. M. Mallet, *Chem. Eur. J.* **2013**, *19*, 531.

[294] G. Xiao, G. A. Cintron-Rosado, D. A. Glazier, B. M. Xi, C. Liu, P. Liu, W. Tang, *J. Am. Chem. Soc.* **2017**, *139*, 4346.

[295] S. A. Blaszczyk, G. Xiao, P. Wen, H. Hao, J. Wu, B. Wang, F. Carattino, Z. Li, D. A. Glazier, B. J. McCarty, P. Liu, W. Tang, *Angew. Chem., Int. Ed.* **2019**, *58*, 9542.

[296] R. S. Porto, M. L. A. A. Vasconcellos, E. Ventura, F. Coelho, *Synthesis* **2005**, *14*, 2297.

[297] A. Hassner, G. Strand, M. Rubinstein, A. Patchornik, *J. Am. Chem. Soc.* **1975**, *97*, 1614.

[298] N. Jeker, C. Tamm, *Helv. Chim. Acta* **1988**, *71*, 1904.

[299] L. G. Baud, M. A. Manning, H. L. Arkless, T. C. Stephens, W. P. Unsworth, *Chem. Eur. J.* **2017**, *23*, 2225.

[300] V. A. Shcherbinin, E. S. Spesivaya, V. V. Konshin, *Tetrahedron Lett.* **2019**, *60*, 957.

[301] D. P. Langlois, H. Wolff, *J. Am. Chem. Soc.* **1948**, *70*, 2624.

[302] V. Petrovic, S. Tomic, M. Matanovic, *Carbohydr. Res.* **2002**, *337*, 863.

[303] W. A. Bonner, *J. Org. Chem.* **1959**, *24*, 1388.

[304] T. O. Oesterling, C. M. Metzler, *J. Pharm. Sci.* **1972**, *61*, 287.

[305] Y. Wang, A. M. Bimmermann, M. Neufurth, P. Besenius, *Adv. Mater.* **2024**, *36*, 2313270.

[306] S. Senler, L. Cui, A. M. Broomes, E. L. Smith, J. N. Wilson, A. E. Kaifer, *J. Phys. Org. Chem.* **2012**, *25*, 592.

[307] L. M. Heitmann, A. B. Taylor, P. J. Hart, A. R. Urbach, *J. Am. Chem. Soc.* **2006**, *128*, 12574.

[308] L. Zou, M. J. Webber, *Chem. Comm.* **2019**, *55*, 9931.

[309] J. O. Morley, R. M. Morley, R. Docherty, M. H. Charlton, *J. Am. Chem. Soc.* **1997**, *119*, 10192.

[310] S. Tang, B. D. Olsen, *Macromolecules* **2016**, *49*, 9163.

[311] U. Steiner, H. Abdel-Kader, lb P. Fischer, E. A. Kramer, *J. Am. Chem. Soc.* **1978**, *100*, 3190.

[312] F. Strieth-Kalthoff, M. J. James, M. Teders, L. Pitzer, F. Glorius, *Chem. Soc. Rev.* **2018**, *47*, 7190.

[313] W. Liu, X. Gong, Y. Zhu, J. Wang, T. Ngai, C. Wu, *Macromolecules* **2019**, *52*, 8956.

[314] D. Bardelang, K. A. Udachin, D. M. Leek, J. C. Margeson, G. Chan, C. I. Ratcliffe, J. A. Ripmeester, *Cryst. Growth Des.* **2011**, *11*, 5598.

[315] O. Chaudhuri, L. Gu, M. Darnell, D. Klumpers, S. A. Bencherif, J. C. Weaver, N. Huebsch, D. J. Mooney, *Nat. Commun.* **2015**, *6*, 6364.

[316] A. R. Cameron, J. E. Frith, J. J. Cooper-White, *Biomaterials* **2011**, *32*, 5979.

[317] A. R. Cameron, J. E. Frith, G. A. Gomez, A. S. Yap, J. J. Cooper-White, *Biomaterials* **2014**, *35*, 1857.

[318] Y. J. Shin, R. T. Shafranek, J. H. Tsui, J. Walcott, A. Nelson, D. H. Kim, *Acta Biomater.* **2021**, *119*, 75.

[319] D. Bratosin, L. Mitrofan, C. Palii, J. Estaquier, J. Montreuil, *Cytometry Part A* **2005**, *66*, 78.

[320] F. Grinnell, C.-H. Ho, E. Tamariz, D. J. Lee, G. Skuta, *Mol. Biol. Cell* **2003**, *14*, 384.

[321] M. Wiens, X. Wang, U. Schlomacher, I. Lieberwirth, G. Glasser, H. Ushijima, H. C. Schröder, W. E. G. Müller, *Calcif. Tissue Int.* **2010**, *87*, 513.

[322] Y. H. Wang, Y. Liu, P. Maye, D. W. Rowe, *Biotechnol. Prog.* **2006**, *22*, 1697.

[323] M. Quesada-Perez, A. Martin-Molina, *Adv. Colloid. Interface Sci.* **2021**, *287*, 102320.

[324] M. Kang, C. A. Day, A. K. Kenworthy, E. DiBenedetto, *Traffic* **2012**, *13*, 1589.

[325] S. Tang, A. Habicht, S. Li, S. Seiffert, B. D. Olsen, *Macromolecules* **2016**, *49*, 5599.

[326] N. W. Goehring, D. Chowdhury, A. A. Hyman, S. W. Grill, *Biophys. J.* **2010**, *99*, 2443.

[327] H. D. Nguyen, D. T. Dang, J. L. J. van Dongen, L. Brunsveld, *Angew. Chem.* **2010**, *122*, 907.

[328] D. K. Cheerambathur, G. Civelekoglu-Scholey, I. Brust-Mascher, P. Sommi, A. Mogilner, J. M. Scholey, *J. Cell Biol.* **2007**, *177*, 995.

[329] E. D. Salmon, R. J. Leslie, W. M. Saxton, M. L. Karow, J. R. Mclntosh, *J. Cell Biol.* **1984**, *99*, 2165.

[330] J. Stricker, P. Maddox, E. D. Salmon, H. P. Erickson, J. R. Mcintosh, *PNAS* **2002**, *99*, 3171.

[331] D. Axelrod, D. E. Koppel, J. Schlessinger, E. Elson, W. W. Webb, *Biophys. J.* **1976**, *16*, 1055.

[332] D. M. Soumpasis, *Biophys. J.* **1983**, *41*, 95.

[333] S. Seiffert, W. Oppermann, *J. Microsc.* **2005**, *220*, 20.

[334] G. I. Hauser, S. Seiffert, W. Oppermann, *J. Microsc.* **2008**, *230*, 353.

[335] E. Atherton, H. Fox, D. Harkiss, C. J. Logan, R. C. Sheppard, B. J. Williams, *Chem. Comm.* **1978**, 537.

[336] S. Kopitzki, K. J. Jensen, J. Thiem, *Chem. Eur. J.* **2010**, *16*, 7017.

[337] C. B. Purves, *J. Am. Chem. Soc.* **1929**, *51*, 3619.

[338] A. K. Whitehead, H. H. Barnett, M. E. Caldorera-Moore, J. J. Newman, *Regen. Biomater.* **2018**, *5*, 167.

9 Abbreviations

[α]	specific rotation
1% $NaHCO_{3\ aq}$	1% solution of sodium bicarbonate
^{13}C-NMR	carbon NMR
^{1}H-NMR	proton NMR
$^{2}J_{H\text{-}X,H\text{-}Y}$	coupling constant of the geminal coupling between the H atom at the X position and the H atom at the Y position
$^{3}J_{H\text{-}X,H\text{-}Y}$	coupling constant of the vicinal coupling between the H atom at the X position and the H atom at the Y position
4 Å MS	molecular sieves with a pore size of 4 Å
4arm PEG-OH	4-arm star-shaped poly(ethylene glycol)
Ac	acetyl
Ac_2O	acetic anhydride
ACN	acetonitrile
AGA	automated glycan assembly
AgOTf	silver trifluoromethanesulfonate
APC	antigen-presenting cells
BAIB	(diacetoxyiodo)benzene
BDMA	benzaldehyde dimethyl acetal
BF_3•OEt_2	boron trifluoride etherate
BM	Brooker's merocyanine
Bn	benzyl
BnBr	benzyl bromide
Boc	butyloxycarbonyl
Boc_2O	di-*tert*-butyl dicarbonate
BTM	benzotetramisole
Bu_2SnO	dibutyltin oxide
Bz	benzoyl
Bz2O	benzoic anhydride
BzOCl	benzoyl chloride
c	concentration
c*	critical overlap concentration
CB[*n*]	cucurbit[*n*]uril with *n* glycouril units
Cbz	benzyoxycarbonyl
CbzCl	benzyoxycarbonyl chloride
CD_2Cl_2	deuterated dichloromethane
$CDCl_3$	deuterated chloroform

CH	cyclohexane
CLSM	confocal laser scanning microscope
conc. $(NH_4)_2SO_{4\ aq}$	concentrated solution of ammonium sulfate in water
conc. $NaCl_{aq}$	concentrated solution of sodium chloride in water
conc. $NaHCO_{3\ aq}$	concentrated solution of sodium bicarbonate in water
CPS	capsular polysacchride
CsF	cesium fluoride
CsF	chondroitin sulfate
C-X	carbon atom on the position X within the saccharide
Cy3	sulfo-cyanine3
D	diffusion coefficient
d	diameter
D2O	deuterated water
DCM	dichloromethane
DCvC	dynamic covalent chemistry
DDQ	2,3-dichloro-5,6-dicyano-1,4-benzoquinone
DFT	density field theory
DIPEA	diisopropylethylamine
DMAP	4-*N*,*N*-dimethylaminopyridine
DMF	*N*,*N*-dimethylformamide
DMSO	dimethylsulfoxide
dmso-d_6	deuterated dimethylsulfoxide
DMTST	dimethyl(methylthio)sulfonium triflate
DN	double network
DNA	deoxyribonucleic acid
DT	diphtheria toxoid
EA	ethyl acetate
ECM	extracellular matrix
***E*comp**	compression modulus
eq.	equivalent(s)
ESI	electron spray ionization
FCS	fetal calf serum
FCS	fluorescence correlation spectroscopy
FGG	tripeptide phenylalanine-glycine-glycine
Fmoc	fluorenylmethoxycarbonyl
FmocCl	fluorenylmethoxycarbonyl chlorid
FRAP	fluorescence recovery after photobleaching
FRC	forced Rayleigh scattering

G'	storage modulus
G''	loss modulus
G*	comlex shear modulus
G_0	plateau modulus
Glc	glucose
GlcA	glucoronic acid
h	hour(s)
H_2SO_4	sulfuric acid
HBr	hydrobromic acid
HBTU	2-(1*H*-benzotriazol-1-yl)-1,1,3,3-tetramethyluronium hexafluorophosphate
HF	hydrogen fluoride
Hib	*Haemophilus influenzae* type b
HIV	human immunodeficiency viruses
HMBC	heteronuclear multiple bond correlation
HOAc	acetic acid
HOBt	1-hydroxybenzotriazole
HOTf	trifluoromethanesulfonic acid
HPLC	high performance liquid chromatography
HR-QToF-MS	high resolution quadrupole time-of-flight mass spectroscopy
HSQC	heteronuclear single quantum coherence
HSQC no dec.	heteronuclear single quantum coherence no decoupling
HSTol	*p*-thiocresol
H-X	hydrogen atom on the position X within the saccharide
I	intensity
IPN	interpenetrating network
LED	light-emitting diode
Lev	levulinoyl
LevOH	levulinic acid
LIFT	light-induced forward transfer
LiOH	lithium hydroxide
m/z	mass-to-charge ratio
Me	methyl
MeOH	methanol
MeOTf	methyl triflate
$Mg(OTf)_2$	magnesium trifluoromethanesulfonate
$MgSO_4$	magnesium sulfate
MHC	major histocompatibility complex
min	minite(s)

MWCO	molecular weight cut-off
NaH	sodium hydride
NaOMe	sodium methoxide
Nap	2-naphthylmethyl
NapBr	2-naphthylmethylbromide
NEt_3	triethylamine
NHS	*N*-hydroxysuccinimide
NIR	near-infrared
NIS	*N*-iodsuccinimide
NMR	nuclear magnetic resonance
NMRd	nuclear magnetic resonance diffusometry
NO_2	nitro
OH	hydroxyl
OMe	methoxy
O-X	oxygen atom on the position X within the saccharide
PAMPs	pathogen-associated molecular patterns
PBS	phosphate-buffered saline
Pd/C	palladium on charcoal
PDA	photo diode array
PEG	poly(ethylene glycol)
PEGDMA	poly(ethylene glycol) dimethacrylate
PEG-FGG	poly(ethylene glycol) end-functionalized with tripeptide phenylalanine-glycine-glycine
PEG-SB	poly(ethylene glycol) end-functionalized with stilbazolium iodide
PG	protecting group
Ph	phenyl
Piv_2O	pivalic anhydride
PPh3	triphenylphosphine
ppm	parts per million
PRRs	pattern-recognition receptors
r	radius
r.t.	room temperature
R_F	refractive index
RGD	arginine-glycine-asparagine
ROI	region of interest
RP	reversed phase
S. pneumoniae	*Streptococcus pneumoniae*
SaOS-2	human osteogenic sarcoma cells

SB	stilbazolium iodide
SiO_2	silica
SN	single network
SPPS	solid phase peptide synthesis
ST3	serotype 3
STP	single particle tracking
t	time
TBAF	tetrabutylammonium fluoride
TBAI	tetrabutylammonium iodide
TBDMS	*tert*-butyldimethylsilyl
TBDMSCl	*tert*-butyldimethylsilyl chloride
TBDPS	*tert*-butyldiphenylsilyl
TBDPSCl	*tert*-butyldiphenylsilyl chloride
TEM	transmission electron microscopy
TEMPO	2,2,6,6-tetramethyl-1-piperidinyloxy
TFA	trifluoroacetic acid
THF	tetrahydrofuran
TIS	triisopropylsilane
TLC	thin-layer chromatography
TLR	toll-like receptors
$TMSCH_2N_2$	trimethylsilyldiazomethane
TMSOTf	Trimethylsilyltrifluormethansulfonat
TOCSY	total correlation spectroscopy
tPG	temporary protecting group
TsOH	*p*-toluenesulfonic acid
TT	tetanus toxoid
UV	ultraviolet light
Vis	visible light
β	network relaxation rate
γ	shear strain
δ	chemical shift (in ppm)
λ	wavelength
σ	standard deviation
τ	relaxation time
$\tau_{1/2}$	fluorescence recovery half-time
ω	angular frequency
ω_0	crossover frequency

10 Additional Data

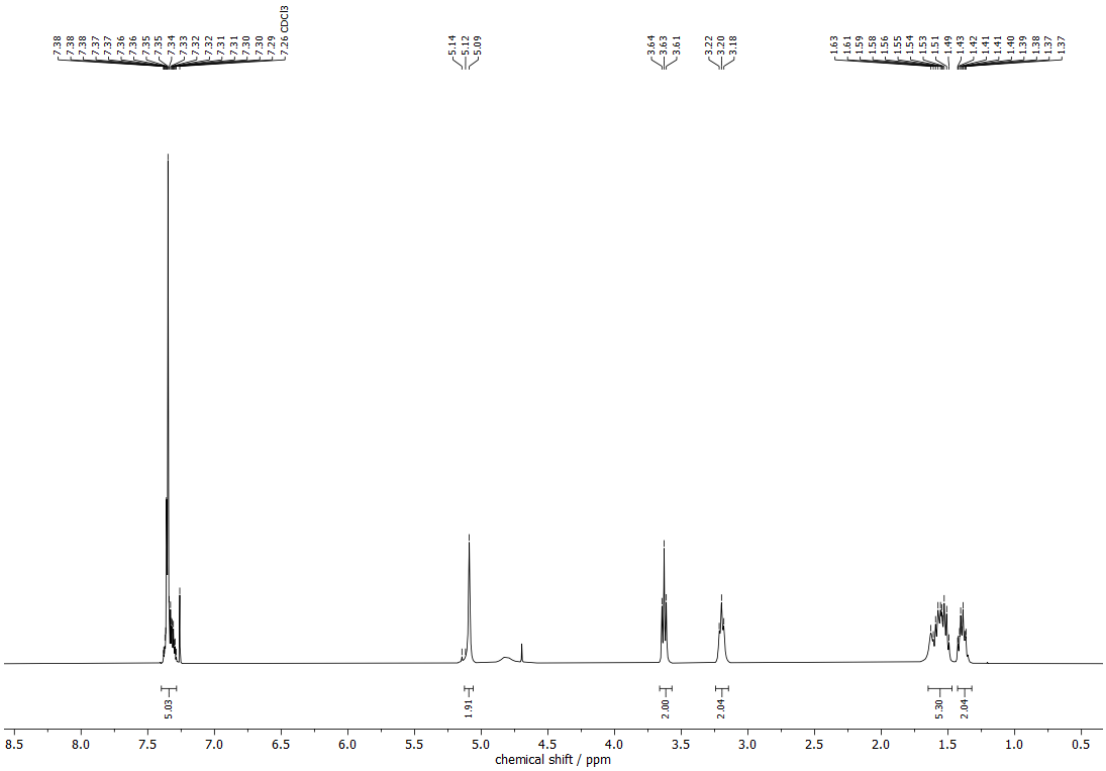

Figure 10.1: ^{1}H-NMR spectrum (300 MHz, $CDCl_3$, 298 K) of *N*-benzyl (5-hydroxypentyl)carbamate (**I-1**).

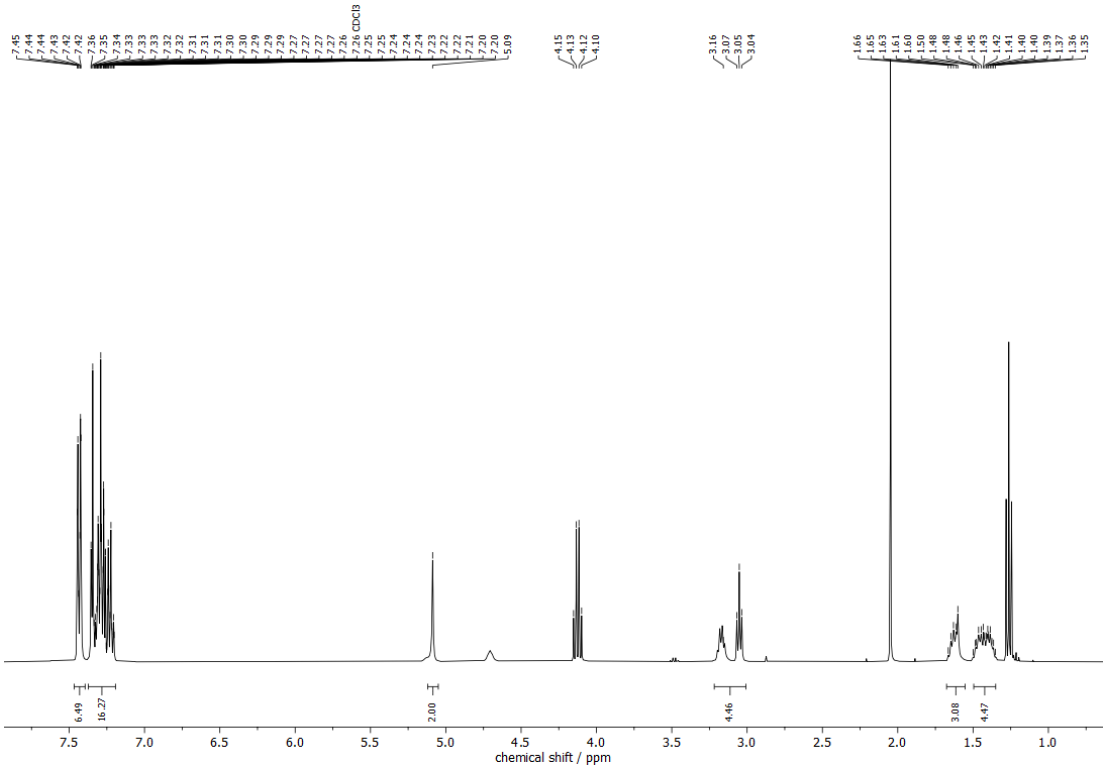

Figure 10.2: ^{1}H-NMR spectrum (300 MHz, $CDCl_3$, 298 K) of *N*-benzyl-(5-oxytrityl)carbamate (**I-2**).

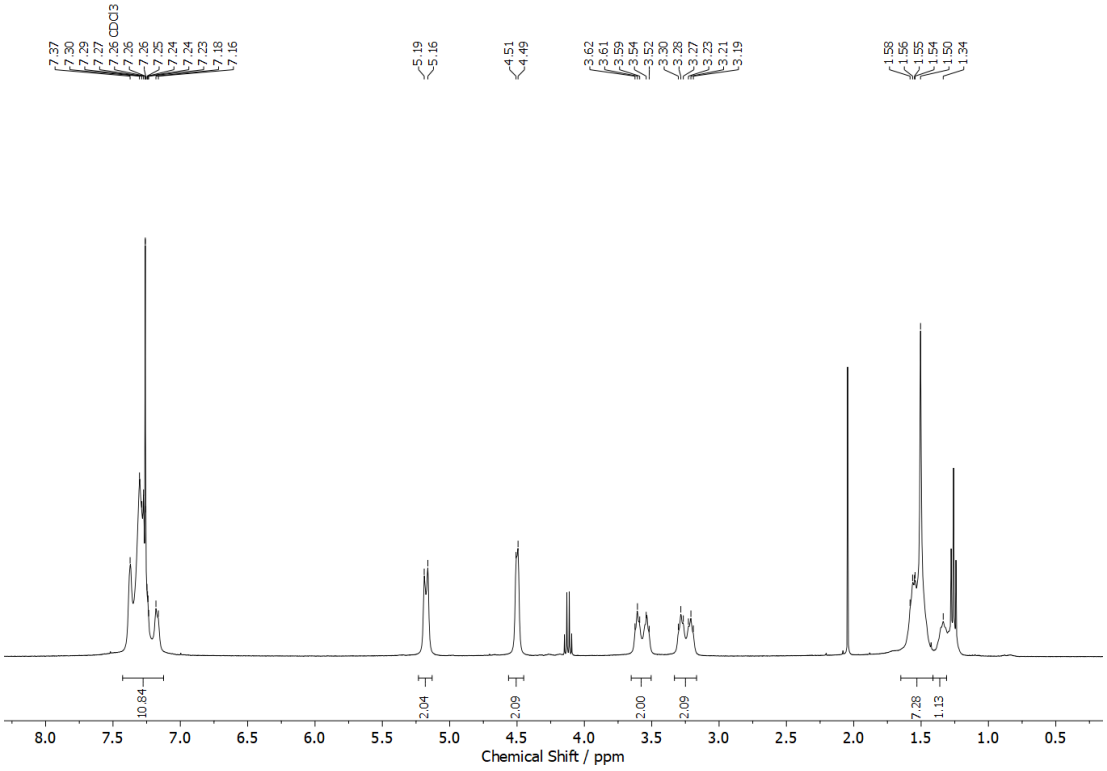

Figure 10.3: ^{1}H-NMR spectrum (400 MHz, $CDCl_3$, 298 K) of *N*-(benzyl)-benzyloxycarbonyl-5-aminopentan-1-ol (**I-4**).

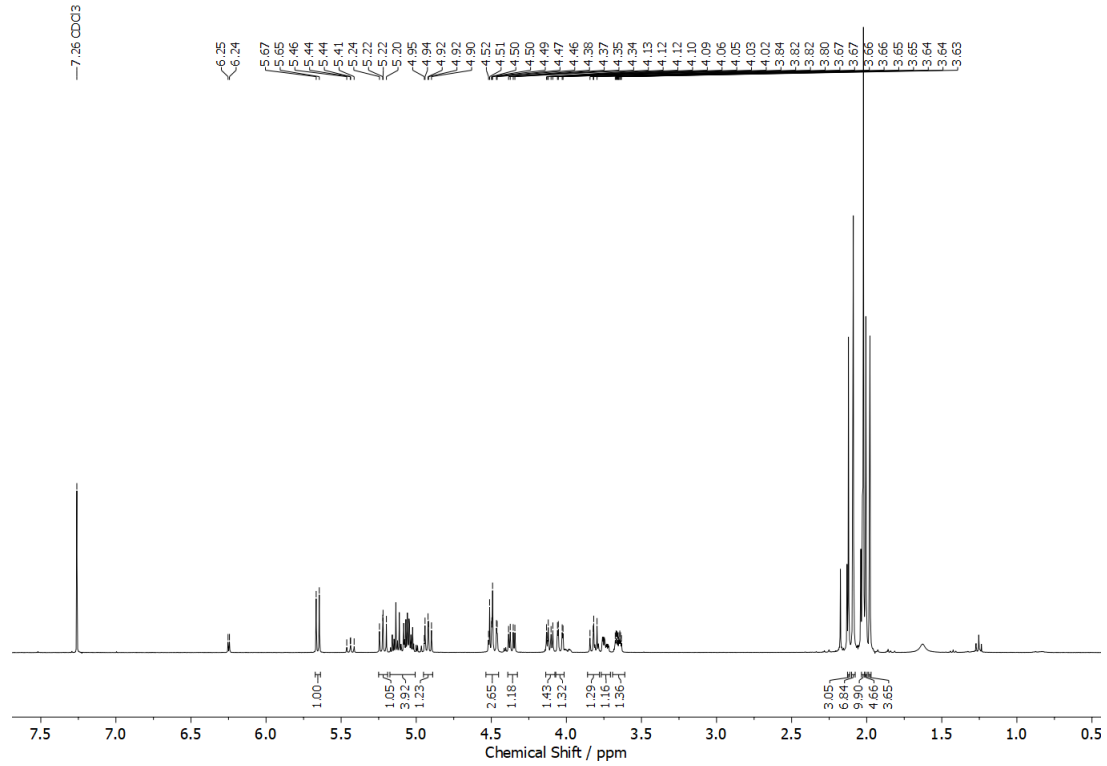

Figure 10.4: ^{1}H-NMR spectrum (600 MHz, $CDCl_3$, 298 K) of 1,2,3,6,2',3',4',6'-octa-*O*-acetyl-α/β-D-cellobiose (**I-7**).

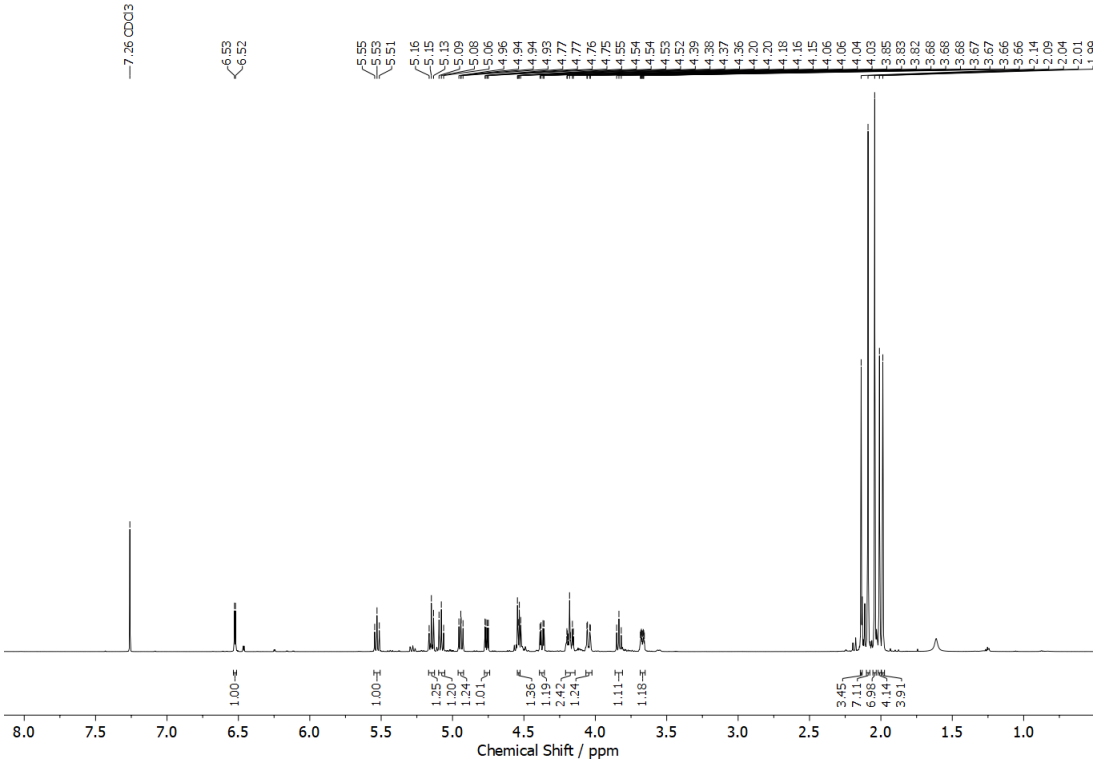

Figure 10.5: ^{1}H-NMR spectrum (600 MHz, $CDCl_3$, 298 K) of 2,3,6,2',3',4',6'-hepta-*O*-acetyl-1-brom-α-D-cellobioside (**I-8**).

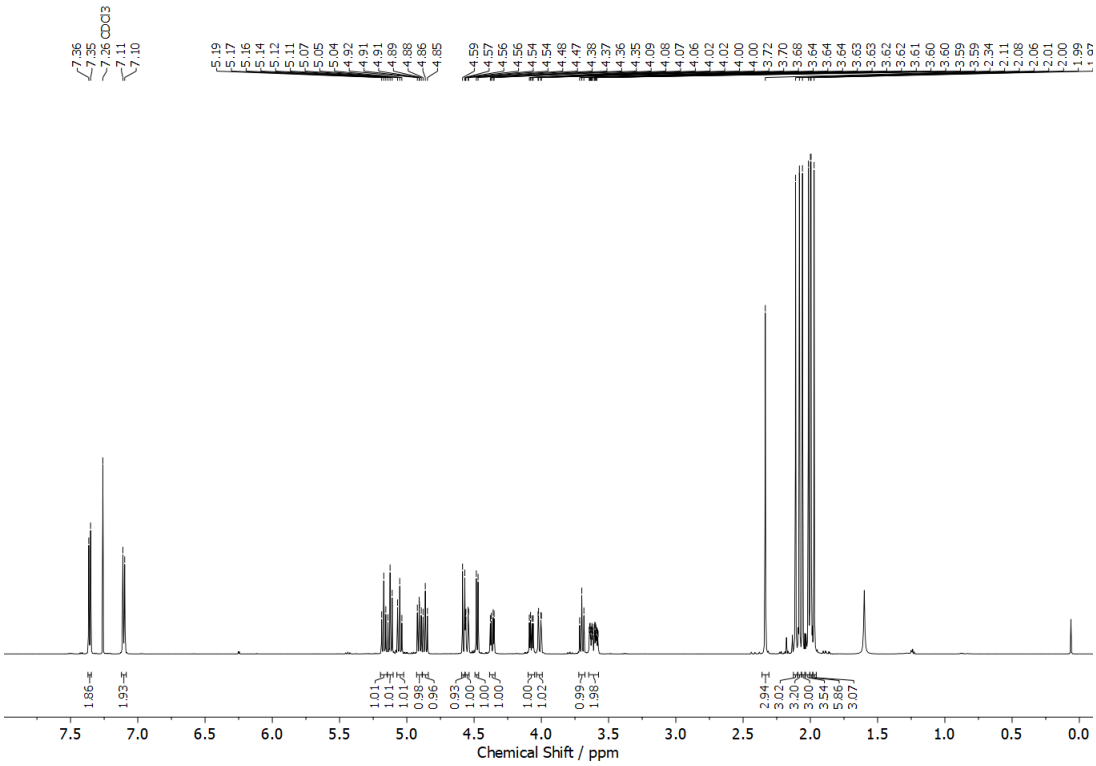

Figure 10.6: ^{1}H-NMR spectrum (600 MHz, $CDCl_3$, 298 K) of *p*-tolyl 2,3,6,2',3',4',6'-hepta-*O*-acetyl-1-thio-β-D-cellobioside (**I-9**).

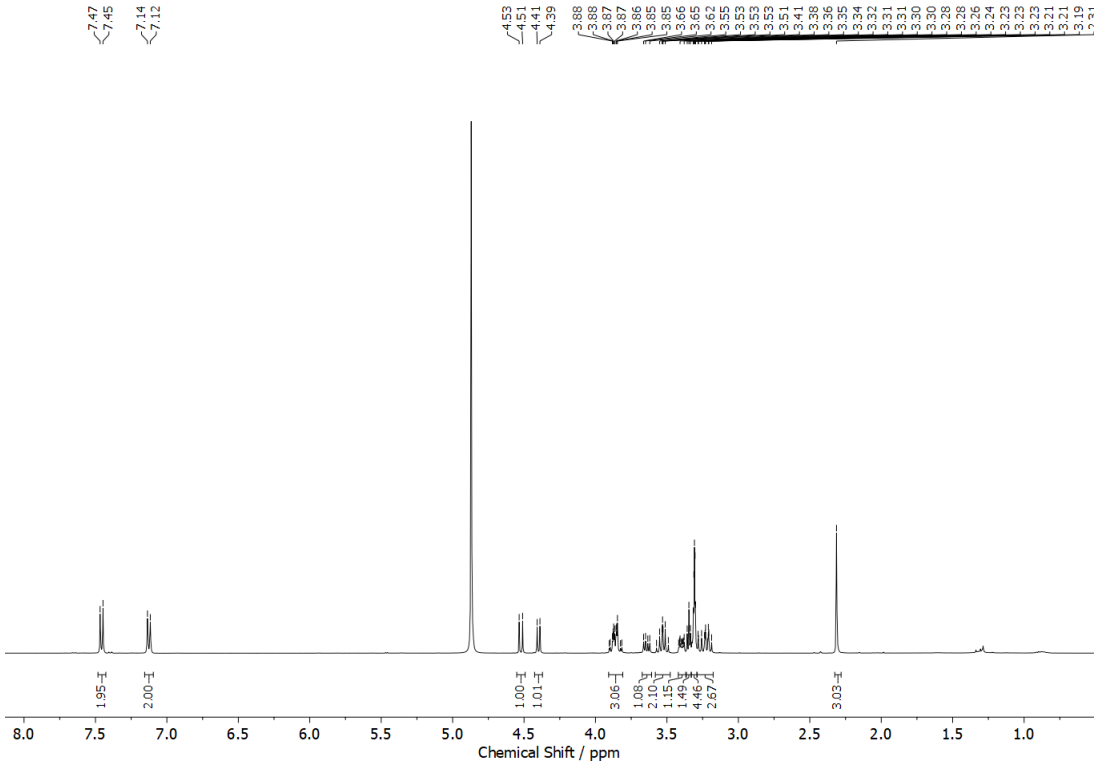

Figure 10.7: ^{1}H-NMR spectrum (400 MHz, methanol-d_4, 298 K) of *p*-tolyl 1-thio-β-D-cellobiosid (**I-10**).

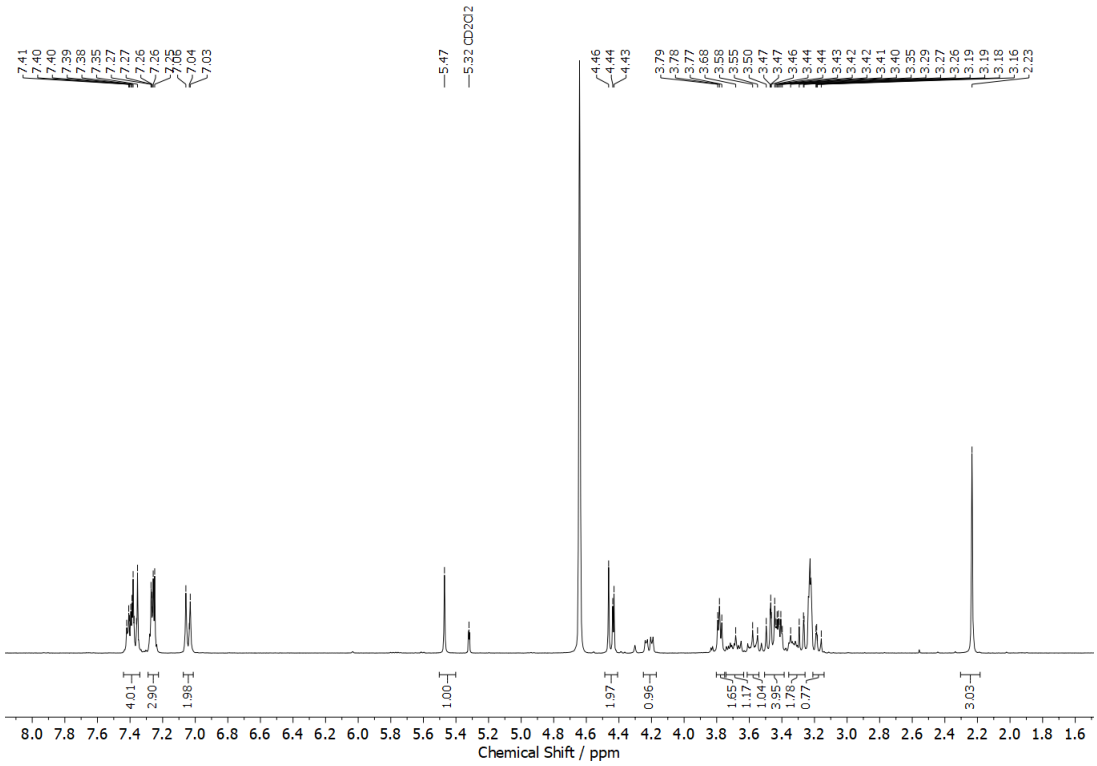

Figure 10.8: ^{1}H-NMR spectrum (400 MHz, methanol-d_4/CD_2Cl_2, 298 K) of *p*-tolyl 4',6'-*O*-benzylidene-1-thio-β-D-cellobioside (**I-11**).

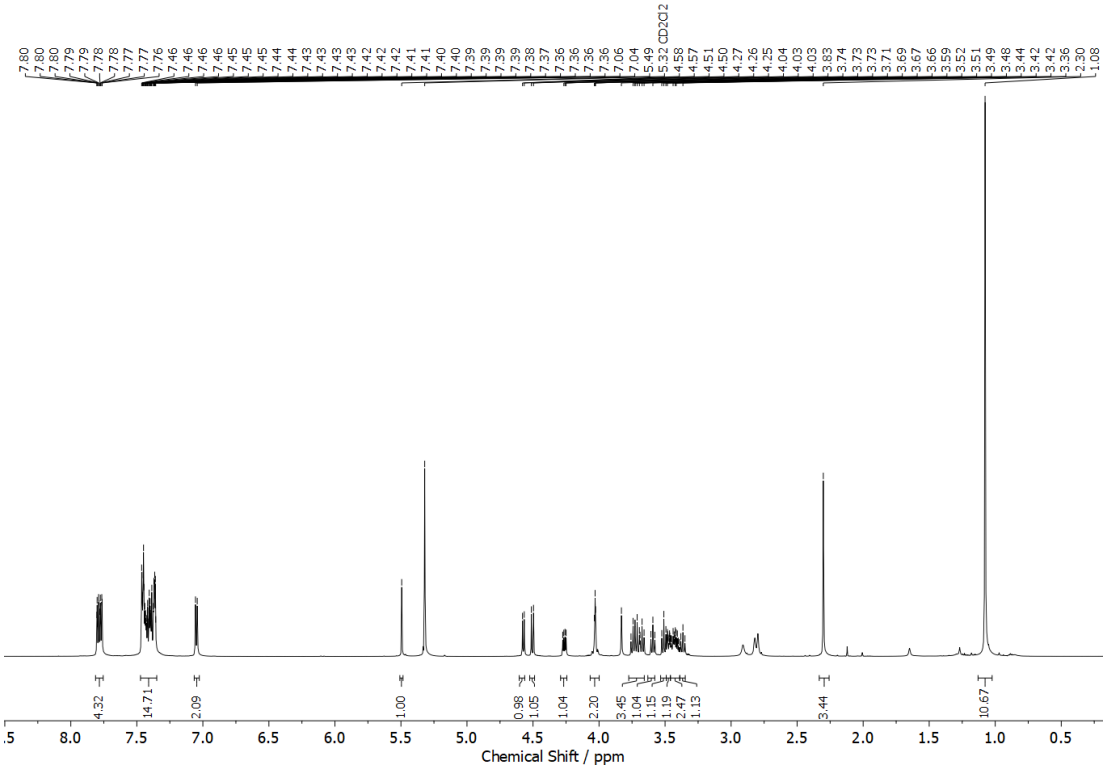

Figure 10.9: [1]H-NMR spectrum (600 MHz, methanol-d_4/CD_2Cl_2, 298 K) of *p*-tolyl 6-*O*-(*tert*-butyldiphenylsilyl)-4',6'-*O*-benzylidene-1-thio-β-D-cellobioside (**I-12**).

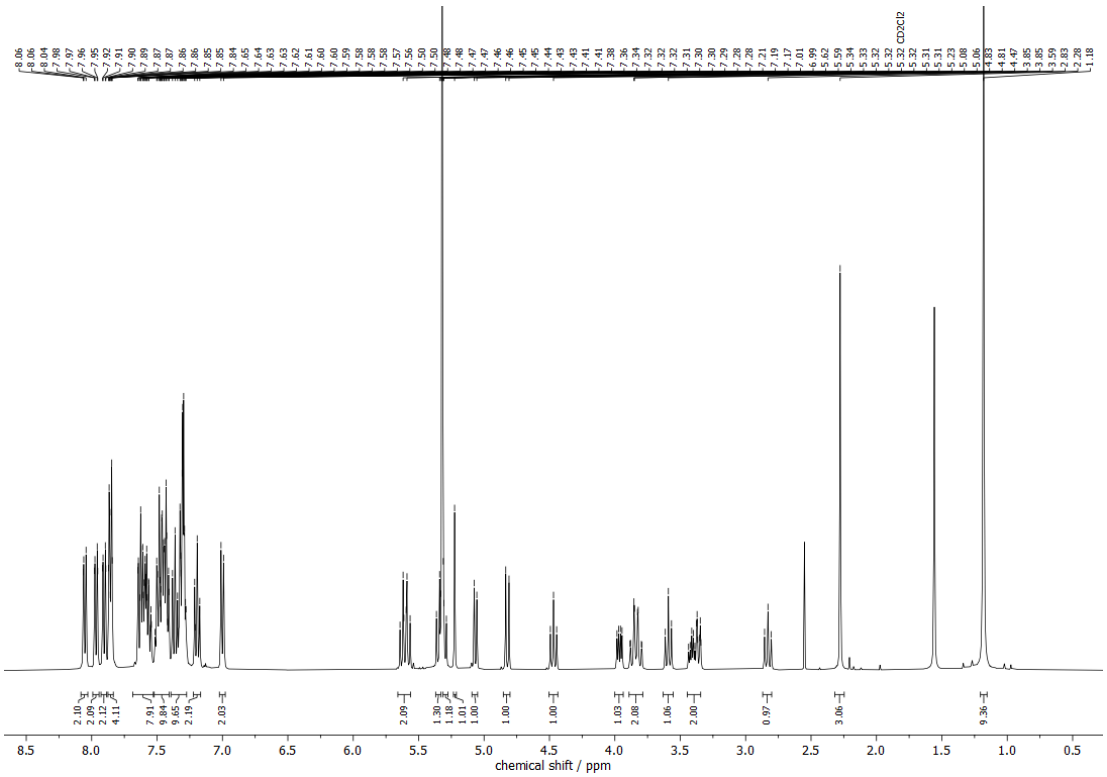

Figure 10.10: [1]H-NMR spectrum (400 MHz, CD_2Cl_2, 298 K) of *p*-tolyl 2,3,2',3'-tetra-*O*-benzoyl-6-*O*-(*tert*-butyldiphenylsilyl)-4',6'-*O*-benzylidene-1-thio-β-D-cellobioside (**I-5**).

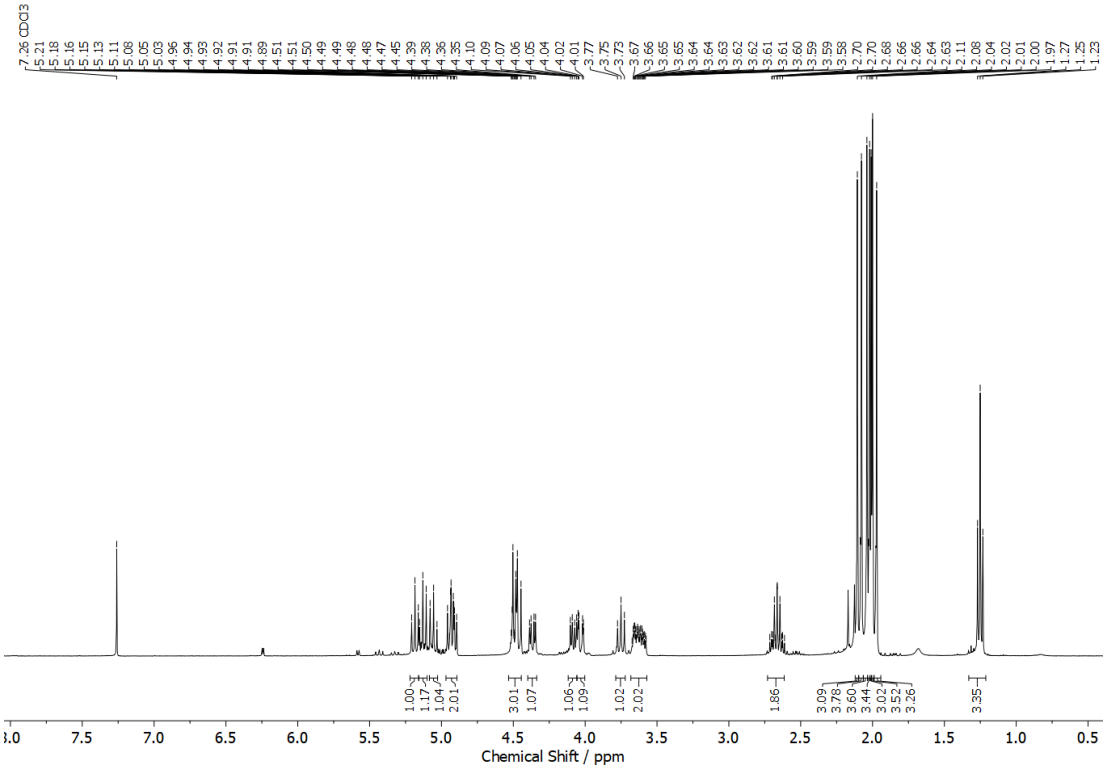

Figure 10.11: ^{1}H-NMR spectrum (400 MHz, $CDCl_3$, 298 K) of ethyl 2,3,6,2',3',4',6'-hepta-*O*-acetyl-1-thio-β-D-cellobioside (**I-14**).

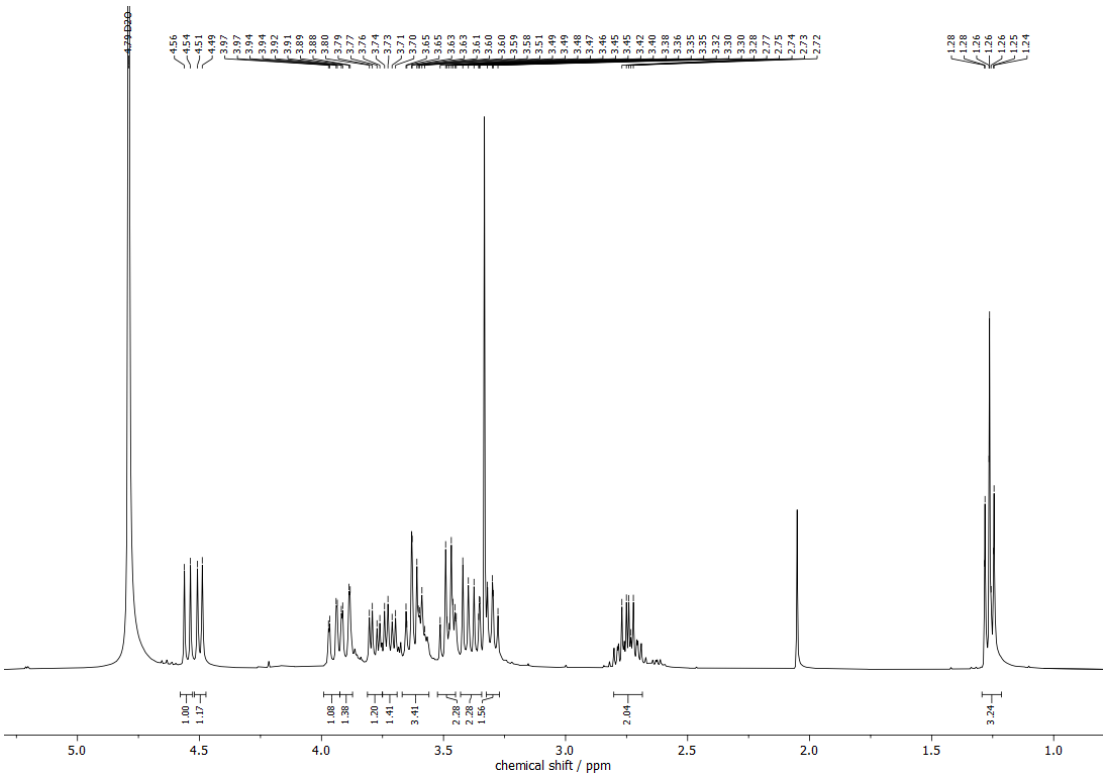

Figure 10.12: ^{1}H-NMR spectrum (400 MHz, D_2O, 298 K) of ethyl 1-thio-β-D-cellobioside (**I-15**).

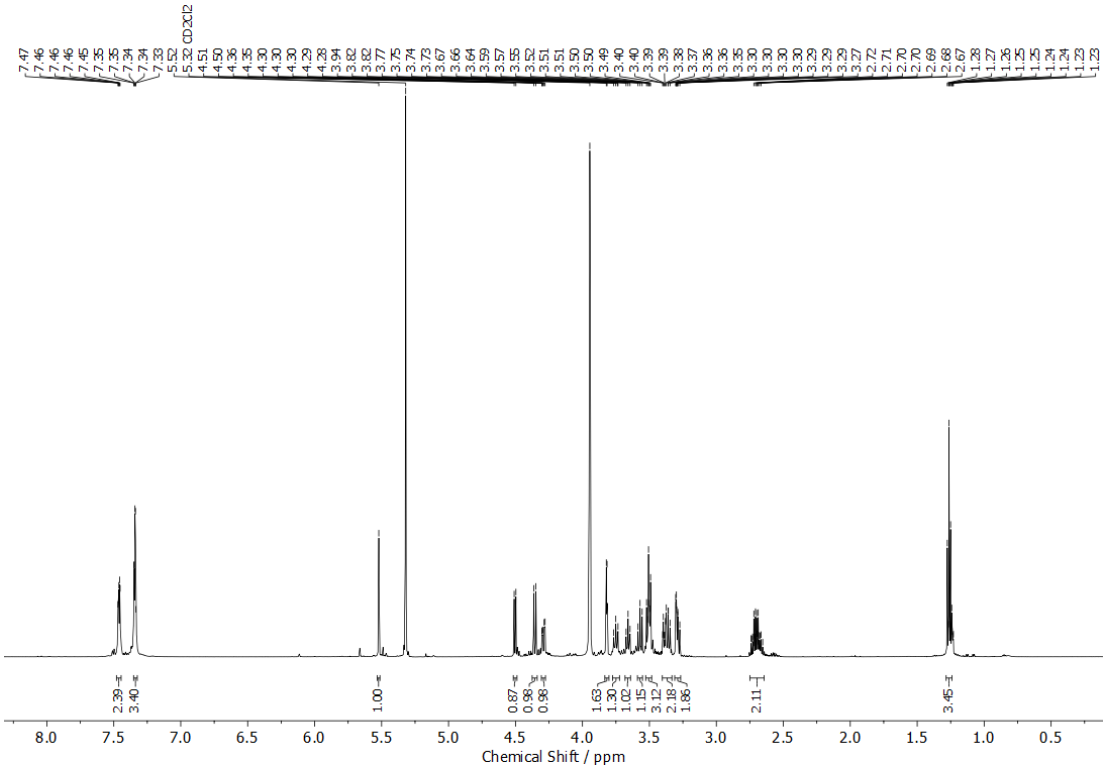

Figure 10.13: ^{1}H-NMR spectrum (600 MHz, CD_2Cl_2, 298 K) of ethyl 4',6'-*O*-benzylidene-1-thio-β-D-cellobioside (**I-16**).

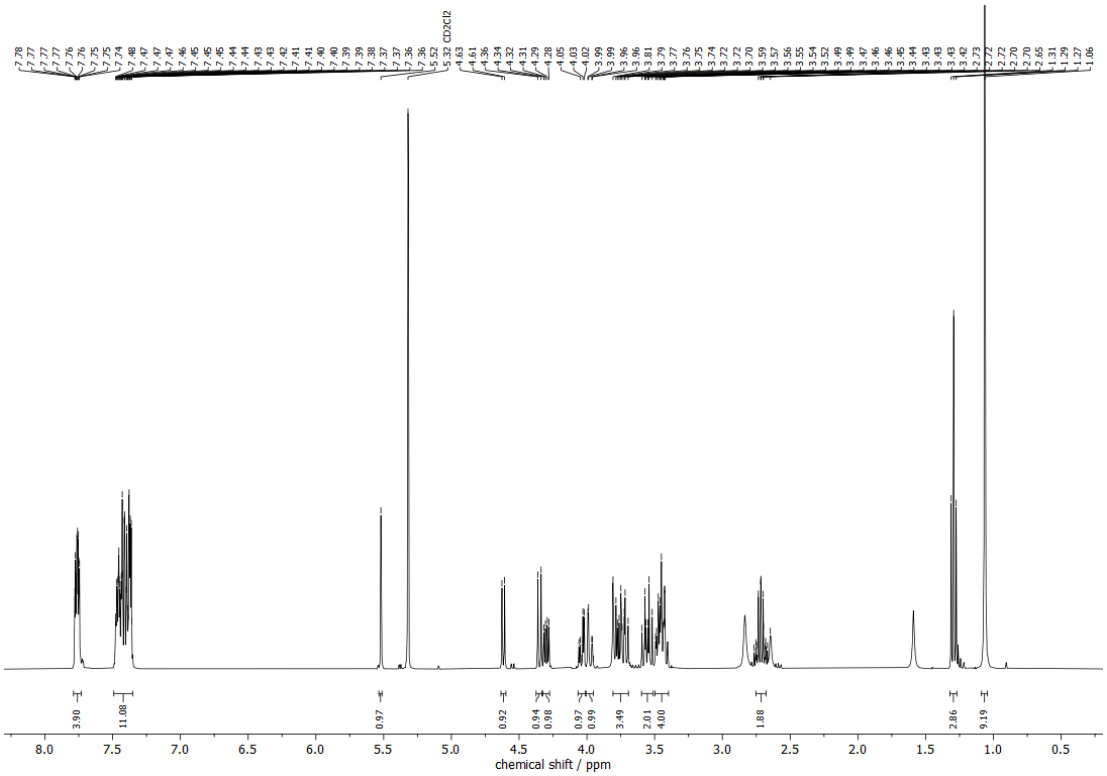

Figure 10.14: ^{1}H-NMR spectrum (400 MHz, CD_2Cl_2, 298 K) of ethyl 6-*O*-(*tert*-butyldiphenylsilyl)-4',6'-*O*-benzylidene-1-thio-β-D-cellobioside (**I-17**).

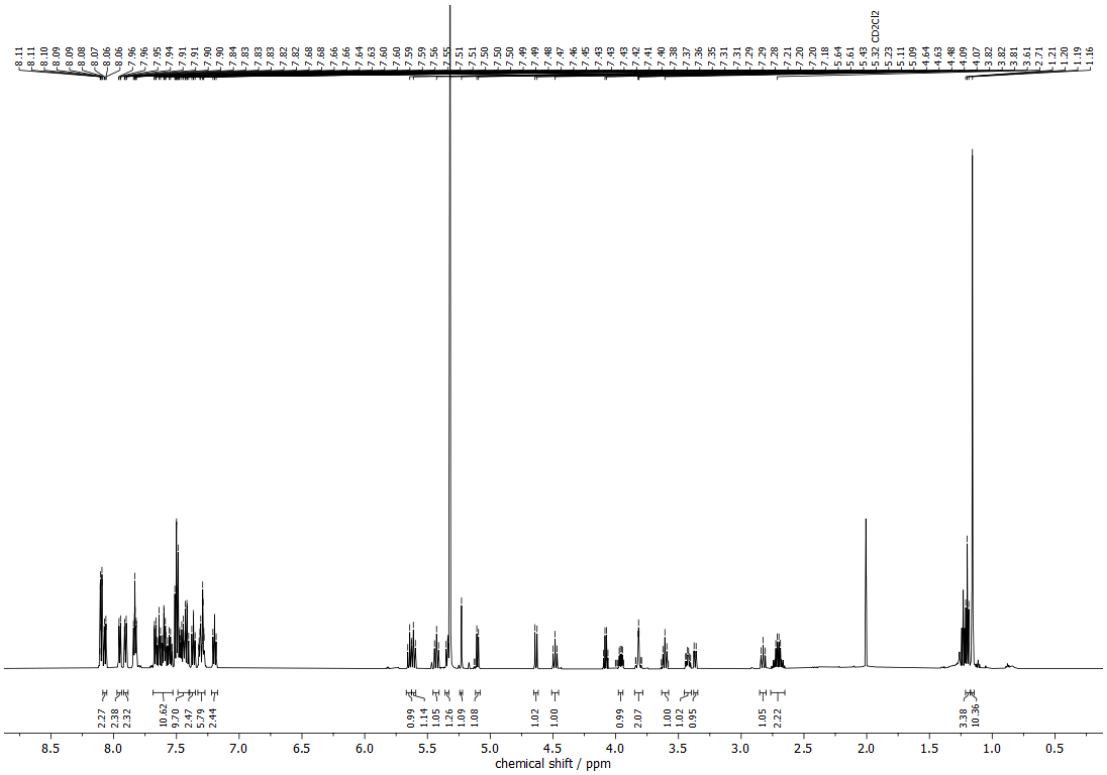

Figure 10.15: ^{1}H-NMR spectrum (400 MHz, CD_2Cl_2, 298 K) of ethyl 2,3,2',3'-tetra-*O*-benzoyl-6-*O*-(*tert*-butyldiphenylsilyl)-4',6'-*O*-benzylidene-1-thio-β-D-cellobioside (**I-6**).

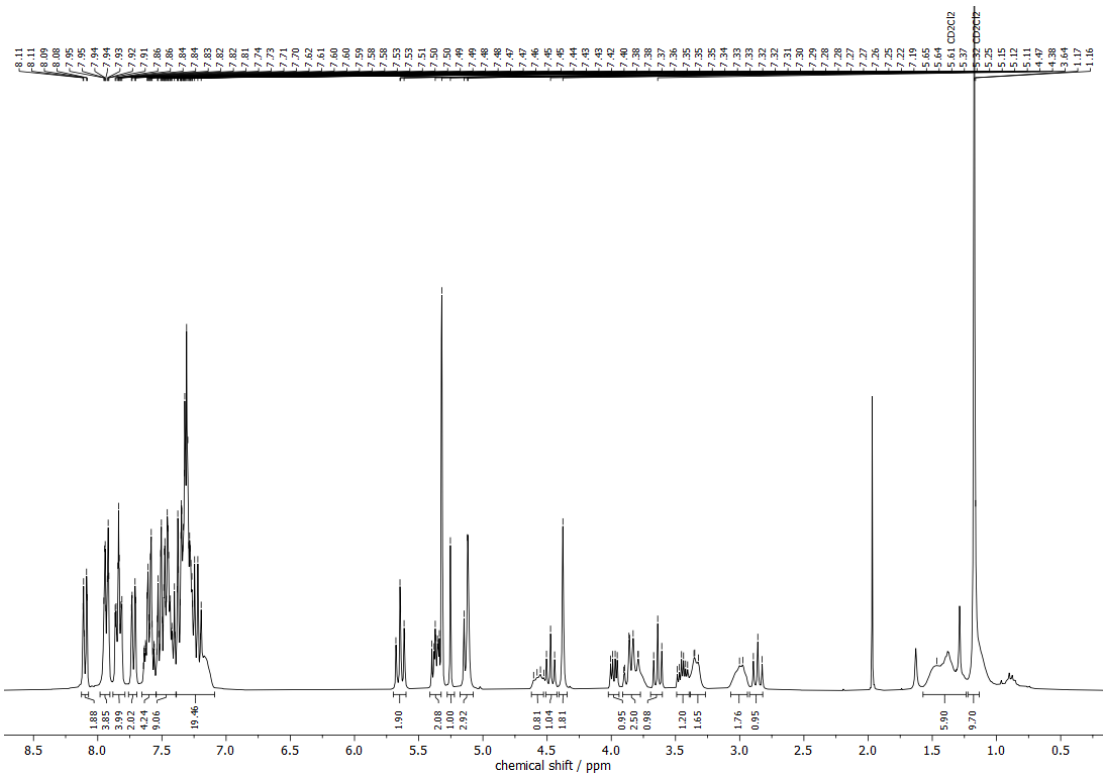

Figure 10.16: ^{1}H-NMR spectrum (300 MHz, CD_2Cl_2, 298 K) of *N*-benzyl(benzyloxy)carbonyl-5-aminopentyl 2,3,2',3'-tetra-*O*-benzoyl-6-*O*-(*tert*-butyldiphenyl-silyl)-4',6'-*O*-benzylidene-β-D-cellobioside (**I-18**).

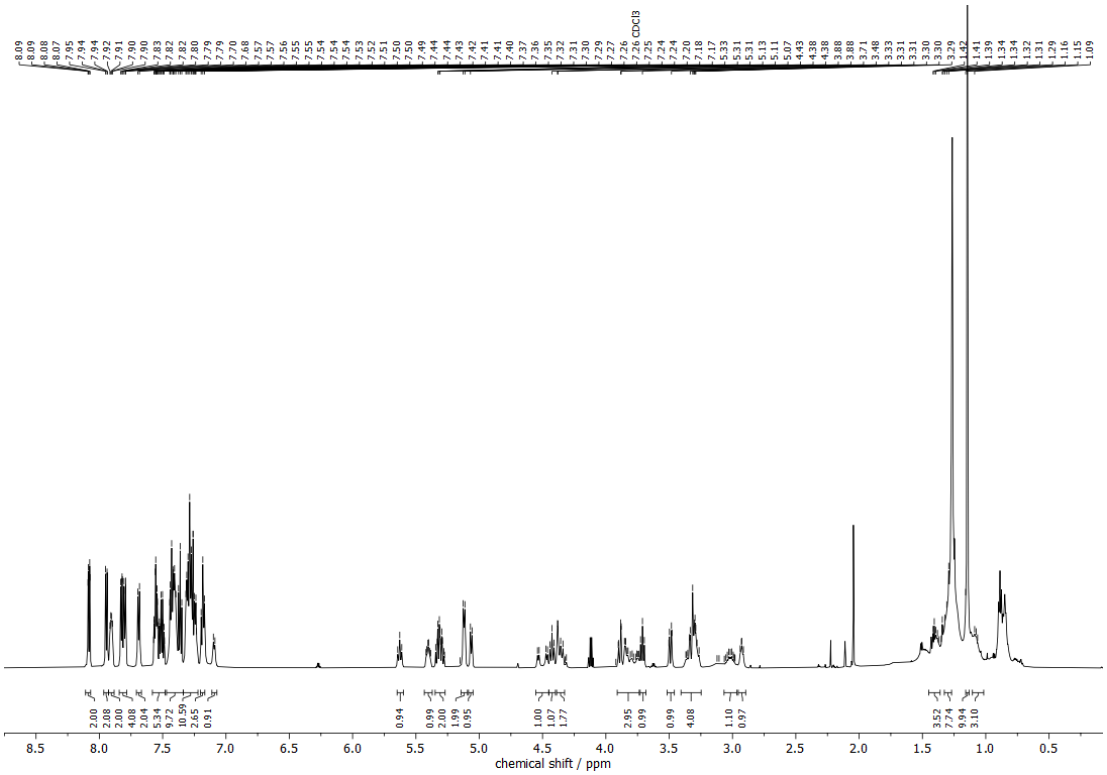

Figure 10.17: ^{1}H-NMR spectrum (600 MHz, $CDCl_3$, 298 K) of *N*-benzyl(benzyloxy)carbonyl-5-aminopentyl 2,3,2',3'-tetra-*O*-benzoyl-6-*O*-(*tert*-butyldiphenyl-silyl)-β-D-cellobioside (**I-20**).

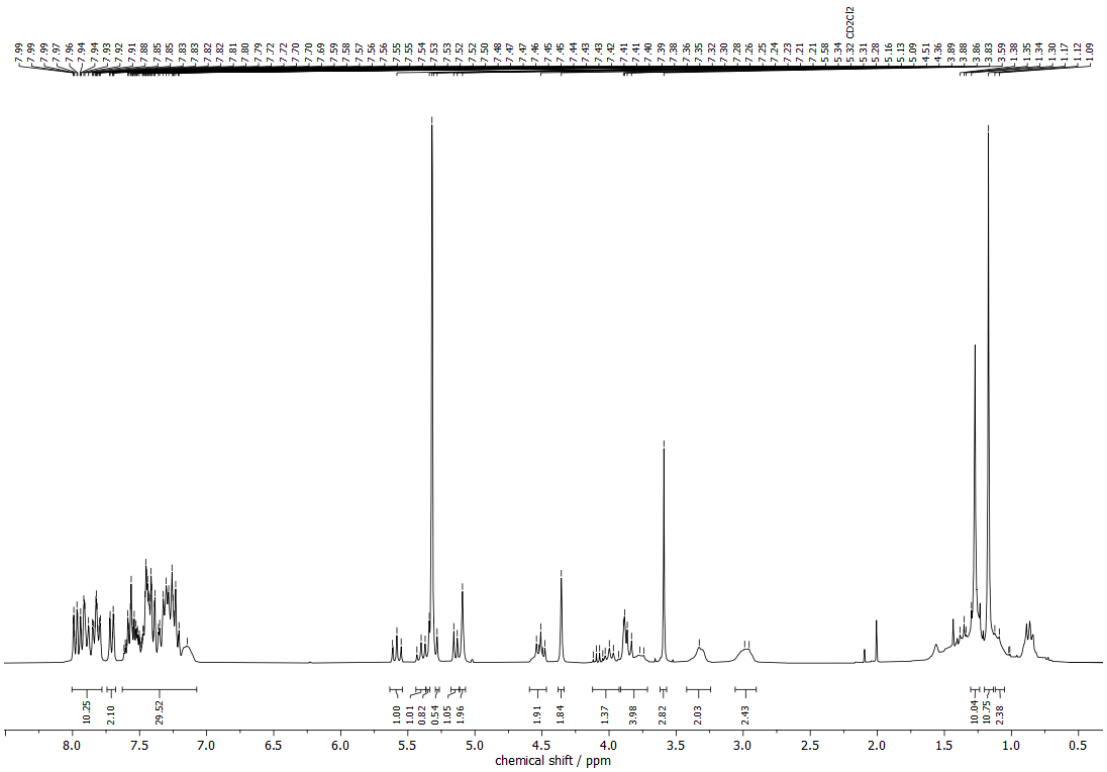

Figure 10.18: ^{1}H-NMR spectrum (600 MHz, CD_2Cl_2, 298 K) of *N*-benzyl(benzyloxy)carbonyl-5-aminopentyl (methyl 2,3,2',3'-tetra-*O*-benzoyl-6-*O*-(*tert*-butyldiphenylsilyl)-1-β-D-cellobiuronate) (**I-21**).

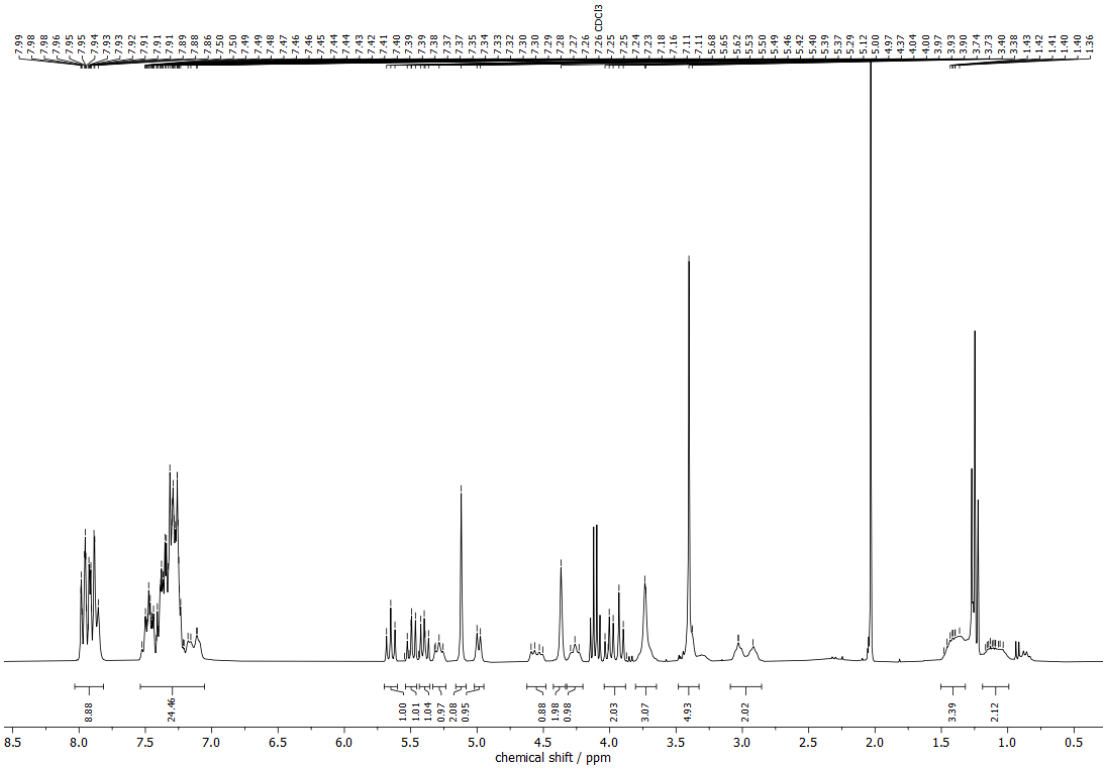

Figure 10.19: ^{1}H-NMR spectrum (300 MHz, $CDCl_3$, 298 K) of *N*-benzyl(benzyloxy)carbonyl-5-aminopentyl (methyl 2,3,2',3'-tetra-*O*-benzoyl-β-D-cellobiuronate) (**I-22**).

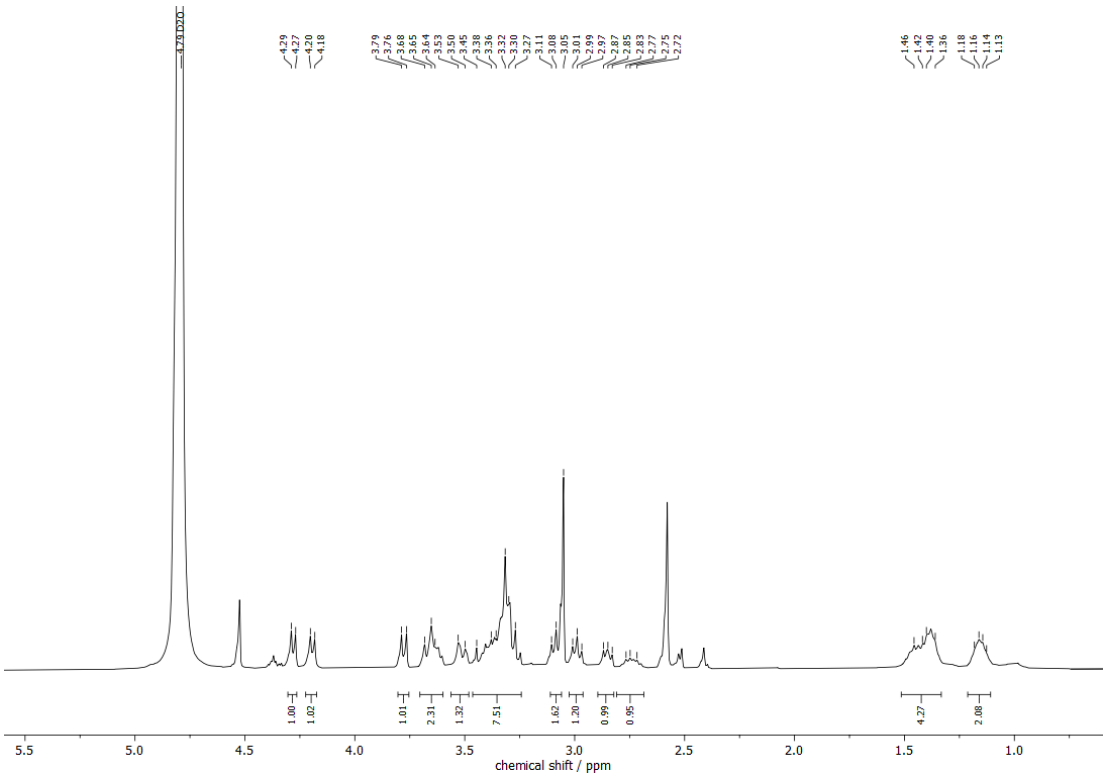

Figure 10.20: ^{1}H-NMR spectrum (400 MHz, D_2O, 298 K) of 5-aminopentyl β-D-cellobiuronic acid (**I-25**).

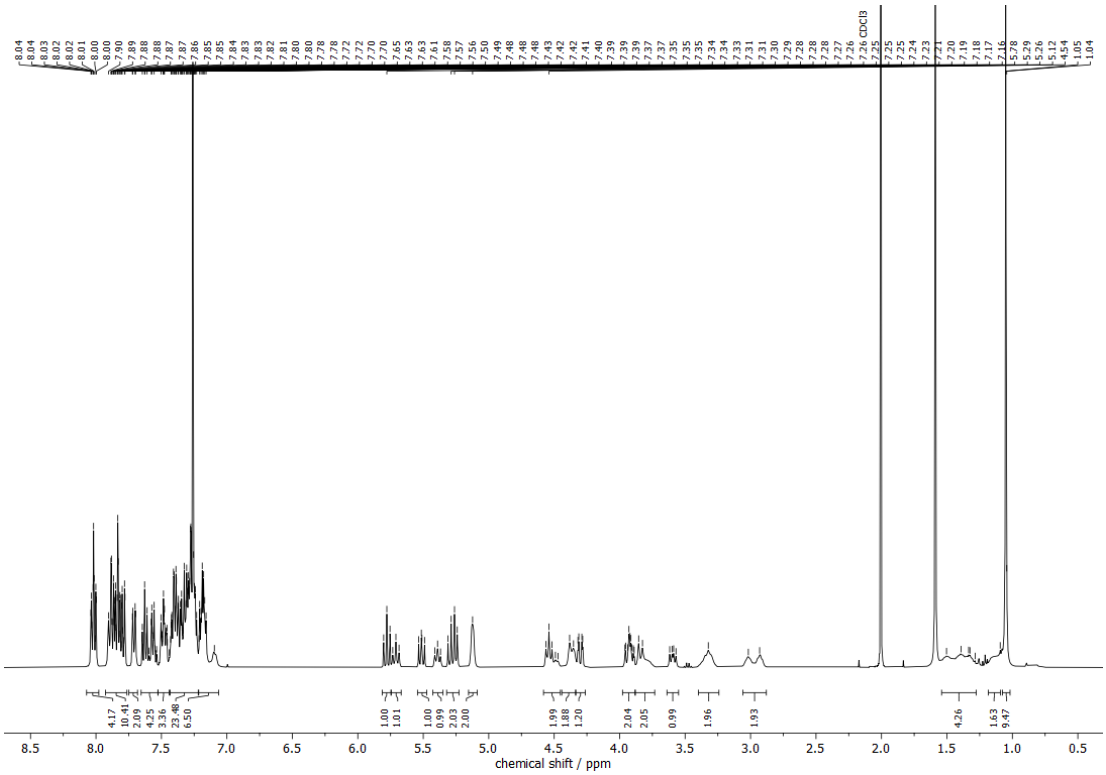

Figure 10.21: ^{1}H-NMR spectrum (400 MHz, $CDCl_3$, 298 K) of *N*-benzyl(benzyloxy)carbonyl-5-aminopentyl 2,3,2',3',4',6'-hexa-*O*-benzoyl-6-*O*-(*tert*-butyldiphenylsilyl)-β-D-cellobioside (**I-26**).

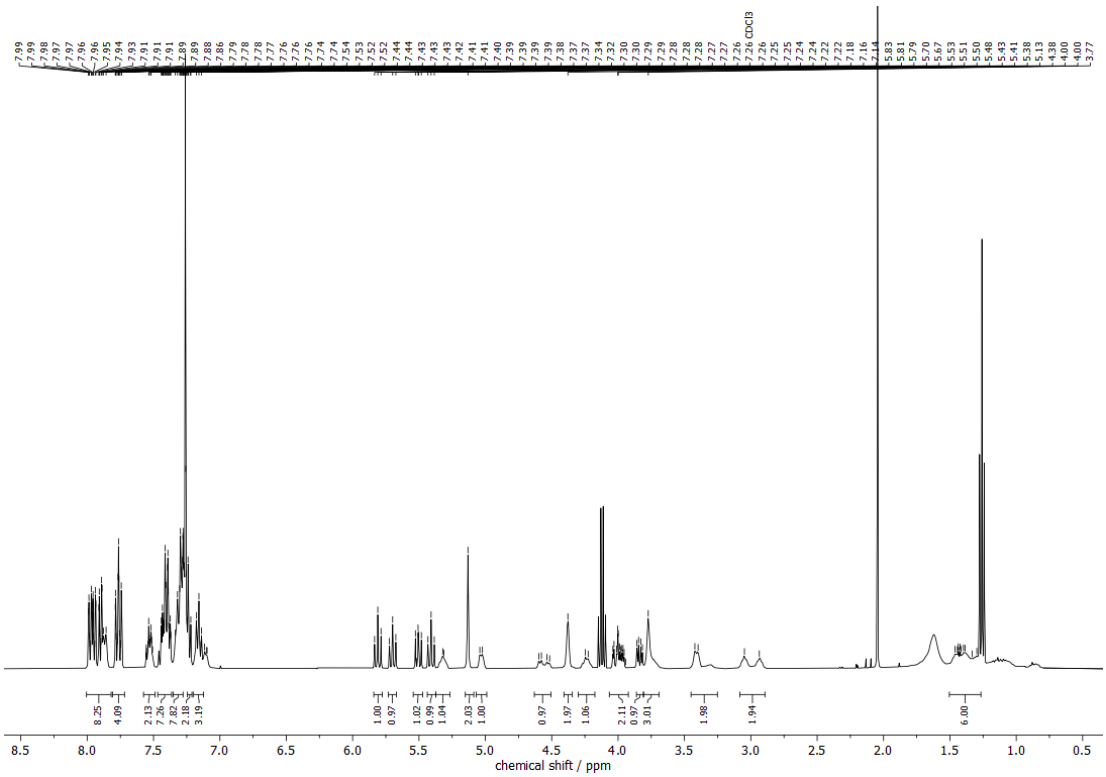

Figure 10.22: ^{1}H-NMR spectrum (400 MHz, $CDCl_3$, 298 K) of *N*-benzyl(benzyloxy)carbonyl-5-aminopentyl 2,3,2',3',4',6'-hexa-*O*-benzoyl-β-D-cellobioside (**I-27**).

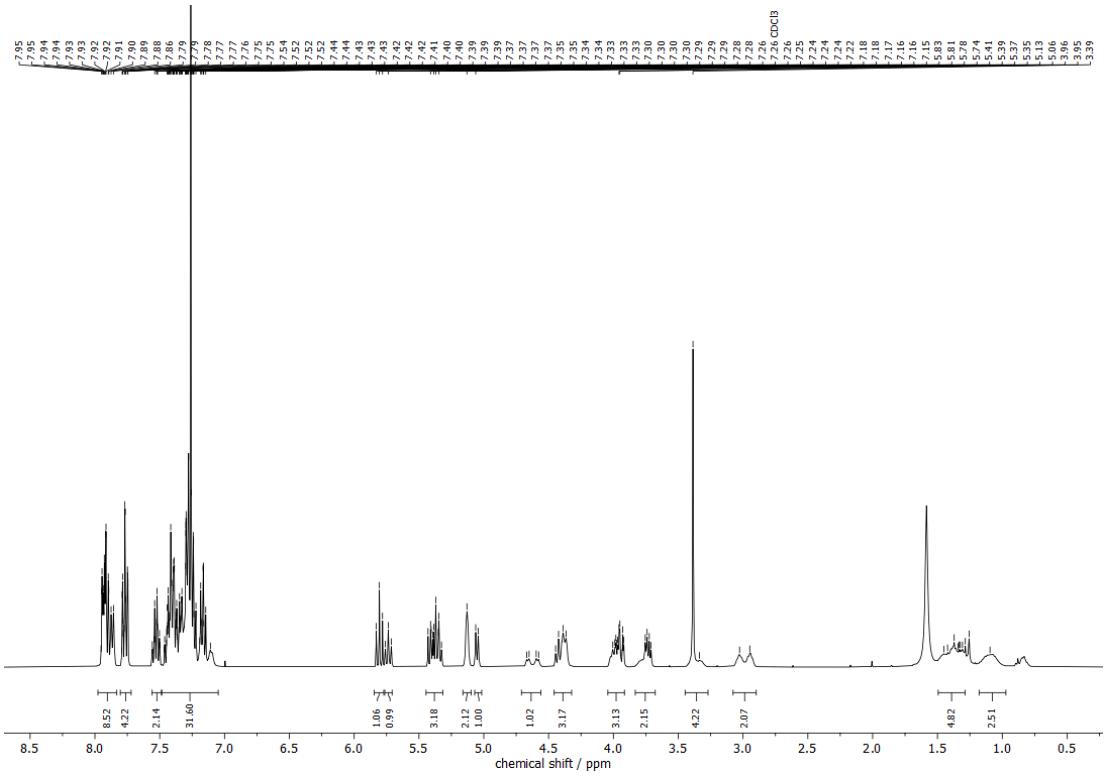

Figure 10.23: ^{1}H-NMR spectrum (400 MHz, $CDCl_3$, 298 K) of *N*-benzyl(benzyloxy)carbonyl-5-aminopentyl 2,3,4,6-tetra-*O*-benzoyl-β-d-glucopyranosyl-(1→4)-(methyl 2,3-di-*O*-benzoyl-β-D-glucopyranosiduronate) (**I-28**).

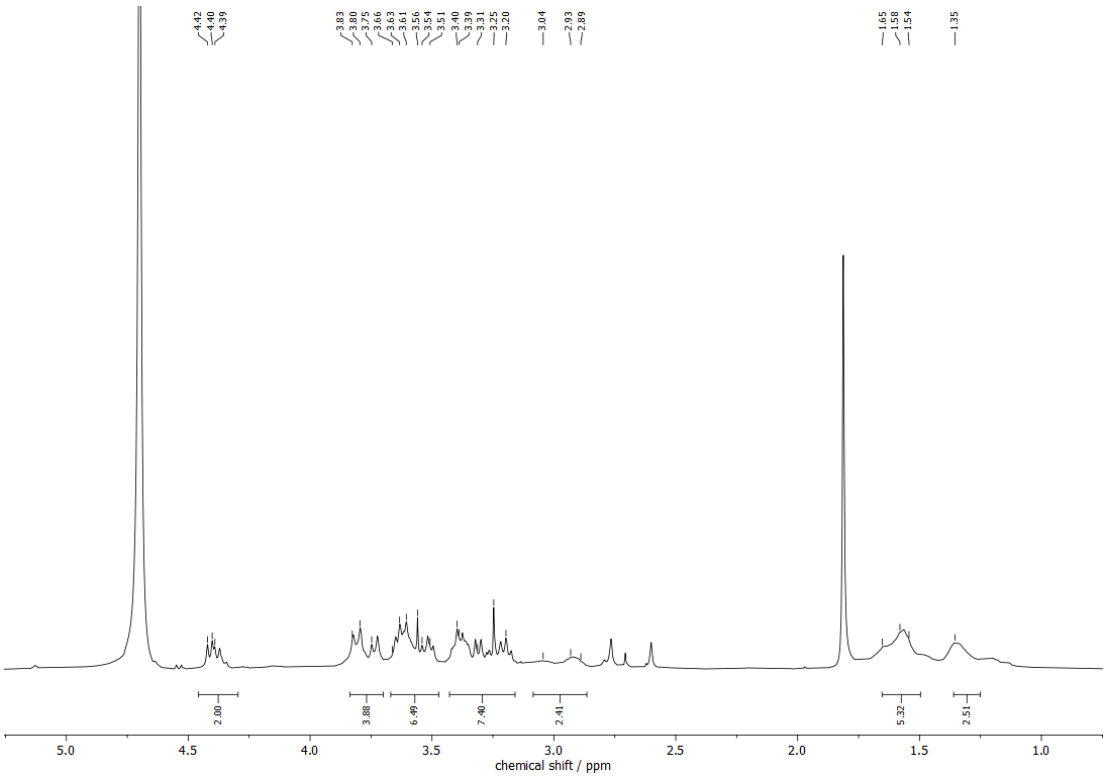

Figure 10.24: ^{1}H-NMR spectrum (400 MHz, D_2O, 298 K) of 5-aminopentyl β-d-glucopyranosyl-(1→4)-β-D-glucoronic acid (**I-30**).

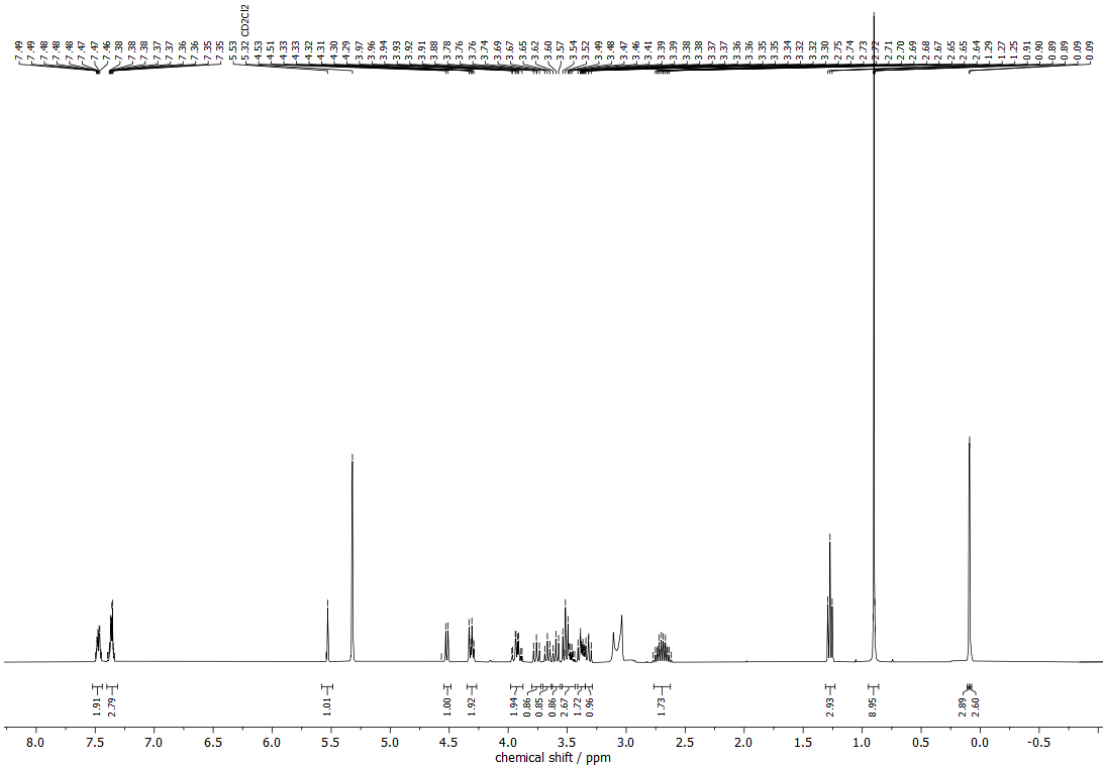

Figure 10.25: ^{1}H-NMR spectrum (400 MHz, CD_2Cl_2, 298 K) of ethyl 6-*O*-(*tert*-butyldimethylsilyl)-4',6'-*O*-benzylidene-1-thio-β-D-cellobioside (**II-3**).

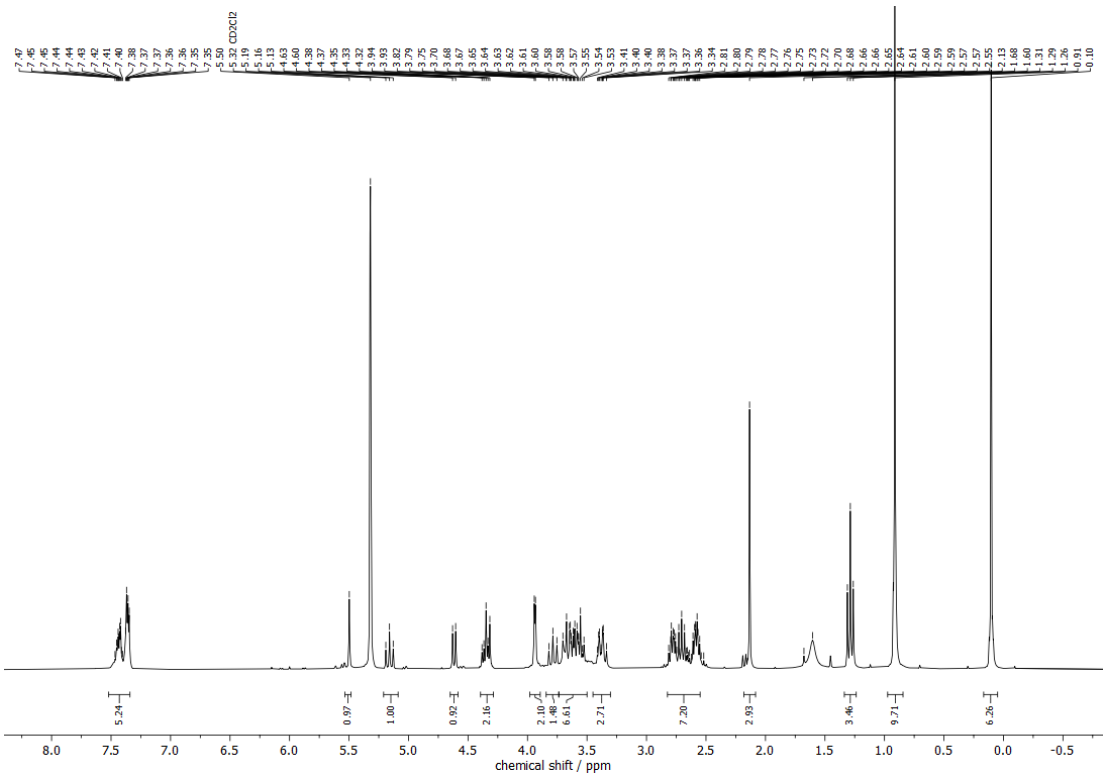

Figure 10.26: ^{1}H-NMR spectrum (300 MHz, CD_2Cl_2, 298 K) of ethyl 6-*O*-(*tert*-butyldimethylsilyl)-3'-*O*-levulinoyl-4',6'-*O*-benzylidene-1-thio-β-D-cellobioside (**II-4**).

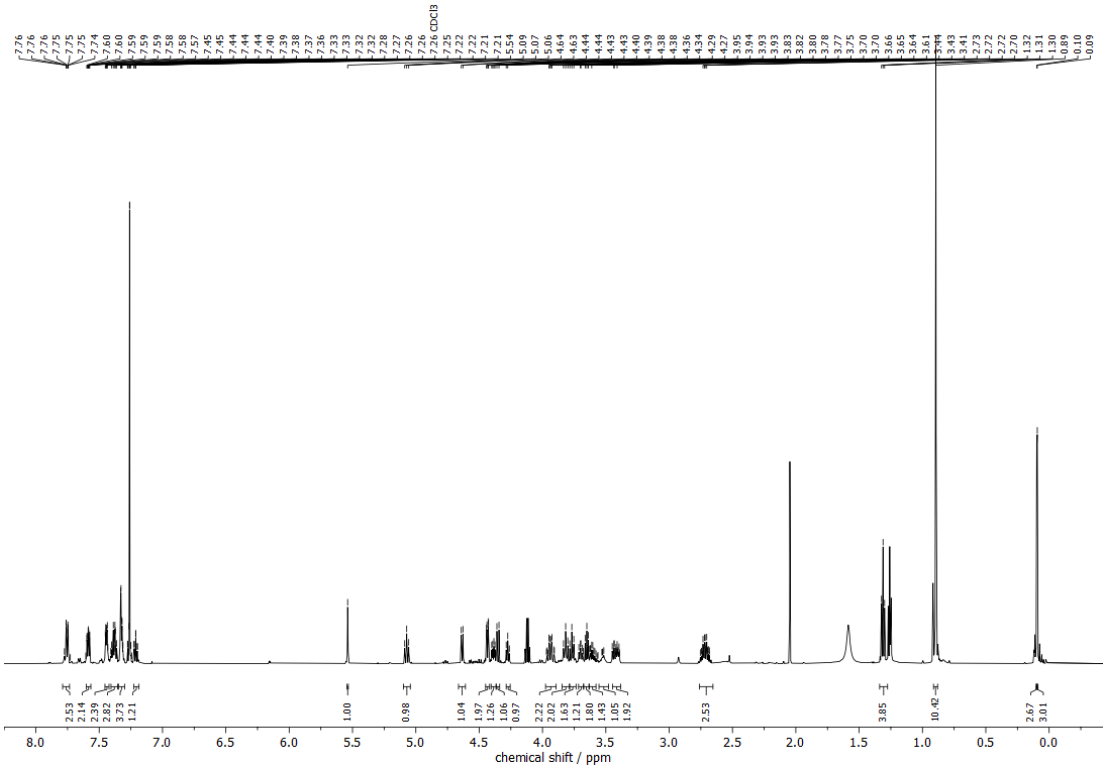

Figure 10.27: ^{1}H-NMR spectrum (600 MHz, $CDCl_3$, 298 K) of ethyl 6-*O*-(*tert*-butyldimethylsilyl)-3'-*O*-(9-fluorenylmethoxycarbonyl)-4',6'-*O*-benzylidene-1-thio-β-D-cellobioside (**II-8**).

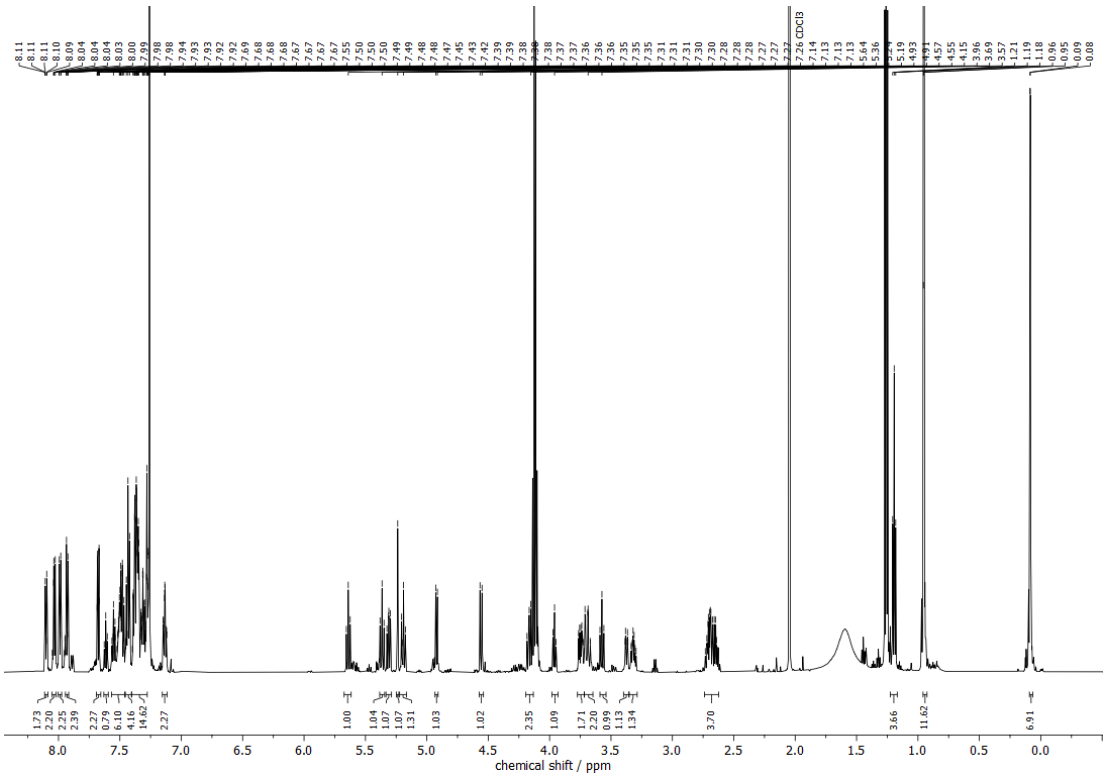

Figure 10.28: ^{1}H-NMR spectrum (600 MHz, $CDCl_3$, 298 K) of ethyl 2,3,2'-tri-*O*-benzoyl-6-*O*-(*tert*-butyldimethylsilyl)-3'-*O*-(9-fluorenylmethoxycarbonyl)-4',6'-*O*-benzylidene-1-thio-β-D-cellobioside (**II-10**).

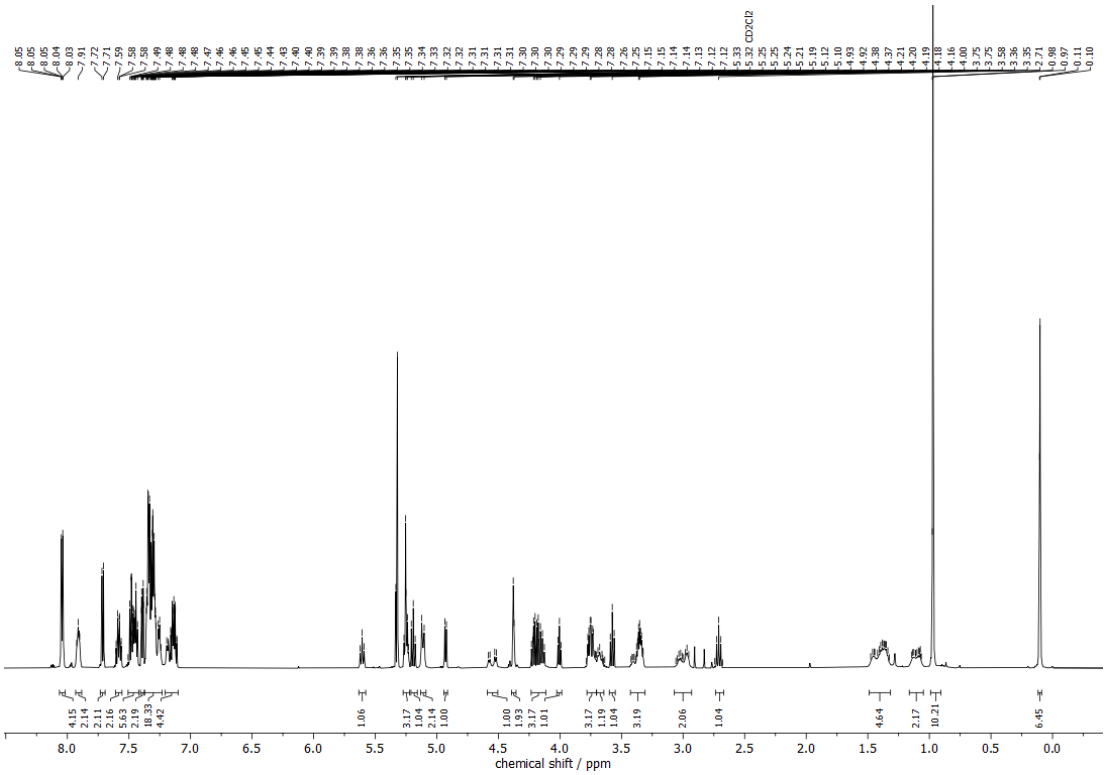

Figure 10.29: ^{1}H-NMR spectrum (600 MHz, CD_2Cl_2, 298 K) of *N*-benzyl(benzyloxy)carbonyl-5-aminopentyl 2,3,2'-tri-*O*-benzoyl-6-*O*-(*tert*-butyldimethylsilyl)-3'-*O*-(9-fluorenylmethoxycarbonyl)-4',6'-*O*-benzylidene-β-D-cellobioside (**II-11**).

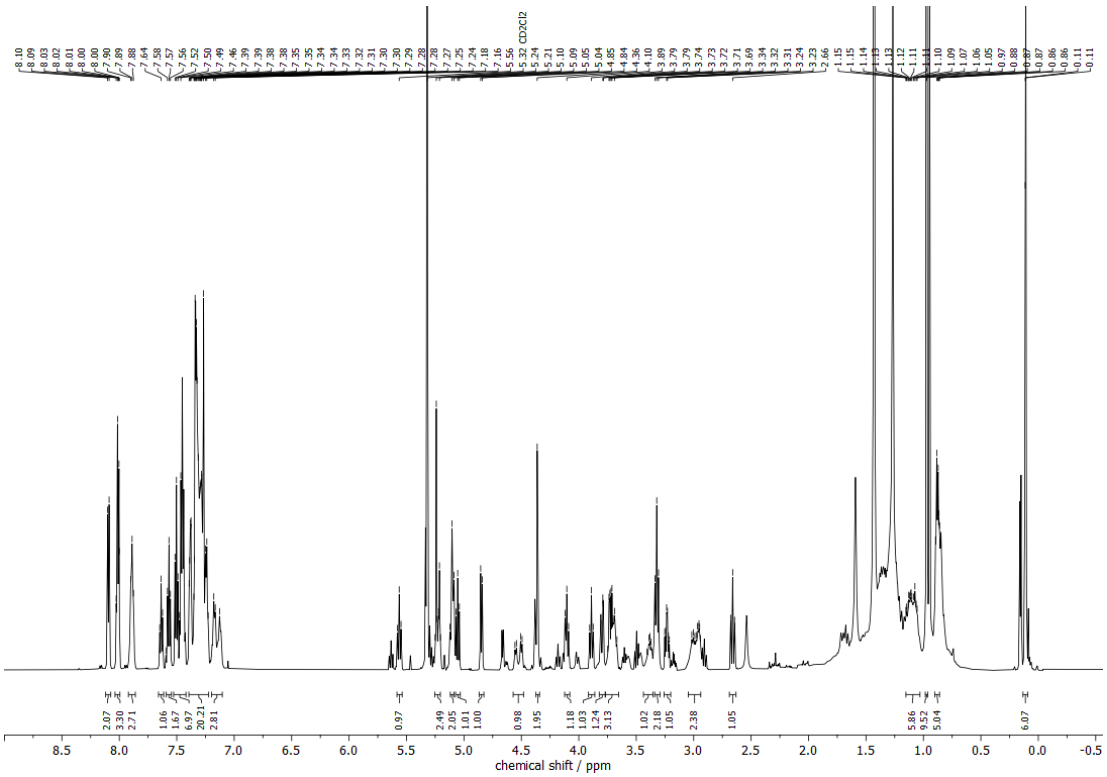

Figure 10.30: ^{1}H-NMR spectrum (600 MHz, CD_2Cl_2, 298 K) of *N*-benzyl(benzyloxy)carbonyl-5-aminopentyl 2,3,2'-tri-*O*-benzoyl-6-*O*-(*tert*-butyldimethylsilyl)-4',6'-*O*-benzylidene-β-D-cellobioside (**II-12**).

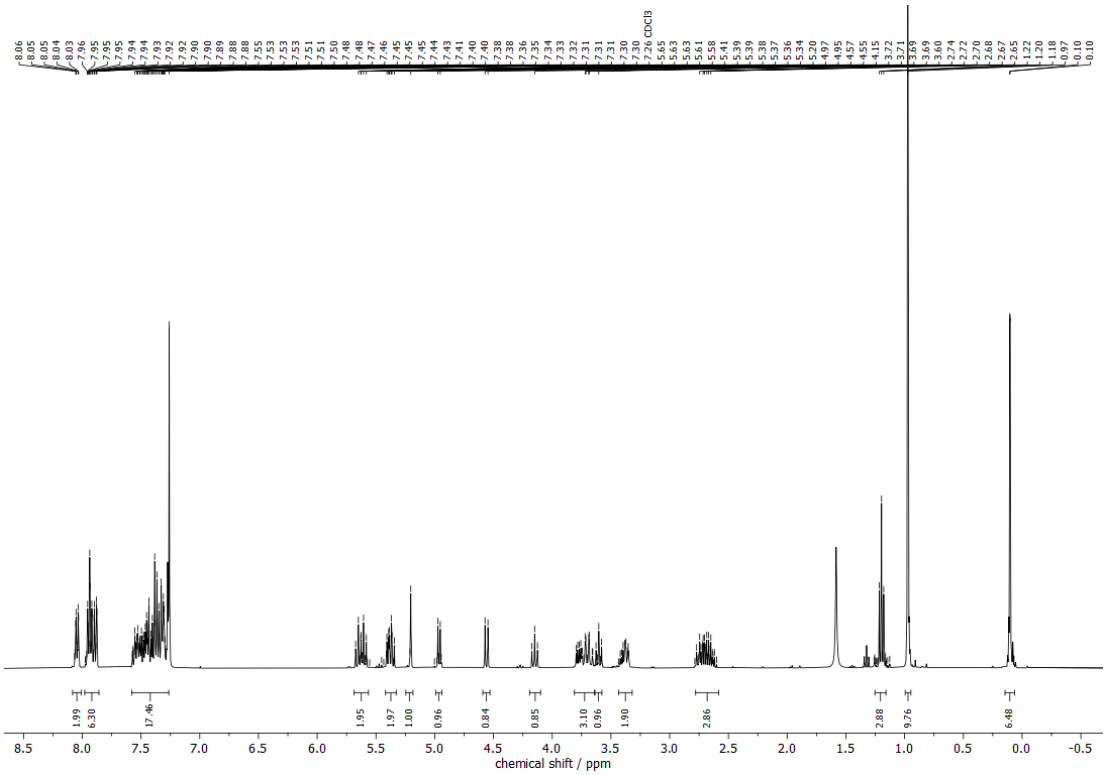

Figure 10.31: [1]H-NMR spectrum (400 MHz, $CDCl_3$, 298 K) of ethyl 2,3,2',3'-tetra-*O*-benzoyl-6-*O*-(*tert*-butyldimethylsilyl)-4',6'-*O*-benzylidene-1-thio-β-D-cellobioside (**II-15**).

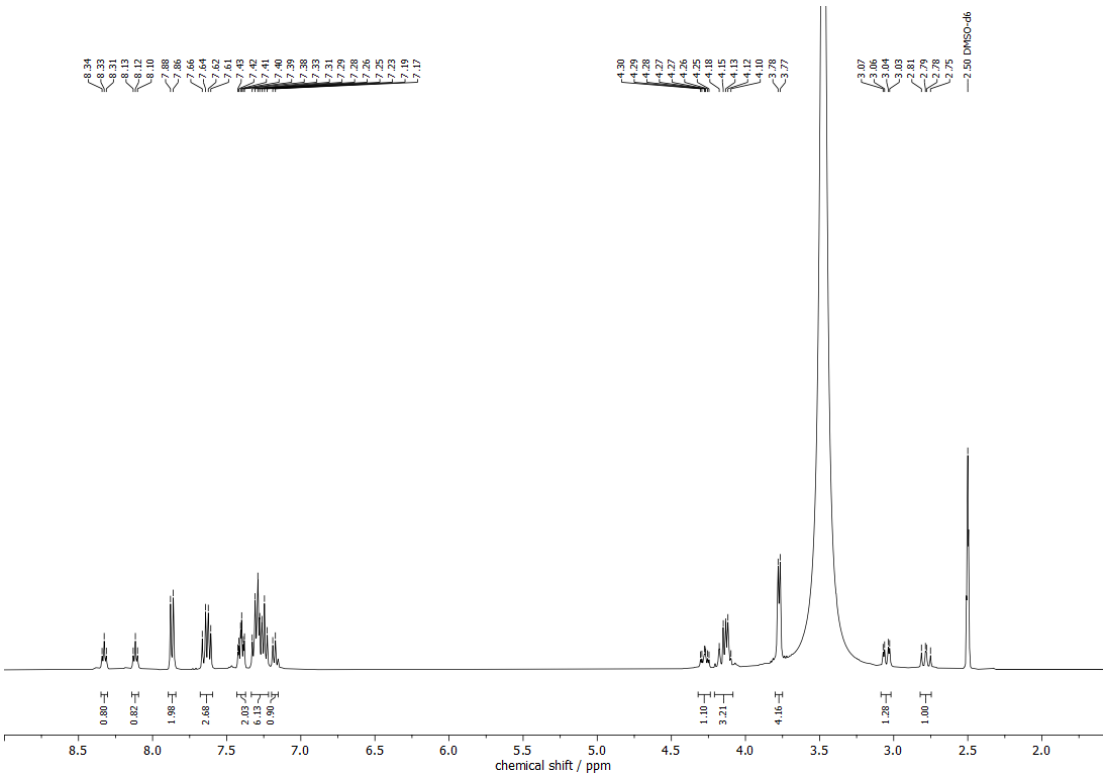

Figure 10.32: [1]H-NMR spectrum (400 MHz, dmso-d_6, 298 K) of FmocFGG-OH (**III-3**).

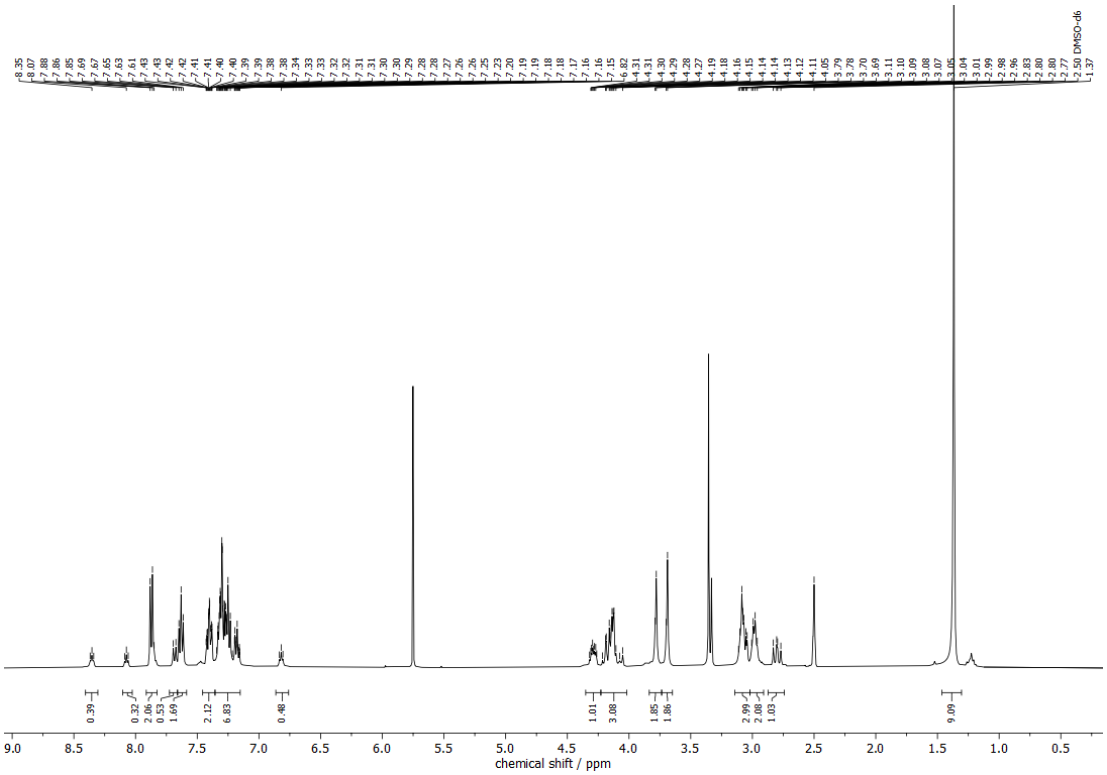

Figure 10.33: ^{1}H-NMR spectrum (400 MHz, dmso-d_6, 298 K) of FmocFGG-C_2-NHBoc (**III-4**).

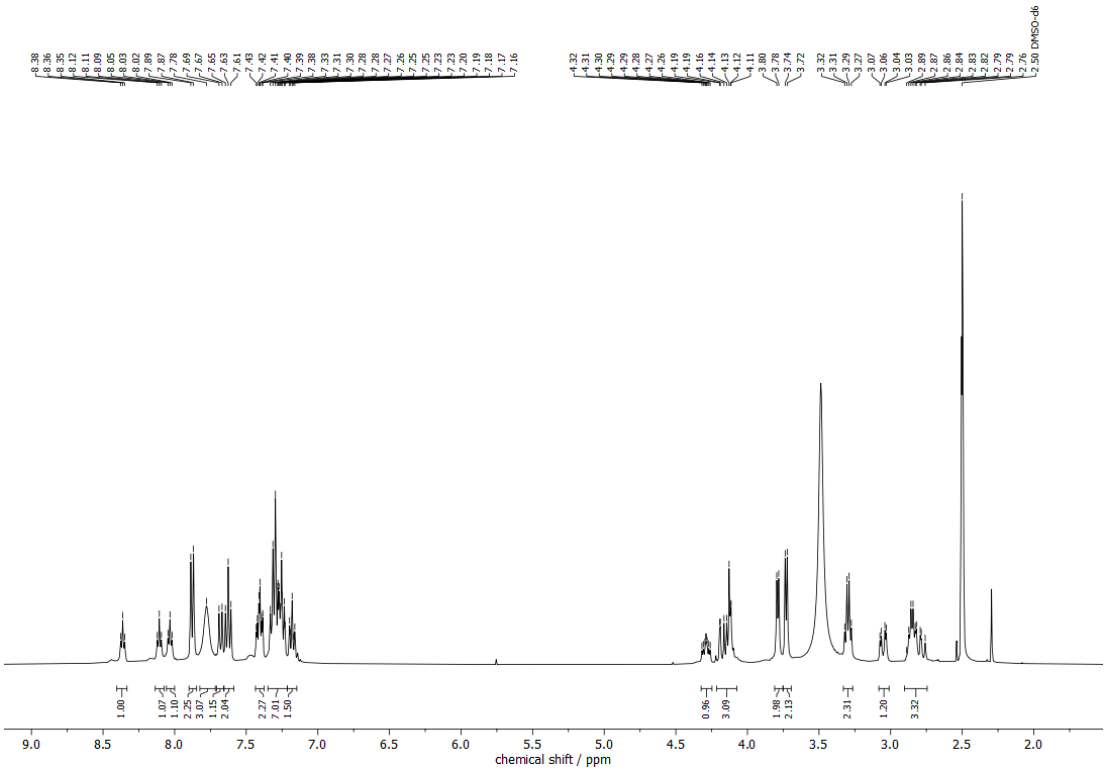

Figure 10.34: ^{1}H-NMR spectrum (400 MHz, dmso-d_6, 298 K) of FmocFGG-C_2-NH_2 (**III-5**).

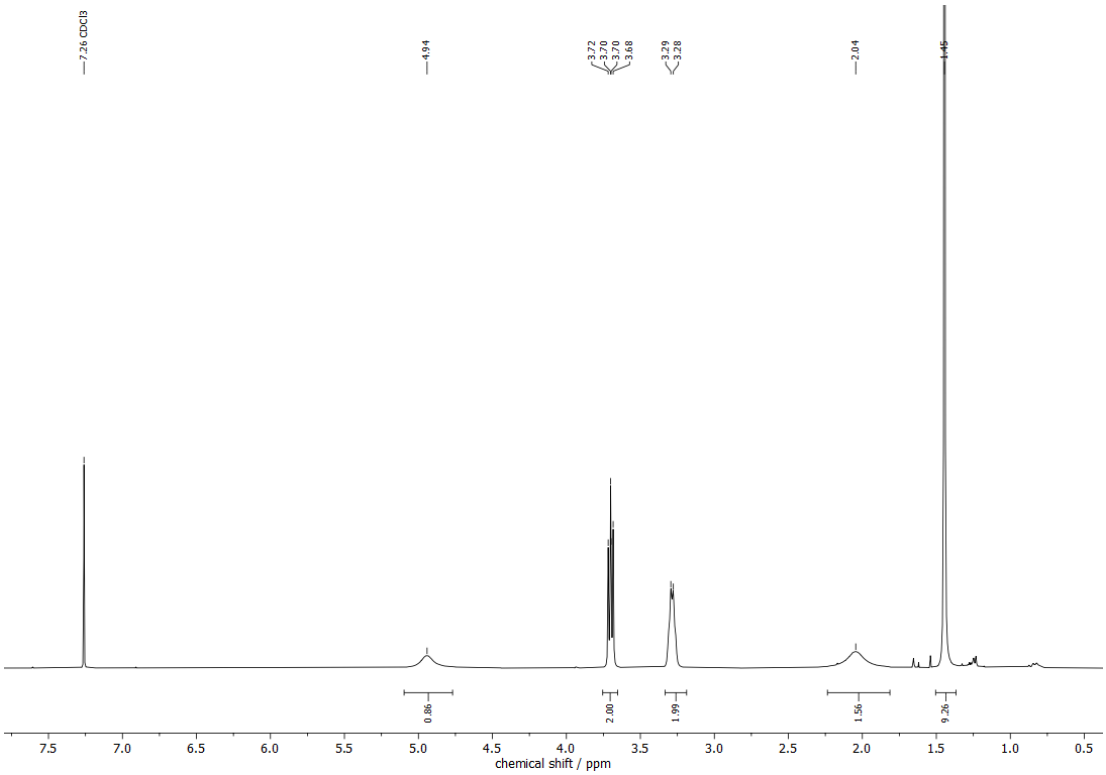

Figure 10.35: ^{1}H-NMR spectrum (300 MHz, $CDCl_3$, 298 K) of *tert*-butyl (2-hydroxyethyl)carbamate (**III-6**).

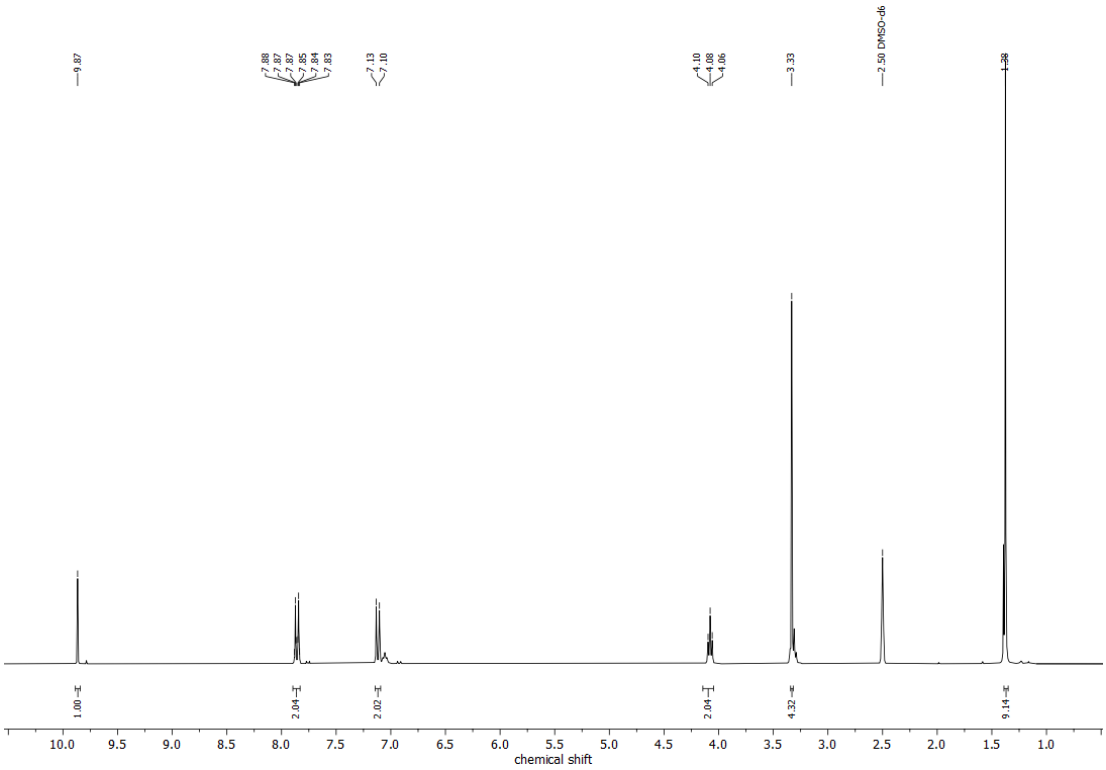

Figure 10.36: ^{1}H-NMR spectrum (300 MHz, dmso-d_6, 298 K) of *tert*-butyl (2-(4-formylphenoxy)ethyl)carbamate (**III-7**).

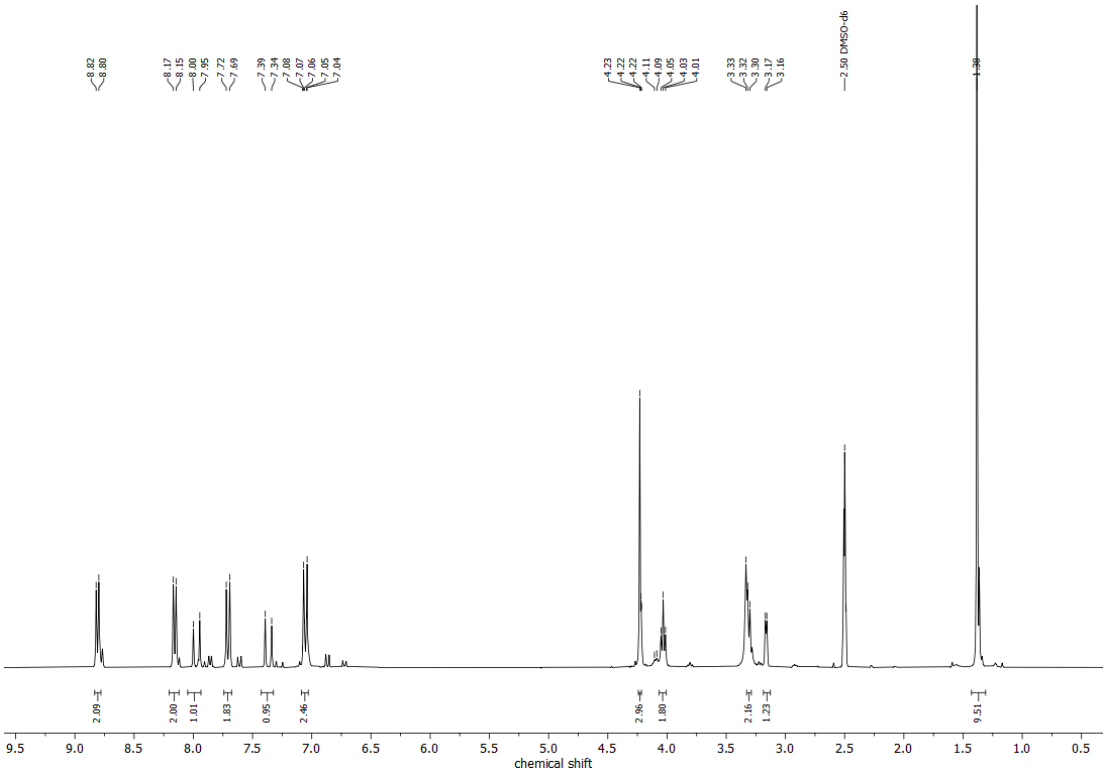

Figure 10.37: ^{1}H-NMR spectrum (300 MHz, dmso-d_6, 298 K) of (*E*)-4-(4-(2-((*tert*-butoxycarbonyl)amino)ethoxy)styryl)-1-methylpyridin-1-ium iodide (**III-8**).

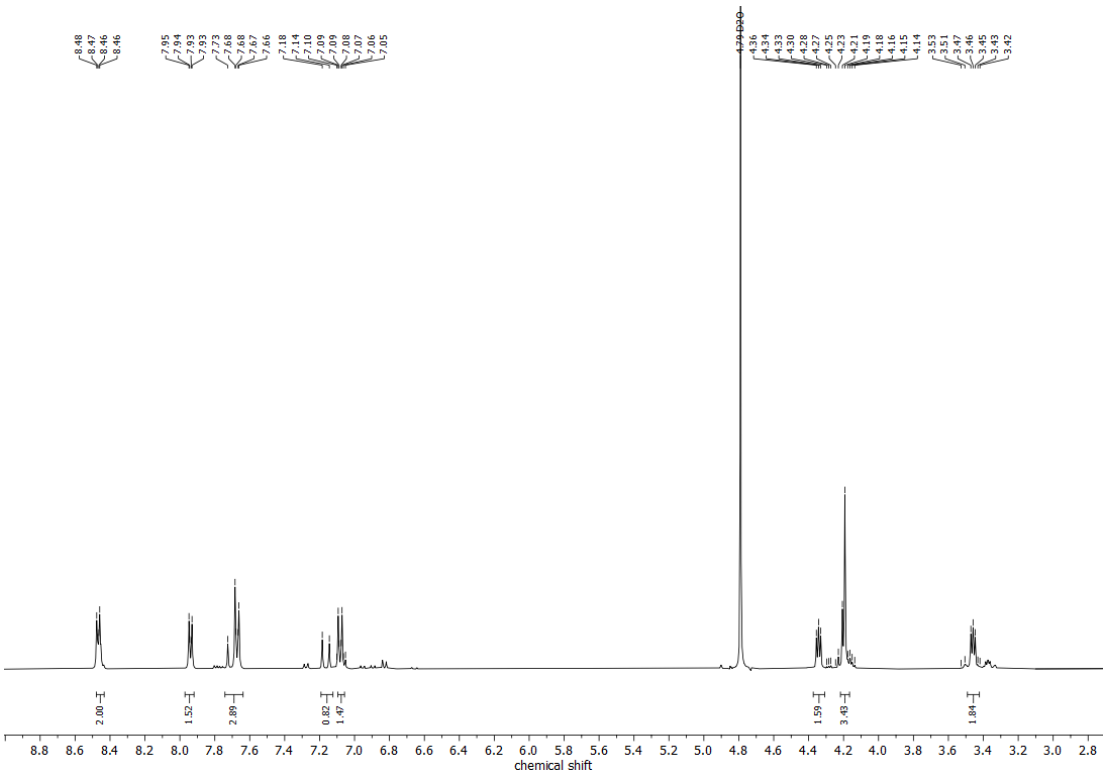

Figure 10.38: ^{1}H-NMR spectrum (400 MHz, D_2O, 298 K) of (*E*)-4-(4-(2-ammonioethoxy)styryl)-1-methylpyridin-1-ium trifluoroacetate iodide (**III-9**).

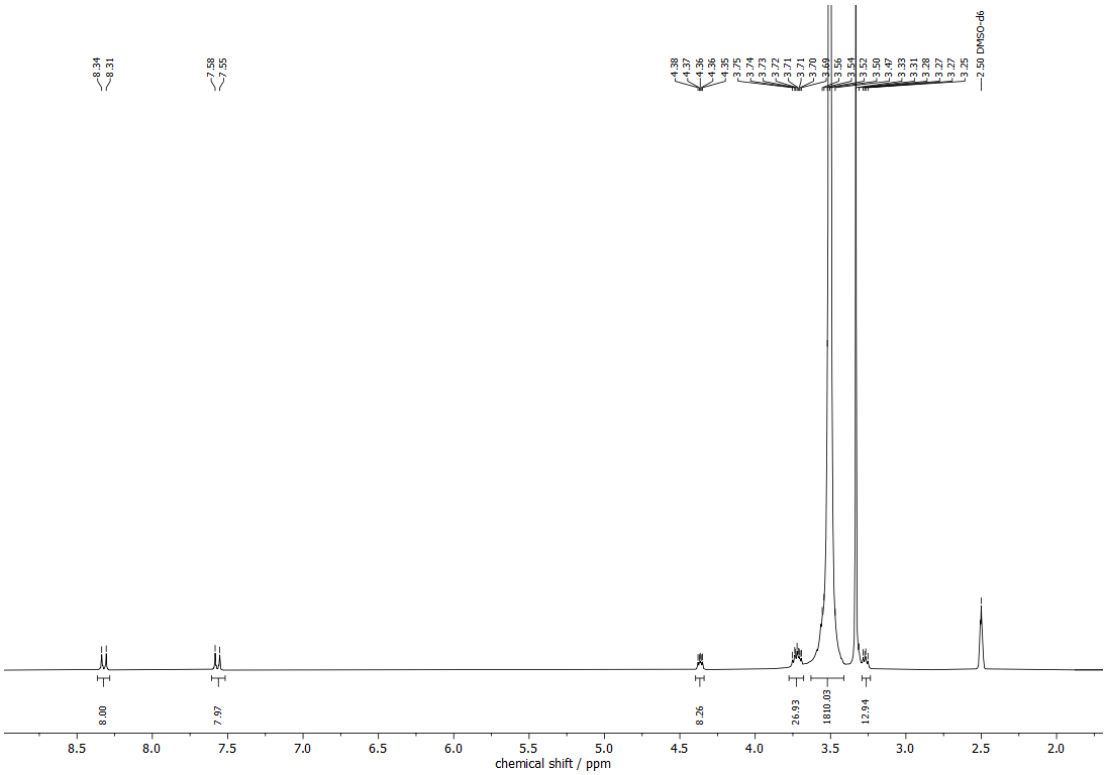

Figure 10.39: ^{1}H-NMR spectrum (300 MHz, CD_2Cl_2, 298 K) of 4arm PEG-*p*-nitrophenylcarbonate (**III-10**).

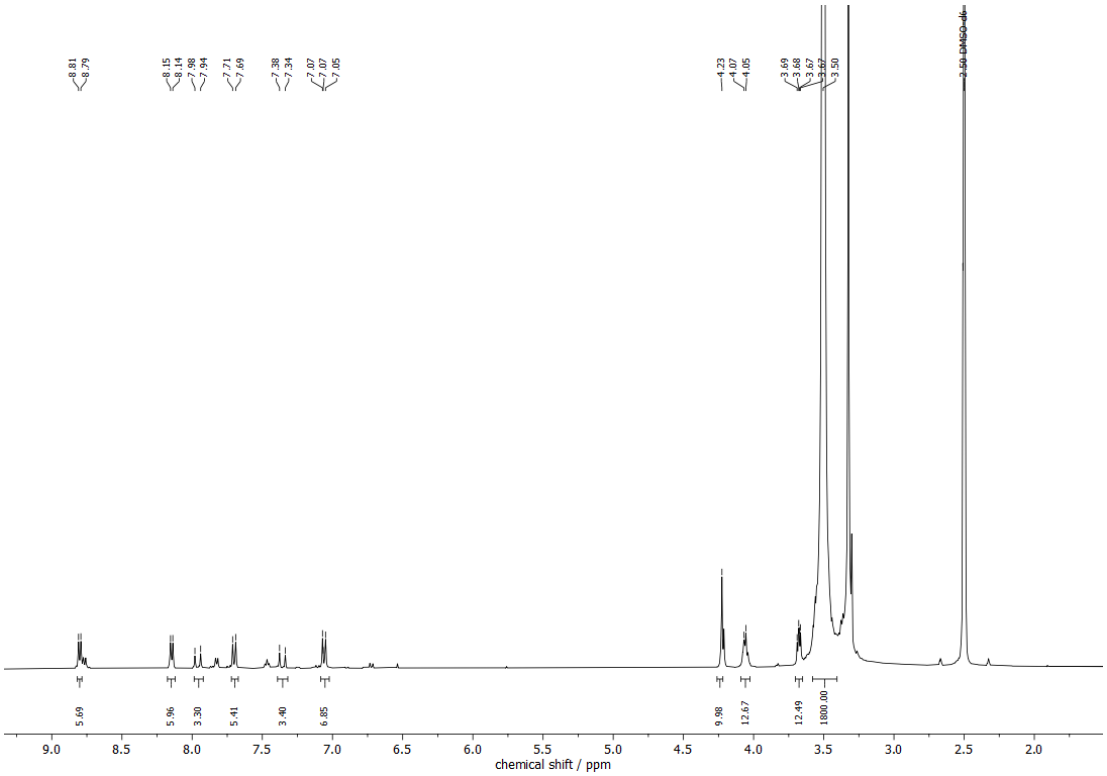

Figure 10.40: ^{1}H-NMR spectrum (400 MHz, dmso-d_6, 298 K) of 4arm PEG-SB (**III-1**).

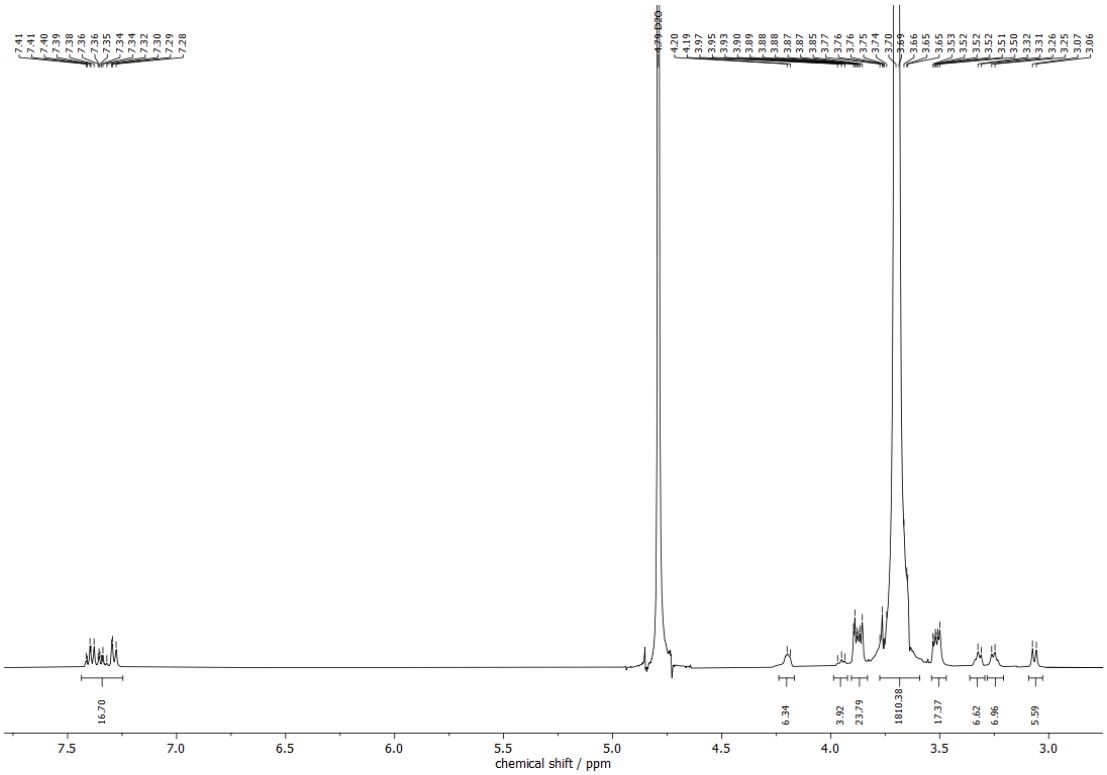

Figure 10.41: ^{1}H-NMR spectrum (400 MHz, D_2O, 298 K) of 4arm PEG-FGG (**III-2**).

Versicherung

für das Gesuch um Zulassung zur Promotion im Fachbereich 09 an der Johannes Gutenberg-Universität Mainz

Hiermit versichere ich gemäß §10 Abs. 3d der Promotionsordnung des Fachbereichs 09 Chemie, Pharmazie und Geowissenschaften der Johannes Gutenberg-Universität Mainz vom 24. Juli 2007 i.d.F.v. 22.08.2012, dass ich die jetzt als Dissertation vorgelegte Arbeit selbständig angefertigt und alle benutzten Hilfsmittel in der Arbeit angegeben habe. Ich habe die Dissertation nicht als Prüfungsarbeit für eine andere Prüfung eingereicht. Ich habe weder die gleiche noch Teile der Abhandlung als Dissertation bei einer anderen Fakultät oder einem anderen Fachbereich eingereicht.

Mainz, 22.09.2024

_____

Yuqing Wang